University of Southampton

Faculty of Engineering and the Environment

Engineering Materials

Fatigue lifing approaches for shot peened turbine components

By Chao You

Thesis for the degree of Doctor of Philosophy

July 2017

UNIVERSITY OF SOUTHAMPTON

ABSTRACT

FACULTY OF ENGINEERING AND THE ENVIRONMENT

ENGINEERING SCIENCES UNIT

Doctor of Philosophy

Fatigue lifing approaches for shot peened turbine components

By Chao You

Life assessment is of great importance to component repair and replacement scheduling of turbine systems which experience cyclic start-up and shut-down operations during their service lives. As vital parts where a severe stress concentration exists, the fir tree blade-disc interfaces are typically shot-peened. Their fatigue resistance is considered to be improved subsequently due to the surface compressive residual stress (CRS) field and strain hardening resulting from shot peening.

However, current life assessment models are relatively conservative, merely considering shot peening as an additional safety factor rather than taking account of the benefits derived from the process. The objective of this research is to develop a life assessment method considering the effects of shot peening in the component lifing protocols. Successful development of this approach will achieve a more cost effective scheduling of repair or replacement of the assets while ensuring sufficient safety margins.

In this study, a low pressure steam turbine material, FV448, has been selected. The shot peening induced residual stress profiles as well as their evolution during fatigue loading were measured using the X-ray diffraction (XRD) technique. In the modelling work, a 3D finite element (FE) modelling approach has been developed to predict the residual stress relaxation behaviour during fatigue loading. Both the CRS and the strain hardening fields arising from shot peening have been reconstructed in the FE model as pre-defined conditions: The reconstruction of residual stresses was realised by the inverse eigenstrain approach. In this study, the application of this approach has been extended from a flat surface to a notched geometry. The strain hardening field was reconstructed by modifying the material parameters at different depths based on the shot peening induced plastic strain distribution, which was evaluated utilising an approach based on previous measurement of electron backscatter diffraction (EBSD) local misorientations. By allowing for both beneficial effects of shot peening, the simulated quasi-static

residual stress relaxation occurring during the first cycle correlated well with corresponding experimental data. The retention of the CRS field in the notched sample during fatigue loading has been highlighted.

The application of total life approaches in predicting the low-cycle fatigue (LCF) life of the shot-peened specimens has been investigated. The Smith-Watson-Topper (SWT) and the Fatemi-Socie (FS) critical plane fatigue criteria have been selected in the present study. The developed FE models incorporating shot peening effects have been used to generate the stress and strain data required by the SWT and FS criteria. A good agreement between experiments and predictions was obtained using this FE-based approach. In addition, the FE analysis shows that the degree of the shot peening benefit in improving fatigue life can be reasonably related to the degree of the reduction in the *mean* stress level within the shot peening affected layer. The application of a critical distance method considering the stress and strain hardening gradients near the shot-peened surface has been found to effectively increase the accuracy of the life prediction.

Damage tolerant approaches have also been employed to assess the fatigue life of the shot-peened notched specimens by predicting the short crack growth behaviour through the shot peening affected layer. This analysis was carried out using both 2D and 3D FE models containing a crack emanating from the notch root. The FE models have been upgraded from the models used to study the residual stress relaxation behaviour. The crack driving force has been appropriately characterised using both linear-elastic and elasto-plastic fracture mechanics (LEFM and EPFM), allowing for the effects of shot peening. An accurate quantification of the retardation of the short crack growth behaviour resulting from shot peening has been subsequently realised. Additionally, the associated crack shape evolution has also been predicted using the developed FE model, which explains the experimentally observed significant differences in crack shape evolution between varying surface conditions. The importance of taking the crack shape effects into account when evaluating the short crack growth behaviour has been emphasised.

Overall, a FE tool has been developed in this study which has been demonstrated to be effective in analysing the benefits of shot peening in improving fatigue life. It also helps unveil the mechanism behind this life improvement, which contributes to the development of a robust and convenient lifing method that can be applied to shot-peened components and can be used to guide shot peening optimisation.

Contents

List of tables

List of figures

DECLARATION OF AUTHORSHIP

I, **Chao You**, declare that the thesis entitled

Fatigue lifing approaches for shot peened turbine components

and the work presented in the thesis are both my own, and have been generated by me as the result of my original research. I confirm that:

1. This work was done wholly or mainly while in candidature for a research degree at this University;
2. Where any part of this thesis has previously been submitted for a degree or any other qualification at this University or any other institution, it has been clearly stated;
3. Where I have consulted the published work of others, it has been clearly attributed;
4. Where the thesis is based on work done by myself jointly with others, I have made clear exactly what was done by others and what I have contributed myself;
5. Parts of this work have been published in:

You, C., Achintha, M., Soady, K., Smyth, N., Fitzpatrick, M., & Reed, P. (2017). *Low cycle fatigue life prediction in shot-peened components of different geometries – Part I: residual stress relaxation*. Fatigue and Fracture of Engineering Materials and Structures, 40(5), 761-775.

You, C., Achintha, M., Soady, K., & Reed, P. (2017). *Low cycle fatigue life prediction in shot-peened components of different geometries – Part II: life prediction*. Fatigue and Fracture of Engineering Materials and Structures, 40(5), 749-760.

You, C., Achintha, M., He, B., & Reed, P. (2017). *A numerical study of the effects of shot peening on the short crack growth behaviour in notched geometries under bending fatigue tests.* International Journal of Fatigue, 103, 99-111.

You, C., He, B., Achintha, M., & Reed, P. (2017). *Numerical modelling of the fatigue crack shape evolution in a shot-peened steam turbine material*. International Journal of Fatigue. 104, 120-135.

Achintha, M., You, C., He, B., Soady, K. A., & Reed, P. A. S. (2014). *Stress relaxation in shot-peened geometric features subjected to fatigue: experiments and modelling*. Advanced Materials Research, 996, 729-735.

Where Soady and He contributed to 85% of the experimental work including residual stress measurements, fatigue life determination and short crack growth characterisation; Smyth and Fitzpatrick provided their X-ray diffraction device and assisted in residual stress measurements; Reed and Achintha provided supervision of

the whole project and were highly involved in relevant discussions; I carried out all of the modelling work and 15% of the experimental work (mainly in residual stress measurements and strain evolution measurements).

Signed: 

Date: 14/07/2017

Acknowledgements

There are a great many people I wish to thank, who have provided me with plenty kind help and support during my four years' PhD study.

First of all, I would like to express my gratitude to my supervisors at the University of Southampton, Prof. Philippa Reed and Dr. Mithila Achintha, for their enlightening guidance, strong support, and continuous encouragement. I am grateful to them so much for generously sharing their time and expertise with me over the past four years, leading my steps through my entire PhD research. The thesis would not have been completed without their significant contributions.

I would also like to thank the examiners of my transfer report, Prof. Janice Barton and Dr. Brian Mellor, who inspired me to think broadly and deeply in my research. Thanks must also be extended to Dr. Katherine Soady (now at Uniper Technologies Ltd.) and Dr. Binyan He, for their fantastic experimental work which has greatly supported the development of my models. I also benefited a lot from the academic discussions with them.

I am also indebted to Dr. Niall Smyth and Prof. Michael Fitzpatrick at Coventry University, for generously offering their XRD, hole drilling and electro-polishing facilities. Dr. Niall Smyth is particularly acknowledged for spending a whole week assisting me with residual stress measurements. Gary Harrison at the University of Manchester is also acknowledged for his help with XRD measurements. I must also thank Dr. Rong Jiang and Dr. Andy Robinson for guiding me to use the Instron servo-hydraulic machine and to use strain gauges. The experimental data generated by relevant tests has played a critical role in validating the models developed during my PhD. Dr. Daniel Child at Rolls-Royce, Dr. Mark Whittaker, Dr. Nick Barnard and Dr. Ben Cockings at Swansea University are greatly thanked for providing me with a large amount of experimental data, which has been extremely useful in extending the application of my models to a new material system. I would also like to thank the administrative staff, particularly Sue Berger and Katherine Day, for their frequent help.

I deeply appreciate the financial support from the University of Southampton, Engineering and Physical Science Research Council (EPSRC), UK, and China Scholarship Council (CSC).

On a personal note, I am lucky to have many friends in the Engineering Materials and nCATS Research Groups, who have made my life in Southampton quite enjoyable. The time spent with you guys is very relaxing and pleasant and that will always be on my

mind. To my parents who have been providing enduring support and encouragement with me, I will be thankful for your love, the love that gives me strength and courage to pursue my dreams, the love without which I would not be who I am today. Being your son is the luckiest thing in my life. My parental grandfather, I have been missing you so much these years and how I wish you could be here to see this moment. My maternal grandparents, aunts, uncles and cousins, thank you all for offering me an extremely warm family atmosphere, which is an invaluable asset in my life.

Last but not least, to my immortal beloved, Qiaoyun Xie, thanks for your appearance in my life, which has sparkled my last year in Southampton and the life thereafter. I am really blessed to have your love and support. You are always where my inner peace comes from through highs and lows.

Nomenclature

a	Half size of the centre crack, depth of a semi-elliptical crack
$\boldsymbol{a}$	Backstresses
a_c	Critical length of the crack
$\boldsymbol{a_k}$	The k^{th} backstress
a_{k_0}	Initial value of the k^{th} backstress during one cycle
a_{max}	The maximum backstress
a/c	Crack aspect ratio
da/dN	Change of the crack length per fatigue cycle
b	Fatigue strength exponent
c	Half surface crack length
d	Fatigue durability exponent
m	Paris law constant
m'	J-integral constant
q	The parameter controlling the curvature in the near threshold region of the da/dN - ΔK plot
r	Rate at which the size of the yield surface changes as plastic strain accumulates in isotropic hardening
s	Loading span in the 3/4 point bend test
$\boldsymbol{u}$	Displacement vector
v	Poisson's ratio
w	Strain energy density
z	Depth from the surface
B	Breadth of the sample
B_i	Fitting parameter used to describe the value of the J-integral in 3D crack modelling
C	Paris law constant
C'	J-integral constant

C_i	Coefficients of Chebyshev polynomials
D_{ij}	Fitting parameter used to describe the value of the J-integral in 3D crack modelling
C_k	Initial kinematic hardening moduli
E	Young's modulus of the material
J	*J*-integral
K	Stress intensity factor
K_{app}	Applied stress intensity factor due to external load
K_{eff}	Effective stress intensity factor
K_{eff_min}	Minimum Effective stress intensity factor
K_{eff_max}	Maximum Effective stress intensity factor
K_I	Onset of crack propagation under monotonic quasi-static loading (tensile cracking mode)
K_{IC}	Fracture toughness
K_{max}	Stress intensity factor under maximum load within one cycle
K_{min}	Stress intensity factor under minimum load within one cycle
K_{open}	Stress intensity factor when the crack is fully open
K_{res}	Residual stress intensity factor
K_p	Equivalent stress intensity factor in EPFM
K_t	Stress concentration factor
ΔK	Stress intensity factor range
ΔK_{th}	Threshold value
ΔK_{eff}	Effective stress intensity factor range
$\Delta K_{eff,A}$	Effective stress intensity factor range at the deepest of a 3D crack
$\Delta K_{eff,C'}$	Effective stress intensity factor range at a near surface point of a 3D crack
ΔK_{p_eff}	Effective equivalent stress intensity factor range
L	Remaining ligament
M	The number of experimental data points in the inverse eigenstrain method

N	Number of Chebyshev polynomials
N_f	Total number of cycles to failure
P	Applied load
P_{max}	Peak load
Q_∞	The maximum change of the size of the yield surface
R_a	Arithmetical mean vertical deviation of the assessed roughness line profile from the mean line
R_ε	Strain ratio
R_p	Load ratio
R_σ	Stress ratio
R_z	Maximum height of roughness profile
R^2	The coefficient of determination
S_a	Arithmetical mean vertical deviation of the assessed roughness areal profile from the mean surface
S_z	Maximum height of the roughness scale limited surface
T_i	Chebyshev polynomials
$\boldsymbol{T}$	Traction vector
W	Width of the sample
γ	Shear strain
γ_k	The decreasing rate of the kinematic hardening moduli with increasing equivalent plastic strain
$\Delta\gamma_{max}$	The maximum shear strain range perpendicular to a plane during fatigue loading
δ_t	Crack tip opening displacement
δ_{tc}	Critical CTOD value
ε^{pl_0}	Initial plastic strain during one cycle
$\bar{\varepsilon}^{pl}$	Equivalent plastic strain
$\dot{\bar{\varepsilon}}^{pl}$	Equivalent plastic strain rate
$\dot{\boldsymbol{\varepsilon}}^{\boldsymbol{pl}}$	Plastic strain rate

ε_e	Sum of the elastic strain
$\varepsilon_f{}'$	Fatigue ductility coefficient
ε_n	Strain perpendicular to a plane
ε_p	Plastic strain
ε_{pxx}	The longitudinal plastic strain
ε_{pyy}	The transverse plastic strain
ε_r^{eigen}	The principal eigenstrain component perpendicular to the notch curvature
ε_t^{eigen}	The principal eigenstrain component tangential to the notch curvature
ε_{xx}^{eigen}	The longitudinal principal eigenstrain component
ε_{yy}^{eigen}	The transverse principal eigenstrain component
ε_{yy}	Total strain in the y (transverse) direction
ε_{zz}^{eigen}	The principal eigenstrain component in the depth direction
$\Delta\varepsilon$	Strain range
$\Delta\varepsilon^{pl}$	Plastic strain range
$\Delta\varepsilon^{pl\_avg}$	Averaged plastic strain range
$\Delta\varepsilon_n$	The strain range perpendicular to a plane during fatigue loading
$\Delta\varepsilon_{xx}$	Strain range in the longitudinal direction
σ^0	Size of the yield surface
$\sigma\vert_0$	Yield stress at zero equivalent plastic strain
$\sigma_{0.2}$	Proof stress at 0.2% plastic strain point
σ_a	Stress amplitude
σ_f	The true fracture strength in a monotonic tension test
$\sigma_f{}'$	Fatigue strength coefficient
σ_m	Mean stress
σ_{m_SP}	The mean stress levels in shot-peened samples
σ_{m_UP}	The mean stress levels in un-peened samples
σ_{max}	Maximum stress

σ_{max_0}	The maximum stress for the first cycle
σ_{max_s}	The maximum stress for the stabilised cycle
σ_{mres}	Peak compressive residual stress
σ_{Mises}	Mises equivalent stress
σ_n	Stress perpendicular to a plane
$\sigma_{n,max}$	The maximum tensile stress perpendicular to a plane during fatigue loading
σ_{nom}	Nominal stress
σ_{res}	Residual stress
σ_{TS}	Tensile strength
σ_{xx}	Residual stress in the x (longitudinal) direction
$\sigma_{xx_i}^{FE}$	The simulated longitudinal residual stress obtained as an elastic response to each eigenstrain base function
σ_{xx}^{FE}	The simulated longitudinal residual stress
σ_y	Yield strength
σ_{yy}	Residual stress in the y (transverse) direction
$\Delta\sigma/2$	Constant stress amplitude
φ	The angle of the plane in critical plane methods

CRS	Compressive residual stress
CTOD	Crack tip opening displacement
EBSD	Electron backscattered diffraction
EDM	Electrical discharge machining
EPFM	Elastic-plastic fracture mechanics
FE	Finite element
FS	Fatemi-Socie
FWHM	Full width at half maximum
HCF	High-cycle fatigue
KAM	Kernel average misorientation
LCF	Low-cycle fatigue

LEFM	Linear elastic fracture mechanics
NDT	Non-destructive testing
PEEQ	Equivalent plastic strain
PID	Proportional-integral-derivative
PBB	Plain bend bar
SEM	Scanning electron microscope
SENT	Single edge notch tension
SWT	Smith-Watson-Topper
XRD	X-ray diffraction

1 Introduction

1.1 Background

1.1.1 Steam turbines and their working conditions

Power generation is the process of generating electricity from other sources of energy, e.g. coal, water, wind, nuclear energy etc. Nowadays, many large-scale power plants across the world use turbine systems, among which steam turbines produce more electrical energy than any other system. The steam turbine is a device that converts thermal energy from pressurised steam to mechanical rotation of an output shaft, which drives the electricity generator. Figure 1-1 illustrates a simplified steam cycle in the power plant. The efficiency of the thermodynamic process in steam turbine systems describes how much of the energy fed into the cycle is converted to electrical energy. To improve the thermal efficiency, typical steam turbines use multiple stages to allow for sufficient expansion of the steam. These stages include the high-pressure (HP), intermediate-pressure (IP) and low-pressure (LP) sections as shown in Figure 1-1.

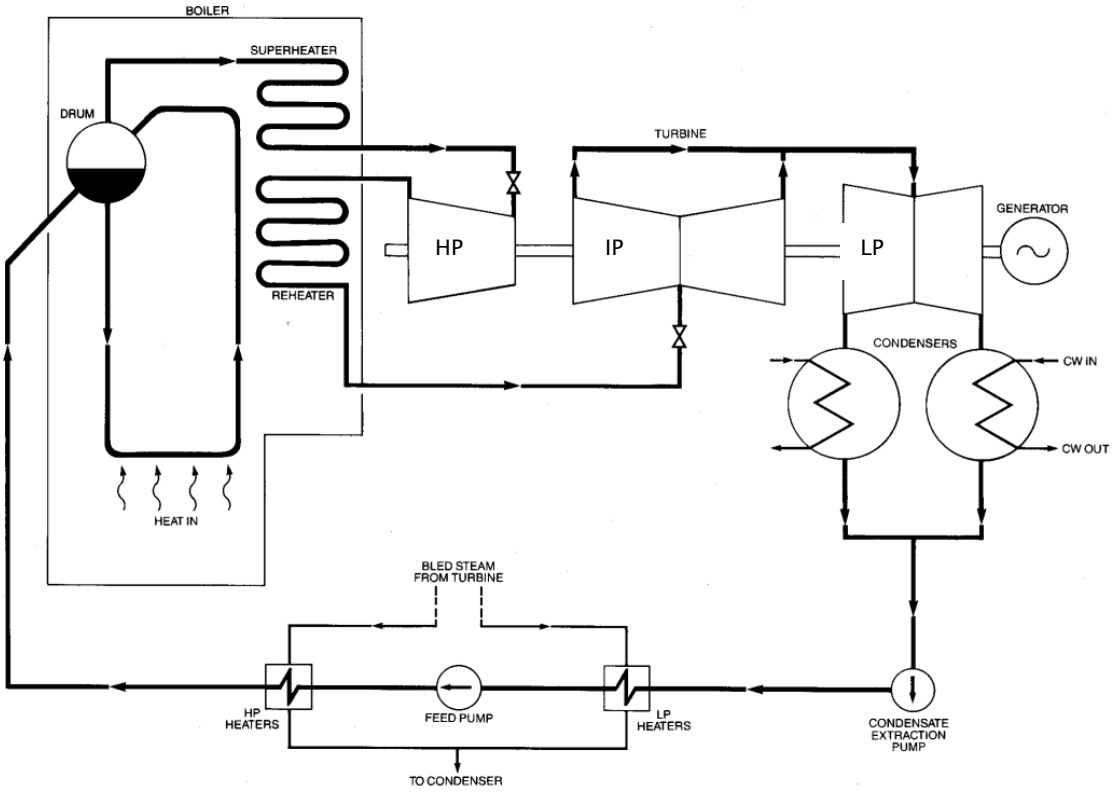

Figure 1-1: Simplified steam cycle in the power plant [1].

Subcritical steam cycle power stations remain the dominant technology in power generation plants of 1960s vintage, such as Ratcliffe on Soar, Nottingham, UK [2]. The steam (~ 568℃, 180 bar) generated by the boiler flows first through the HP turbine in steam turbine systems. Both the temperature and pressure of the steam drop during this process and the steam is reheated (~ 568℃, 30 bar) before entering the IP turbine. After the IP turbine, the steam passes through the LP turbine with much lower temperature and pressure (< 350℃, 10 bar) as much energy has been extracted. Each turbine section is mainly composed of a number of sets of blades which are connected to the central disc using the fir tree interface (as shown in Figure 1-2). The rotation speed is usually ~ 3000 rpm [2]. In the LP turbine section, since the velocity and pressure of the steam is lower than in the HP and IP turbines, the blades are usually larger in size than those used in HP and IP turbines in order to increase the effective area.

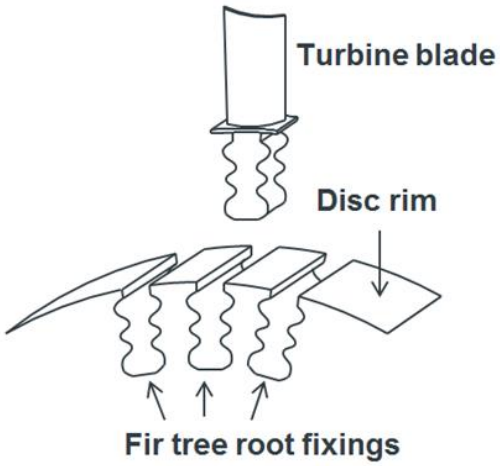

Figure 1-2: Connection of blades to disc [3].

In service, steam turbine components are subjected to fatigue, which is similar to other machine components. In general, the stresses acting on the blades that invoke fatigue mainly originate from centrifugal loading and the vibration caused by the asymmetric steam flow [4]. Statistics show that LP turbine blades are generally more susceptible to fatigue failure compared to those of the HP and IP, which is due to the greater centrifugal forces and higher possibility of the occurrence of resonance resulting from the increased blade length in LP turbines [4, 5]. Creep damage is not important for the LP blades due to its relatively low working temperature compared with the IP and HP blades.

It is reported that fatigue failure may initiate from various locations of the LP blade, such as the shroud, the lacing hole, the aerofoil region and the fir-tree root [6], implying the varying failure mechanisms along the length of the blade. In general, high-cycle fatigue (HCF, the total number of cycles $N_f > 1 \times 10^5$) may occur when the blade experiences

high dynamic stresses resulting from the vibration and resonance at critical speeds [5]. On the other hand, the alternating centrifugal force generated during the repeated start-up and shut-down operation may induce low-cycle fatigue (LCF, $N_f < 1 \times 10^5$), especially in the fir tree root with a high stress concentration (as shown in Figure 1-2) [7].

In steam turbine systems, since the blades are responsible for extracting energy from high pressure and high temperature steam, their design has a direct effect on the efficiency and reliability of the whole system. In light of the complexity of the working environment and the stress condition of the blade, 9-12% Cr ferritic heat resistant steels have been widely used in steam turbine blades. This is due to their lower coefficient of thermal expansion and higher thermal conductivity compared with other candidate materials (such as austenitic stainless steels) as shown in Table 1-1. Use of this material can reduce the thermal stresses experienced during start-up and shut-down, resulting in lower susceptibility to fatigue in steam turbines [8].

Table 1-1: Comparison of coefficient of thermal expansion and thermal conductivity for a ferritic and an austenitic stainless steel [9].

	12Cr ferritic steel	20Cr1Ni austenitic steel
Thermal conductivity / μK^{-1}	24.9	13.5
Coefficient of Thermal expansion at room temperature / $Wm^{-1}K^{-1}$	9.9	15.3

1.1.2 Shot peening treatment to increase fatigue resistance of components

Shot peening is a surface treatment which is commonly used in a range of engineering applications to increase the fatigue resistance of metallic components containing stress concentration features (such as the fir tree interface of the turbine). This improvement is normally attributed to surface compressive residual stresses and strain hardening resulting from shot peening acting to mitigate crack initiation and propagation, which is reviewed in more detail in Sections 2.2.2 and 2.2.3.

During the process of shot peening, the surface of the workpiece is bombarded by a stream of small spherical shots acting as tiny peening hammers. As shown in Figure 1-3, the kinematic energy of the shots causes small indentations or dimples on the impacted surface. To create the dimples, the material in the surface layer yields in tension, resulting in a plastic misfit strain (i.e. the eigenstrain) between the peening-affected layer and the bulk (elastic) material. As a result of this, a compressive residual stress field

near the peened surface is generated with a counterbalancing tensile residual stress field below to achieve overall stress equilibrium within the workpiece.

Shot peening is controlled in practice by monitoring two parameters, known as peening intensity and coverage. The intensity is referred to as the Almen intensity which is evaluated by measuring the deflection of a shot-peened normalised strip (i.e. the Almen strip). There are three kinds of Almen strips with different thickness, namely 'N', 'A' and 'C'; an intensity value of 10A indicates a 0.01 inches (0.254 mm) deflection of an 'A' strip. The coverage represents the percentage of the peened area to the whole surface; a coverage higher than 100% indicates that the peening time achieving 100% coverage has been increased by the corresponding factor.

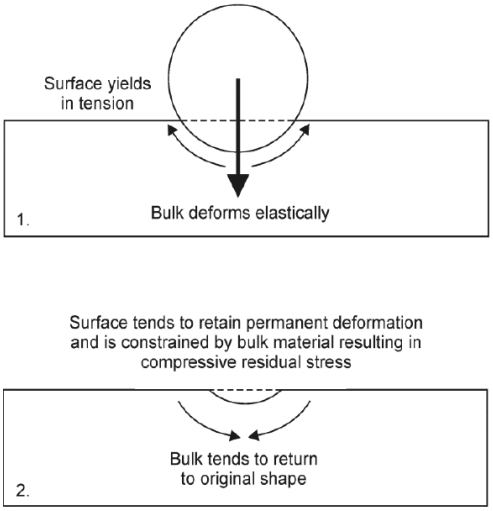

Figure 1-3: Mechanism of formation of compressive residual stresses during shot peening [10].

1.1.3 Steam turbine maintenance practice

Steam turbine inspections are carried out approximately every 12 years. Non-destructive testing (NDT) is used to determine the critical condition of defects during the inspection, especially in the regions where crack initiation and subsequent propagation will most probably occur, e.g. the fir tree interface. Common NDT methods include the application of ultrasonics, remote visual inspection, magnetic particle inspection, eddy current testing, etc. [11]. The inspection results are then used as the basis of applying a damage tolerant lifing approach (such as linear elastic fracture mechanics) to predict the remaining life of the components and determine their repair schedule.

Many steam turbine systems in the UK were built in the 1960s and have therefore undergone more than 3500 start-up/shut-down cycles [10]. These aging components must be safely assessed to allow appropriate repair or replacement. A major outage of

a conventional power plant commonly takes 8-12 weeks, which will cause a substantial cost in the lost generation of electricity over this period [10]. Thus developing life assessment methods with reduced conservatism is of significant economic benefit to reduce the refurbishment scope and frequency safely.

1.2 Fatigue in metallic materials

Fatigue is an important failure mode of materials or components subjected to alternating loads. Suresh [12] defined fatigue as a term which 'applies to changes in properties which can occur in a material due to the repeated application of stresses or strains'. It is usually influenced by the material microstructure, material mechanical properties, geometry of the component, loading conditions, environmental conditions, etc. Before the main literature review (Chapter 2), which focuses on discussing the effects of shot peening on the fatigue behaviour of metals and the development of relevant lifing methodologies, it is essential to introduce the main processes involved in the fatigue damage process. Fatigue damage generally progresses through three stages, namely initial cyclic damage (cyclic hardening or softening), crack initiation and crack propagation (including both short and long crack propagation processes). The general background of each stage is briefly introduced in Sections 1.2.1 to 1.2.3. The majority of this introduction is based on Suresh's Fatigue of Materials [12], unless otherwise cited.

1.2.1 Cyclic deformation behaviour of metals

It is possible for a material to harden, soften, or experience a combination of both during cyclic loading. Cyclic hardening and softening behaviours are commonly represented by the evolution of stress range during a strain-controlled test with a constant strain amplitude. The stress range usually reaches a stable saturation value after an initial 'shakedown' period. Strain-controlled tests are usually chosen over the stress-controlled tests to determine the cyclic behaviour of the material since they represent the fully constrained loading condition, which is consistent with the constraint condition of the material at fatigue-critical sites in real engineering components.

The typical cyclic hardening and softening behaviours are illustrated in Figure 1-4(a) and (b) respectively. As shown in Figure 1-4(a), cyclic hardening results in an increase of the stress range with increasing number of cycles before reaching saturation represented by a plateau. In contrast, cyclic softening results in a decrease of stress range with increasing number of cycles, the decreasing rate considerably slows down before achieving a quasi-plateau, which is illustrated in Figure 1-4(b).

The evolution of the dislocation substructure is an important indicator of the cyclic hardening and softening behaviour. There is usually a continual change in dislocation substructure during the 'shakedown' stage before the saturation is achieved, with much less significant changes during progressive cycling until the failure occurs. However, it is noteworthy that the evolution of the dislocation substructure is not the only mechanism of the cyclic hardening and softening behaviour. For example, the interaction between dislocations and precipitates can result in additional softening by destroying the precipitates through to-and-fro motion of dislocations, or leads to hardening effects caused by secondary precipitations assisted by moving dislocations [13].

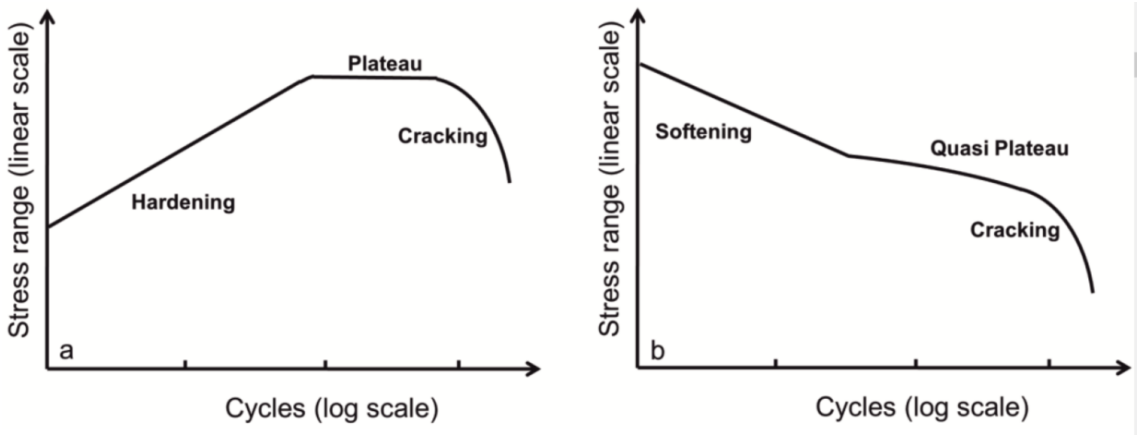

Figure 1-4: Variation of stress range with cycles under constant amplitude strain controlled loading for (a) a cyclically hardening material and (b) a cyclically softening material [14].

1.2.2 Crack initiation

In defect-free (un-notched) metals and alloys, fatigue cracks are normally observed at the free surface, which has been postulated to be caused by the repeated cyclic straining of the material leading to different amounts of net slip on different glide planes. The irreversibility of the shear displacement along the slip bands then results in a roughened surface of the material. The resultant microscopic 'hills' and 'valleys' (along the slip bands) at the roughened surface (as shown in Figure 1-5) are commonly referred to as 'intrusions' and 'extrusions' respectively. The intrusions act as micro-notches with a stress concentration feature promoting additional slip and crack nucleation. Fatigue cracks generally nucleate in this manner along those bands where slip is particularly intense. These slip lines are termed as persistent slip bands (PSBs), which appears to be closely related to the occurrence of the plateau shown in Figure 1-4. The interface between the PSB and matrix is a preferential site for crack nucleation due to the abrupt gradients in the density and distribution of dislocations across the plane.

However, it is noted that the above mechanism only applies to crack initiation in defect-free materials. In engineering components, the crack nucleation process may be facilitated by the presence of inclusions, voids, macroscopic stress concentrations and other manufacturing defects or surface processes (such as shot peening). In engineering terms, the crack initiation life is often defined as the time taken to initiate and grow a crack to a length detectable by the NDT technique. This is different from the definition widely used by material scientists who commonly consider the nucleation of a flaw from PSBs as representing fatigue initiation.

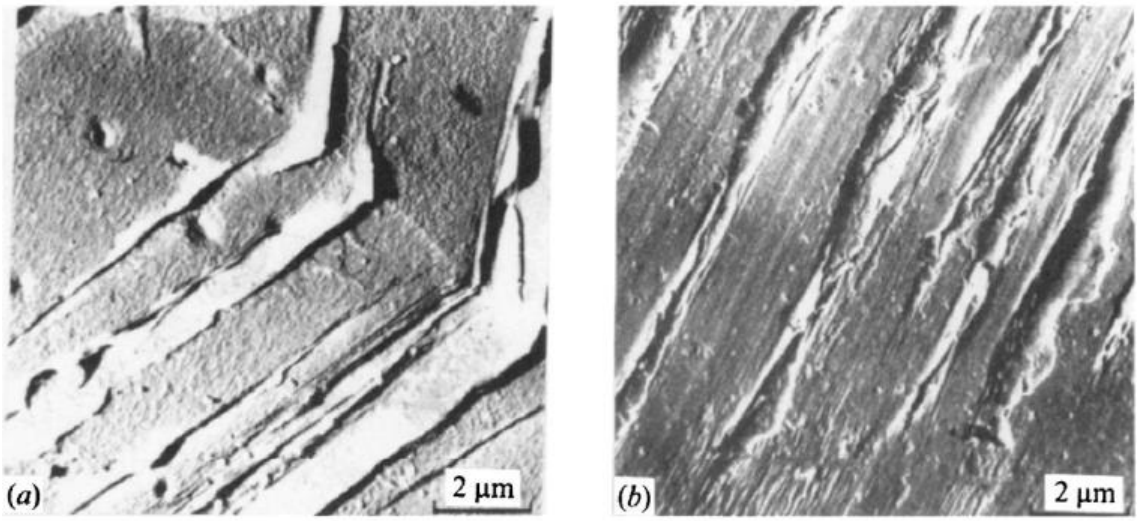

Figure 1-5: (a) Intrusions and (b) extrusions along slip bands in polycrystalline Cu fatigued at -183℃ [15].

1.2.3 Crack propagation

The fatigue crack propagation process in polycrystalline materials can be typically classified into two stages in terms of the differing micromechanism by which the fatigue crack grows.

In stage I, the crack and the zone of plastic deformation surrounding the crack tip are confined within a few grain diameters. This type of crack growth is highly microstructurally dependent; the dislocation along the primary slip plane experiencing the maximum shear stress is likely to cause crack growth, leading to a zigzag crack path.

In stage II, the plastic zone at the crack tip encompasses many grains because of higher stress intensity range values, resulting in simultaneous dislocation movement along multiple slip systems. This mechanism leads to a crack growth path perpendicular to the remote applied stress. It has been observed that the crack growth at this stage in many engineering alloys leads to the formation of fatigue striations at fracture surfaces. It has

also been found that the spacing between adjacent striations correlates with the experimentally measured average crack growth rate per cycle. However, fatigue striations occur very infrequently in steels and are often barely visible in cold-worked alloys.

The crack growth behaviour can be described using either the linear-elastic or elasto-plastic fracture mechanics (LEFM and EPFM). These can be reliable methods enabling a quantification of the intrinsic resistance of the material to fatigue crack growth. Both approaches are reviewed in detail in Section 2.3.2.

1.3 Motivation and objectives

Since shot peening has beneficial effects on the fatigue behaviour of safety critical components, it is important to incorporate its effects into life assessment methods. However, current lifing models are relatively conservative without explicitly taking account of the benefits derived from this treatment in the lifing calculation, merely considering shot peening as an additional safety factor. This could be improved if the effects of shot peening were included in the component lifing protocols. For example, modelling how the stress and strain evolve and how a fatigue crack initiates and grows in the shot peening affected layer. Successful development of this approach will achieve a more cost effective scheduling of repair or replacement of the assets while ensuring sufficient safety margins.

The overall project aims at developing a life assessment model incorporating the effects of shot peening on low-cycle fatigue (LCF) behaviour of a low-pressure (LP) turbine blade material (9-12% Cr ferritic heat resistant steel). U-notched samples representing the LP turbine blade to disc interface have been selected as the component for method development. The main objectives of this study are:

a. Numerical/experimental modelling of stress concentration and strain hardening development in notched bend samples representing real components when subjected to fatigue;
b. Development of a finite element (FE) model to simulate the as-peened surface condition in notched samples subjected to shot peening;
c. Experimental/Numerical modelling of the residual stress relaxation behaviour in shot-peened components during LCF;
d. Development of total life approaches for the simplified shot-peened component;
e. Experimental/Numerical modelling of the mechanisms of propagation of microcracks (starting from a pre-initiated defect, as seen in parallel experimental studies) in shot-peened samples;

f. Development of damage tolerant approaches for the simplified shot-peened component.

This project is an extension of previous work [10, 16] undertaken by Dr. Katherine Soady and Dr. Binyan He, who carried out extensive experimental tests on residual stress measurements, fatigue life determination and short crack growth characterisation. In the present study, most experimental data that have been used as either input or validation of the developed numerical models were referenced from their work, as indicated in detail in each chapter.

1.4 Arrangement of the thesis

This thesis comprises nine chapters and the remaining chapters are arranged as follows:

Chapter 2 is the literature review which provides a more detailed context of the present study. It reviews the outcomes of previous research focusing on the effects of shot peening on fatigue, relevant modelling work and the associated life assessment methods. A summary is presented at the end of this chapter to shed light on how the prior work affects the direction of the present research and how the current proposed study contributes to this field.

Chapter 3 introduces the development of the preliminary FE model before shot peening effects are taken into account. Different material models have been developed and compared in this chapter in order to make the most appropriate choice. Some results with respect to the validation of this preliminary FE model are also presented in this chapter.

Chapter 4 details modelling of the interactions between the shot peening induced effects and service conditions. The methods applied to realise the reconstruction of the as-peened compressive residual stress (CRS) and strain hardening field are firstly introduced in this chapter. This chapter also presents the simulation of the residual stress relaxation behaviour in shot-peened samples after the quasi-static loading cycle (the first cycle). Experimental data acting as validation resources are provided together with corresponding modelling results. In addition, the mechanisms for residual stress relaxation are elaborated using the modelling results.

Chapter 5 introduces the application of the total life approaches in predicting the fatigue life of the shot-peened specimens. The applied lifing procedure is detailed in this chapter. Methods that can be used to improve the accuracy of the life prediction are also discussed. Finally, a comparison between different total life approaches is carried out and their limitations are discussed.

Chapters 6 and 7 elaborate the application of damage tolerant approaches to the shot-peened samples. Both 2D (Chapter 6) and 3D (Chapter 7) FE models containing a crack have been developed based on the FE model introduced in Chapter 4. The investigation of the short crack growth behaviour through the shot peening affected layer using the developed models are discussed in this chapter, along with some experimental observations. The prediction of the short crack growth process affected by shot peening is also presented. In addition, the importance of considering the crack shape when studying the short crack growth behaviour is comprehensively discussed.

Finally, the conclusions based on the results obtained in the current study are given in Chapter 8. The potential future directions arising from the current study are presented in Chapter 9.

2 Literature review

As introduced in Section 1.1.2, shot peening is an effective surface treatment method used to improve the fatigue resistance of metallic components, particularly in regions with stress concentration features. Surface roughness, together with near-surface compressive residual stresses and strain hardening, are considered to be the three main effects caused by shot peening. The compressive residual stress field is generally considered to be the main factor accounting for the improvement in fatigue resistance due to its counteraction of external applied tensile stresses. Strain hardening is also considered as a beneficial factor because it may restrict plastic deformation, which is advantageous in prolonging fatigue life; whilst surface roughness, on the other hand, may exert a detrimental influence on fatigue resistance due to the increased local stress concentration. Generally, the overall influence of shot peening on fatigue is attributed to the combined effects of these three factors. Consequently, an accurate estimation of the fatigue life of shot-peened components requires a robust tool which can comprehensively analyse the interaction between these shot peening induced effects and the applied service conditions. Such a tool could also accurately quantify this interaction based on the fundamental mechanisms and provide a valuable optimisation approach. During recent years, in order to reduce the conservatism of current lifing approaches applied to shot-peened components, there has been an increasing interest in this topic.

This chapter provides a comprehensive review regarding this topic. The first part (Section 2.1) of this chapter introduces methods used to characterise the shot-peened surfaces and surface layers. This lays the foundation for the investigation of the influence of shot peening on fatigue life of components, which is reviewed in the second part (Section 2.2) of this chapter. Then, the classical fatigue lifing approaches (total life and damage tolerant approaches), as well as their further development considering shot peening effects, are reviewed in the third part (Section 2.3) of this chapter. Finally, the key gaps in the current understanding are summarised based on the literature review, according to which the direction of the present study is more clearly specified, as summarised in the last part of this chapter (Section 2.4).

2.1 Quantitative characterisation of shot-peened surfaces and surface layers

How to accurately characterise the surface roughness, the residual stress and strain hardening distributions resulting from shot peening, and how to effectively use the obtained characterisation data in any subsequent fatigue analysis, are the preliminary,

critical steps in the development of appropriate lifing approaches. Hence the first part of the literature review summarises and discusses: (1) experimental techniques used to characterise the surface roughness (Section 2.1.1), (2) the residual stress (Section 2.1.2) and (3) strain hardening (Section 2.1.3) distributions. Relevant modelling approaches, which are used to incorporate this experimentally determined information (representing the effects induced by shot peening) into finite element (FE) models, are then reviewed.

2.1.1 Surface roughness

Surface roughness, which is normally used to describe the surface condition after shot peening, can be represented by many parameters. R_a, which is defined by Equation 2-1, is the arithmetical mean vertical deviation of the assessed 2D roughness profile from the nominal (mean) line (as shown in Figure 2-1). Another parameter is R_z, which indicates the peak to valley measurements. Both R_a and R_z remain the two most popular parameters which are used to quantify the surface roughness caused by shot peening. Their values can be measured by a profilometer. Both contact (tactile) and non-contact (optical) measurements can be applied but it has been found that there is no significant difference between the results obtained using these two methods for shot-peened surfaces [17].

$$R_a = \int_0^{L_m} \frac{|y|}{L_m} dx \tag{2-1}$$

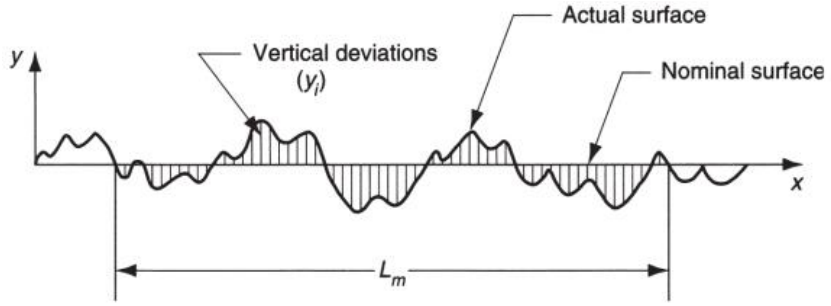

Figure 2-1: Deviations of the actual surface from the nominal surface [18].

In addition to the 2D techniques, 3D topographical characterisation has also been used to evaluate the surface roughness by introducing areal equivalent parameters, S_a [19]. A typical 3D topography of the roughened surface is shown by Figure 2-2. Soady et al. [17] compared the results measured by 2D line and 3D areal scanning techniques and indicated that although the average amplitude parameters (R_a and S_a) were consistent, S_z (areal equivalent parameter to R_z) was significantly higher than R_z, which implied the greater probability of the 3D areal scanning method in capturing the worst (more extreme) case across a surface.

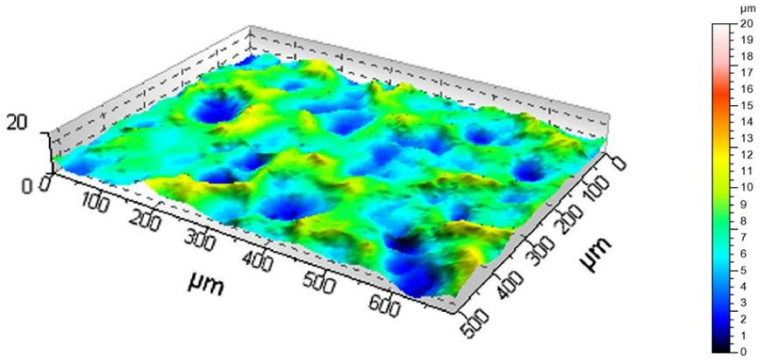

Figure 2-2: Three-dimensional reconstruction by white light interferometry of 6-8A intensity and 200% coverage peening applied to Ni based alloy Udimet 720Li illustrating surface topography (S_a = 1.51) [19].

The degree of roughening of the peened surface was found to increase monotonically with increasing peening intensity [20-22]. However, a saturation point has been discovered by some researchers if the peening intensity increases continuously [19, 23].

2.1.2 Residual stress profiles

A typical compressive residual stress (CRS) distribution as a result of shot peening has a 'hook' shape as shown in Figure 2-3, which is directly related to the plastic strain distribution generated by shot peening; the generation of residual stresses is essentially a process of self-equilibrium in reaction to the plastic misfit strain (eigenstrain) within the workpiece. Wohlfahrt [24] indicated that there were two basic processes inducing plastic deformation during shot peening, namely the Hertzian pressure and stretching of the surface layer, as illustrated in Figure 2-4. The Hertzian pressure, which is a consequence of the vertical force resulting from the impact of shots, generates the maximum plastic deformation beneath the peened surface at the depth where the maximum shear stress occurs. In contrast, stretching of the surface layer results in a significant difference between the plastically extended surface layer and the bulk material, generating the maximum plastic strain at the surface. The actual peening process is a combination of these two basic processes, and the influence of Hertzian pressure is usually more dominant when relatively soft shots impinge on hard materials [25]. The peak CRS, σ_{res_max}, normally exists at the depth experiencing the greatest reverse plastic flow during the bouncing-back of the shot [26].

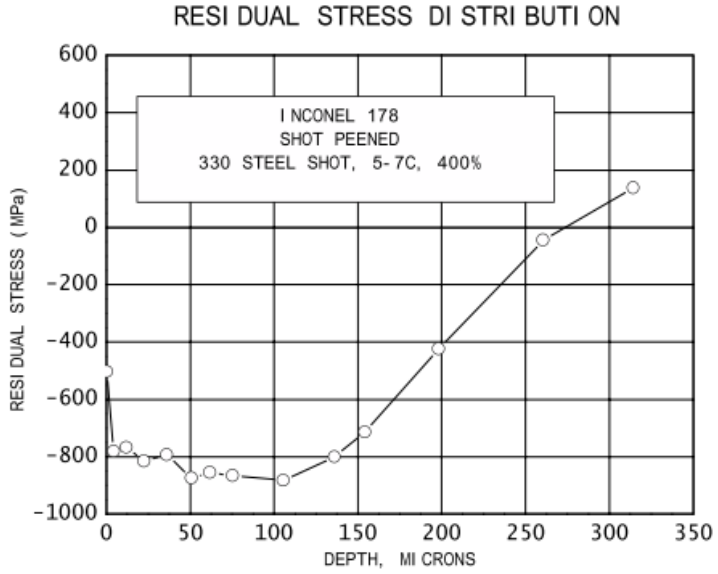

Figure 2-3: Residual stress distribution produced by high intensity (5-7A, 400%) shot peening of Inconel 718 [27].

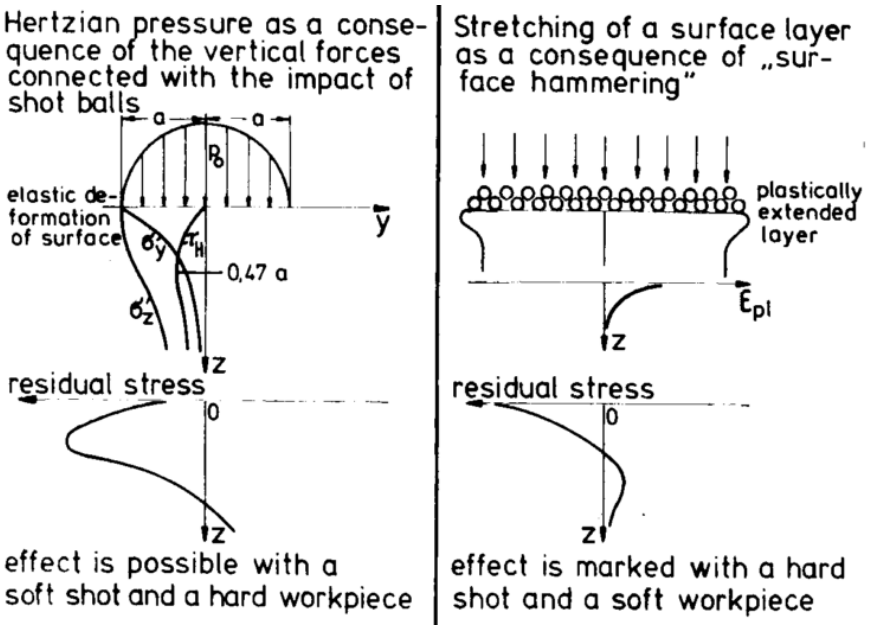

Figure 2-4: Schematic illustration of the formation of residual stresses as a consequence of two competing processes in shot peening: Hertzian pressure (left) and direct stretching of a surface layer (right) [24].

The depth of the CRS field has been demonstrated to increase with increasing peening intensities [23, 25, 28]. However, when σ_{res_max} is comparable to the local yield strength of the mateiral, simply increasing the peening intensity may not necessarily increase σ_{res_max} [28]. Additionally, surface residual stress relief may occur due to the Bauschinger

effect [1] when a high peening intensity is applied [29], resulting in an enlarged difference between σ_{res_surf} and σ_{res_max}. It is noteworthy that peening intensities are not unambiguously correlated with the induced residual stress distributions; different combinations of shot sizes and velocities resulting in the same peening intensity may, however, lead to different residual stress profiles [28]. In addition, the thickness (constraint) of the workpiece may also influence the residual stress profile; Tosha [30] found that in order to induce sufficient residual stresses by shot peening in specimens made of S45C (a medium carbon steel), the thickness of the workpiece should be at least five times the depth of the strain hardened layer.

2.1.2.1 Experimental methods

Many experimental methods have been applied to characterise residual stresses in engineering materials, which has been reviewed in detail by Withers and Bhadeshia [31]. Among these methods, conventional laboratory X-ray diffraction, neutron diffraction and synchrotron X-ray diffraction are the three widely utilised techniques. The working principles of these are similar; the strain in the crystal lattice is measured based on the diffraction of crystals, from which the associated residual stress is then determined, assuming a linear elastic distortion of the appropriate crystal lattice plane. Each technique has its own advantages and drawbacks. A theoretical comparison between them has been reported by Tanaka et al. [32]. In general, a laboratory XRD technique only detects the stress very near the surface because the penetration depth of X-rays is a few tens of microns at most (so it is usually utilised accompanied with successive electropolishing to obtain residual stress distributions beneath a surface). In contrast, neutron diffraction can measure the stress in the interior of the material up to thousands of times deeper than conventional laboratory XRD. The major drawbacks of this technique are its requirement of an intense neutron source, and the lower resolution [33]. Synchrotron XRD is a relatively new technique which provides X-rays with extremely high intensity, achieving a penetration depth between that of the other two techniques. In addition, it also provides a narrow divergent angle, which enables the stress measurement in a very localised area. In terms of the availability of the facilities, both neutron diffraction and synchrotron XRD systems are much harder to access than laboratory XRD facilities [33].

In addition to the technologies based on diffraction, hole-drilling is another popular method. It is based on the measurement of surface relaxed strains using strain gauges

[1] The Bauschinger effect refers to the experimental result that, after a certain amount of forward plastic deformation in tension or compression, the material yields at a lower stress when the direction of loading is reversed than for continued forward deformation.

during the incremental drilling of a small hole at the sample surface. Compared with diffraction methods, the hole-drilling method is more convenient to implement. However, the selection of appropriate strain gauges is subject to the dimension and the geometry of the specimen. Furthermore, the application of this approach is limited to the situation where residual stresses are within 50 - 70% of the yield strength of the local material [34, 35]. This is due to the fact that higher residual stresses may lead to local plastic deformation caused by the stress concentration of the drilled hole, which strongly affects the residual stress evaluation based on the linear-elastic material behaviour [35]. But in shot-peened cases, residual stresses exceeding 70% of the bulk material's yield strength are still likely to be accurately determined, which is attributed to the increased local yield strength resulting from strain hardening [36].

To achieve the residual stress measurement in large and thick components, the deep hole drilling (DHD) method has been developed. It originated as a technique arising from its application in rock mechanics. The measuring procedure involves drilling a hole to the depth required for stress measurement, measuring the diameter of the hole, trepanning a cylindrical core of material from around the hole to relax the residual stresses in the core, and re-measuring the diameter of the hole [37]. The residual stress distribution can be finally determined based on the change in diameter of the hole using the elastic assumption. A detailed introduction of this method can be found in [38].

2.1.2.2 Modelling methods

It should be noted that the experimental approaches introduced above are commonly used to measure residual stresses at certain points and directions, rather than to determine the full residual stress field. To overcome this limitation, finite element modelling techniques are widely used to achieve the reconstruction of the full residual stress field.

One such modelling approach is the contour method, which has been widely used to determine the residual stress distribution resulting from various surface treatments and manufacturing processes [39]. As a first step in this approach, a specimen containing residual stresses is cut in half, resulting in deformation on the traction-free face due to residual stress release. This deformation is then experimentally mapped and incorporated into an FE model. Finally, the residual stress field is numerically reconstructed through forcing the experimentally determined deformation back to its original state in the FE model. The conventional contour method can only be used to determine one component of the residual stress over the cross section of a part. This method has been extended to measure multiple residual stress components by making multiple cuts [40, 41].

In addition, some researchers have directly introduced the experimentally measured residual stress profile into the FE model as an initial condition, assuming a homogeneous residual stress distribution within the component (i.e. the residual stress distribution only varies with depth, being independent of the location on the surface) [42-44]. The full residual stress distribution within the component can be determined by exerting a subsequent stress equilibrium step before the fatigue loads are simulated. Coules et al. [45] indicated that an iterative process could increase the accuracy of this approach, since the predefined residual stress field in the FE model was allowed to change during the stress equilibrium step. This process is illustrated in Figure 2-5; the difference between the experimental residual stress data and the reconstructed residual stress distribution is gradually reduced during an iteration, finally achieving a converged solution satisfying the stress equilibrium state. Nevertheless, this iterative process can be time-consuming, which reduces the efficiency of the modelling work.

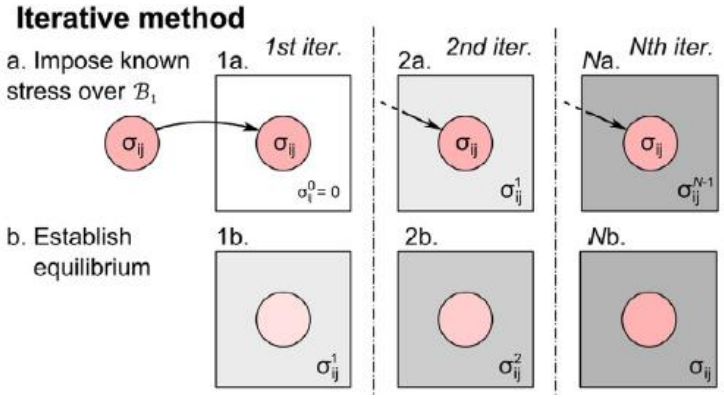

Figure 2-5: Scheme for finding the complete residual stress field using the iterative method [45].

To date, one of the most successful and widely used modelling methods to obtain the complete residual stress field is the eigenstrain approach. This approach has been applied to various conditions, such as shot peening [46, 47], laser shock peening [48, 49], welding [50], machining [51, 52], glass structural designs [53-55], etc. The eigenstrain is defined as the permanent inelastic strain (caused by plasticity, creep, thermal expansion, etc.) acting as the perturbation that causes the material to respond elastically to achieve the self-equilibrium within the component, which reflects the mechanism of the generation of residual stresses [56]. It is noted that the eigenstrain cannot be equivalent to total inelastic strain in some cases; e.g. in the condition of uniaxial loading, since the plastic strain is uniformly distributed in the workpiece, there is no strain incompatibility thus no residual stress is generated. Hence, to be more precise, the eigenstrain should be considered as the 'misfit' strain in components after certain treatments. It is also important to note that the accommodation of eigenstrain is

defined as an elastic process. Any further change of the inelastic strain is classified as eigenstrain modification rather than accommodation [51]. This definition ensures that the whole process of the eigenstrain method is linear such that the problem is significantly simplified. Although the concept of eigenstrain was not explicitly mentioned in some studies [57, 58], the reported residual stress modelling process was essentially consistent with the mechanism of residual stress generation in terms of eigenstrain.

In eigenstrain approaches, the eigenstrain is predicted and incorporated into the FE model first. Then the residual stress field can be generated to accommodate the eigenstrain by exerting a stress equilibrium step. Korsunsky [56] calculated the eigenstrain distribution in a shot-peened plate based on the measured residual stress data using the flexible plate theory. This process is known as the direct eigenstrain method. However, the eigenstrain distribution is sometimes difficult to directly measure or calculate from experimental results due to the non-ideal geometry of the specimen or scarce experimental data. In order to solve this problem, Korsunsky [48] developed an inverse approach to determine the eigenstrain profile backwards from experimental residual stress data, through a mathematical algorithm minimising the difference between the experimental and modelled results. This inverse eigenstrain method significantly simplifies the residual stress reconstruction work and has been implemented in many applications, demonstrating its good applicability [46, 47, 59].

Despite the high accuracy and efficiency of the inverse eigenstrain method, the eigenstrain distribution has been commonly assumed to be only dependent on one direction (the direction perpendicular to the treated surface). Although this assumption is true for shot-peened components with simple geometries (e.g. smooth samples) due to the non-directional nature of the shot peening process, it may not be reasonable in shot-peened complex geometries (e.g. in notched geometries). Investigation regarding accurate residual stress reconstruction in shot-peened complex geometries is still very limited due to the difficulties in accurately predicting the effect of geometries on eigenstrain components [60, 61]. King et al. [62] used an iterative approach to determine the eigenstrain distribution in both the longitudinal and transverse directions in a laser shock peened notched sample. However, this method tends to be time-consuming and inconvenient to implement due to the involved iterative process.

Additionally, there is another popular modelling approach which aims to simulate the shot peening process, utilising the explicit dynamic modelling technique [63-66]. Unlike other reconstructing methods which rely on some pre-measured experimental data, this dynamic approach explicitly simulates the dynamic process of shot peening. The main

advantage of this approach is that the full residual stress field can be directly obtained from the modelling work, without the requirement of additional experimental measurements. However, this approach requires a careful definition of many factors which the modelling results are very sensitive to, such as the strain rate dependency of the target material, the material and the size of shots, the contact property of the peened surface, etc.

2.1.3 Strain hardening profiles

During the shot peening process, strain hardening usually occurs, but strain softening may also be observed in a few circumstances where hardened steels or cold-formed materials are used [25]. In this section, only the determination of the strain hardening profile is discussed.

2.1.3.1 Experimental methods

Microhardness, XRD line broadening and electron backscattered diffraction (EBSD) are three techniques commonly used to evaluate the degree of strain hardening in shot-peened materials. Microhardness testing is an approach to determine the distribution of the local material hardness by measuring a series of points along the depth of the specimen. The straining hardening effects can be demonstrated by the increased local material hardness, compared with the hardness of the bulk material. XRD line broadening is commonly indicated by the full width at half maximum (FWHM) measurement. The broadening is caused by inhomogeneous deformation between or within grains as a consequence of the evolution of dislocation density which is related to plastic strain [67]. Hence the local strain hardening degree can be identified by the increase of the local FWHM value. EBSD measurement is a scanning electron microscope (SEM) based electron diffraction technique allowing the mapping of crystal orientations. The degree of crystal misorientation within a grain due to plastic deformation can also be quantified to illustrate the strain hardening degree [68].

Although the strain hardening level can be evaluated by using the techniques introduced above, none of them is capable of directly measuring the increased local yield strength or plastic strain caused by shot peening. This hinders utilizing the strain hardening profile in life assessment methods. To solve this problem, Cahoon et al. [69] suggested a linear relation between the hardness and yield strength for both 65S aluminium and 1040 steel specimens, which showed an acceptable agreement with experiments. This monotonic relationship seems reasonable (at least for the investigated materials) since the increased yield strength strengthens the resistance of material to permanent shape changes, resulting in the increased measured hardness. In addition, an approach relating

FWHM to plastic strain using uniaxial loading (monotonic tension and compression) calibration tests was applied by Prevéy [27]. A similar approach has also been used to correlate the misorientation measured by EBSD to plastic strain magnitudes [68, 70].

Further to this, Soady et al. [17] compared the plastic strain and yield strength profiles calibrated from the measured data in FV448 tempered martensitic steel using microhardness, XRD FWHM and EBSD techniques (Figure 2-6). The calibration was based on uniaxial monotonic tests which were similar to the work of Prevéy [27]. The results show that XRD FWHM and EBSD approaches have more consistent results whereas microhardness tests seem to overestimate the depth of the strain hardened region. This overestimation has also been indicated by others [19, 25, 71], and has been attributed to the additional influence of the CRS field, which resists the formation of indentations during microhardness measurements, resulting in higher measured hardness data than in stress-free specimens; the associated error was estimated to be within 5% [17] or 12 HV0.1 per 100 MPa [25].

Soady et al. [17] also suggested that compared with XRD FWHM measurements which only resulted in discrete data points, EBSD provided more data points and hence a higher confidence due to the more averaged data. However, the calibration based on XRD FWHM data had a higher coefficient of determination (R^2) value and could be conveniently carried out along with the measurement of residual stresses; R^2 = 0.9780 for the XRD FWHM calibration, R^2 = 0.9428 for the EBSD calibration. Therefore, the choice of the measurement approach is still open and can be chosen according to the requirements of a particular study.

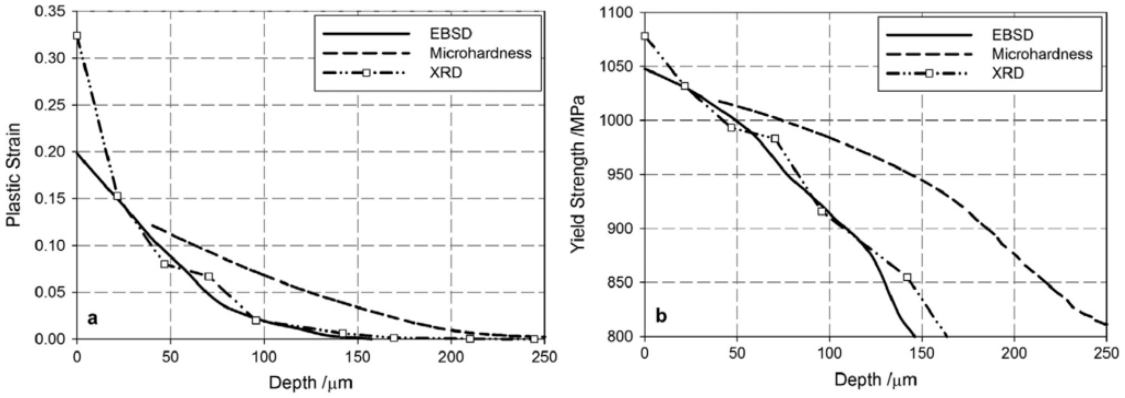

Figure 2-6: Comparison of (a) plastic strain measured by the three different methods and (b) the corresponding yield strength distributions calculated using the Ramberg Osgood relationship resulting from shot peening (intensity: 13A, coverage: 200%) in FV448 (a tempered martensitic steel) [17].

It should be noted that the actual strain hardened depth can be underestimated by experimental measurements to some degree. This is because the variation caused by a small plastic strain may not be captured by experimental measurements, especially when the variation is within the scale of the error introduced by the measurement itself.

2.1.3.2 Modelling methods

It is necessary to incorporate the strain hardening effects caused by shot peening into the FE model in addition to the effects of CRS. Otherwise, the plastic deformation of the surface layer during fatigue loading would probably be overestimated by the FE model. This would potentially degrade the accuracy of the simulated residual stress relaxation, thus reducing the accuracy of the developed life assessment method.

Yin and Fatemi [43] proposed a four-layer model to represent the strain hardening profile, as shown in Figure 2-7. Based on a number of uniaxial loading tests using specimens with different hardness values, different stress-strain curves related to the measured hardness were defined by interpolation between layers, thus achieving the incorporation of strain hardening in the FE model. However, it is apparent that this approach only roughly represents the real strain hardening profile, resulting in abrupt changes in mechanical properties of the local material at particular depths. Therefore, this approach is only appropriate in a qualitative study rather than in any simulation used in developing a life assessment method.

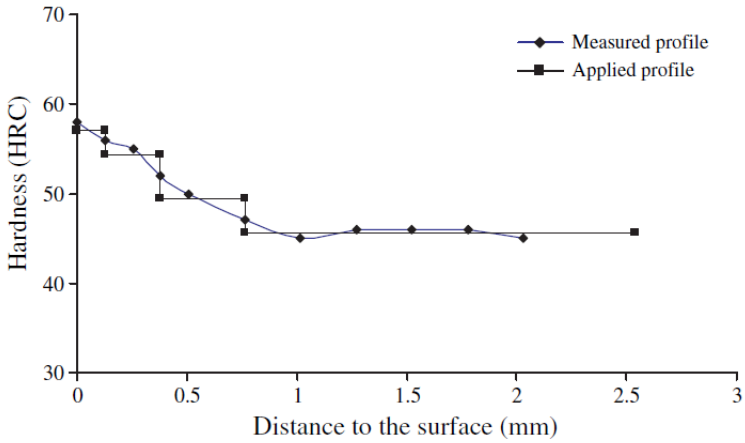

Figure 2-7: The measured hardness profile and approximated hardness profile in a four-layer FE model [43].

A more accurate approach has been proposed by Benedetti et al. [46] who defined a smooth variation of the cyclic yield strength along the depth in an FE model. The cyclic stress-strain curve was scaled at each depth according to the degree of local strain hardening, as illustrated in Figure 2-8; the elastic regime was extended to the local cyclic yield strength which was calibrated based on the measured microhardness on the shot-

peened samples; the hardening curve was then shifted to compensate the offset due to the residual deformation [46]. A similar approach has also been applied by Dalaei at al. [72] and Zhuang and Halford [73]. However, as indicated in section 2.1.3.1, the measured hardness is affected by both strain hardening and residual stresses, so the degree of strain hardening caused by shot peening may be overestimated due to the CRS field.

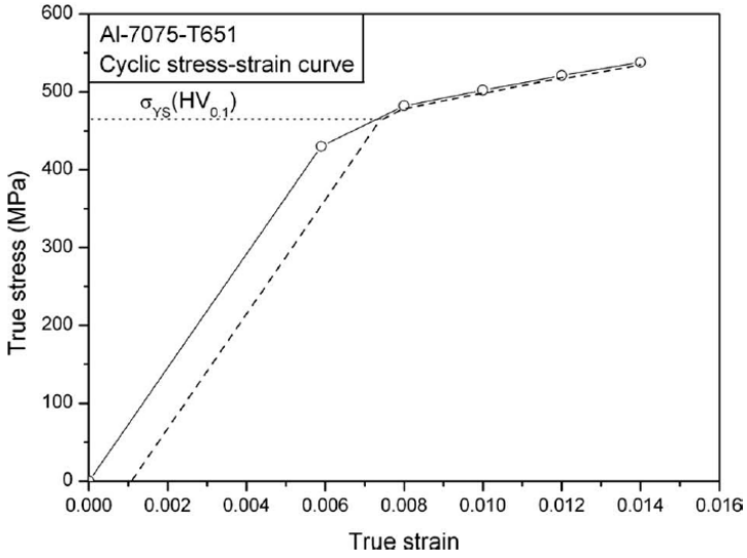

Figure 2-8: Cyclic stress/strain curve of the base material and determination of the cyclic stress/strain curve of the hardened layers [46].

In addition, by simulating a single-shot peening process, Song et al. [74] found a linear relation between the backstress in the kinematic hardening component of the applied material model and the shot peening induced plastic strain. This relation was used to define the initial strain hardening distribution based on the predicted eigenstrain profile resulting from shot peening. However, this method still needs experimental validation.

2.2 Influence of shot peening on fatigue life

The effect of shot peening on high-cycle fatigue (HCF) has been relatively well documented [22, 75]; the fatigue resistance of components can be improved by the beneficial effects of the compressive residual stresses (CRS) and near surface strain hardening. However, the effect of shot peening on low cycle fatigue (LCF) is less well established. This is due to the potential relaxation of CRS or strain hardening profiles in the LCF regime which may reduce the benefit of shot peening. In addition, the roughened surface resulting from the peening process may exert a detrimental effect on fatigue resistance, which is not the case in the (elastic) HCF regime The following section aims

at reviewing how the shot peening induced effects influence fatigue life as well as their interaction with the applied service conditions.

2.2.1 Effects of the imperfect surface on fatigue life

As discussed in Section 2.1.1, the indentations and dimples caused by shot peening significantly roughen the peened surface, which may facilitate crack initiation because of the high stress concentration at the roughened area [76]. In addition, pre-existing microcracks may also exist at shot-peened surfaces, which are usually ascribed to the high intensity of shot peening [77, 78]. These pre-existing microcracks can potentially propagate to a critical length leading to fracture. However, the specific role of the imperfect surface in the fatigue behaviour of shot-peened components needs to be assessed along with the CRS state.

In the HCF regime where low stress levels are applied or in conditions where smooth samples without stress concentration features are used, cracks initiating from surface imperfections are usually arrested shortly after initiation, or the main crack onset area shifts from surface (in un-peened samples) to subsurface areas (in shot-peened samples). These phenomena are attributed to the dominance of CRS in surface layers [23, 78-80]. Under such circumstances, the effect of the imperfect surface is negligible.

In the LCF regime or in conditions where geometric stress concentrations play an important role, crack onset tends to occur at the surface or the region close to the surface due to the high external stress level and more evident residual stress relaxation [75, 79, 81]. This usually leads to a competition between the effects of the imperfect surface and CRS on fatigue resistance [79, 82-86], which directly determines the degree to which the shot peening improves fatigue life. Under circumstances when low or moderate peening intensities are applied, the effect of the imperfect surface might still be negligible, as long as sufficient CRS is retained during fatigue loading [87]. The CRS field can delay crack initiation from the roughened surface [88] and early crack growth from the pre-existing crack-like defects [78, 84, 89-91]. However, in conditions where significant surface defects are introduced by excessively high peening intensities, or a severe CRS relaxation occurs during fatigue loading, the detrimental effects of the imperfect surface may overwhelm the benefits of the CRS field, resulting in a significant acceleration of the crack initiation and early propagation processes. For example, Dorr et al. [20] observed a degradation of the degree of fatigue life improvement resulting from shot peening on magnesium alloy AZ80, when higher peening intensities than the optimal point (the intensity most evidently improving the fatigue life) were applied. This degradation was demonstrated to be mainly related to the presence of the microcracks

which were a result of the high peening intensity. Similar situations were also observed by Zhang and Lindemann [22].

2.2.2 Effects of compressive residual stress on fatigue life

Generally speaking, due to the CRS introduced by shot peening, any applied tensile stress at the surface is balanced to some degree, in spite of the stress concentration features of the roughened surface, which makes a pronounced contribution to the improvement of fatigue life.

As discussed in Section 2.2.1, in the HCF regime, due to the dominant effect of CRS at the peened surface, cracks tend to nucleate from subsurface regions, which significantly contributes to the improvement of fatigue life [23, 78-80]. To understand the relevant mechanisms, Wagner [78] indicated that HCF cracks usually developed in the subsurface tensile residual stress region which balanced the outer beneficial CRS field. Starker el al [92] further indicated that fatigue cracks usually developed in layers where the local loading stress was higher than the local fatigue strength, which could be predicted using the Goodman relation allowing for the distribution of local residual stresses. This work reasonably explains the variance of crack initiation sites at different loading levels. A similar analysis has also been conducted by Torres and Voorwald [79].

In addition to crack initiation, the CRS field has been found to effectively reduce the short crack growth rate [82, 93-96], or even result in non-propagation of small cracks at surfaces shortly after their initiation [90-92]. This is deemed to be caused by the reduction of the plastic deformation around the crack tip [97], and the crack closure phenomenon [1] [94, 96]; both effects result in a reduced effective crack driving force until the crack penetrates through the whole CRS field.

However, the advantages of CRS can be considerably degraded by residual stress relaxation occurring during fatigue [84]. This phenomenon has been observed by many researchers [44, 72, 86, 98-101]. The mechanism of the residual stress relaxation behaviour is related to the change in plastic strain distribution, which results in the modification of the eigenstrain. This explanation is supported by the work conducted by Song et al. [74], who corroborated that the beginning of residual stress relaxation correlated with the onset of the reduction of the eigenstrain, and residual stresses

[1] Crack closure occurs when crack faces touch under remote tensile load; the crack cannot propagate if the faces are in contact. There are several mechanisms inducing crack closure, such as plasticity, oxide and roughness induced mechanisms

completely relaxed when the eigenstrain layer was eventually eliminated by external loads.

The most significant residual stress relaxation induced by mechanical loading has been normally observed during the first cycle, when the superposition of applied stresses and residual stresses exceeds the local yield strength, causing plastic deformation. This is regarded as the quasi-static loading phase which depends on the monotonic yield strength of the material in tension and compression. According to the work of Dalaei et al. [86], in samples with the same dimensions subjected to the same shot peening treatment, higher loading levels tended to result in more evident residual stress relief due to the greater reduction in eigenstrain. Relevant results are shown in Figure 2-9; a small strain level (0.25%) does not modify the residual stress distribution while an excessively high strain level (1%) causes a complete relaxation of residual stresses during the first cycle.

During quasi-static loading, the eigenstrain is likely to be reduced by both tension and compression. However, when the specimen is loaded in tension, the combined effect of the increased tensile yield strength (resulting from strain hardening) and the CRS field hinders the tensile yielding of the material near the surface [102]. In contrast, during compression, the applied stress and CRS encourage the compressive yielding of the material in the near-surface region. This process may be further facilitated by the Bauschinger effect occurring during shot peening, resulting in a lower compressive yield strength near the peened surface compared with the core material [103]. Therefore, residual stress relaxation during the first cycle in shot-peened samples is more sensitive to compression than tension, which has been observed in [98, 103, 104].

During subsequent cycles, residual stress relaxation becomes much slower compared with the first cycle and usually exhibits a linear reduction with the logarithm of the number of cycles, which has been observed by many researchers [86, 104, 105]; an example is shown in Figure 2-10. The difference between the first and subsequent cycles is due to the greatly reduced plastic deformation of both the surface layer and the core material during the cycles after the quasi-static loading stage, which considerably slows the relaxation rate of residual stresses. This reduction depends on the cyclic yield strength of the material, the evolution of which is controlled by the cyclic softening (or hardening) behaviour of the material.

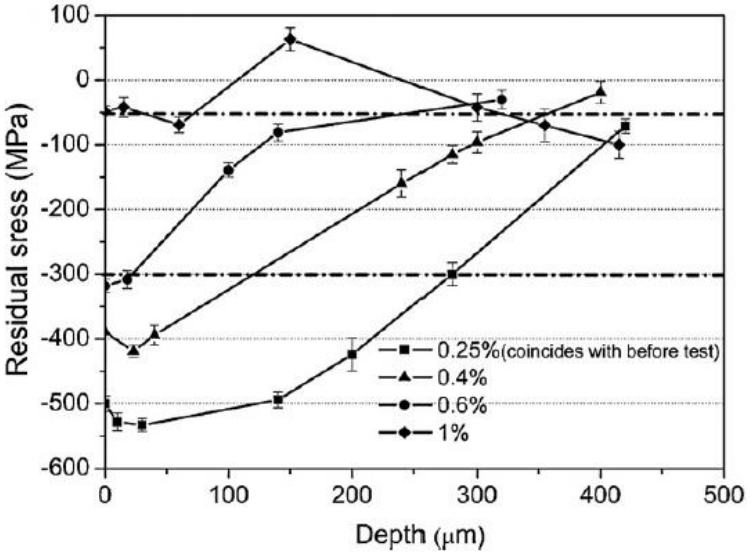

Figure 2-9: The longitudinal residual stress distribution after one cycle in a shot peened normalised steel [86].

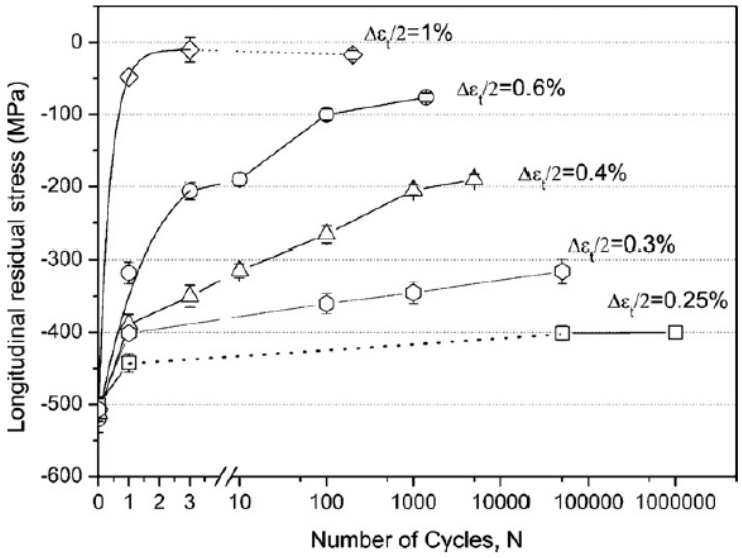

Figure 2-10: Relaxation of the surface residual stresses at different strain amplitudes cycle in a shot peened normalised steel [86].

It is noteworthy that shot-peened components normally show more considerable residual stress relaxation in the longitudinal direction (the direction parallel to the external load) than in the transverse direction under uniaxial loading or reverse bending tests [46, 98, 102]. This anisotropic state has been attributed to the effect of Poisson's ratio; when the specimen is plastically deformed in the loading direction, plastic strain is also generated in the transverse direction but with a lower magnitude, which results in a greater reduction of eigenstrain in the loading direction.

At high service temperatures, residual stress relaxation is not simply attributed to mechanical loading, but also affected by thermal exposure [103]. Kim et al. [102] reported that after exposure for 10 hours at 650℃, 700℃ and 725℃, the maximum compressive residual stress in a shot peened Udimet 720Li superalloy was reduced by 35%, 50% and 60% respectively (as shown in Figure 2-11). But for materials working at lower temperatures, thermal effects are negligible and residual stress relaxation is dominated by mechanical loading.

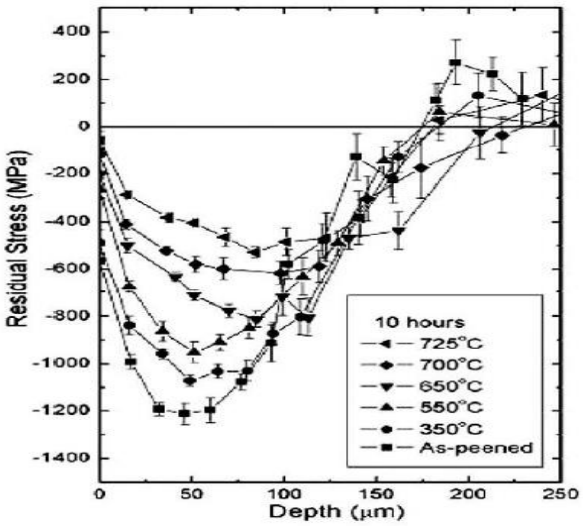

Figure 2-11: Residual stress distributions in a shot peened Udimet 720Li superalloy after thermal exposure for 10 hours at different temperatures [102].

Overall, it can be concluded that a stable CRS distribution is advantageous in maintaining the benefit of shot peening via two mechanisms: firstly, resist crack initiation or push crack sources to subsurface areas; secondly, delay early crack growth through the shot peening affected layer by reducing the crack driving force. Residual stress relaxation has to be taken into account when evaluating the benefits of CRS which may be weakened by this relaxation behaviour, especially in the LCF regime.

2.2.3 Effects of strain hardening on fatigue life

The effect of strain hardening is more complex to understand than that of surface roughness and residual stresses. The role of strain hardening in crack initiation and propagation processes is still controversial.

Wagner and Luetjering [23] investigated the effect of strain hardening individually by comparing the fatigue limit of mechanically and electrolytically polished specimens. The mechanical polishing process introduced a high dislocation density into the surface layer while maintaining a smooth surface topography. In contrast, the electropolishing

process resulted in a surface state with negligible residual stress and strain hardening effects. The results of this comparison indicated that strain hardening had a positive effect in improving fatigue resistance, but this improvement became less notable at high stress levels where crack propagation dominated, implying that strain hardening mainly retarded crack initiation. It is noted that the above conclusion was based upon an assumption that the effect of residual stresses in mechanically polished samples were negligible, which required validation. In addition, Eleiche et al. [106] compared the fatigue behaviour of specimens treated with shot peening, and shot peening plus stress relief (at 400℃ for 1 hour). The results of this comparison are shown in Figure 2-12; it is clear that the fatigue limit of the specimen was improved by ~ 20% by shot peening and this improvement was only slightly reduced by the stress relief treatment, highlighting the benefit of strain hardening in retarding crack initiation. Altenberger et al. [107] further explained the role of strain hardening in crack initiation in terms of the microstructure of the material, suggesting that the dislocation movement associated with crack initiation tended to be hindered by the increased dislocation density of the strain hardened layer. In addition to the retardation of crack initiation, the strain hardened layer may also make a contribution to the reduced crack growth rate because of the increased resistance to plastic deformation at the crack tip, as indicated by de los Rios et al. [89].

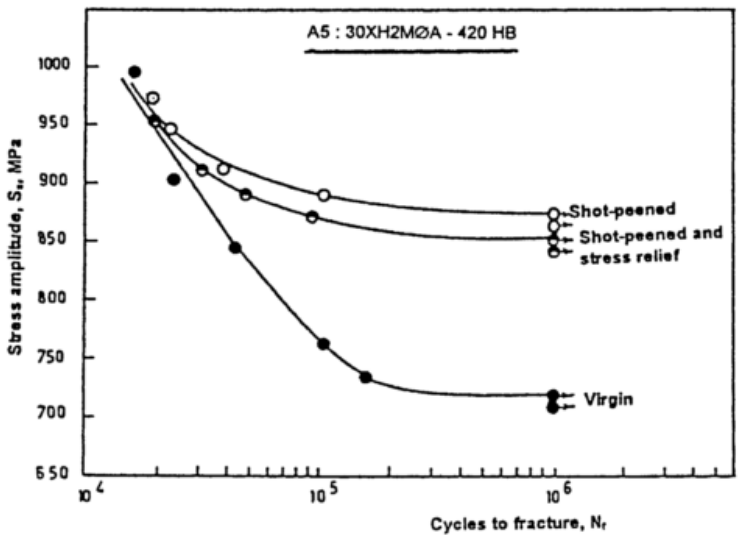

Figure 2-12: S-N fatigue curves for smooth samples of a high strength martensitic steel tested under rotating bend illustrating the relative contribution of residual stresses and strain hardening to fatigue resistance [106].

On the contrary, Benedetti [100] indicated that intense strain hardening might induce an earlier microcrack nucleation, resulting in less pronounced improvement in fatigue life

by shot peening. This was attributed to the low residual ductility in the strain hardened layer associated with the high dislocation density. In this situation, the crack propagation process is also potentially accelerated [33].

The reasons behind the contradictory effects of strain hardening observed by different researchers can be explained to some extent by the work carried out by Pangborn et al. [108]. They reported that strain hardening acted as a barrier opposing the motion of dislocations, however, when the barrier became sufficiently strong reaching a critical value, fracture easily occurred with propagating fatigue cracks. This implies that a modest degree of strain hardening exerts beneficial effects on fatigue life especially in retarding crack nucleation, while excessive strain hardening potentially accelerates crack initiation and propagation processes, which is more likely to occur in materials with low ductility.

Similar to the residual stress state, strain hardening may also evolve during cyclic loading. This evolution represents the intrinsic response of the material and has been demonstrated to be independent of residual stress evolution. Nalla et al. [99] reported a stable distribution of the FWHM rather than them following the evolution of residual stresses in specimens made of Ti-6Al-4V after they were axially loaded for half the predicted life to failure under a constant load ratio R_p = -1. Even after thermal annealing for 45 minutes at 450℃ when the residual stress had virtually completely relaxed, merely a ~ 16% reduction of the FWHM was observed at the surface with no clear reduction in subsurface areas. This insensitivity of strain hardening to fatigue cycles and thermal exposure was attributed to the ultrafine grain size and the high dislocation density of the strain hardened material [99]. However, on the contrary, Dalaei et al. [86] reported an evident decrease of the FWHM in a normalised steel under a fully reversed push-pull test controlled by total strain levels at room temperature. This decrease was analogous to the residual stress relaxation behaviour; at a small strain amplitude of 0.25%, the FWHM was virtually unchanged during the fatigue life, but at a large strain level (1%), full recovery of dislocations occurred in the component apart from the region near the surface. Furthermore, according to the work of Kim et al. [102], the redistribution of the FWHM in Udimet 720Li superalloy is due to the combined effect of cyclic loading and thermal exposure; as shown in Figure 2-13(a), at 350℃, despite a notable residual stress relaxation during fatigue loading, there is no evident variation of the FWHM profile; in contrast, as shown in Figure 2-13(b), when the temperature increases to 700℃ (which is the service temperature for the investigated material), a gradual recovery of the dislocations is observed to a subsurface depth of 100 μm during fatigue cycling.

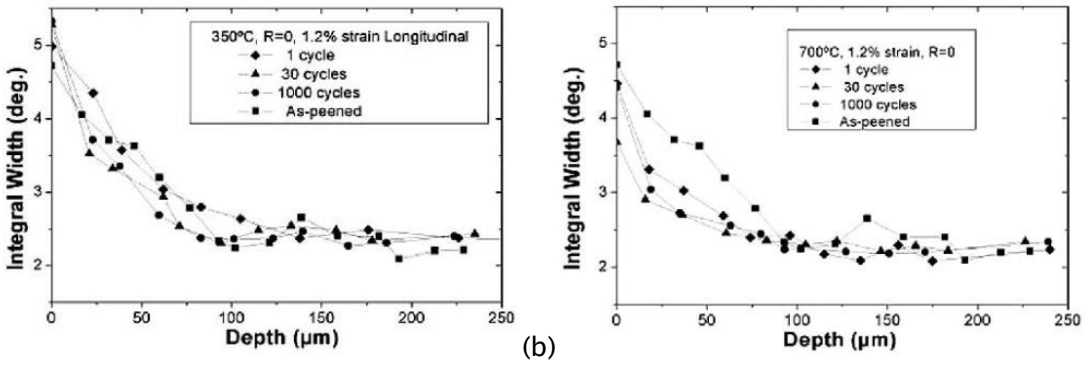

(a) (b)

Figure 2-13: FWHM profiles after uniaxial fatigue test (strain ratio R_ε = 0) in Udimet 720Li superalloy under 1.2% strain range at (a) 350℃ and (b) 700℃ [102].

2.3 Fatigue lifing approaches

Traditionally, life assessment methods can be classified as total life and damage tolerant approaches. Total life approaches define the fatigue life of a component as the total number of cycles, N_f, including both crack nucleation and crack growth stages. Damage tolerant approaches only consider the fatigue life of the propagation of a pre-existing flaw to a critical size. Both approaches can be used to predict the fatigue life of shot-peened components but they require an understanding of the residual stress and strain hardening profiles resulting from shot peening and the manner in which they may evolve during operation, which has been reviewed in preceding sections (Sections 2.1 and 2.2). The present section focuses on reviewing the classical lifing approaches and the current methods realising the incorporation of the shot peening effects into these.

2.3.1 Classical total life approaches

In classical total life approaches, the number of stress or strain cycles necessary to induce fatigue failure in un-cracked smooth-surfaced laboratory specimens is estimated under controlled amplitudes of cyclic stress or strain. These methods have been found to be appealing in predicting the life of crack initiation and early propagation in safety critical regions in engineering components [109], as schematically illustrated by Figure 2-14.

The stress-life approach has been widely used to characterise HCF. A component experiencing HCF usually has a long fatigue life because the deformation process is primarily elastic. In a fully reversed fatigue test controlled by a constant stress amplitude, $\Delta\sigma/2$, the stress-life approach can be described by Equation 2-2, where σ_f' is the fatigue strength coefficient (which approximately equals the true facture strength σ_f

in a monotonic tension test for most materials) and b is known as the fatigue strength exponent. When considerable plastic deformation occurs during fatigue loading, the fatigue life is notably reduced, resulting in LCF. The strain-life approach is normally used to characterise LCF, highlighting the important role of plastic strain in controlling the fatigue resistance of a component. Similar to the stress-life approach, a linear relation between the plastic strain amplitude $\Delta\varepsilon_p/2$ and the number of load reversals to failure $2N_f$, can be determined by a fully reversed test controlled by constant plastic strain amplitudes. This relationship, known as the Coffin-Manson relation [110, 111], is described by Equation 2-3, where ε_f' is the fatigue ductility coefficient and d is the fatigue ductility exponent. Since the total strain ε is the sum of the elastic strain ε_e and the plastic strain ε_p, Equation 2-4 is obtained by combining Equation 2-2 and Equation 2-3, where E is the Young's modulus of the material.

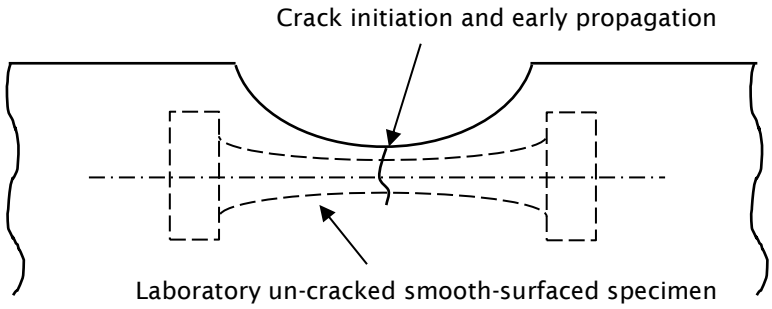

Figure 2-14: Schematic diagram illustrating the application of total life approaches in an engineering component.

$$\frac{\Delta\sigma}{2} = \sigma_f'\left(2N_f\right)^b \tag{2-2}$$

$$\frac{\Delta\varepsilon_p}{2} = \varepsilon_f'\left(2N_f\right)^d \tag{2-3}$$

$$\frac{\Delta\varepsilon}{2} = \frac{\Delta\varepsilon_e}{2} + \frac{\Delta\varepsilon_p}{2} = \frac{\sigma_f'}{E}\left(2N_f\right)^b + \varepsilon_f'\left(2N_f\right)^d \tag{2-4}$$

It is noted that the above empirical descriptions of fatigue life are based on the fully reversed test where the mean stress σ_m is zero, which, however, cannot represent all service load applications. The stress range $\Delta\sigma$, the stress amplitude σ_a and the mean stress σ_m in a nonzero mean stress test can be defined by Equation 2-5 according to Figure 2-15 which schematically shows a sinusoidal waveform used in the fatigue test.

$$\Delta\sigma = \sigma_{max} - \sigma_{min}, \quad \sigma_a = \frac{\sigma_{max} - \sigma_{min}}{2}, \quad \sigma_m = \frac{\sigma_{max} + \sigma_{min}}{2} \tag{2-5}$$

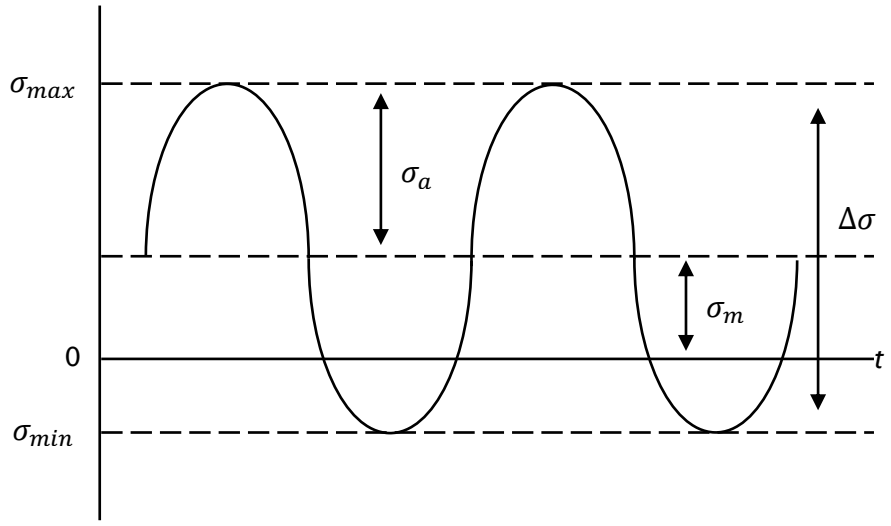

Figure 2-15: A schematic demonstration of the sinusoidal waveform with nonzero mean stress.

In order to consider the mean stress effects, the basic approaches described by Equation 2-2 to 2-4 should be corrected accordingly. For the HCF stress-life approach, the most well-known corrections are Gerber [112], Goodman [113] and Soderberg [114] relations, which depend on the ratio of the mean stress σ_m to the tensile strength σ_{TS} or the yield strength σ_y. These relations are described by Equation 2-6 to 2-8 respectively where $\frac{\Delta\sigma}{2}|_{\sigma_{m=0}}$ represents the stress amplitude for fully reversed loading. Mean stress effects have also been considered in the LCF strain-life approach by applying specific corrections, one of which is the Smith-Watson-Topper (SWT) approach [115] described by Equation 2-9, considering the effect of the maximum stress σ_{max}.

$$\frac{\Delta\sigma}{2} = \frac{\Delta\sigma}{2}|_{\sigma_{m=0}} \left\{1 - \frac{\sigma_m}{\sigma_y}\right\} \tag{2-6}$$

$$\frac{\Delta\sigma}{2} = \frac{\Delta\sigma}{2}|_{\sigma_{m=0}} \left\{1 - \frac{\sigma_m}{\sigma_{TS}}\right\} \tag{2-7}$$

$$\frac{\Delta\sigma}{2} = \frac{\Delta\sigma}{2}|_{\sigma_{m=0}} \left\{1 - \left(\frac{\sigma_m}{\sigma_{TS}}\right)^2\right\} \tag{2-8}$$

$$\sigma_{max}\frac{\Delta\varepsilon}{2} = \frac{(\sigma_f')^2}{E}(2N_f)^{2b} + \sigma_f\varepsilon_f'(2N_f)^{b+d} \tag{2-9}$$

The approaches introduced above normally only apply to simple laboratory specimens under uniaxial loading. In real engineering components subjected to complex loading conditions or treated with surface processes introducing multiaxial residual stresses (e.g. shot peening), the stress or strain states during service might be multiaxial; each stress or strain component could make a contribution to the total damage accumulation leading to the failure of components [116]. Hence, multiaxial fatigue criteria considering

mean stress effects have been developed and widely investigated to extend the application of total life approaches. One type of these approaches depends on the octahedral shear stress amplitude (or equivalently the Von Mises stress) and the hydrostatic pressure; e.g. the Sines [117] and the Crossland [118] criteria. They are mainly suitable for proportional loading [1] since they assume a fixed orientation of principal axes associated with alternating stress components. Another type of approach is based on the critical plane criterion, such as the Dang Van [119], the Findley [120], the SWT (the interpretation of Equation 2-9 was changed by Socie [121] to represent a critical plane multiaxial fatigue criterion) and the Fatemi-Socie (FS) [122] criteria. The critical plane is defined as the most severely loaded plane where cracks are expected to nucleate; typically based on either the maximum shear plane or the maximum principal plane failure mode. This type of approach can be used for both proportional and non-proportional loading and is deemed to be more reliable than other approaches since it reflects the physical nature of fatigue damage by defining the critical plane [123]. In terms of the range of application, the SWT and FS criteria are believed to be most robust among multiaxial fatigue criteria since they are strain-stress-based, hence can be used for both LCF and HCF regimes. In contrast, all the other multiaxial fatigue criterion (the Sines, the Crossland, the Dang Van and the Findley criteria) mentioned above are simply stress-based and hence are only suitable for the HCF regime where plastic deformation is small or negligible. Although in some cases the stress-based approaches can successfully predict the LCF behaviour [124-126], they cannot reflect the constitutive behaviour of the material when the fatigue response changes completely from the HCF to LCF regime [123].

Although total life approaches can be conveniently used to predict crack initiation and early crack growth life in engineering components, it is difficult to directly apply them in predicting the remaining life of a component containing defects which is a concern for industrial lifing strategies, because of the inherent limitation/inapplicability of this defect-free assumption.

2.3.2 Classical damage tolerant approaches

Damage tolerance is a property of a structure relating to its ability to sustain defects safely until repair can be implemented. Damage tolerant approaches are normally used to estimate the growth of damage in structures, and consequently estimate the remaining fatigue life of a structure containing defects with detectable sizes, which

[1] In multiaxial loading, the principal direction of cyclic loading remains fixed in proportional loading but rotates in non-proportional loading.

allows definition of maintenance or repair schedules for a structure. Therefore, this type of approach is generally more attractive in many industrial lifing strategies for engineering structures than total life approaches.

Linear elastic fracture mechanics (LEFM) are widely used to characterise the long crack growth behaviour under small-scale yielding conditions when the plastic zone at the crack tip has a much smaller size than the crack, which is typically several millimetres or more in dimension. The stress intensity factor, *K*, describing the stress state near the crack tip caused by the applied loads, can be calculated based on specimen dimensions and external loading conditions. It is an attractive parameter in that it invokes similitude; for two cracks with different sizes, the crack tip plastic zones are equal in size with equal stress and strain distributions as long as they have the same value of *K* at the crack tips; hence the crack tip driving forces are equal as well and an equal increment in crack length per cycle can be expected for these two cracks.

The cracking mode can be classified into three basic modes in terms of crack surface displacements, as schematically shown in Figure 2-16. In Mode I, crack opening is dominated by the tensile stress normal to the plane of the crack. In Mode II, in-plane sliding occurs as a result of the stress acting parallel to the plane of the crack and perpendicular to the crack front. In contrast, Mode III indicates a tearing mode arising from the shear stress acting parallel to the plane of the crack and parallel to the crack front. For simplicity, only theories relevant to the mode I (tensile opening) are presented here. The stress intensity factor for mode I, K_I, can be calculated using Equation 2-10, where σ_a is the applied nominal stress and *a* is the half size of the centre crack. However, it is noted that this relation is obtained by assuming a centre crack in an infinite plate, which is usually not true in practice. Therefore, a correction, as shown by Equation 2-11 where *W* is the width of the specimen, is required for the application of K_I in more general cases.

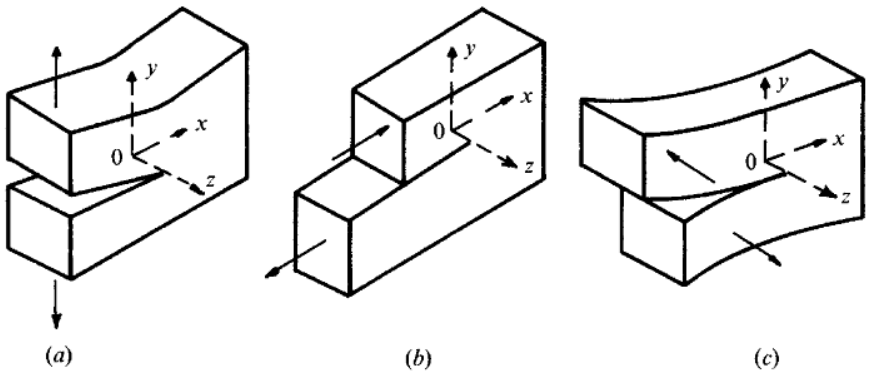

Figure 2-16: The three basic modes of fracture. (a) Tensile opening (mode I). (b) In-plane sliding (mode II). (c) Anti-plane shear (mode III) [12].

In LEFM, the critical value of K_I defining the onset of crack propagation under monotonic quasi-static loading is referred to as the fracture toughness, K_{IC}. However, under cyclic loading conditions, crack growth from a pre-existing flaw or defect usually occurs at a much lower stress intensity factor level (as low as one-hundredth of K_{IC} in very ductile metallic materials).

$$K_I = \sigma_{nom}\sqrt{\pi a} \tag{2-10}$$

$$K_I = f\left(\frac{a}{W}\right)\sigma_{nom}\sqrt{\pi a} \tag{2-11}$$

The stress intensity factor range, ΔK, is defined by Equation 2-12, where K_{max} and K_{min} are the stress intensity factors under maximum and minimum load within one cycle. ΔK is especially useful in quantifying fatigue crack growth in terms of crack growth rates in the regime of LEFM. The growth of a crack under cyclic loading can be illustrated in Figure 2-17, where the crack propagation rate d*a*/d*N* (the change of the crack length per fatigue cycle) is plotted versus the stress intensity factor range, ΔK, on a log-log plot. This sigmoidal curve is separated into three regimes. In the first regime (region A), cracks start to propagate when ΔK is higher than the threshold stress intensity factor range, ΔK_{th}, at a small growth increment per cycle (smaller than a lattice spacing). Cracks either remain dormant or grow at undetectable rates below this threshold value. The second regime (region B), known as the Paris regime, exhibits a linear relation between log d*a*/d*N* and log ΔK, which can be described by the Paris Law defined by Equation 2-13, where *C* and *m* are empirical constants determined by material properties, loading conditions, geometry, stress state, etc. In the third regime (region C), the crack growth rate increases rapidly at high ΔK values, leading to the final failure of the specimen. The Paris Law can also be extended to account for region A in Figure 2-17 using Equation 2-14, where the constant *q* is introduced to control the curvature in the near threshold region of the d*a*/d*N* - ΔK plot.

$$\Delta K = K_{max} - K_{min} \tag{2-12}$$

$$\frac{da}{dN} = C\Delta K^m \tag{2-13}$$

$$\frac{da}{dN} = C\Delta K^m\left(1 - \frac{\Delta K_{th}}{\Delta K}\right)^q \tag{2-14}$$

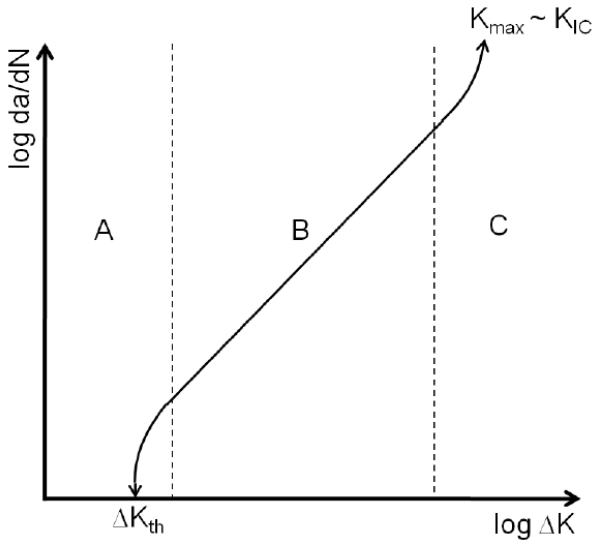

Figure 2-17: Typical d*a*/d*N* curve [12].

The characterisation of crack growth based on the LEFM approach primarily relies on experimental fatigue tests on samples containing long cracks which are typically tens of millimetres in length. In the case of short cracks, the plastic zone around the crack tip is comparable to the crack length, which may invalidate the elastic assumptions of the LEFM approach. Generally, short cracks can be identified as one of the four types presented as follows:

a. Microstructurally short cracks. The crack size is comparable to the scale of the characteristic microstructural dimension (e.g. the size of grain, precipitates or pores). The crack growth path and rate can be affected by grain boundaries, inclusions and precipitates.
b. Mechanically short cracks. As the crack grows with its length exceeding several grain sizes, the significant effect of microstructure gradually diminishes and eventually becomes negligible. The crack may still be termed as a short crack (mechanically) if the near-tip plasticity is comparable to the crack size, which contradicts the basic assumptions of the LEFM approach.
c. Physically short cracks. Although sometimes fatigue cracks are significantly larger than the characteristic microstructural dimension and the scale of the near-tip plastic zone, they are still physically small (with length smaller than 1 or 2 mm). This type of crack is termed as physically short crack and LEFM may now apply in this case but any effects of closure may be absent as insufficient crack wake has built up.
d. Chemically small cracks. This type of crack shows anomalous propagation rates below a certain size as a result of the dependence of environmental stress corrosion at the crack tip on crack length.

It has been found that the propagation of short cracks usually shows anomalous behaviour compared with long cracks if LEFM is applied; they usually start growing below the ΔK_{th} determined for long cracks, and grow much faster (with highly fluctuating growth rate) than the long cracks under the same ΔK level until merging with long crack growth data. Hence the application of LEFM to components containing short cracks can result in dangerous non-conservatism of the lifing approach.

To overcome the limitation of LEFM in characterising short crack growth, elastic-plastic fracture mechanics (EPFM) approaches can be applied. One of these is the J-integral method proposed by Rice [127]. Considering a cracked component subjected to a monotonic loading condition as shown in Figure 2-18, the J-integral, representing a way to calculate the nonlinear strain energy release rate, is a path independent line integral along any contour Γ which encircles the crack tip. The J-integral is expressed by Equation 2-15, where $\boldsymbol{u}$ is the displacement vector, y is the distance along the direction normal to the plane of the crack, s is the arc length along the contour, $\boldsymbol{T}$ is the traction vector and w is the strain energy density of the material. This approach can be used to characterise crack advance as expressed by Equation 2-16, which provides good characterisation of the growth of short cracks having a length comparable with the size of the near-tip plastic zone and long cracks in extensively yielded samples [12].

$$J = \int_{\Gamma} \left(w dy - \boldsymbol{T} \cdot \frac{\partial \boldsymbol{u}}{\partial x} ds \right) \tag{2-15}$$

$$\frac{da}{dN} = C' \Delta J^{m'} \tag{2-16}$$

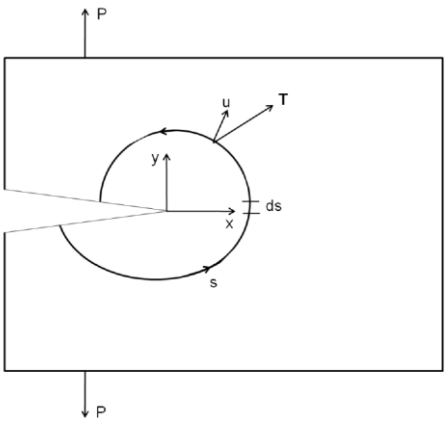

Figure 2-18: A contour around a crack tip and the nomenclature used in the definition of the J-integral [12].

In addition, the crack tip opening displacement (CTOD), δ_t, can also be used to characterise the fatigue crack growth driving force under elastic-plastic conditions [128]. The onset of quasi-static fracture can be described as $\delta_t = \delta_{tc}$, where δ_{tc} is a critical

CTOD value for the material. A commonly used definition of δ_t is based on the distance between two points on the upper and lower crack faces where two 45° lines drawn from the deformed crack tip intercept the crack faces (as shown in Figure 2-19). This approach, linking the crack propagation rate da/dN with crack tip blunting caused by plastic flow at the crack tip, is sometimes appealing because δ_t provides a physical length scale for fracture.

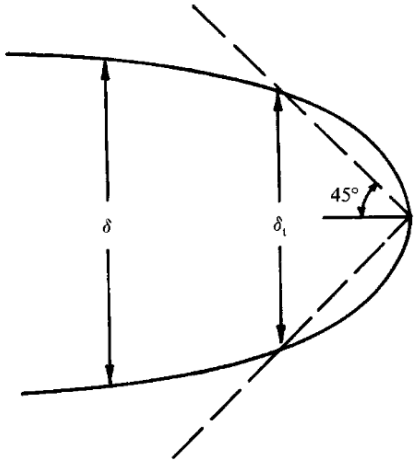

Figure 2-19: Definition of crack tip opening displacement, δ_t [12].

Under conditions of LEFM, both parameters of J-integral and δ_t can be related to K, as described by Equation 2-17 and 2-18, where E' equals E and $\frac{E}{1-\nu^2}$ for the plane stress and plane strain conditions respectively.

$$J = \frac{K^2}{E'} \tag{2-17}$$

$$\delta_t = \frac{K^2}{\sigma^0 E'} \tag{2-18}$$

2.3.3 Approaches to fatigue lifing after shot peening

Classical lifing approaches (i.e. total life and damage tolerant approaches) are typically developed without consideration of shot peening effects. Many researchers have taken shot peening effects into account by modifying the way in which the dependent variables (such as the stress range $\Delta\sigma$, the strain range $\Delta\varepsilon$ and the fracture mechanics parameter ΔK) in classical lifing protocols are calculated. To realise this, an accurate prediction of the stress and strain state during cyclic loading is always a prerequisite, especially when residual stress relaxation occurs. Neglecting the residual stress relaxation behaviour may lead to a significant overestimation of the fatigue life [125, 129], which is unacceptable. Therefore, this section firstly reviews the development in modelling the

residual stress relaxation behaviour (Section 2.3.3.1), which is followed by reviewing the application of the classical total life (Section 2.3.3.2) and damage tolerant approaches (Section 2.3.3.3) in shot-peened conditions.

2.3.3.1 Modelling of residual stress relaxation

As discussed in Section 2.2.2, residual stress relaxation is mainly affected by local material properties, local stress states during fatigue loading and working temperatures. An accurate prediction of residual stress relaxation taking these effects into account is regarded as one of the key considerations in the development of life assessment methods for shot-peened components. Some analytical approaches have been developed to facilitate this prediction [124, 130-132]. However, these approaches either only focus on the surface residual stress rather than the complete residual stress profile into the depth, or require further validation to ensure their applicability in a new system (with a new geometry or a material). To overcome the limitations of the analytical approaches, finite element (FE) modelling has aroused more interest and has been demonstrated to be an effective approach in the prediction of residual stress relaxation [42, 44, 46, 57, 58, 72, 74, 133, 134]. The FE approach is especially advantageous in investigating specimens with complex geometries, where it is sometimes impractical to apply analytical approaches. Another advantage of FE modelling over analytical approaches is that the residual stress and strain hardening effects can be effectively incorporated into FE models, as reviewed in Sections 2.1.2.2 and 2.1.3.2.

Modelling of the thermal residual stress relaxation usually requires the definition of a thermal dependent material model, such as the Johnson-Cook material model. Relevant modelling work can be found in [135-137]. Since thermal residual stress relaxation is beyond the scope of the current project, it is not reviewed here and this section mainly focuses on the modelling approach used to simulate the mechanically induced residual stress relaxation behaviour.

It is noted that reconstructing the as-peened residual stress and strain hardening field is the necessary first step to accurately simulate residual stress relaxation, although a qualitative study can also be carried out by simply considering the residual stress effects [57, 58]. In addition to this, an appropriate material model representing the cyclic behaviour of the investigated material should also be selected to ensure the accuracy of the simulation. According to the literature, isotropic and kinematic hardening components are commonly used to define the material model in order to describe the cyclic behaviour of materials [138]. An isotropic hardening component induces uniform expansion of the yield surface without translation or change of its shape, a kinematic hardening component represents the translation of the yield surface in terms of the

backstress. Both hardening components can be calibrated based on stress-strain data obtained from uniaxial loading experiments.

In the work of Song et al. [74], the cyclic behaviour of a GW103 magnesium alloy was calibrated using a linear kinematic hardening material model. This material model, together with the initial material state considering the residual stress and strain hardening effects resulting from shot peening, was employed in a 2D FE model which was used to predict the eigenstrain redistribution during fatigue loading. Although the residual stress relaxation behaviour was not directly predicted, the associated redistribution of residual elastic strain was reasonably interpreted using the predicted eigenstrain redistribution, demonstrating the potential of the applied method in accurately simulating the residual stress relaxation behaviour.

Benedetti et al. [46] developed a 3D FE model to simulate the residual stress relaxation behaviour in a shot-peened 7075-T651 aluminium alloy plate under reverse bending. The hardening rule used in this simulation was represented by a nonlinear kinematic hardening material model which was calibrated based on a number of fully reversed axial tests at various strain amplitudes. After incorporating the residual stress and strain hardening field caused by shot peening into the FE model, the stabilised stress state after residual stress relaxation during cyclic loading was simulated. It is noted that only one cycle was simulated since the material model was developed based on stabilised stress-strain states. This modelling approach was applied to three different shot peening conditions. The results of one are shown in Figure 2-20, where the numerically predicted longitudinal residual stress distributions at different stress levels agree well with counterparts in the experiment. Similar work has also been carried out by others [42, 44], but the simulation results seem less successful than the work of Benedetti in terms of the accuracy of the prediction. The reasons for this might be multiple; the simplification of the FE model, the mesh type as well as the modelling approaches reconstructing the initial condition of residual stresses and strain hardening all play a decisive role in the accuracy of the simulation.

Due to the importance of the quasi-static residual stress relaxation during the first cycle (as discussed in Section 2.2.2), simulation work is sometimes only carried out for the first loading cycle without considering the cyclic mechanical property of the material. This can to some degree alleviate the difficulties regarding the development of the cyclic material model, especially when cyclic stress-strain data are not available. Buchanan and John [133] developed a FE model incorporating both residual stress and strain hardening effects. A monotonic material model was used and the yield strength of the material in the strain hardened layer was modified according to the predicted true plastic strain profile caused by shot peening, following the calibration methods (XRD FWHM)

introduced in Section 2.1.3.1. This FE model successfully predicted the residual stress relaxation behaviour after one cycle in several service conditions. Using similar assumptions, the quasi-static residual stress relaxation under either tension or compression uniaxial loading has also been satisfactorily modelled by Dalaei et al. [72].

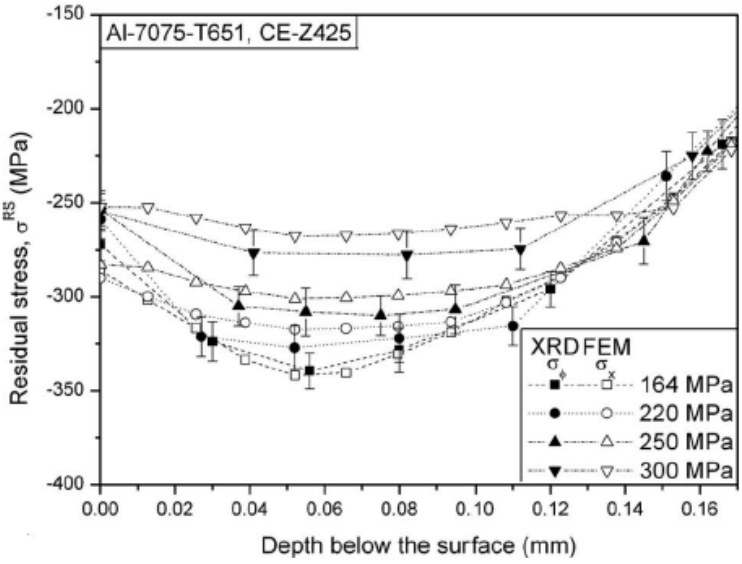

Figure 2-20: Comparison between the experimentally and numerically predicted evolutions of the residual stress field in the shot peened specimen (Almen intensity: 4.5A, coverage: 100%) tested at several fatigue load levels [46].

Based on the discussion above, in order to accurately simulate the residual stress relaxation behaviour, both cyclic and monotonic material models can be applied as long as the residual stress and strain hardened field in the as-peened condition is appropriately reconstructed. The specific choice depends on the objective of the modelling work and the availability of relevant experimental data. It is also noted that most of the quantitative modelling work that has been reported so far only focuses on smooth specimens without stress concentration features, due to the difficulties in accurately reconstructing the residual stress field in shot-peened complex geometries (e.g. notched components). Hence, the modelling of residual stress relaxation behaviour in complex geometries still remains limited to qualitative investigations [58, 133].

2.3.3.2 Developments based on classical total life approaches

As discussed in Section 2.3.1, multiaxial fatigue criteria are thought to be most appropriate compared with other total life approaches for the shot-peened state due to the multiaxial residual stress pattern. The application of the multiaxial fatigue criteria in shot-peened specimens normally relies on the predicted stabilised stress and strain state

(e.g. from FE models), which are used to calculate the stress or strain parameters required by the criteria.

Benedetti et al. [75, 100] predicted the plane bending fatigue (four-point bending and reverse bending) response by considering the residual stresses caused by shot peening using the Sines criterion. To determine the stress parameters required by the Sines criterion, the stabilised surface residual stresses were treated as mean stresses superimposed on the external surface stress which was analytically evaluated, following the suggestion provided in [116]. The effect of surface roughness was also considered by reducing the predicted fatigue strength based on the evaluated stress concentration caused by surface dimples; K_t was calculated based on dimple sizes. Acceptable prediction was achieved when dominant cracks nucleated from the shot-peened surface. Nevertheless, the fatigue life dominated by cracks initiating from the subsurface area was overestimated as the stress state beneath the surface was not taken into account during the lifing approach. It can be therefore concluded that the accuracy of total life approaches is sensitive to the consistency between the investigated regions and the area where crack initiation most probably occurs.

Benedetti et al. [125] then improved their method and demonstrated its application using two notched samples ($K_t = 1.53$ and 2.33 respectively). One improvement was realised by the development of an FE model, which incorporated residual stresses and strain hardening caused by shot peening [46]. This model was used to more accurately determine the applied bending stress amplitude as well as the stabilised surface residual stresses along the notch bisector (the hotspot region). Then the stabilised residual stress in the hotspot region was treated as the mean stress superimposed onto the oscillating stress introduced by external loads, as explained in their previous work [75, 100]. Another improvement was the application of a critical distance method [139, 140] to determine the effective stress governing the notch fatigue response. Then the total fatigue life of the two notched specimens under the as-received and different shot peening conditions was predicted using the Sines criterion. As shown in Figure 2-21, all the predicted results match well with corresponding experimental data, apart from the HCF behaviour of the sharp-notched samples ($K_t = 2.33$) treated with a high peening intensity. In addition, overestimation of the fatigue life resulting from the replacement of the stabilised residual stress state with the initial (as-peened) condition is also highlighted in Figure 2-21. This overestimation is more evident at high stress amplitudes where residual stress relaxation is expected to be more evident. More work conducted by Benedetti et al. using similar approaches is reported in [129, 141-143].

Despite the fact that all of the work reported by Benedetti et al. was conducted in the medium- to high-cycle fatigue regime, it indicates the critical requirements in developing

an approach applicable to the LCF regime: an accurate prediction of residual stress relaxation, and an appropriate application of the critical distance method.

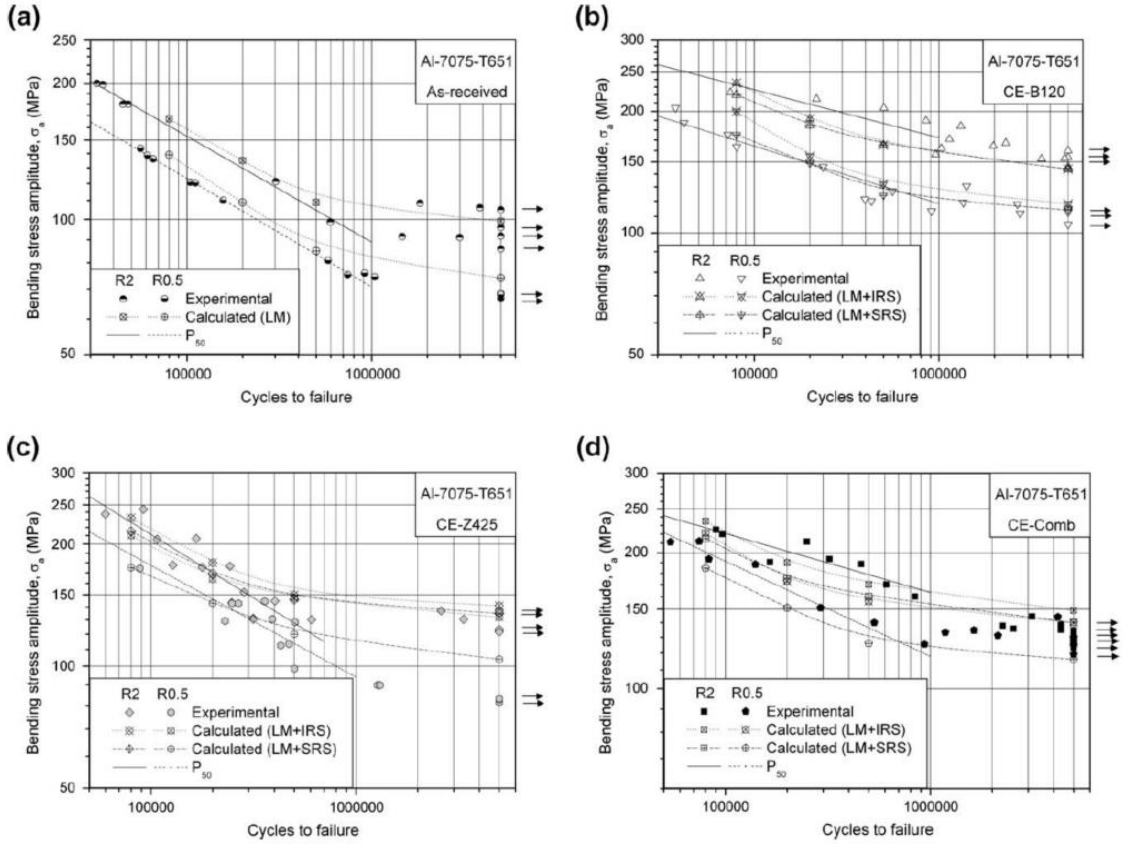

Figure 2-21: Comparison between experimental and calculated half-life fatigue curves: (a) as-received samples, (b) CE-B120: intensity = 4.5N, coverage = 100%, (c) CE-Z425: intensity = 4.5A, coverage = 100%, (d) CE-Z425 followed by CE-B120. IRS: initial residual stresses, SRS: stabilised stresses [125].

One example of an application to the LCF regime is the work carried out by Cláudio et al. [57]. They firstly used a FE model to determine the stabilised stress and strain in a shot-peened washer specimen (K_t = 1.32) under uniaxial loading. These results were then used to predict the total fatigue life (LCF) using the Goodman, the SWT and energy-based approaches. A critical distance method was applied to define averaged parameters over a sensible distance in the near-notch region [139, 140], and was applied combined with the Goodman and the energy-based approaches. Different definitions of the critical distance were used and it was concluded that the greater the distance over which the average stress was assumed to hold from the surface, the greater is the life predicted. In contrast, the application of the SWT approach was simply based on surface stress/strain states. It was found that all three approaches resulted in overly conservative predictions (less than half the experimental value), which was suggested to be due to the difficulty in appropriately defining the critical distance since the residual stress

gradients were high near the surface. In addition, the strain hardening effects were not included in the FE model and as such the predicted residual stress relaxation still needs validation.

Additionally, Cuellar et al. [144] used the SWT criterion to predict the LCF life of a central-holed laser shock peened titanium plate utilising a FE model. The residual stress distribution around the hole resulting from laser shock peening was determined using the contour method and was directly used in evaluating the stress parameters required by the SWT criterion. Although the predicted fatigue lives were found to be in reasonable agreement, this work neglected the effect of strain hardening and assumed no stress relief occurred during fatigue loading, which is not physically realistic.

In addition to lifing applications, the critical plane criteria have been found to be robust in predicting crack initiation sites. Prasannavenkatesan et al. [145] developed a 3D FE model incorporating both shot peening and inclusion effects, which was used to characterise the driving force of fatigue crack nucleation under HCF in shot-peened components. The FS criterion was applied to indicate the damage accumulation level in different areas, indicating a strong propensity for crack nucleation at inclusion clusters, which was in agreement with experimental observations. In addition, Fridrici et al. [146] has used the SWT criterion to successfully predict the crack nucleation area in shot-peened titanium alloy under fretting fatigue. Similar work can also be found in [147-149] for different materials and loading systems. This application of the critical plane criteria (FS and SWT) is particularly useful in determining the safety-critical point in components where geometrical stress concentration features facilitating crack nucleation are not evident.

Overall, the methodologies for the HCF life prediction of shot-peened specimens using total life approaches have been well established. However, investigations regarding the application of total life approaches in LCF for shot-peened samples are still limited. This might be due to the more evident plastic deformation during LCF especially in stress concentration areas, which might hinder an accurate prediction of the stress evolution during fatigue loading and the selection of an appropriate fatigue criterion. Another reason might be related to the short crack growth behaviour, which has been demonstrated to be effectively delayed by shot peening (as reviewed in Section 2.2.2), contributing to the main benefit of shot peening especially in LCF where crack growth plays a more dominant role than in HCF. However, this cannot be explicitly considered in the total life approaches.

2.3.3.3 Developments based on classical damage tolerant approaches

Considering the limitations of total life approaches, damage tolerant approaches have been utilised to assess how short crack growth behaviour may be affected by shot peening (or other surface treatments resulting in CRS, such as laser shock peening), which is more appealing in terms of industrial applications. To date, the applied methodologies can be generally classified as two types: the first type is normally based on analytical solutions, which modify the way in which the damage parameters are calculated (e.g. *K*, *J* and CTOD) to take the shot peening effects (i.e. surface roughness, strain hardening and CRS) into account. The second type, which is more widely applied, replaces ΔK with an effective SIF range (ΔK_{eff}) in the classical d*a*/d*N* - ΔK relations (e.g. the Paris Law), based on the concept of crack closure.

a. Methodology based on modifying the calculation of the damage parameters

A typical example of this methodology is the work conducted by Rio et al. [150]. An analytical microstructure-sensitive model based on CTOD was applied. Barrier strength at the grain boundary, which is significant for short fatigue cracks at low load where non-propagation can occur, has been taken into account by introducing a stress term representing the stress level at the grain boundary. This stress term was evaluated based on applied stress conditions and local grain orientations. The application of this approach was extended to the shot peening condition, by introducing a closure stress (caused by CRS), as well as a term describing the material resistance to plastic deformation (calibrated microhardness profiles were used to represent strain hardening effects) to the expression describing CTOD. Although this method has shown reasonable correlation in the HCF regime, it is yet to find widespread application. Its applicability in the LCF regime also needs further validation.

Another example was reported by Xiang and Liu [151], who proposed a model based on LEFM. The effect of plastic deformation during LCF was included into the model by defining an equivalent crack length, which equals the summation of the real crack length and the estimated plastic zone size. The effects of residual stress relaxation were also considered. This was realised by evaluating the changes in the stress ratio based on an employed logarithm function describing the surface residual stress evolution during cyclic loading. Relevant parameters were determined by fitting based on experimentally observed surface residual stress relaxation. Additionally, this model also allows for the effects of surface roughness by employing an asymptotic solution [152] which evaluates the SIF for cracks emanating from the notch (the surface dimples can be simplified as small notches). Again, reasonable life predictions were made in the HCF regime but its reliability in the LCF regime is uncertain.

b. Methodology based on the concept of crack closure

Crack closure occurs when crack faces touch under remote tensile load; the crack cannot propagate if the faces are in contact. There are several mechanisms inducing crack closure, such as plasticity, oxide and roughness induced mechanisms [12]. In the shot-peened condition, the CRS field is considered the main reason accounting for this phenomenon compared with other mechanisms [153]. To quantify the crack closure effects, ΔK_{eff} is normally used instead of the nominal range ΔK, and can be calculated using Equation 2-19, where K_{eff_max} represents the effective SIF at the peak load as a result of both external loads and residual stresses, and K_{open} refers to the SIF when the crack is fully opened. K_{open} is normally greater than K_{eff_min}, the effective SIF at the minimum load during a cycle, which results in ΔK_{eff} (see equation 2.19) being lower than ΔK, implying delayed crack growth affected by crack closure. Compared with the first methodology based on modifying the calculation of the damage parameters, the one based on crack closure has been demonstrated to be more versatile. It has been effectively applied to conditions with various geometries and CRS origins [91, 94, 96, 154, 155].

$$\Delta K_{eff} = K_{eff\_max} - K_{open} \tag{2-19}$$

Gao and Wu [96] predicted the fatigue life for single edge notch tension (SENT) samples with and without shot peening effects. In this study, the SIFs for short cracks subjected to both external loads and residual stresses induced by shot peening were determined by the weight function method [156]. This method has been widely applied to calculate the values of the SIF in various geometries or stress distributions due to its high accuracy and convenience. It avoids the requirement of a precise analysis regarding the stress distribution ahead of a crack tip, and facilitates the calculation of K_{eff_max} based on the linear superposition principle when residual stresses are present. In Gao and Wu's work, the fatigue lives of both the shot-peened and un-peened specimens were predicted using the FASTRAN method, which was a crack closure-based code developed by Newman to calculate K_{open} [157]. A good match was obtained between the predicted results and experimental results for both shot-peened and un-peened specimens. Other examples utilising the weight function method combined with the crack closure concept can be found in [94, 158-162], demonstrating its satisfactory applicability.

In addition to the weight function method, FE modelling has also been widely applied to determine ΔK_{eff} in various systems containing residual stresses [94, 158, 162, 163]. This involves modelling a crack with appropriately defined crack tip and crack wakes. The associated SIFs are normally directly obtained from the FE package, preferably using

the J-integral method [164]. In spite of the drawback in the increased computing time arising from crack modelling, one of the main advantages of the FE approach compared with the weight function method is its robustness in handling problems involved with complex geometries or boundary conditions, where the associated weight function is difficult to determine. Secondly, in the LCF regime, the effects of plastic deformation can be captured well using FE models, which is more reliable than the linear superposition principle which is commonly applied together with the weight function method to include residual stress effects.

Cláudio et al. [154, 155] assessed the LCF crack propagation life of a shot-peened notched geometry using a 2D plane strain FE model. In order to account for the closure effects of short cracks, the J-integral values calculated by the FE model containing cracks with different lengths were used to determine ΔK_{eff}. The predicted crack propagation life was then combined with the predicted crack initiation life [57] (as discussed in Section 2.3.3.2) to determine the total fatigue life. Although the predicted results were generally consistent with the experimental data, some results became non-conservative illustrating the requirement of an appropriate safety factor. It is also noted that this FE model did not consider the effects of strain hardening, neither were experimental validations for the predicted stress or strain redistribution during cyclic loading provided, which may restrict its application in other systems. The work of Cláudio et al. [154, 155] is nonetheless a useful contribution since it demonstrates the effectiveness of the FE approach in calculating ΔK_{eff} in relatively complex geometries subjected to shot peening.

It is noted that most of the work mentioned above only focuses on the effects of the CRS field and neglects the strain hardening effects (apart from some analytical approaches), which may degrade the accuracy of the evaluation of ΔK_{eff}. Another issue is with respect to residual stress redistribution, which can be triggered by both mechanical loading (as discussed in Section 2.2.2) and the presence of a crack. The influence of this behaviour and how it could be considered in the modelling work have been rarely mentioned. In addition, He et al. [82, 165] recently reported a significant discrepancy between the short crack shape evolution in polished and shot-peened notched samples, which was closely related to the shot peening process and the microstructure of the material. This implied the necessity of taking the crack shape effects into account when evaluating the influence exerted by shot peening on short crack growth. However, relevant work is relatively scarce, mainly due to the lack of reliable quantitative experimental data describing crack propagation in the bulk of the material to support relevant modelling work.

2.4 Summary of the literature review

In this chapter, both experimental methods used to characterise the shot peening effects and the numerical methods applied to reconstruct them are firstly reviewed (Section 2.1). Relevant work provides a prerequisite for further analysis in quantitatively assessing the shot peening effects on fatigue. To date, most of the residual stress reconstruction work was based on plain geometries. More complex situations, such as when a geometry with stress concentration features is involved (which is more representative of the real applications) has been scarcely investigated.

Generally speaking, the benefit of shot peening in improving the fatigue resistance of components can be attributed to the induced compressive residual stress and strain hardening field, while imperfection of the peened surface may exert some negative effects. Although the effect of shot peening on HCF has been well documented, the effect on LCF has been relatively less well established due to: 1) more significant residual stress relaxation associated with the cyclic softening behaviour of the material, and 2) its competition with the accelerated crack nucleation caused by the imperfect surface. Therefore, investigating the interaction between the shot peening induced effects and service conditions is necessary in the development of an effective lifing approach.

Both total life and damage tolerant approaches have been applied to predict the fatigue life of shot-peened components. The main factor influencing the reliability of the life prediction is whether the selected fatigue driving parameters (e.g. $\Delta\sigma$, $\Delta\varepsilon$ and ΔK_{eff}) can be accurately calculated considering shot peening effects, which can be facilitated by the application of FE modelling.

Among total life approaches (Section 2.3.3.2), the multiaxial fatigue criteria have been demonstrated to be most reliable, particularly in the HCF regime. The required stress and strain parameters can be evaluated based on the predicted stabilised stress and strain states in safety-critical areas where cracks most probably nucleate. The critical distance method can be used to account for the effect of stress or strain gradients which may have a significant influence on crack initiation and early propagation behaviours. However, investigations in the LCF regime are still limited. The postulated reasons are the difficulties in considering the influences derived from the plastic deformation and the short crack growth behaviour, which govern the LCF life.

In terms of damage tolerant approaches, local stress states affected by shot peening have to be taken into account when calculating SIFs. Since shot peening improves fatigue resistance mainly by retarding the early crack growth process, the short crack growth behaviour needs to be explicitly considered when applying fracture mechanics. The

concept of crack closure has been demonstrated to be powerful in explaining and quantifying the variation in short crack growth affected by compressive residual stresses, using ΔK_{eff}. Both the weight function method and the FE-based method can be used to accurately determine ΔK_{eff}. However, the effects derived from strain hardening, residual stress redistribution (caused by both mechanical loading and the appearance of a crack) as well as crack shape evolution need to be taken into account in order to develop a more robust model with wider applicability.

2.5 Methodology framework

Based on the literature review discussed in this chapter, a methodology framework has been built up to support this project, attempting to fill some gaps in the development of a robust life assessment tool that can be applied to shot-peened notched geometries.

FE modelling has been selected as the main approach to achieve the objectives of the project, due to its versatility in reconstructing the as-peened condition (Sections 2.1.2.2 and 2.1.3.2), in determining the mechanical response of the structure to service conditions (Section 2.3.3.1), and in crack modelling (Section 2.3.3.3). The modelling work in this thesis has been carried out using ABAQUS/Standard (v6.13). Some experimentally measured results were used to provide either validation or input data for the modelling work. The experimental data were obtained either from previous studies [10, 17, 77, 82, 166] or supplementary measurements which have been carried out as part of this thesis. The flowchart shown in Figure 2-22 illustrates the modelling procedures as well as how the experimental techniques support the modelling work in the present study. The main modelling steps were carried out for the plain bend bar (PBB) specimen first since it had a simple geometry. After validation of the applied modelling techniques, they were applied to the notched specimen where the geometrical effects need to be taken into account.

As shown in Figure 2-22, the first step is the development of a preliminary FE model without shot peening effects. This model needs validation before shot peening effects are accounted for in the modelling work to make sure the geometries, the mesh, the boundary conditions, the material model, etc. have been appropriately defined. The preliminary model has been validated by comparing the FE predicted strain evolution at safety-critical regions during fatigue loading with corresponding experimentally measured results. Details of this step are presented in Chapter 3.

In the next step, the as-peened residual stress field has been reconstructed based on XRD measurements. An inverse eigenstrain method, which was based on the elastic

behaviour of the material, has been used to determine the eigenstrain distribution caused by shot peening in flat samples. The determined eigenstrain profile has been incorporated into the FE models as the source of residual stresses. The application of this residual stress modelling approach has been extended to the notched case by considering the effects of the notched geometry on eigenstrain profiles. Furthermore, to account for the shot peening induced strain hardening effects, varying mechanical properties have been defined for the material within the surface layer in the FE model. This has been achieved by defining the initial condition (plastic strain caused by shot peening) of the elasto-plastic material model at different depths, based on measurements from an electron back-scatter diffraction (EBSD) based approach [17]. Finally, the residual stress relaxation behaviour occurring during fatigue in both un-notched and notched specimens has been investigated using the developed FE model, and also compared with corresponding experimental results measured by XRD. Details of this step are elaborated in Chapter 4.

In the last step, the developed FE models allowing for shot peening effects have been utilised to facilitate the development of life assessment methods that can be applied in the LCF regime. The application of total life approaches has been firstly investigated and is presented in detail in Chapter 5. The stress-strain-based Smith-Watson-Topper (SWT) and Fatemi-Socie (FS) critical plane criteria have been applied together with a critical distance method. The required stress and strain parameters are evaluated based on the modelling results. In addition, the application of damage tolerant approaches has also been investigated. Both 2D and 3D FE models containing a crack have been developed from the 'un-cracked' model that has been used in the preceding chapters. ΔK_{eff} has been determined using both the weight function and the FE-based (based on the calculation of J-integral) methods. The short crack growth behaviour affected by shot peening has been subsequently predicted in terms of its evolution in sizes and shapes, using the developed FE model. This part of work is introduced in Chapters 6 and 7 for the 2D and 3D modelling work respectively.

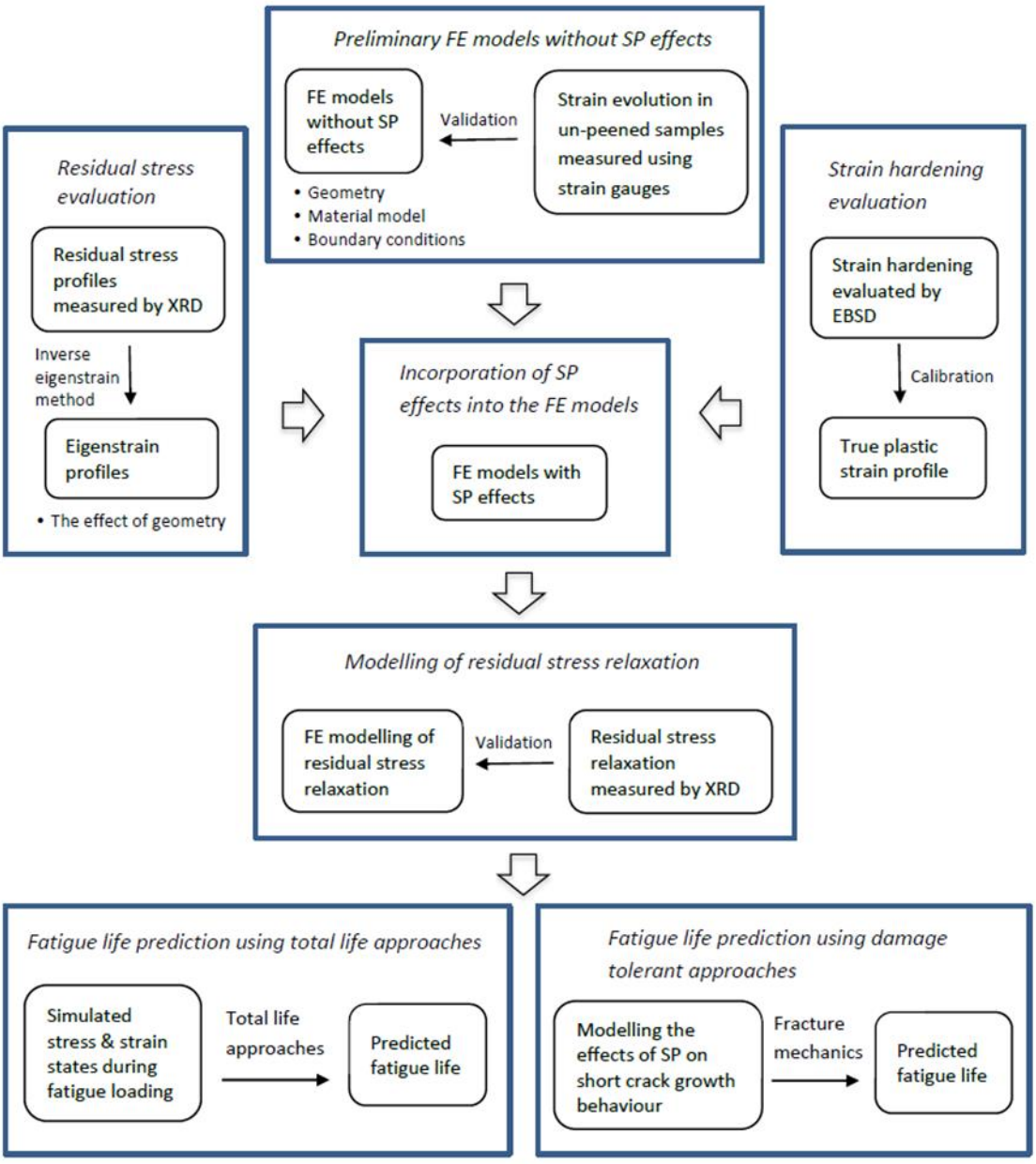

Figure 2-22: Flowchart of the modelling work in the present study.

3 Development of the preliminary finite element model without shot peening effects

3.1 Introduction

In this chapter, the investigated material, shot peening parameters and specimens are introduced. Modelling details regarding the boundary conditions, the mesh and the material model are also presented. The calibration of different material models and the comparison between them are detailed and discussed in this chapter in order to make an appropriate choice of the material model. In addition, experimental validation of the preliminary FE model is also provided. At this stage, no shot peening effects are incorporated. Some aspects of the work presented in this chapter have been published in the following paper:

You, C., Achintha, M., Soady, K., Smyth, N., Fitzpatrick, M., & Reed, P. (2017). *Low cycle fatigue life prediction in shot-peened components of different geometries – Part I: residual stress relaxation*. Fatigue and Fracture of Engineering Materials and Structures, 40(5), 761-775.

3.2 Material characterisation

FV448, a 9-12 %Cr tempered martensitic steel is under investigation in the current research. It is a material widely used in low pressure (LP) turbine blades. This material is typically austenitised at 1150℃, oil quenched, tempered at 650℃ and then air cooled. Its chemical composition is presented in Table 3-1.

Table 3-1: Composition of FV448

Element	C	Mn	Si	Ni	Cr	Mo	W	V	Nb	Fe
wt%	0.12	0.94	0.31	0.74	11.0	0.58	<0.01	0.31	0.34	Bal

3.2.1 Material microstructure

The microstructure of FV448 has been investigated in previous research [10, 167]. Optical micrographs showing the microstructure relative to the longitudinal (rolling direction), L, transverse, T and short-transverse, S directions of the bar stock are shown

in Figure 3-1, where both the prior austenite grain boundaries and carbides at the grain boundaries are easy to identify. According to Figure 3-1, it seems that there are no obvious differences in these orientations from the microstructure point of view. However, stringers (alumina and MnS) were found along the longitudinal direction in the L-T and L-S faces, as clearly illustrated in Figure 3-2, which is consistent with an observation in the similar FV566 [168].

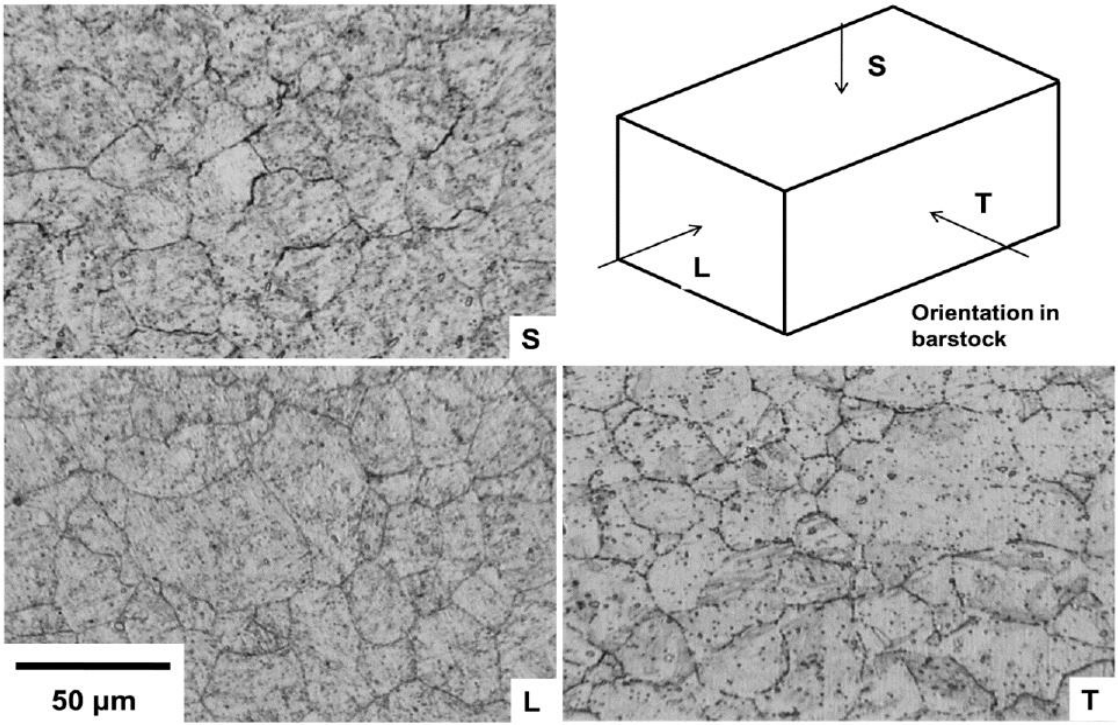

Figure 3-1: Optical micrographs of FV448 showing microstructural directionality [10].

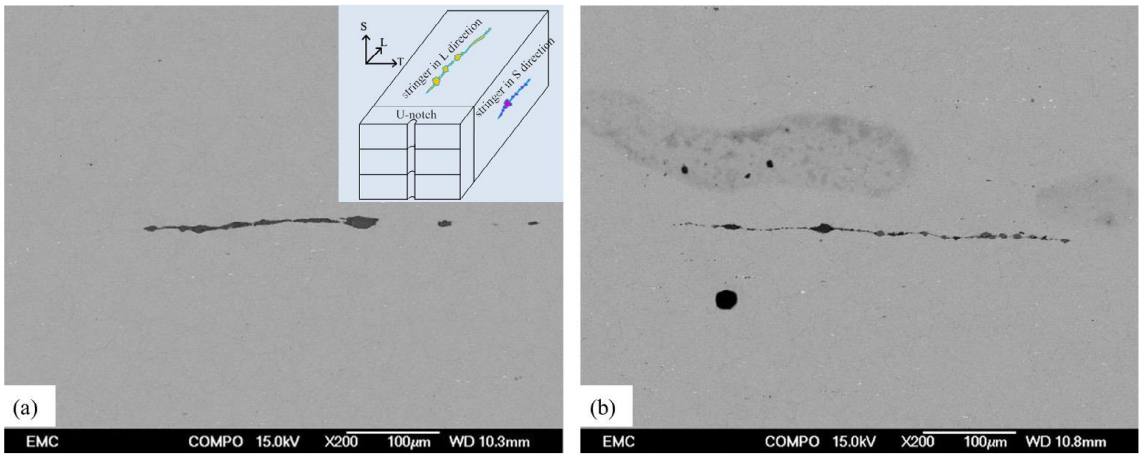

Figure 3-2: The schematic illustration in (a) shows the positions of the stringers in the barstock; inclusions of aluminium oxide/silicate and manganese sulphide aligned in the longitudinal direction (a) on the L–T face; (b) on the L–S face within the FV448 matrix [82].

3.2.2 Mechanical properties

Both the monotonic and cyclic mechanical properties of FV448 have been determined in previous experiments by Soady [10]. The specimens used for uniaxial loading tests were machined perpendicular to the rolling direction (transverse direction) of the bar stock material. This direction was selected for analysis since it corresponded with the tensile direction in all samples used for bending tests (as introduced in Section 3.5). Both tensile and compression testing were carried out on Instron 5569 using samples of the dimensions shown in Figure 3-3. The strain evolution during tensile testing was measured using an extensometer (with a gauge length of 12.5 mm) fitted to the centre of the parallel section. The load-displacement data of the load frame corrected for machine compliance were used to measure the strain in compression testing. The Young's modulus and Poisson's ratio that are most representative of the material were determined to be E = 201.3 GPa and v = 0.3 respectively. The yield strength $\sigma_{0.2}$ (0.2% plastic strain point) in tension was 806 MPa, which was lower than that in compression of 842 MPa (4.5% difference). This tension-compression asymmetry has also been reported in a similar 9Cr-1Mo steel where the increase in $\sigma_{0.2}$ in compression compared to tension was 3.8% [169].

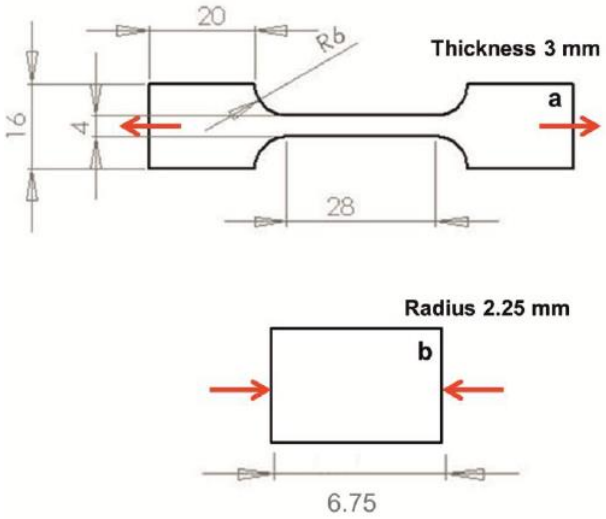

Figure 3-3: (a) Tensile and (b) compression test sample dimensions in mm [10].

In addition, tensile data were also obtained in the longitudinal (rolling) direction of the bar stock. This direction was used because it was the only direction from which cyclic stress-strain samples of the geometry shown in Figure 3-4 could be obtained. An increase in tensile $\sigma_{0.2}$ to 858 MPa in the longitudinal direction was observed. This difference in mechanical properties in two directions is attributed to the manufacturing process (rolling or extrusion) of bar stock and the orientation of the stringers.

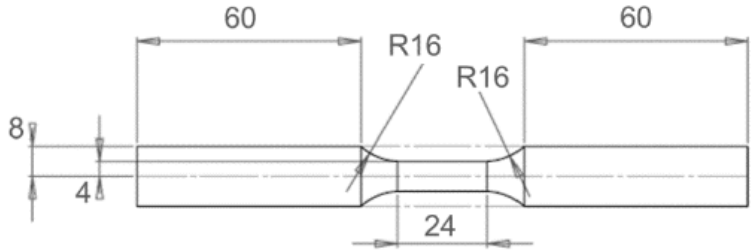

Figure 3-4: Cyclic stress-strain test sample dimensions in mm [17].

To determine the cyclic mechanical properties of FV448, constant amplitude strain controlled axial tests were carried out at different total strain ranges using a triangular waveform at a strain rate of $3 \times 10^{-3} S^{-1}$. Strain was measured using a 12.5 mm gauge length extensometer. As illustrated in Figure 3-5, the cyclic softening behaviour is evident in the early stage of fatigue and then develops more slowly during subsequent cycles (achieving a quasi-plateau). It can be also seen that this behaviour becomes more evident when the strain level increases.

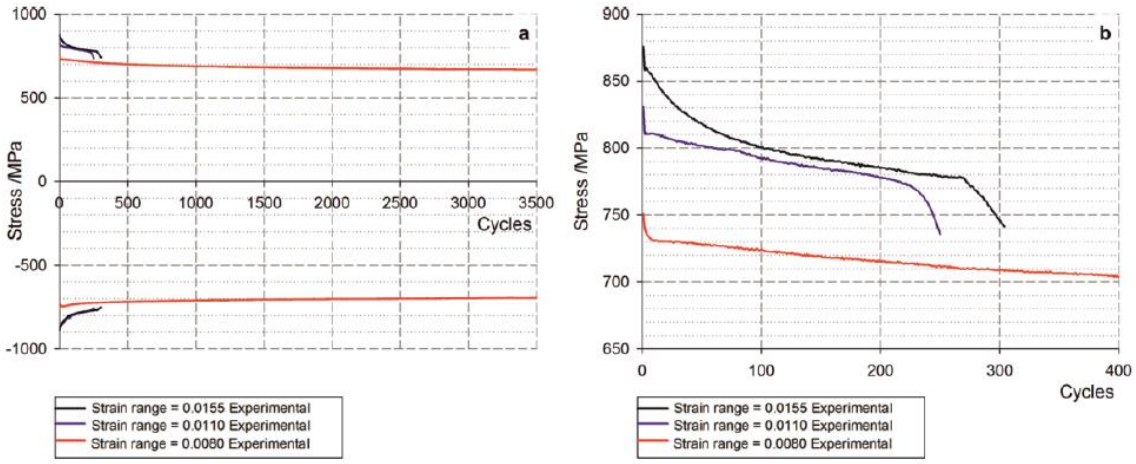

Figure 3-5: Development of peak stresses through life at $\Delta\varepsilon$ = 0.008, 0.0110, 0.0155, R_ε = -1 showing (a) through life behaviour and (b) tensile behaviour at the start of life [10].

3.3 Material model

3.3.1 Definition of the material model

A combined nonlinear isotropic-kinematic hardening material model proposed by Chaboche [138] has been chosen in this study to describe the mechanical properties of FV448. This constitutive model has been widely applied in the modelling work and has been demonstrated to be robust in describing the mechanical properties of the material [44, 73, 74]. It consists of two components: the isotropic and the kinematic hardening

components, as illustrated in Figure 3-6. The isotropic component is used to indicate the size of the yield surface (σ^0), and the kinematic component describes the position of the yield surface in terms of the backstress ($\boldsymbol{a}$), considering the Bauschinger effect. So far, this material model has been modified into different formats to account for the effect of creep, strain rate or strain range memory [170]. Since the present study focuses on investigating the effect of shot peening on fatigue life, rather than developing an explicit material model suitable for all conditions, only the basic format of this material model (without the effects stated above) has been applied. This format is available in ABAQUS as in-built functions [171].

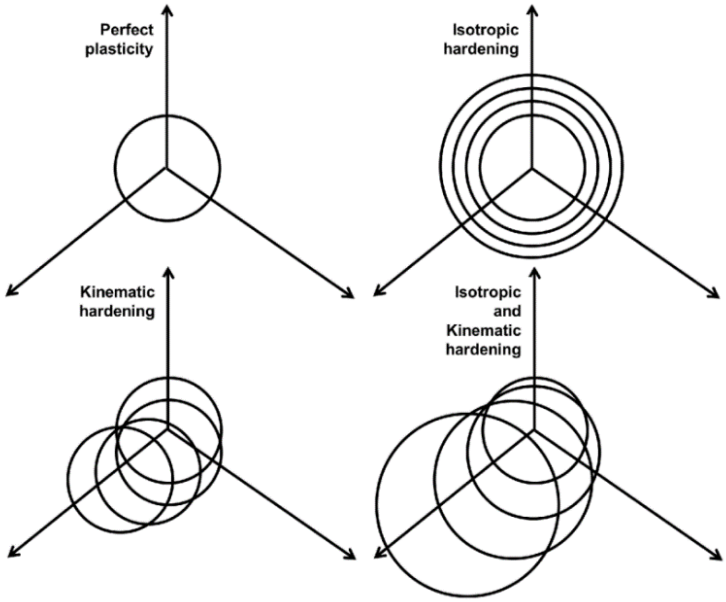

Figure 3-6: Definitions of the isotropic and kinematic components.

In this model, the yield surface is defined by Equation 3-1, where $f(\boldsymbol{\sigma} - \boldsymbol{a})$ is the equivalent Mises stress; $F < 0$ indicates the elastic domain and plastic flow takes place if $F = 0$. Equation 3-2 describes the calculation of the equivalent plastic strain rate, $\dot{\bar{\varepsilon}}^{pl}$, using the plastic strain rate component, $\dot{\boldsymbol{\varepsilon}}^{\boldsymbol{pl}}$. The isotropic and the kinematic hardening components are expressed by Equations 3-3 and 3-4 respectively:

$$F = f(\boldsymbol{\sigma} - \boldsymbol{a}) - \sigma^0 \tag{3-1}$$

$$\dot{\bar{\varepsilon}}^{pl} = \sqrt{\left(\frac{2}{3}\right)\dot{\boldsymbol{\varepsilon}}^{\boldsymbol{pl}} : \dot{\boldsymbol{\varepsilon}}^{\boldsymbol{pl}}} \tag{3-2}$$

$$\sigma^0 = \sigma|_0 + Q_\infty(1 - e^{-b\bar{\varepsilon}^{pl}}) \tag{3-3}$$

$$\dot{\boldsymbol{a}}_{\boldsymbol{k}} = \frac{2}{3} C_k \dot{\varepsilon}^{pl} - \gamma_k \boldsymbol{a}_{\boldsymbol{k}} \left|\dot{\bar{\varepsilon}}^{pl}\right|, \quad \boldsymbol{a} = \sum_{k=1}^{N} \boldsymbol{a}_{\boldsymbol{k}} \tag{3-4}$$

where $\sigma|_0$ is the yield stress at zero equivalent plastic strain ($\bar{\varepsilon}^{pl}$), Q_∞ indicates the maximum change of σ^0, and b defines the rate at which σ^0 changes with the accumulation of $\bar{\varepsilon}^{pl}$. N is the total number of backstresses. C_k is the initial kinematic hardening moduli and γ_k determines the decreasing rate of the kinematic hardening moduli with increasing $\bar{\varepsilon}^{pl}$.

3.3.2 Identification of the material coefficients

Soady [10] indicated that for FV448, a material model calibrated based on the monotonic stress-strain curve tends to result in an underestimation of the Bauschinger effect and a large error in predicting the cyclic mechanical property of the material. In contrast, a good representation of the cyclic hysteresis loops can be obtained by a calibration based on the second cycle onwards, which may, however, lead to a poor representation of the monotonic behaviour. This situation was ascribed to the notable discrepancy between the monotonic and the subsequent cyclic curves, which was due to the significant cyclic softening behaviour occurring during the first cycle (as shown in Figure 3-5). Similar situations were also found by others for varying materials [64, 172, 173]. Consequently, in order to calibrate a material model which is most appropriate for the current research, material models representative of the monotonic and cyclic mechanical properties were developed separately and a comparison was made between them.

There are various methods to identify the material coefficients based on experimental data. Basically they can be classified as two categories:

a. The step-by-step approach

In this approach, the material coefficients are given corresponding physical meanings. A group of them can be determined at a single step using a set of experimental data to which they are sensitive. After several steps, all the coefficients can be identified.

b. The simultaneous determination approach

In this approach, all the material coefficients are identified simultaneously in one step based on sufficient independent experiments. This process can be achieved by using an appropriate fitting procedure to minimise the difference between experimental and predicted results.

In the current research, the step-by-step approach was applied to identify the material coefficients representative of the cyclic mechanical property of FV448. It is noted that in order to better simulate the cyclic hysteresis loops, the first cycle was neglected and the calibration was carried out based on the second cycle onwards as suggested by Soady

[10]. Experimental data used for this calibration work were supplied by Soady [10], which were generated by uniaxial tests under strain control ($R_\varepsilon = -1$) at different strain ranges ($\Delta\varepsilon$). In contrast, material coefficients for the monotonic material model were identified based on the monotonic stress-strain curve of FV448, using the simultaneous determination approach. Once calibrated, both the cyclic and monotonic material models were implemented in ABAQUS using a single element model under displacement control to check their accuracy in different loading conditions.

3.3.2.1 Calibration based on the cyclic mechanical property

Material coefficients representing the cyclic mechanical properties of the material are usually determined from the knowledge of the cyclic hysteresis loops and the cyclic softening or hardening curve determining the relation between peak strains and peak stresses. In the present study, the cyclic material model has been calibrated in two different ways. In the first approach, the material model was defined to be dependent on strain range, which allows the variance of the material parameters with strain ranges. In the second approach, one set of material coefficients was identified to represent the cyclic behaviour for all strain ranges. Both calibration procedures have been used in the literatures for various materials and a comparison between them is presented here in order to determine the more appropriate one for FV448.

3.3.2.1.1 The cyclic material model dependent on strain range

This work for FV448 was initially carried out by Soady [10], and was repeated in the present study for three different strain ranges respectively. The procedure has been detailed in [171]. To calibrate the isotropic component, Equation 3-3 was fitted to the curve describing the evolution of σ^0 with accumulating $\bar{\varepsilon}^{pl}$. $\bar{\varepsilon}^{pl}$ was approximated using Equation 3-5, where *N* indicates the number of cycles and $\Delta\varepsilon^{pl\_avg}$ is the averaged plastic strain range. $\Delta\varepsilon^{pl\_avg}$ was approximated by averaging the plastic strain range $\Delta\varepsilon^{pl}$ for the second and the stabilised cycles.

$$\bar{\varepsilon}^{pl} = 2N\Delta\varepsilon^{pl\_avg} \tag{3-5}$$

Only one kinematic component was used in this model, which was calibrated based on the first half of the second cycle using Equation 3-6 which was integrated from Equation 3-4, where ε^{pl_0} was the initial plastic strain for this cycle and a_{k_0} denoted the initial value of the k^{th} backstress for this cycle. Both ε^{pl_0} and a_{k_0} were evaluated based on the stress-strain curve of the first cycle.

$$a_k = \frac{C_k}{\gamma_k}\left[1 - e^{-\gamma_k(\varepsilon^{pl} - \varepsilon^{pl\_0})}\right] + a_{k\_0}e^{-\gamma_k(\varepsilon^{pl} - \varepsilon^{pl\_0})} \tag{3-6}$$

The identified material coefficients for each strain range are listed in Table 3-2. The comparison between the experimental data and the predicted results using these identified coefficients are shown in Figure 3-7. It can be seen from Figure 3-7(a) that the stabilised stress-strain loops have been satisfactorily predicted using the material coefficients calibrated for corresponding strain ranges. In addition, the through-life evolutions of peak stresses have also been predicted well with an overall standard deviation error smaller than 2%. However, peak stresses in the first cycle have been significantly underestimated for all strain ranges by 5.4 – 7.6%. Details of the errors in the predicted peak stresses are shown in Table 3-3.

Table 3-2: Cyclic material coefficients dependent on strain range.

$\Delta\varepsilon$	$\sigma\|_0$/MPa	Isotropic component		Kinematic component	
		Q_∞/MPa	r	C/MPa	γ
0.008	493	-71	0.695	710000	2165
0.011	501	-56	0.693	340000	1053
0.0155	508	-79	1.078	191000	506

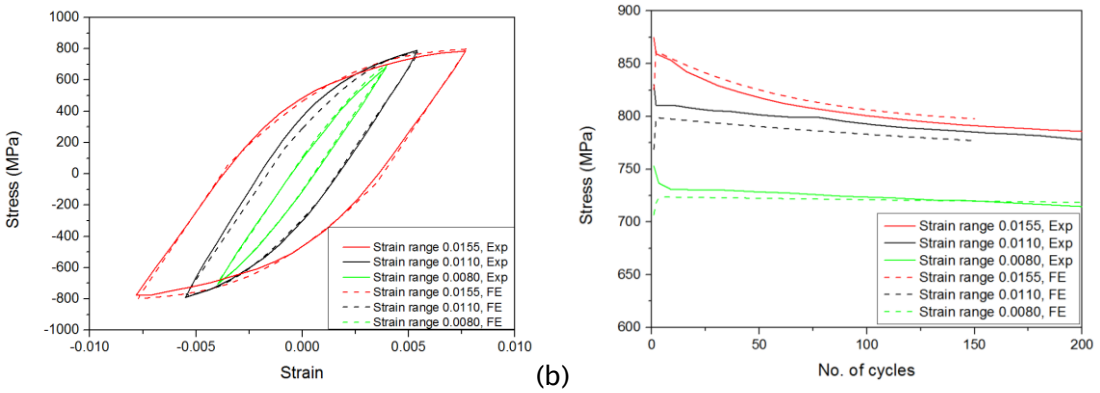

Figure 3-7: Comparison between the experimental data and the predicted results using coefficients in Table 3-2 at R_ε = -1; (a) stabilised hysteresis loops and (b) evolution of peak stresses.

Table 3-3: Statistical comparison of the predicted peak stresses using the combined material dependent on strain range at R_ε = -1.

$\Delta\varepsilon$	Standard deviation error per half cycle /%	Absolute error in the first half cycle /%
0.008	0.64	5.4
0.0110	1.66	7.6
0.0155	0.74	6.2

3.3.2.1.2 The cyclic material model independent of strain range

The calibration work for the cyclic material model independent of strain range has been carried out following the procedure detailed in [138, 174]. Under symmetric cyclic loading, the relation between the maximum stress σ_{max} and the maximum backstress a_{max} is defined by Equation 3-7. By substituting $\sigma^0(\bar{\varepsilon}^{pl})$ with Equations 3-3 and 3-5, and then applying Equation 3-7 to each cycle, Equation 3-8 can be obtained, where σ_{max_0} and σ_{max_s} are the maximum stresses for the first cycle and the stabilised cycle respectively. Apparently, Equation 3-8 only depends on $\bar{\varepsilon}^{pl}$ and is independent of the strain amplitude, implying that the isotropic component can be calibrated identically for all strain ranges. This has been verified by experiments for different materials [138, 175]. The experimental data for FV448 and the corresponding fitted curve are shown in Figure 3-8(a), determining the value of b in Equation 3-8. Q_∞ was determined by averaging the three values used for single strain ranges shown in Table 3-2. The identified results of b and Q_∞ independent of strain range for the isotropic component are shown in Table 3-4.

$$\sigma_{max} = a_{max}(\varepsilon^{pl}) + \sigma^0(\bar{\varepsilon}^{pl}) \tag{3-7}$$

$$\frac{\sigma_{max}-\sigma_{max\_0}}{\sigma_{max\_s}-\sigma_{max\_0}} \approx \frac{Q_\infty\left(1-e^{-b\bar{\varepsilon}^{pl}}\right)}{Q_\infty} = \left(1-e^{-r\bar{\varepsilon}^{pl}}\right) \approx \left(1-e^{-2rN\Delta\varepsilon^{pl\_avg}}\right) \tag{3-8}$$

In order to improve modelling of the ratcheting behaviour, two kinematic components were used and one of them was linear, as suggested by [171, 176]. Hence, Equation 3-9 was used to describe the kinematic component. By integrating Equation 3-9 on two half cycles of tension and compression in the stabilised loop, the relation between stress amplitudes $\frac{\Delta\sigma}{2}$ and strain amplitudes $\frac{\Delta\varepsilon^{pl}}{2}$ in the stabilised cycle was obtained, as described by Equation 3-10, using an assumption that $\sigma_{\max\_s}$ approximately equalled $\frac{\Delta\sigma}{2}$

when R_ε = -1. This equation was used to identify the kinematic coefficients, as shown in Figure 3-8(b); in order to have enough data for the fitting process, one data point was approximated using the cyclic Ramberg Osgood model calibrated for FV448 [10]. The determined values of the kinematic coefficients are shown in Table 3-4.

$$\dot{\boldsymbol{a}}_1 = C_1\dot{\varepsilon}^{pl} - \gamma_1\boldsymbol{a}_1|\dot{\varepsilon}^{pl}|,\ \dot{\boldsymbol{a}}_2 = C_2\dot{\varepsilon}^{pl},\ \boldsymbol{a} = \boldsymbol{a}_1 + \boldsymbol{a}_2 \tag{3-9}$$

$$\frac{\Delta\sigma}{2} = \frac{C_1}{\gamma_1}\tanh\left(\gamma_1\frac{\Delta\varepsilon^{pl}}{2}\right) + C_2\Delta\varepsilon^{pl} + \sigma|_0 + Q_\infty \tag{3-10}$$

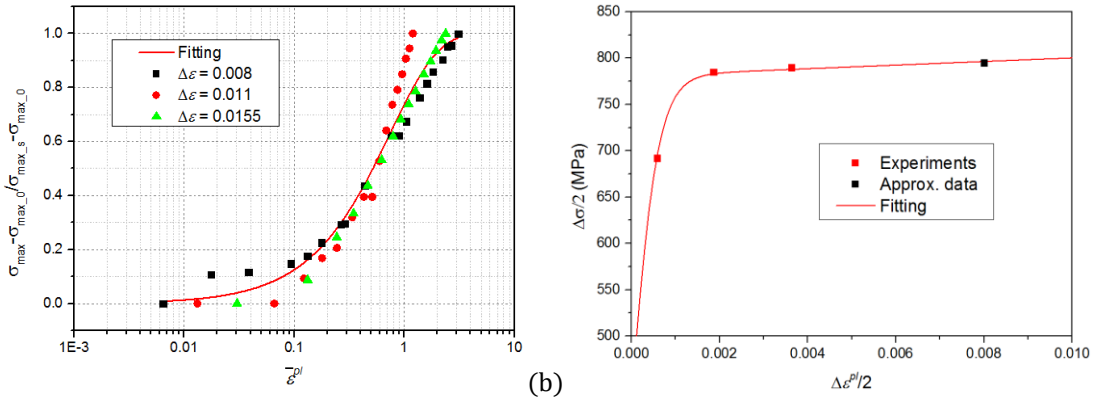

(a) (b)

Figure 3-8: Development of the cyclic combined material model independent of strain range, illustrating the calibration of (a) the isotropic component and (b) the kinematic component.

Table 3-4: Cyclic material coefficients independent of strain range

$\sigma\|_0$/MPa	Isotropic component		Kinematic component			
	Q_∞/MPa	b	C_1/MPa	γ_1	C_2/MPa	γ_2
501	-69	1.33801	572631	1656	1950	0

The predicted cyclic mechanical properties using the material coefficients shown in Table 3-4 are compared with corresponding experimental data in Figure 3-9. It can be seen from Figure 3-9(b) that the peak stress evolutions have been generally well predicted for different strain ranges apart from the first few cycles, which is similar to the results predicted using the cyclic material model dependent on strain range. The errors of the predicted peak stresses are shown in Table 3-5. However, the hardening phase of the stabilised loop has been overestimated, especially at high strain ranges as shown in

Figure 3-9(a); the maximum error at $\Delta\varepsilon$ = 0.0155 is 35% in terms of the strain difference between the predicted and experimental results at the same stress level.

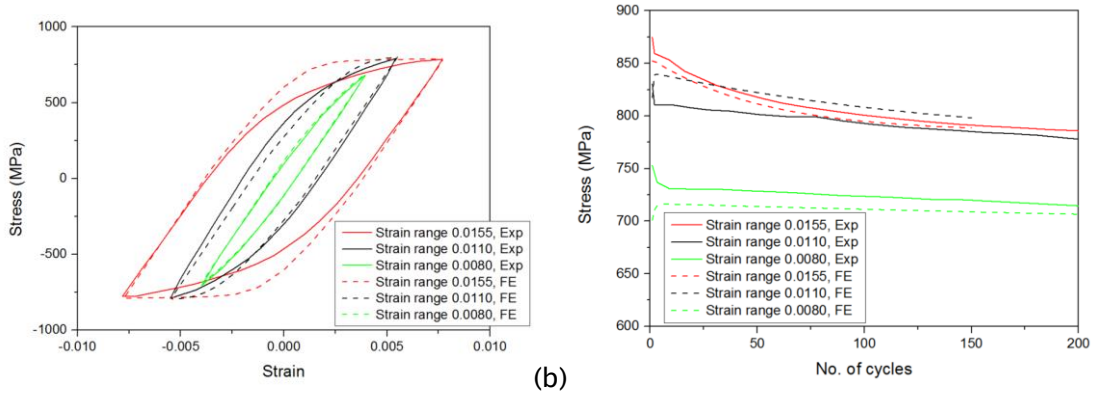

(a) (b)

Figure 3-9: Comparison between the experimental data and the predicted results using coefficients in Table 3-4 at R_ε = -1; (a) stabilised hysteresis loops and (b) evolution of peak stresses.

Table 3-5: Errors of the predicted peak stresses using the combined material independent of strain range at R_ε = -1.

$\Delta\varepsilon$	Standard deviation error per half cycle /%	Absolute error in the first half cycle /%
0.008	1.95	6.89
0.0110	2.47	1.55
0.0155	0.98	2.57

Since the combined material model is usually developed based on tests at R_ε = -1 for certain strain ranges, the transferability of the material model has to be checked before it is applied to other loading conditions with different R_ε and $\Delta\varepsilon$. As a result of this, the developed material model was applied to predict the cyclic behaviour of FV448 under uniaxial loading at R_ε = 0. The comparison between the predicted evolutions of peak stresses and the experimental data for two strain ranges ($\Delta\varepsilon$ = 0.0155 and 0.005) are illustrated in Figure 3-10. As shown in Figure 3-10(a), the evolution of peak stresses for $\Delta\varepsilon$ = 0.0155 has been generally modelled well with an overall standard deviation error of 3.34% (as shown in Table 3-6). However, a significant overestimation of mean stress relaxation for $\Delta\varepsilon$ = 0.005 can be seen in Figure 3-10(b) with an overall standard deviation error up to 51.99%. This large error is probably attributed to the overestimation of the

ratcheting behaviour, which implies a poor transferability of this material model in this loading condition.

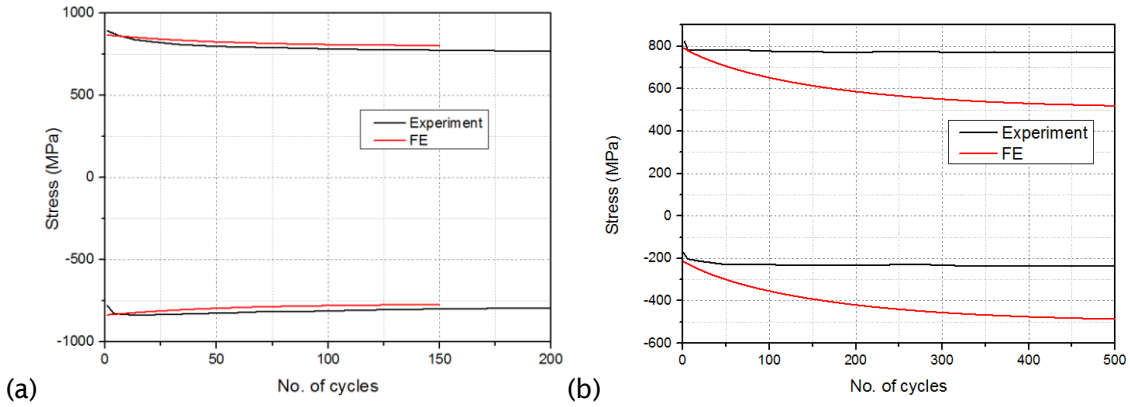

Figure 3-10: Comparison between the experimental data and the predicted results using the coefficients provided in Table 3-4 at R_ε = 0; the evolution of peak stresses when (a) $\Delta\varepsilon$ = 0.0155 and (b) $\Delta\varepsilon$ = 0.005.

Table 3-6: Errors of the predicted peak stresses using the combined material independent of strain range at R_ε = 0.

$\Delta\varepsilon$	Standard deviation error per half cycle /%	Absolute error in the first half cycle /%
0.005	51.99	3.74
0.0155	3.34	2.90

3.3.2.2 Calibration based on the monotonic mechanical property

The combined material model can also be used to represent the monotonic mechanical properties of FV448. In order to achieve a satisfactory modelling of the monotonic stress-strain relation, two kinematic components have been used, one of which was linear (the same choice as the cyclic material model independent of strain range). Hence, the kinematic component can be also described using Equation 3-9, which was then used to determine Equation 3-11 after an integration based on monotonic loading; the initial plastic strain and backstresses were determined to be zero. By combining Equation 3-3 (the isotropic component) and 3-11 (the kinematic component), the relation between stress and strain during monotonic loading was obtained, as described using Equation 3-12. It is noted that $\bar{\varepsilon}^{pl} = \varepsilon^{pl}$ during tensile monotonic loading.

$$a = \frac{C_1}{\gamma_1}\left(1 - e^{-\gamma_1 \varepsilon^{pl}}\right) + C_2 \varepsilon^{pl} \tag{3-11}$$

$$\sigma = \sigma|_0 + Q_\infty \left(1 - e^{-b\bar{\varepsilon}^{pl}}\right) + \frac{C_1}{\gamma_1}\left(1 - e^{-\gamma_1 \varepsilon^{pl}}\right) + C_2 \varepsilon^{pl} \tag{3-12}$$

A monotonic Ramberg Osgood model representative of the monotonic mechanical property of FV448, which was calibrated by [10], was used to generate the (ε^{pl}, σ) data pairs required by the calibration work of Equation 3-12. All the material coefficients were identified simultaneously during the calibration process. The calibrated material coefficients are listed in Table 3-7, which were found to be largely independent of their initialised values of the calibration work. The calibrated results are shown in Figure 3-11, with the coefficient of determination (R^2) of 0.99.

Table 3-7: Material coefficients describing the monotonic mechanical properties

$\sigma\|_0$/MPa	Isotropic component		Kinematic component			
	Q_∞/MPa	b	C_1/MPa	γ_1	C_2/MPa	γ_2
697	171	35	203621	1139	349	0

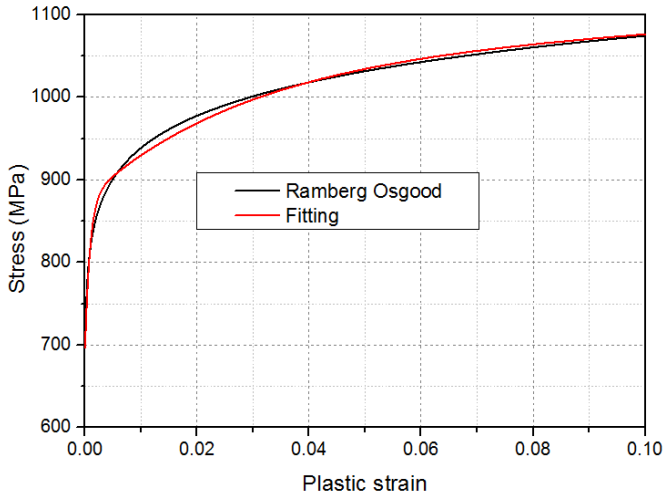

Figure 3-11: Development of the monotonic combined material model.

3.3.3 Application of the developed material models

In the 3 and 4-point bend tests used in this project, the strain ranges at different depths below the sample top-surface are different, which makes the application of a cyclic material model dependent on strain range non-trivial despite its expected higher

accuracy than a cyclic model independent of strain range. For simplification of the modelling process, only the cyclic material model independent of strain range and the monotonic material model were considered. A comparison between the two material models has been carried out by applying them to a plain bend bar model under 4-point bend and a notched model under 3-point bend at a load ratio R_p = 0.1. The development of the FE models is introduced in the following section (Section 3.6). Relevant modelling results and discussions are presented in Section 3.6.3, which also provides an experimental validation of the preliminary FE model choice before shot peening effects are considered.

3.4 Shot peening treatments

Two shot peening processes were used in this study and relevant details are shown in Table 3-8. MI230R 13A 200%, labelled as T0, is the baseline shot peening process used throughout this research since it is industrially applied to steam turbine blades. Another process, MI110R 04A 200% (T1) with a lower peening intensity was also considered in order to investigate the effect of peening intensities on the benefit of shot peening in improving fatigue life. All shot peening processes were carried out by Metal Improvement Company Derby Division.

Table 3-8: Shot peening process parameters

Process	Label	Intensity	Coverage /%	Shot diameter/ mm	Shot hardness/ HRC	Shot velocity/ ms^{-1}
MI110R 04A 200%	T1	4A	200	0.28	45-52	26
MI230R 13A 200%	T0	13A	200	0.58	45-52	57

3.5 Specimens

To assess the effect of varying component geometry on the efficacy of shot peening, an un-notched and four different notch geometries have been used. All sample notches were manufactured with a circular profile defined by diameter and depth, as illustrated in Figure 3-12. The investigated notch geometries are detailed in Table 3-9. Figure 3-13(a) and (b) show the dimensions of the plain bend bar specimen with an un-notched geometry and the 4.5 × 1.25 notched specimen (notch diameter: 4.5 mm, notch depth: 1.25 mm) respectively. The other three types of the notched specimen used in this study have the same bend bar dimension as the 4.5 × 1.25 notched sample (i.e. 7.75 mm in

width and 8.00 mm in breadth). The only geometric difference between different notched specimens is the notch diameter and depth. The stress concentration factor, K_t, of each notch geometry shown in Table 3-9 was calculated by comparing the stress parallel to the tensile axis (resulting from an elastic FE analysis using the models without shot peening effects introduced in Section 3.6) with the equivalent elastic stress calculated using the simple beam theory (for a plain bend bar).

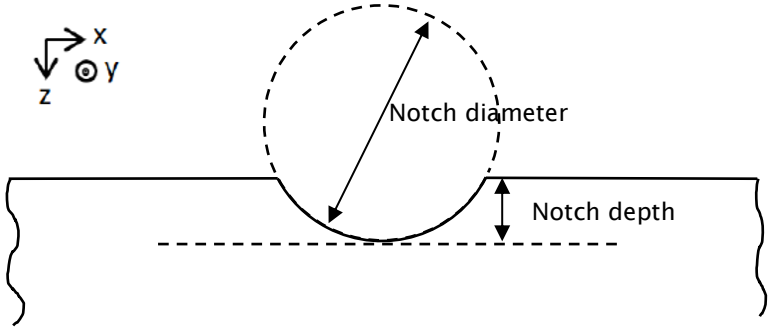

Figure 3-12: Illustration of the definition of the notch geometry.

Table 3-9: Notch geometry variation.

		Notch diameter / mm	
		4.5	10.5
Notch depth / mm	1.25	Simulate blade connection geometry (K_t = 1.58)	Simulate repair like geometry (K_t = 1.28)
	3.00	Most severe service geometry (K_t = 1.46)	Complete test matrix (K_t = 1.22)

All the samples were machined perpendicular to the rolling direction of the bar stock material by electrical discharge machining (EDM) process. Before shot peening was applied, 0.25 mm was removed from the sample surface by a grinding process in order to remove artefacts such as any white layer and the heat affected zone (HAZ) caused by the EDM process. This depth was approximated by the microhardness test determining the variation of hardness near the surface [10]. The finished surface after grinding met the industrial machined component and pre-peen specification of R_a < 0.8 µm [17].

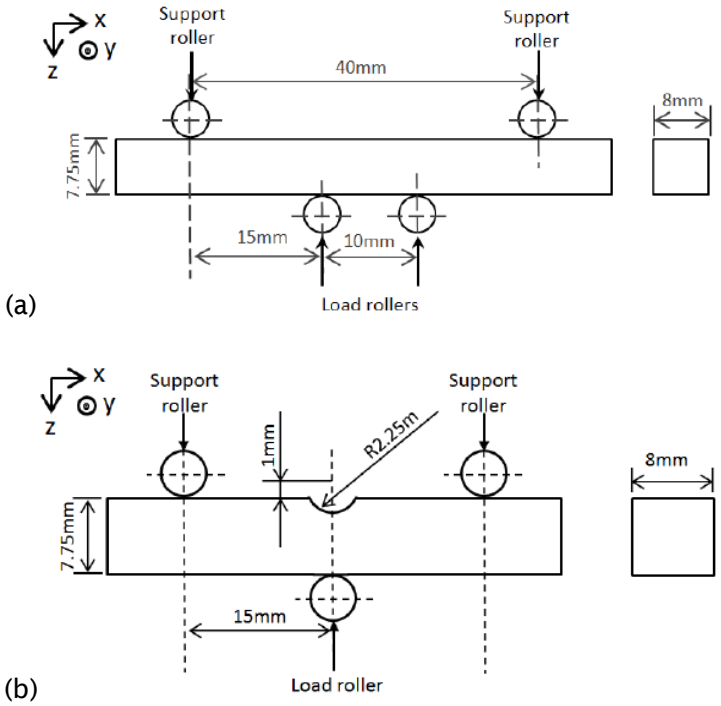

Figure 3-13: Dimensions of the (a) plain and (b) the 4.5 × 1.25 notched samples.

3.6 Finite element model

3.6.1 Boundary conditions and meshing

Models for the plain and the 4.5 × 1.25 notched samples have been developed as shown in Figure 3-14(a) and (b) respectively. Only a quarter of the real specimens shown in Figure 3-13 was modelled, by applying boundary conditions for symmetry; displacements along the x axis and y axis were constrained on face 1 and face 2 respectively.

The element C3D20R (20 node reduced integration three dimensional solid element) was chosen and applied to the model. This type of second-order reduced-integration element is expected to generate more accurate results than corresponding fully integrated elements because there are no hourglassing issues and volumetric locking is less likely to occur [171]. The computational efficiency is also expected to be improved by roughly 3.5 times compared with corresponding fully integrated elements [171].

A structured meshing technique can be used to generate meshes based on simple predefined mesh topologies; the mesh of a regularly shaped region (such as a square or a cube) is transformed onto the geometry to be meshed. Because of the regular shape of the mesh, this meshing technique is usually expected to generate more accurate

simulation results than other meshing techniques. As shown in Figure 3-14, the refined structured mesh has been applied to the surface layer with a thickness of 0.7 mm in order to accurately simulate the stress and strain gradients when shot peening effects are introduced. The elements at the top surface have a minimum thickness of 25 µm which gradually increases to 50 µm at the depth of 0.7 mm. In the most interesting region where crack growth has been observed in experiments, the aspect ratio of the element is below five to produce higher accuracy. In addition, structured meshes with a minimum size of 50 µm were applied to the loading area where a high stress level was expected during the loading process. In order to ensure a good computing efficiency, a coarse mesh was applied to the less important regions with a global element size of 0.5 mm using the free meshing technique. This meshing technique was used in order to achieve a transition from small elements to larger ones. The applied mesh sizes were determined by a mesh sensitivity analysis, which showed that the simulated results have converged at this mesh density level. Details regarding the mesh sensitivity analysis are presented in Appendix A.

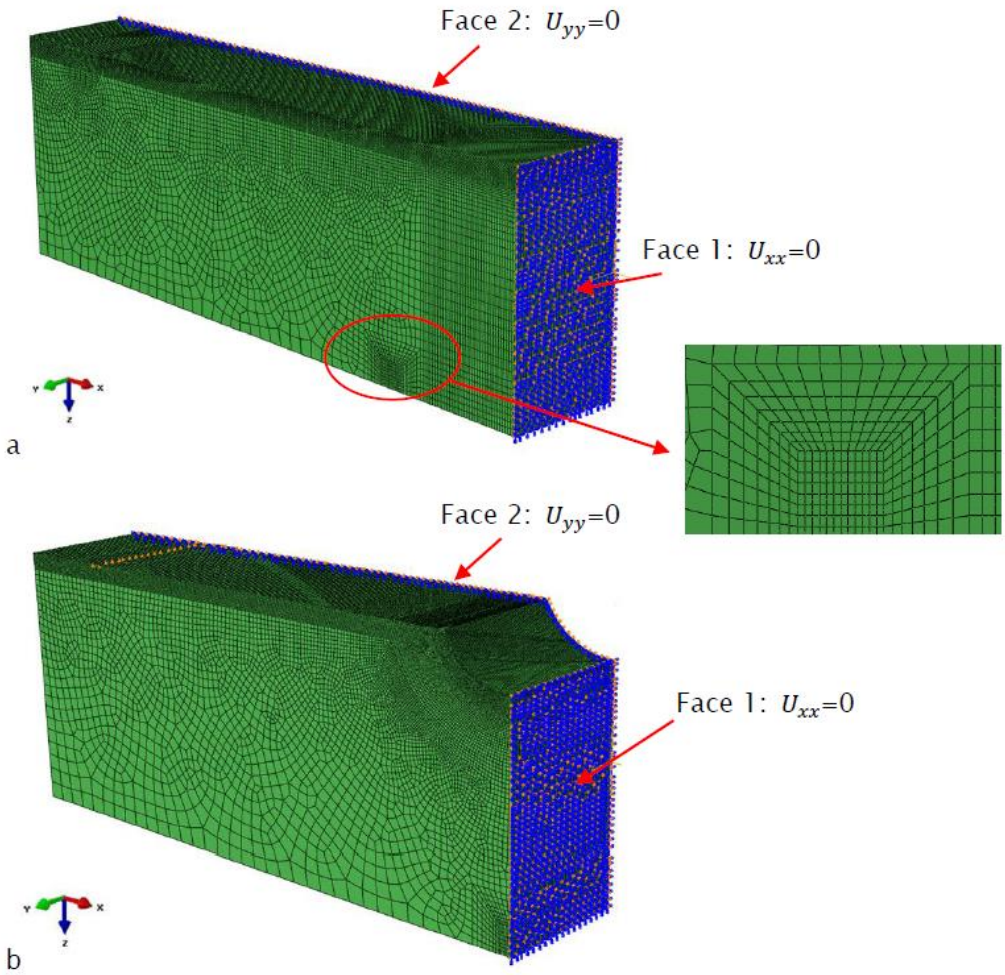

Figure 3-14: FE models for (a) the plain and (b) the 4.5 × 1.25 notched samples.

3.6.2 Loading methods

In 3 and 4 point bend experiments, the load was applied via rollers. In simulation, it is difficult to precisely define the contact faces between the sample and rollers during fatigue loading since the friction coefficient is unknown and difficult to determine. Thus it is important to simulate the applied load with appropriate assumptions or simplifications. Two different loading methods have been compared in this study; the first method, which was developed by Soady [10], treated the load exerted on the sample as a uniform pressure distribution; in the second method, simplified rollers were modelled in order to be more consistent with experimental conditions.

In the first loading method, the width of the contact area between the sample and rollers were roughly approximated using Hertzian contact theory. As illustrated in Figure 3-15, the loading roller is simulated by a uniform pressure distributed over the defined loading area, and the supporting roller is simulated by restricting the vertical displacement (normal to the contact surface) of the defined supporting area. A purely elastic material model (E = 201.3 GPa, v = 0.3) was used in the regions near the contact face to avoid non-convergence of the model.

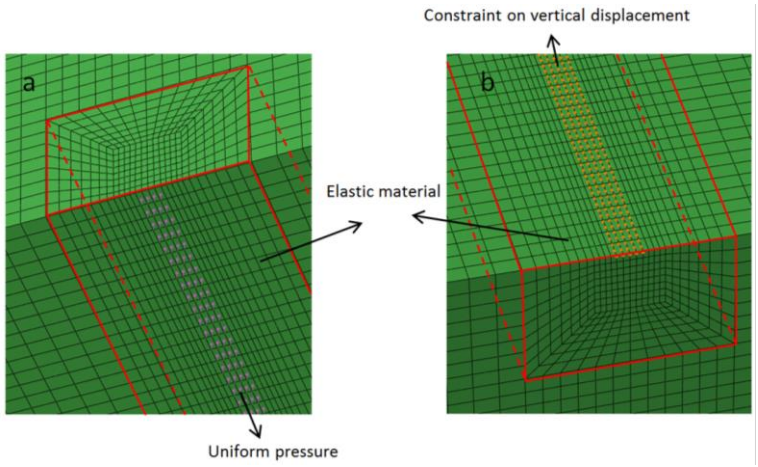

Figure 3-15: Simulation of the applied load using uniform pressure: the (a) loading and (b) supporting areas.

In the second loading method, rollers were modelled as analytical rigid bodies as shown in Figure 3-16. This rigid definition is based on ABAQUS in-built functions such that it is independent of mesh. The load and constraints were applied on the reference node of the rigid body. The supporting roller was fully constrained and the loading roller was only allowed to move along the loading direction (normal to the contact surface between the roller and the sample). The contact faces were defined using a frictionless assumption due to the difficulty in measuring the coefficient of friction between the

sample and rollers. The error introduced by this assumption was not expected to be significant, as the loading direction was basically maintained normal to the contact face during the loading process such that the tangential force was relatively small.

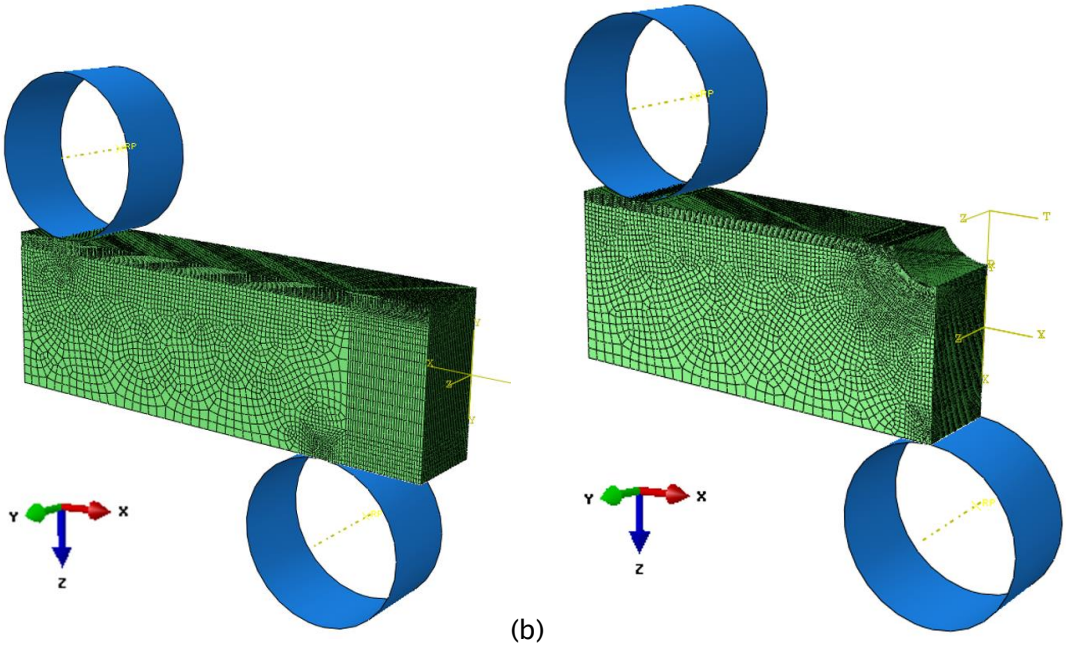

(a) (b)

Figure 3-16: The (a) plain bend bar and (b) the 4.5 × 1.25 notched models with analytical rollers.

Although the method with analytical rigid rollers was deemed to be more consistent with the real test than using the uniform pressure, it would result in a much lower computing efficiency due to the need for definition of the contact surface. In order to have a trade-off between the accuracy and the efficiency of the model, a comparison between both loading methods was carried out by applying them to the plain bend bar and the 4.5 × 1.25 notched models. In this work, the monotonic material model introduced in Section 3.3.2.2 was used. The evolution of the longitudinal total strain, ε_{xx}, at the notch root (or in the centre of the top surface in the plain model) was extracted from the modelling results. The nominal bending stress, σ_{nom}, which indicates the load level, is defined by Equation 3-13, where *P* is the applied load, *B*, *W*, *s* are the breadth, the width and the loading span of the sample respectively as shown in Figure 3-13 (for the notched sample, σ_{nom} was calculated using the same equation but substituting *W* with the remaining ligament of the notched sample).

$$\sigma_{nom} = \frac{3Ps}{BW^2} \tag{3-13}$$

The result of the comparison between the two loading methods is shown in Figure 3-17. It can be seen that in the plain bend bar model, a 20% - 60% greater ε_{xx} is obtained using

the uniform pressure than using the analytical rigid rollers at the same σ_{nom} level when plastic deformation happens; the error becomes greater at higher σ_{nom} levels. In contrast, a good consistency between the two loading methods is seen for the notched model, even beyond the elastic regime. A comparison between the loading pressure distributions simulated using analytical rollers for the plain bend bar and the notched samples when σ_{nom} = 1500 MPa is shown in Figure 3-18. It can be seen that the pressure is not technically uniformly distributed on the contact face between the sample and loading rollers in both geometries, which is attributed to the transverse deformation of the sample during loading. In the plain bend bar model, the contact area exhibits a sharp shape; the width of the contact area decreases from 0.5 mm in the centre to zero at the edge (please note that only half of the contact face was modelled for symmetry), along with a maximum pressure drop of ~ 2800 MPa. In contrast, the contact area in the notched model approximates a rectangular (~ 0.4 mm in width considering symmetry), despite the non-uniform pressure distribution; the maximum pressure drop from the centre to the edge is ~ 2700 MPa (from ~ 5200 - ~ 2500 MPa), being less evident than in the plain bend bar model. Hence, the loading method based on uniform pressure better represents the real loading condition in the notched sample than in the plain bend bar sample, which to some degree explains the better consistency between the two loading methods (i.e. uniform pressure and analytical rigid rollers) in the notched model, as shown in Figure 3-17.

Consequently, the loading method using analytical rigid rollers was considered to be more appropriate for the plain bend bar model, while the loading method with uniform pressure was chosen for the notched model owning to its lower computational cost while ensuring enough consistency with the method using analytical rollers. To add further justify to this choice, experimental validations are provided in Section 3.6.3.

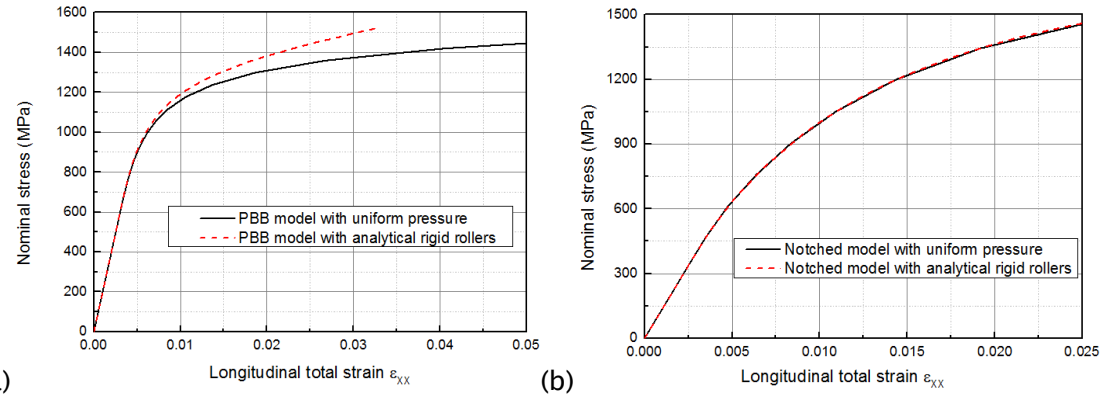

Figure 3-17: Comparison between two loading methods in (a) the plain bend bar and (b) the 4.5 × 1.25 notched models.

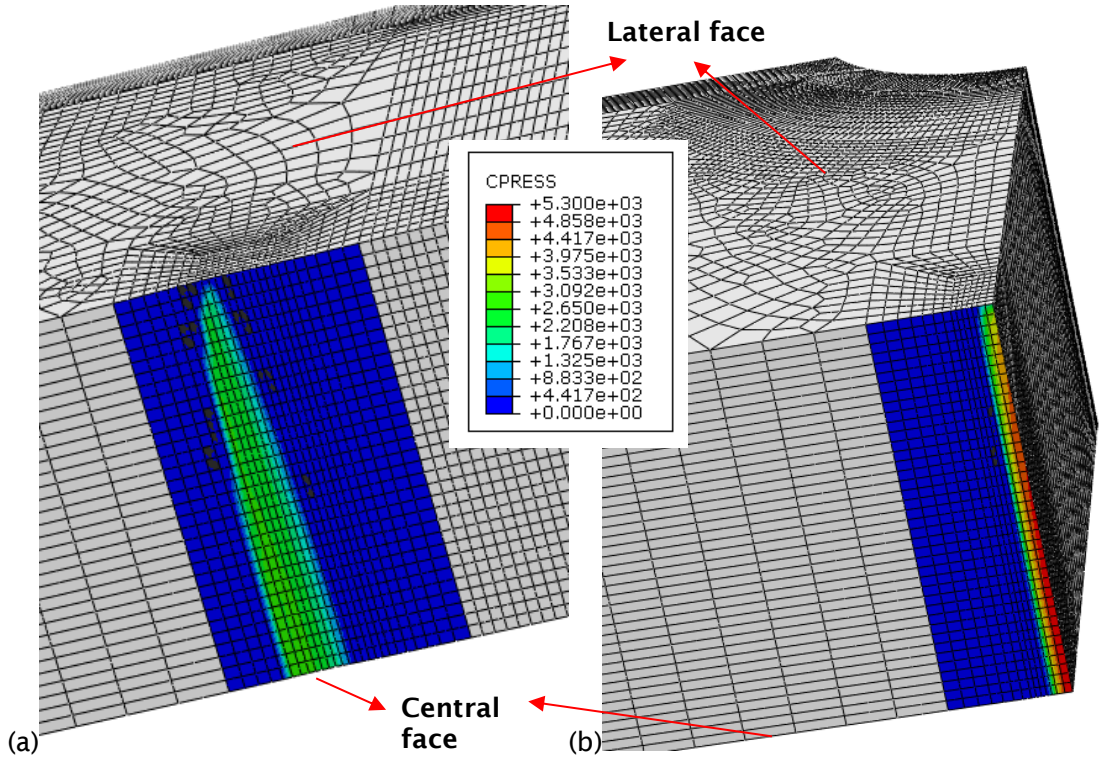

Figure 3-18: Comparison between contact pressure distributions in (a) the plain bend bar and (b) the 4.5 × 1.25 notched model when σ_{nom} = 1500 MPa.

3.6.3 Experimental validation

As indicated in Figure 2-22, the preliminary FE model (before shot peening effects are included) has to be experimentally validated. To achieve this, some ground samples were electropolished instead of being shot-peened to remove the surface layer affected by the grinding process (~ 200 µm). These electropolished samples were used to carry out validation tests measuring the strain evolution in specific regions of interest during fatigue loading, which was then used to validate the counterparts predicted by the preliminary FE model. In order to successfully attach a strain gauge to the notch root, a larger notched specimen (notch size: 9 × 2.5 mm, width: 15.5 mm, breadth: 16.00 mm) was used. Dimensions of the plain bend bar sample used in this validation test were the same as the shot-peened plain sample shown in Figure 3-13(a).

The longitudinal strain (ε_{xx}) evolution in the centre of the top surface of the plain bend bar sample and at the notch root of the larger notched specimen during fatigue loading was measured using a strain gauge. A strain gauge with a gauge length of 3.18 mm and a strain range of ±5% was chosen for the plain sample. For the notched specimen, it is important to choose a strain gauge with an appropriate gauge length in order to minimise the error caused by the curvature of the notch. According to Table 3-10, which

summarises the selection reported by others for different notch radii, a strain gauge with a gauge length of 0.38 mm and a strain range of ±3% was selected for the 9 × 2.5 notched specimen (notch radius: 4.5 mm). Both types of strain gauge were supplied by Vishay Precision Group.

Table 3-10: Selection of the gauge length for different notch radius.

	J.H. Crews [177]			Fatemi et al. [178]	Shingai [179]		
Notch radius /mm	42.47	7.62	3.1	9.128	2	4	10
Gauge length /mm	1.6	0.4	0.4	0.79	0.2		

In the modelling work, the loading methods with analytical rigid rollers and uniform pressure have been applied to the plain and the 9 × 2.5 notched models respectively, as discussed in the preceding section (Section 3.6.2). The strain evolution under a load level corresponding to a surface strain range $\Delta\varepsilon_{xx}$ = 0.69% has been simulated using both the cyclic material model (Section 3.3.2.1.2) and the monotonic material model (Section 3.3.2.2).

The comparison between the simulated results and corresponding experimental results are shown in Figure 3-19, which demonstrates the relation between the nominal stress (indicating the load level) and ε_{xx} for the plain and the 9 × 2.5 notched samples. According to the experimental results, ratcheting occurs in the plain sample until stabilisation is achieved after ~30 cycles, as illustrated in Figure 3-19(a). In contrast, elastic shakedown is observed in the notched sample as shown in Figure 3-19(b), with no clear plastic deformation beyond the first cycle. As for the modelling results, although the application of the cyclic material model has accurately simulated the monotonic $\varepsilon_{xx} - \sigma_{nom}$ curve of the notched sample, the monotonic hardening stage in the plain sample is underestimated by ~ 35%. Furthermore, the ratcheting behaviour is overestimated by 48% and 12% for the plain and notched samples respectively in terms of the stabilised ε_{xx}. This is consistent with the situation shown in Figure 3-10(b), demonstrating an overestimation of the cyclic softening behaviour by the cyclic material model. In contrast, the monotonic property has been reasonably modelled for both geometries using the monotonic material model, despite a slight overestimation of the final hardening stage when ε_{xx} > 1.5% in the plain sample and ε_{xx} > 0.8% in the notched sample, which may be attributed to the measurement errors in the experiments and/or the limitation of the assumed material model. The discrepancy between the FE modelling and experiments at high strains is not critical to the results of the present study since the chosen load ranges

in the plain bend bar and the notched geometries are well covered by this experimental validation. However, it is noted that the cyclic behaviour was not considered by the monotonic material model, which is unable to simulate the cyclic softening/hardening behaviour.

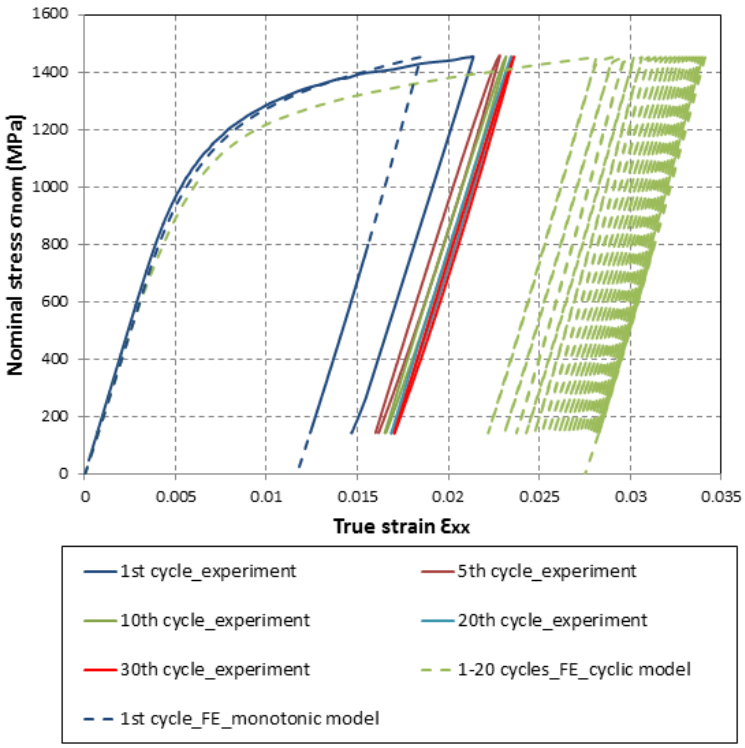

(a)

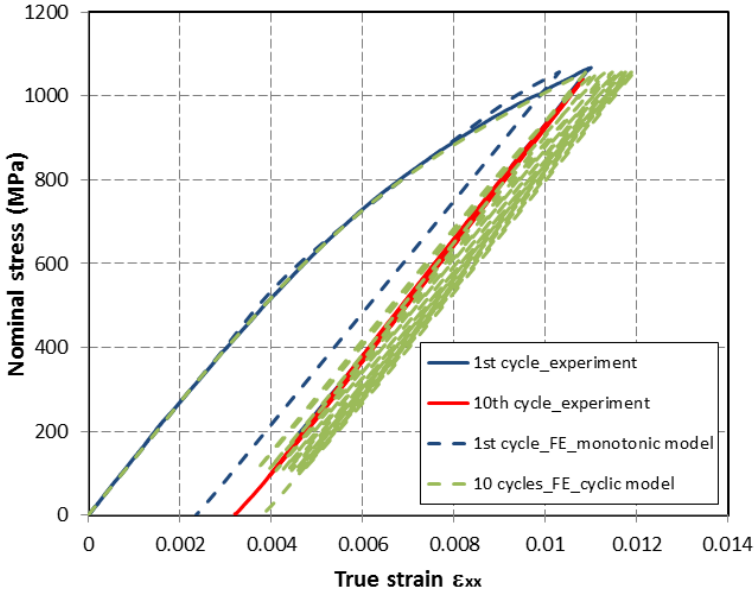

(b)

Figure 3-19: Comparison between the strain evolution obtained by experiments and modelling in the (a) plain bend bar and (b) the 9 × 2.5 notched samples under $\Delta\varepsilon_{xx}$ = 0.69%.

3.7 Discussion

From Figure 3-19, it can be concluded that the preliminary FE model (before shot peening effects are included) has been appropriately developed and its accuracy mainly depends on the applied material model. Both the advantages and disadvantages of the cyclic and monotonic material models are summarised:

a. The cyclic material model independent of strain range

Although this material model is independent of strain range and can be conveniently applied to bending conditions. The ratcheting behaviour under asymmetric loading tends to be significantly overestimated due to its poor transferability as discussed in Section 3.3.2.1.2.

b. The monotonic material model

This material model has been calibrated based on the monotonic stress-strain relation. It can satisfactorily predict the strain evolution in both the plain and the notched samples during monotonic loading. However, the cyclic softening behaviour of FV448 was not considered by this material model.

Considering both the advantages and disadvantages of the two material models, the monotonic material model has been finally selected in this project. Although this model cannot predict the cyclic softening behaviour of FV448, it seems an appropriate starting point to simulate the quasi-static stress-strain evolution within the first cycle, especially for the notched specimen where cyclic effects are not evident due to the high constraint of the notch geometry. This simplification tends to effectively reduce the computational time.

However, it is noted that an apparent ratcheting behaviour happens in the plain bend bar sample during cyclic loading as shown in Figure 3-19(a), implying that the stabilised residual stress state is less likely to be achieved simply after one loading cycle in the plain sample. Hence, the application of the monotonic material model may underestimate residual stress relaxation in the plain sample during fatigue loading. Nevertheless, considering the fact that residual stresses usually relax most significantly during the first cycle (especially in the LCF regime) as reviewed in Section 2.2.2, an accurate prediction of the residual stress relaxation behaviour during the first cycle may still be able to explain the benefit of shot peening on fatigue life of the plain sample, although this benefit is less likely to be explicitly quantified than in the notched sample.

It is also noteworthy that the choice of the monotonic material model is only appropriate within the scope of the current research. For different materials, geometries, loading conditions and objectives, the most appropriate material model may be different. In order to make the most appropriate choice, a detailed comparison between different material models should always be carried out.

3.8 Conclusion

This chapter mainly introduces the fundamental modelling work that needed to be established before shot peening effects are taken into account. The applied assumptions regarding the FE model have been detailed and validated by experiments.

A large part of this chapter has focused on introducing the development and the selection of the most appropriate material model. The modelling results have been found to be sensitive to the selection of the material model. The monotonic material model has been chosen against the cyclic material model in this project to simulate the residual stress relaxation behaviour in both the plain and notched samples. This material model can be regarded as an appropriate starting point considering the high importance of residual stress relaxation during the first cycle.

Approaches regarding the incorporation of shot peening effects into the FE model are introduced in detail in the subsequent chapter.

4 Modelling of the interaction between shot peening induced effects and service conditions

4.1 Introduction

This chapter aims to introduce the approaches adopted to achieve incorporation of the shot peening induced effects into the preliminary FE model (which has been developed in Chapter 3). To reconstruct the residual stress field caused by shot peening, the inverse eigenstrain method was applied to the plain bend bar sample and its application was extended to the notched specimen by considering the effect of notched geometries on the eigenstrain profile. Furthermore, the effect of strain hardening has also been incorporated into the FE model by modifying the local material yield strength based on data from an EBSD-based approach which has been introduced in [17]. Finally, the residual stress relaxation behaviour occurring during fatigue in both the plain bend bar and the notched specimens was investigated using the developed FE model, and compared with corresponding experimental results measured by XRD.

This chapter is largely based on two papers listed below. In addition, this chapter also contains more details regarding the application of the eigenstrain method.

You, C., Achintha, M., Soady, K., Smyth, N., Fitzpatrick, M., & Reed, P. (2017). *Low cycle fatigue life prediction in shot-peened components of different geometries – Part I: residual stress relaxation*. Fatigue and Fracture of Engineering Materials and Structures, 40(5), 761-775.

Achintha, M., You, C., He, B., Soady, K. A., & Reed, P. A. S. (2014). *Stress relaxation in shot-peened geometric features subjected to fatigue: experiments and modelling*. Advanced Materials Research, 996, 729-735.

4.2 Experimental techniques and results

4.2.1 Residual stress measurements

Both the T0 and T1 shot peening processes (as introduced in Table 3-8) have been investigated. The residual stress distribution in the shot-peened plain and 4.5 × 1.25 notched samples was measured using the XRD technique with a Cr-Kα X-ray source, and

an incremental layer removal method achieved by electropolishing was used to characterise the residual stress profile in the depth (*z*) direction. One of the main advantages of XRD is that it can differentiate between the macrostresses and the microstresses which result from strains over distances of the order of, or less, than crystal dimensions (which are introduced, for example, by strain hardening) [27]. The $sin^2\psi$ method, which is the most common method to determine the residual macrostresses based on the interaction between the wave front of the X-ray beam and crystal lattices, was applied in the present investigation. Its detailed theoretical background has been well described elsewhere [180].

The electrolyte used for electropolishing contained 8% (by volume) of 60% perchloric acid solution and 92% (by volume) of glacial acetic acid solution. During the electropolishing process, the specimen was connected to the positive terminal of a DC power supply and acted as the anode. The cathode was attached to the negative terminal and was approximately five times the area of the anode. The voltage used was 60V in order to achieve a fast polish with less chance of passivation. During polishing, the anode was kept 10 mm away from the cathode; the removal of surface layers was achieved by current flow from the polarised anode to the cathode. The thickness of the removed layer at each step was determined by measuring the remaining thickness of the specimen before and after each electropolishing step. In order to accurately capture the distribution of residual stresses in the subsurface region, 20 to 30 μm in depth was removed from the surface before each new measurement. The thickness of the removed layer was increased to ~ 40 μm when the residual stress magnitude was observed to decrease rapidly. The specimen was cleaned after each step using methanol and was washed thoroughly with water to remove any solution or anodic film.

As illustrated in Figure 4-1, residual stress data were collected in two orthogonal directions (σ_{xx} and σ_{yy}) at the notch root of the notched sample (or in the centre of the top surface of the plain sample). The measurements were taken on the {211} diffraction peak at a 2θ angle of 156.4°. A collimator of 1 mm diameter was used for residual stress measurements taken on the plain sample. In order to minimise the error associated with taking residual stress measurements on a curved surface, a collimator of 0.5 mm diameter was used for the notched sample. The X-ray penetration depth in ferrite was estimated to be 5 μm [166]. Since there were no notch shadowing effects in the plain sample and in the y direction of the notched sample when the X-ray beam is rotating, angles varying from -39° to $+39^\circ$ have been used across the two detectors. However, in the x direction of the notched sample, the notch shadowing effects become significant so the applied range of the angles has been decreased to -30° - $+30^\circ$ during the measurement.

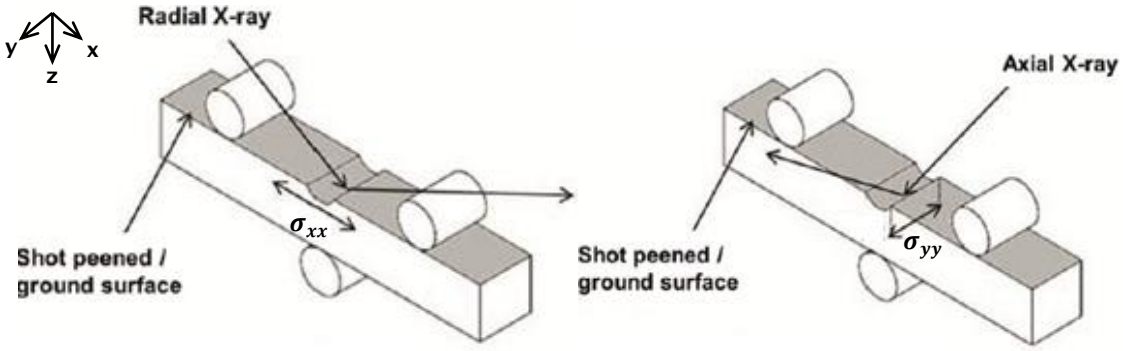

Figure 4-1: XRD setup.

To evaluate the residual stress relaxation behaviour, the residual stress distribution was determined in samples at different total life fractions (as-peened, after 1 cycle and at estimated 50% life). 3- and 4-point bend tests were carried out on a servo-hydraulic Instron 8502 for the notched and plain specimens with a loading span of 15 mm, as shown in Figure 3-13. It is noted that two XRD devices (a Proto iXRD device in the University of Manchester and an Xstress device in Coventry University) were used in the measurements for different samples, as indicated by Table 4-1; the measurement using the Proto iXRD device was carried out in previous research [166]. Although the consistency between the two XRD devices in terms of their settings before the measurement was ensured, the measurement error resulting from different devices was inevitable, and hence was investigated by determining the residual stress profile in the as-peened T0 plain bend bar sample using both devices. It is also noted that the residual stress profile representing the as-peened T1 plain bend bar sample was actually measured from the un-notched surface of a notched sample (due to the specimen supply issues), as schematically illustrated in Figure 4-2. Since the point of measurement was 10 mm away from the notched area, the obtained residual stress distribution was less likely to be significantly affected by the stress concentration of the notch, and was therefore regarded as an appropriate representation of the residual stress condition in the T1 plain bend bar samples.

Table 4-1: The XRD devices used for residual stress measurements for different samples.

	T0		T1	
	As-peened	Loaded	As-peened	Loaded
Plain bend bar sample	Proto iXRD	Xstress	Xstress	N/A
4.5 × 1.25 notched sample	Proto iXRD	Proto iXRD	Xstress	N/A

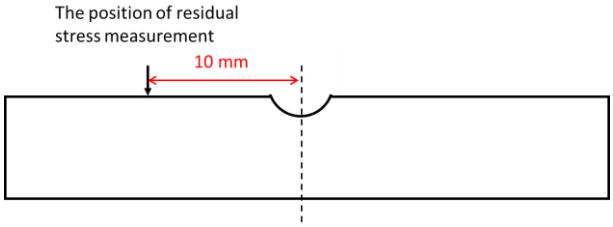

Figure 4-2: Schematic illustration of the residual stress measurement point representing the plain bend bar area in the T1 notched sample.

4.2.2 Residual stress data

The measured results were corrected using the algorithms supplied in the Proto control and analysis package XRDWIN which account for the effect of the subsequently removed layers on the successive redistribution of the subsurface residual stresses and are shown in Figure 4-3. The error was determined by calculating the sample standard deviation over 5 bi-directional measurements (10 data points) at different locations on the as-peened plain bend bar shot-peened sample [166]; the 95% confidence range was ± 50 MPa. Due to time constraints and equipment availability, this was assumed to be the confidence with which all data could be quoted rather than carrying out extensive repeat measurements for each sample.

Figure 4-3(a) shows the measured residual stress distributions in the plain bend bar specimens. The T0 residual stress profiles obtained using the two XRD devices are both presented, demonstrating overall consistent trends but some relative differences ($\leq$ 100 MPa) at $z < 0.15$ mm. To avoid ambiguity, the results measured in Manchester have been used to represent the T0 plain bend bar condition in subsequent analyses, unless specifically indicated. The effects of the error (resulting from any source) on the accuracy of subsequent analysis have been investigated by a sensitivity analysis, which is detailed in Section 4.5.

Figure 4-3(a) also shows that the T0 process results in a notably deeper and greater compressive residual stress distribution than the T1 process owing to its higher peening intensity. In addition, there is no significant difference between the σ_{xx} and σ_{yy} profiles in the plain bend bar specimen for either peening condition (i.e. an equi-biaxial residual stress state is seen), which is consistent with the results measured on other shot-peened flat components as reported elsewhere [86, 181, 182]. In contrast, as shown in Figure 4-3(b), σ_{xx} appears to be ~ 16% more compressive than σ_{yy} in the T0 shot-peened notched sample. This biaxial difference in residual stress distribution also exists in the T1 notched sample, despite being less evident. The discrepancy between the residual stress profiles in different geometries subjected to the same peening process has also

been observed by others [181, 183]. However, the depth of the compressive residual stress layer seems unaffected by the notched geometry, remaining the same as in the plain bend bar specimen; at 0.35 and 0.15 mm for the T0 and T1 processes respectively.

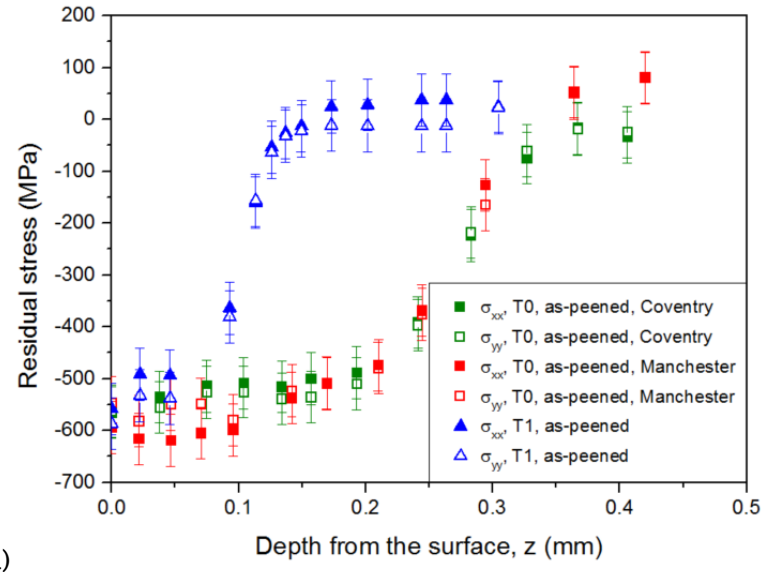

(a)

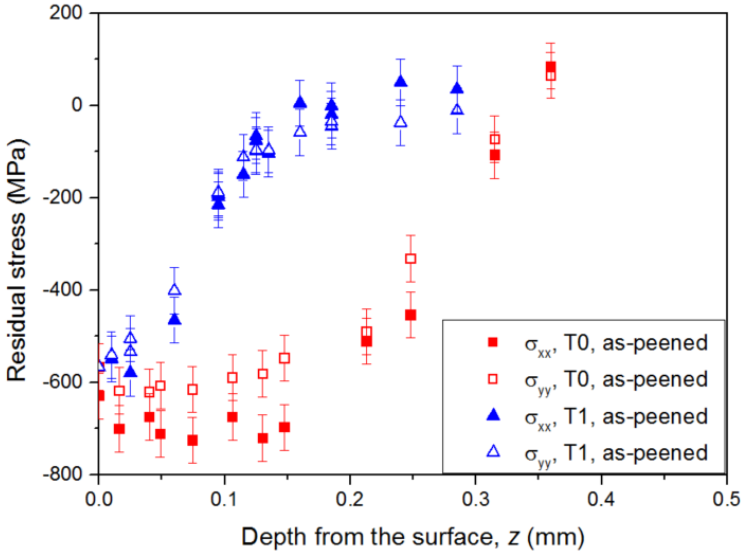

(b)

Figure 4-3: Residual stress distributions measured by XRD in the shot-peened (a) plain bend bar and (b) 4.5×1.25 notched samples.

To investigate the residual stress relaxation behaviour, the T0 plain bend bar samples were loaded for one cycle in this test. The corresponding surface strain ranges ($\Delta\varepsilon_{xx}$) were predicted using the developed FE model including shot peening effects and are detailed in Section 4.3. In order to investigate the link between residual stress relaxation and the retention of the benefits of shot peening, two load levels with $\Delta\varepsilon_{xx} = 0.42\%$ and 0.55% were chosen based on the corresponding total life reported in [77].

Compared with the un-peened samples, the T0 process showed no clear benefits in improving fatigue life when $\Delta\varepsilon_{xx} = 0.55\%$ but doubled the fatigue life when $\Delta\varepsilon_{xx} = 0.42\%$. The measured residual stresses shown in Figure 4-4 indicate that no clear relaxation is observed when $\Delta\varepsilon_{xx} = 0.42\%$ but a 30-40% stress relief occurs in both directions (σ_{xx} and σ_{yy}) when $\Delta\varepsilon_{xx} = 0.55\%$.

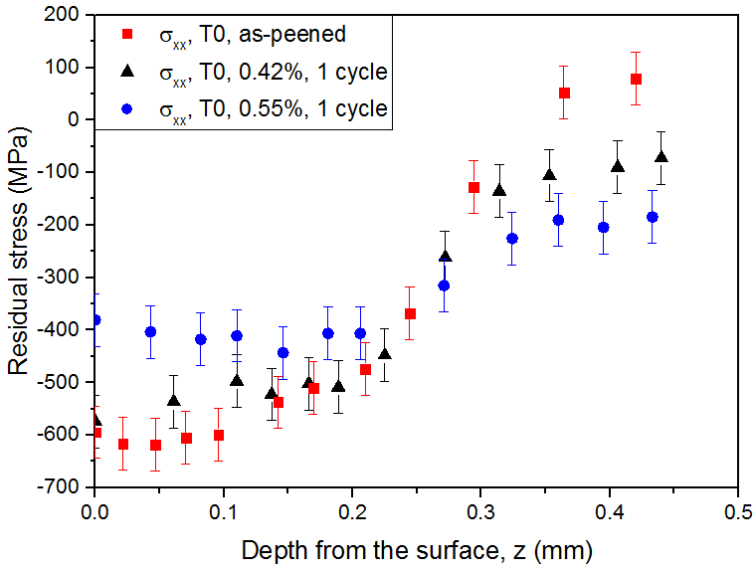

(a)

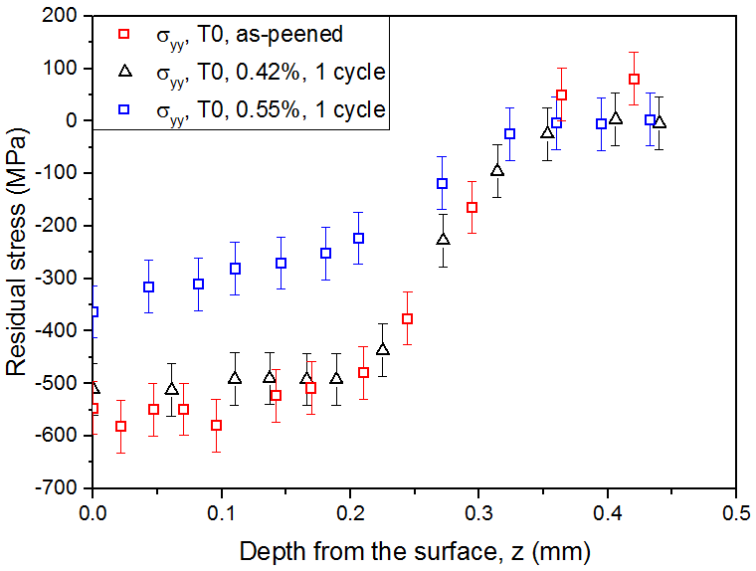

(b)

Figure 4-4: Residual stress relaxation after 1 cycle in the T0 plain bend bar sample $\Delta\varepsilon_{xx}$.0.42% and 0.55%): (a) σ_{xx} and (b) σ_{yy}.

The T0 4.5×1.25 notched samples were loaded with an estimated notch root strain range of $\Delta\varepsilon_{xx}$ = 0.69%. This value was chosen also because the fatigue life of the un-peened notched sample was found to be doubled by the T0 process at this load level [166]. As

shown in Figure 4-5, there is no clear relaxation of σ_{xx} after either 1 loading cycle nor after 50% total life, which is in contrast to the results of the plain bend bar specimen. However, there is a 20% relaxation of σ_{yy} during the first cycle but no further relaxation can be seen in subsequent cycles. This lack of stress relief during fatigue loading can be explained by the mechanism illustrated in Figure 3-19; the high constraint of the notch geometry tends to restrict the cyclic plastic deformation of the material at the notch root, making a stabilised stress/strain state much easier to be realised during fatigue loading.

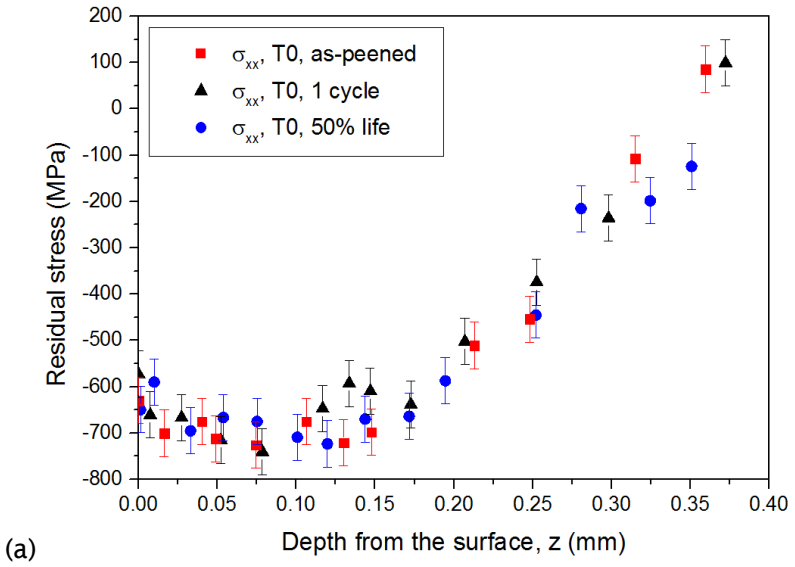

(a)

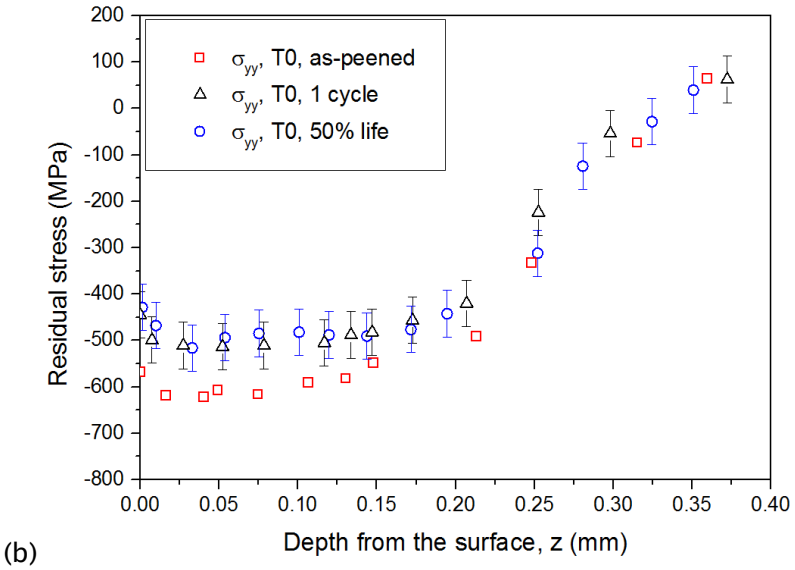

(b)

Figure 4-5: Residual stress relaxation at different total life fractions in the T0 4.5×1.25 notched sample ($\Delta\varepsilon_{xx}$= 0.69%): (a) σ_{xx} and (b) σ_{yy}

4.3 Incorporation of shot peening effects into finite element models

4.3.1 Residual stress modelling using the inverse eigenstrain approach

The eigenstrain approach has been chosen to achieve the incorporation of residual stresses into the FE model. The full residual stress field can be modelled by applying a stress-equilibrium step in a model containing eigenstrains. The eigenstrain distribution can be conveniently implemented at each point in the FE model by specifying anisotropic thermal expansion coefficients that vary with position, together with a uniform temperature rise. Since the eigenstrain profile is usually unknown and difficult to directly predict, the inverse eigenstrain approach developed by Korsunsky et al. [50] has been implemented. It is essentially an approach to back-fit the eigenstrain distribution from the known residual stress (or residual elastic strain) distribution determined by experimental measurements (e.g. XRD), using a least squares analysis. This analysis requires a choice of a suitable parametric form for the eigenstrain distribution. Once an accurate estimate of the eigenstrain profile is established, the complete residual stress field in the whole component can be determined in the usual way. The advantage of this approach is that the elastic response of the workpiece to the eigenstrain will satisfy equilibrium, compatibility and boundary conditions, and the residual stress field produced will be entirely self-consistent.

In the current study, the objective is to demonstrate how compressive residual stress profiles, either measured or predicted using appropriate empirical or analytical techniques, can be incorporated into FE models and to predict the complete initial residual stress distribution and, most significantly, any changes to it under fatigue loading. Hence the complexities associated with dynamic modelling (such as the strain rate dependency of the target material, the material and size of shots, the contact property of the peened surface, etc.) were not considered in this work. It is reasonable to employ a linear elastic model with properties broadly representative of FV448 (Young's modulus E = 201.3GPa; Poisson's ratio v = 0.3) in the inverse eigenstrain analysis. However, it should be noted that the elasto-plastic material introduced in Section 3.3.2.2 has to be used in subsequent residual stress relaxation analysis. This inverse eigenstrain approach was first applied to the plain bend bar sample and then its application was extended to the notched sample.

4.3.1.1 Application in the plain bend bar specimen

In simple geometries such as the plain bend bar sample, the eigenstrain distribution is usually assumed to be equi-biaxial owing to the non-directional nature of the plastic deformation induced by the shot peening process. This assumption has been adopted in the present work to determine the in-plane principal eigenstrain components; $\varepsilon_{xx}^{eigen} = \varepsilon_{yy}^{eigen}$. Although this assumption may not be reasonable in the vicinity of sample edges, it can be applied as an appropriate simplification in areas where the edge effects are negligible [49]. Considering volume conservation in plastic deformation, the third principal component perpendicular to the peened surface has been defined as $\varepsilon_{zz}^{eigen} = -2\varepsilon_{xx}^{eigen}$. In the present study, Chebyshev polynomials have been adopted to describe the eigenstrain profiles due to its wide application in least squares analysis [49-52, 59]. The procedure of the inverse eigenstrain method is illustrated in Figure 4-6. ε_{xx}^{eigen} is assumed to vary with depth (z) and is expressed as a linear combination of Chebyshev polynomials $T_i(z)$ multiplied by unknown coefficients C_i, as defined by Equation 4-1, where N is the number of polynomials. The values of C_i were determined by minimising the difference between the experimentally measured residual stress data $\sigma_{xx}(z)$ and the weighted sum of individual modelling results $\sigma_{xx_i}^{FE}(z)$ obtained as an elastic response to each eigenstrain base function $T_i(z)$, as expressed by Equation 4-2 where M is the number of experimental data points.

$$\varepsilon_{xx}^{eigen}(z) = \sum_{i=0}^{N-1} C_i T_i(z) \tag{4-1}$$

$$min(J) = \sum_{j=1}^{M} \left[\sigma_{xx}(z) - \sum_{i=0}^{N-1} C_i \sigma_{xx_i}^{FE}(z)\right]^2 \tag{4-2}$$

There are a few key points worthy of careful consideration in the application of the inverse eigenstrain method. One is that the depth of the eigenstrain distribution should be appropriately approximated to ensure that the simulated results are largely independent of the chosen depth. The value of the depth can be evaluated by XRD FWHM measurement which indicates the strain hardening degree of the material [49], or it can also be predicted by the depth of the peak tensile residual stress (or residual elastic strain) according to the theory of bending [48]. In addition, a knowledge of the shape of the eigenstrain profile is also required in order to make a sensible choice of the number of Chebyshev polynomials. The number of polynomials should be sufficiently large to capture the expected shape of the eigenstrain profile, but should be smaller than the number of experimental data points ($N < M$), otherwise the weight coefficients C_i cannot be determined. In addition, an excessively large number of polynomials may result in significant over-fitting of the predicted eigenstrain profile containing details that cannot be justified with sufficient confidence [48].

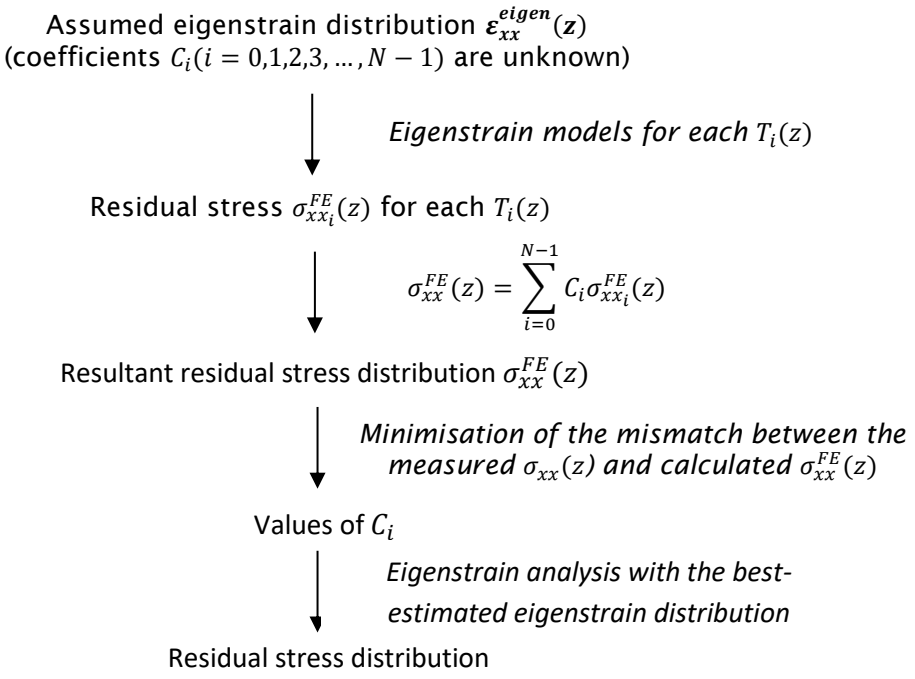

Figure 4-6: Procedure of the inverse eigenstrain method [49].

Reconstruction of the residual stress distribution in the T0 shot-peened plain bend bar sample was first carried out. According to Figure 4-3, the depth of the eigenstrain was roughly estimated to be 0.4 mm. This depth was first chosen and the inverse eigenstrain method was carried out using different numbers of Chebyshev polynomials; N = 7, 8 and 9 respectively, following the procedures illustrated in Figure 4-6. The obtained results are shown in Figure 4-7. It can be found that both the eigenstrain and the residual stress distribution predicted using different polynomial numbers are almost identical apart from the region near the depth of 0.4 mm. This difference at the tail of the profiles is due to the fact that the predicted eigenstrain profile has been forced to reach zero at this depth in the modelling work. Compared with the choices of N = 7 and 9, N = 8 has been finally chosen for further analysis since it induced less abrupt changes in the results when the eigenstrain approached zero.

In addition to the number of polynomials, the effect of the chosen depth of the eigenstrain profile on the predicted results has also been investigated. A comparison between the results using different eigenstrain depths of 0.35, 0.40 and 0.45 mm has been carried out. The most appropriate polynomial number, N = 8, which had been determined based on Figure 4-7, was used in this analysis. Relevant results are shown in Figure 4-8. It can be seen that the predicted eigenstrain and residual stress distributions based on the analysis using different eigenstrain depths are almost identical within the depth range 0.00 – 0.35 mm, which suggests that the predicted

results near the surface are almost independent of the chosen eigenstrain depth. However, abrupt changes in the results are also seen when the eigenstrain is forced to reach zero, which is similar to the situation shown in Figure 4-7. According to this analysis, the actual eigenstrain depth has been approximated to be 0.40 mm, which produces the smoothest eigenstrain and residual stress profiles.

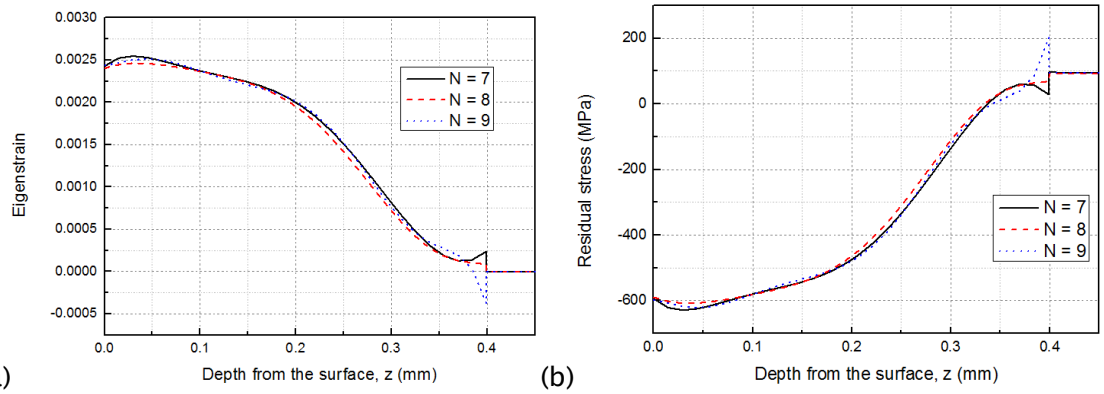

Figure 4-7: (a) Predicted eigenstrain distribution and (b) corresponding residual stress distribution (σ_{xx}) in the T0 plain bend bar sample based on the analysis using an eigenstrain depth of 0.4 mm and varying number of Chebyshev polynomials.

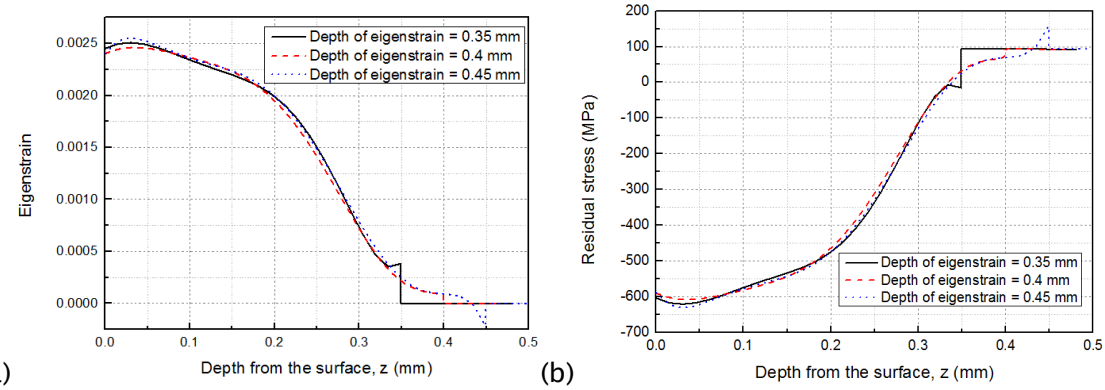

Figure 4-8: (a) Predicted eigenstrain distribution and (b) corresponding residual stress distribution (σ_{xx}) in the T0 plain bend bar sample based on the analysis using eight Chebyshev polynomials and varying depth of the eigenstrain profile.

Based on the analysis above, the eigenstrain distribution predicted using N = 8 and a depth of 0.40 mm was selected for the T0 process. It has been shown that, providing the selections are physically reasonable, the best-estimated eigenstrain profile is largely independent of N and the assumed depth of the eigenstrain profile [49]. In order to avoid abrupt changes in the predicted results (as shown in Figure 4-7 and Figure 4-8), the tail of the eigenstrain profile (predicted using N = 8 and an eigenstrain depth of 0. 40 mm) was optimised to achieve a smooth transition to zero. This optimised profile is shown in Figure 4-9(a) and is incorporated into the plain bend bar model. The resultant modelling

results of the residual stress distribution in the T0 plain bend bar sample are presented in Figure 4-9(b), which shows a successful incorporation of the shot peening induced residual stress into the FE model. It is also noteworthy that only σ_{xx} was used in the inverse eigenstrain method to determine the eigenstrain profile, however, σ_{yy} was also simulated well; this further validates the present model and the applicability of the eigenstrain approach. In addition to σ_{xx} and σ_{yy}, all the other residual stress components can be conveniently obtained from the FE results as well, which is a significant advantage of the present approach.

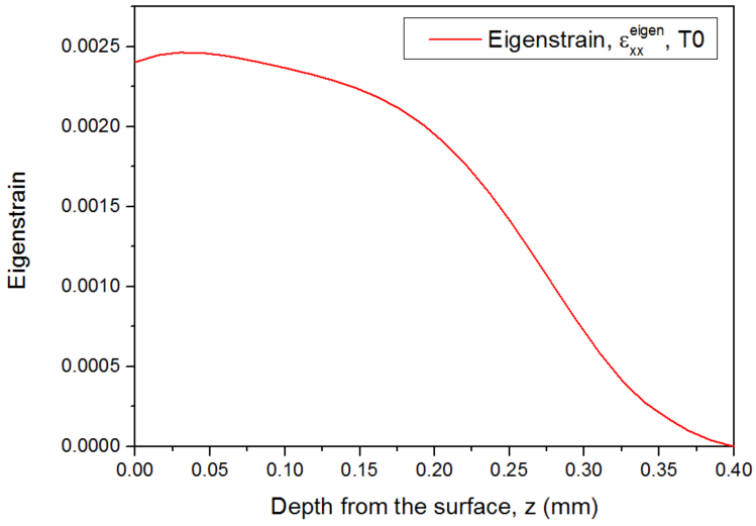

(a)

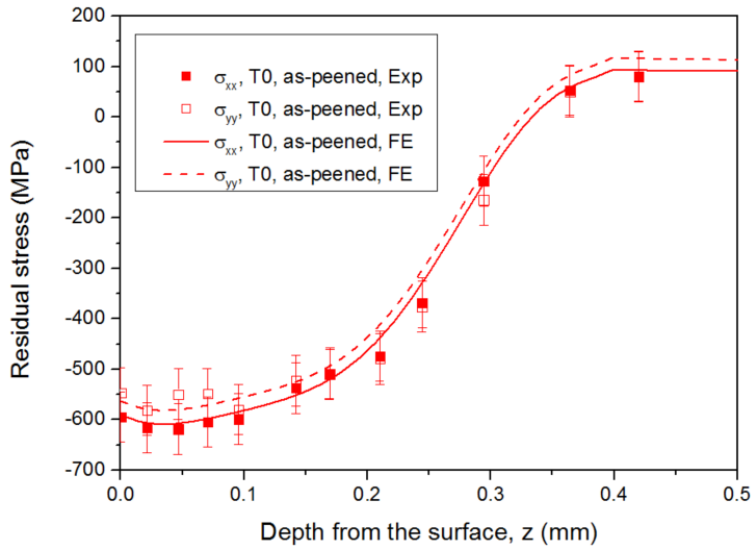

(b)

Figure 4-9: (a) the optimised eigenstrain distribution in the T0 shot-peened plain bend bar sample and (b) the resultant residual stress distribution predicted using the FE model.

Similarly, the residual stress distribution in the T1 plain bend bar condition has also been reconstructed. Following the procedure discussed above for the T0 process, the eigenstrain depth has been estimated to be 0.2 mm and the most appropriate number of Chebyshev polynomials has been determined to be N = 4. The best-estimated eigenstrain profile and the modelled residual stress distribution are shown in Figure 4-10, which again shows a good agreement with experimental results.

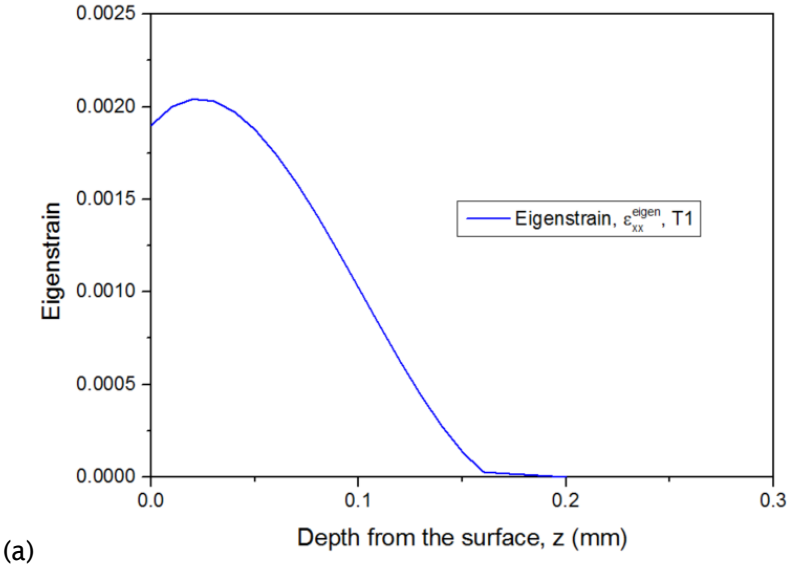

(a)

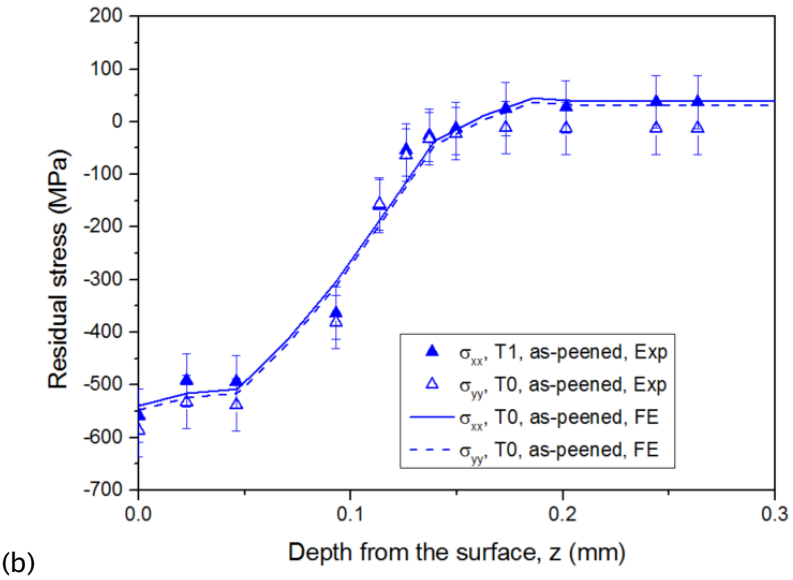

(b)

Figure 4-10: (a) the optimised eigenstrain distribution in the T1 shot-peened plain bend bar sample and (b) the resultant residual stress distribution predicted using the FE model.

4.3.1.2 Application in the notched specimen

The residual stress distribution in the T0 shot-peened 4.5×1.25 notched sample has also been reconstructed using the inverse eigenstrain method. In the modelling work for the notched sample, a cylindrical coordinate system was used in order to facilitate defining the eigenstrain distribution around the notch. The transformation between the Cartesian and cylindrical coordinate systems is illustrated in Figure 4-11. Eigenstrain components $\varepsilon_{\theta}^{eigen}$ (tangential to the notch curvature) and ε_{r}^{eigen} (perpendicular to the notch curvature) have been used as new principal eigenstrain components instead of ε_{xx}^{eigen} and ε_{zz}^{eigen} respectively. Another principal component in the transverse direction is still defined as ε_{yy}^{eigen} (in the transverse direction). Considering the residual stress data presented in this study for notched samples were collected at the notch root, for consistency with the experimental data shown in Figure 4-3, the residual stress in the longitudinal direction is still presented as σ_{xx}.

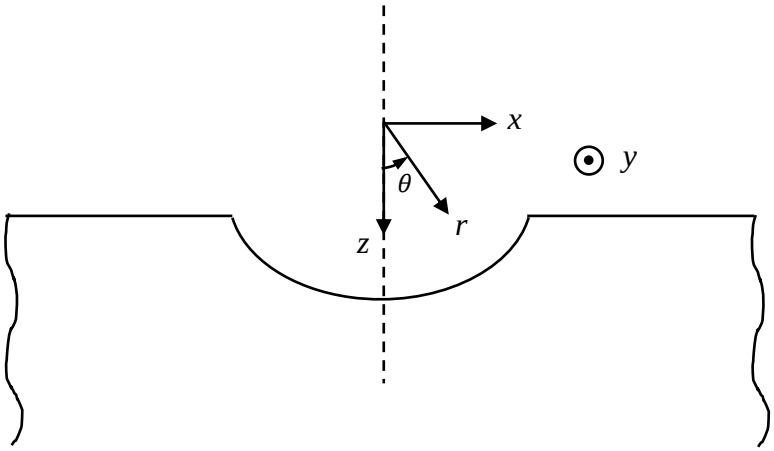

Figure 4-11: Illustration of the transformation between the Cartesian and cylindrical coordinate systems.

As discussed previously, the eigenstrain distribution may be affected by the geometry of the sample. This effect has to be properly accounted for in order to more accurately model the residual stress field. Anoop et al. [183, 184] indicated that the same peening condition would induce less surface stretching in convex geometries than in flat geometries. In contrast, more stretching near the peened surface would be expected in concave geometries, leading to a greater misfit layer and thus a greater compressive residual stress, which is consistent with the results obtained in the present work as shown in Figure 4-3. Hence, directly using the equi-biaxial eigenstrain distribution ($\varepsilon_{t}^{eigen} = \varepsilon_{yy}^{eigen}$ as shown in Figure 4-12(a), $\varepsilon_{r}^{eigen} = -2\varepsilon_{yy}^{eigen}$) determined from the simple geometry may result in an inaccurate reconstruction of the residual stress field in

complex geometries even though the same shot peening process was applied. This hypothesis is confirmed by Figure 4-12(b), which shows a 25-30% underestimation of σ_{xx} in the T0 4.5×1.25 notched sample by directly using the equi-biaxial eigenstrain profiles determined from the T0 plain sample. Other examples showing unsatisfactory modelling results using similar assumptions can be found in [60, 61].

In the notched sample, since more stretching is expected to occur along the notch curvature during the shot peening process, the assumption $\varepsilon_{\theta}^{eigen} = \varepsilon_{yy}^{eigen}$ seems less reasonable. So a more accurate simulation can be expected if $\varepsilon_{\theta}^{eigen}$ and ε_{yy}^{eigen} can be predicted individually rather than simply assuming an equi-biaxial state ($\varepsilon_{\theta}^{eigen} = \varepsilon_{yy}^{eigen}$). However, it is noted that the conventional inverse eigenstrain method is simply a 1-D solution and evaluating two eigenstrain components simultaneously is non-trivial for the least square analysis. In order to solve this problem, ε_{yy}^{eigen} in the notched sample has been assumed to be identical to that in the plain bend bar sample subjected to the same shot peening process, as shown in Figure 4-9 and Figure 4-10. It is anticipated that ε_{yy}^{eigen} is much less affected by the curved geometry than $\varepsilon_{\theta}^{eigen}$. A detailed study of the stress concentration in the y direction of the notched samples is beyond the scope of the current study. For simplicity, no stress concentration feature in the transverse direction of the notch is assumed in the current modelling work. Based on this assumption, the problem was degraded to 1-D. Then the inverse eigenstrain approach was implemented again to predict $\varepsilon_{\theta}^{eigen}$. ε_{r}^{eigen} can be determined using the relation $\varepsilon_{r}^{eigen} = -(\varepsilon_{\theta}^{eigen} + \varepsilon_{yy}^{eigen})$ considering volume conservation in plastic deformation. Although there may be some stress concentration effect in the transverse direction, it is likely that the inverse eigenstrain analysis used in the current modelling work will to some extent counter any effect due to the relatively low stress concentration in the transverse direction. As can be seen from the results presented in this study, the model predictions are at least consistent with the experimental results of the test specimens analysed in the current study.

Figure 4-12(c) shows the predicted biaxial eigenstrain profiles for the T0 notched specimen; $\varepsilon_{\theta}^{eigen}$ is ~1.58 times ε_{yy}^{eigen}, demonstrating more stretching along the notch curvature as expected. The subsequent residual stress modelling results are presented in Figure 4-12(d), which shows a good correlation with experimental data. Following the same modelling procedure, the residual stress field induced by the T1 shot peening process was also reconstructed in the notched model. Consistent results between modelling and experiments were obtained by assuming $\varepsilon_{\theta}^{eigen} = 1.15\varepsilon_{yy}^{eigen}$, as shown in Figure 4-13. The comparison between the T0 and T1 conditions implies that the relation

between $\varepsilon_{\theta}^{eigen}$ and ε_{yy}^{eigen} depends on the stress concentration level of the notched geometry as well as the peening intensity. In order to build up a quantitative physical correlation between $\varepsilon_{\theta}^{eigen}$ and ε_{yy}^{eigen}, a detailed analysis of the interaction between shot peening and the geometry of a range of practical peening applications is required. However it is beyond the scope of the current analysis since the primary objective of the current analysis is to predict the stress relaxation in the notched geometry considered in the study.

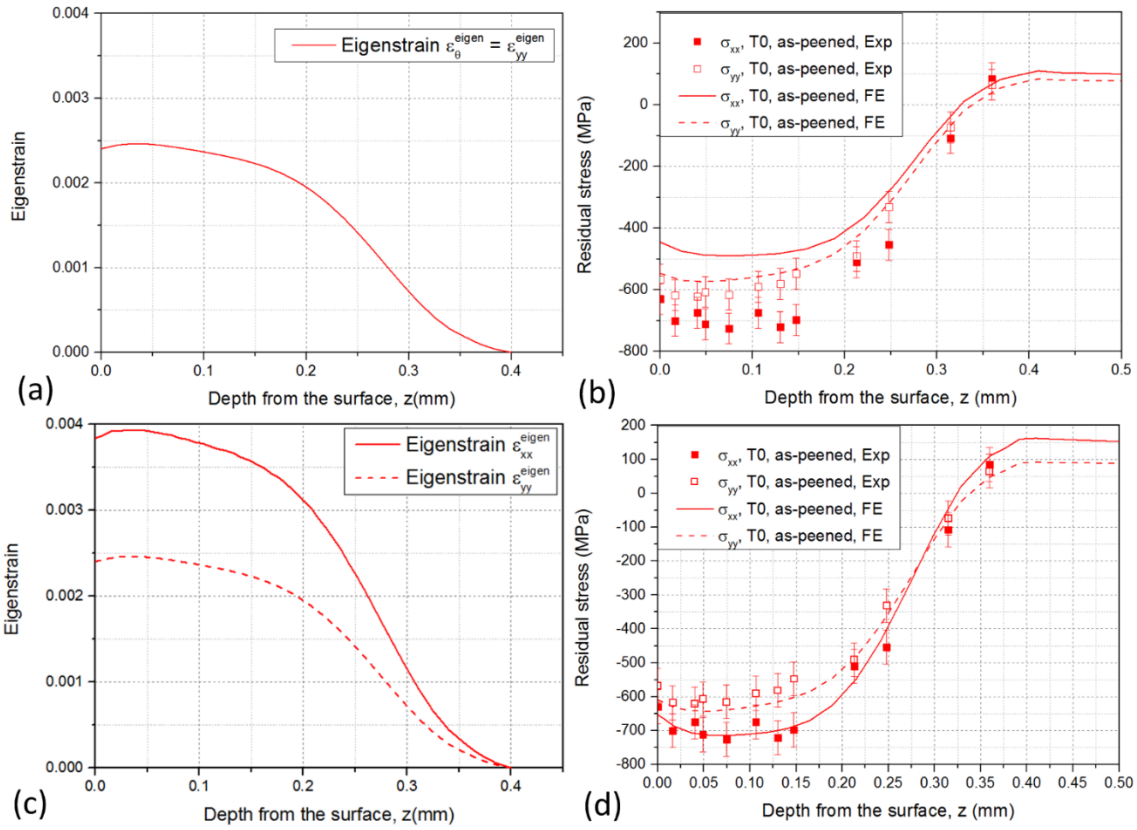

Figure 4-12: A comparison between two eigenstrain assumptions in the T0 4.5×1.25 notched sample: (a) the equi-biaxial eigenstrain profiles and (b) the reconstructed residual stresses; (c) the predicted differing biaxial eigenstrain profiles and (d) the reconstructed residual stresses.

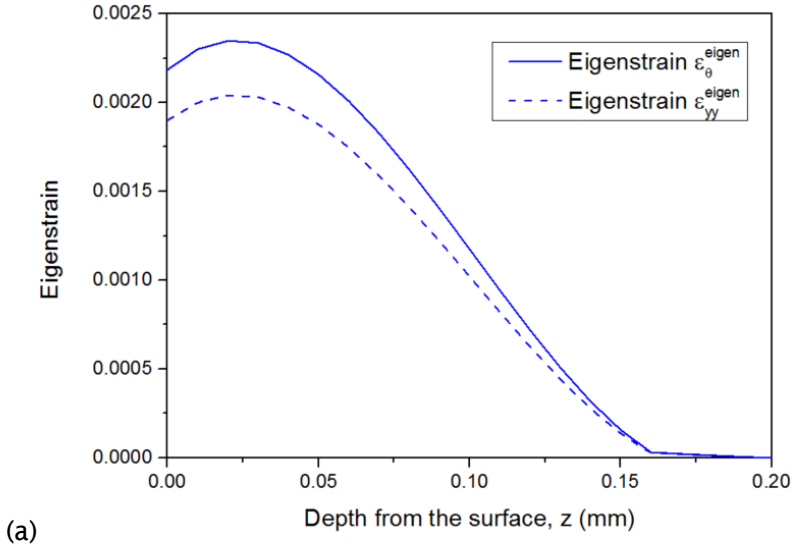

(a)

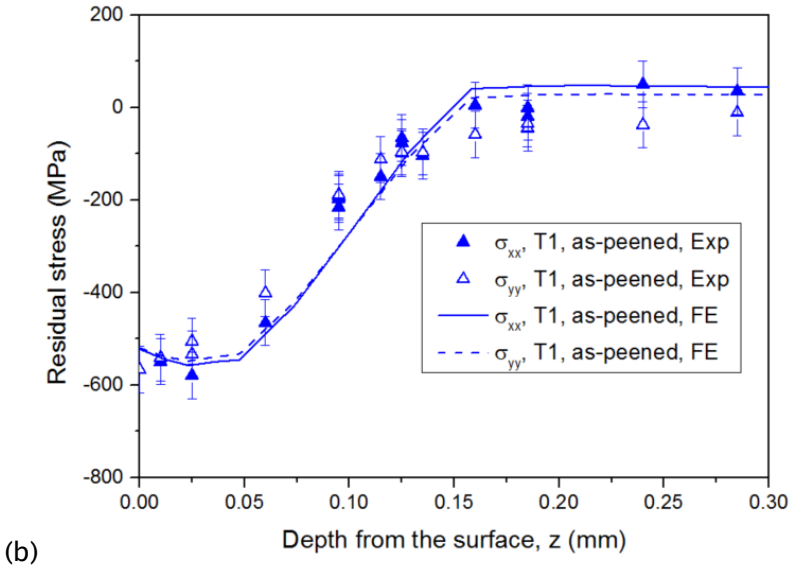

(b)

Figure 4-13: (a) The predicted biaxial eigenstrain profiles and (b) the reconstructed residual stresses in the T1 4.5×1.25 notched sample.

4.3.2 Strain hardening modelling

Since the surface layer is usually strain hardened by the shot peening process, it is necessary to incorporate these effects into the FE model in addition to the compressive residual stress effects. Neglecting the strain hardening effects will potentially degrade the accuracy of the simulated residual stress relaxation, thus reducing the accuracy of the developed life assessment method, as discussed in Section 2.3.3.1.

EBSD local misorientation data were used to evaluate the plastic strain distribution caused by shot peening, as detailed in [17]. This evaluation was based on a linear relation

between the true plastic strain and the kernel average misorientation (KAM). This relation was obtained by calibration based on uniaxial tension and compression tests experiencing known strain hardening levels. Figure 4-14 shows the predicted true plastic strain profiles caused by the T0 and T1 shot peening processes respectively. This plastic strain profile was incorporated into the FE model as an initial condition of the material model before the loading step. As reviewed in Section 2.1.3.1, the EBSD technique was chosen over the XRD FWHM and microhardness techniques due to the fact that more data points were obtained by EBSD approach so the data was more averaged over the larger number of data points and the confidence in the data was higher.

To predict the increased yield strength caused by strain hardening, the size of the yield surface, σ^0 (Equation 3-3), and backstresses, $\boldsymbol{a_k}$ (Equation 3-4), at different depths were modified according to the incorporated true plastic strain profile. It is noted that surface stretching was assumed to be dominant during the peening process such that plasticity reversal which potentially occurred between each single shot was omitted in this study. Hence, plastic deformations occurring during the peening process have been simplified as following the monotonic plastic strain-stress relation of FV448 (shown in Figure 3-11). Similar assumptions have also been used in [73, 133] and have been validated to be appropriate in different systems subjected to shot peening.

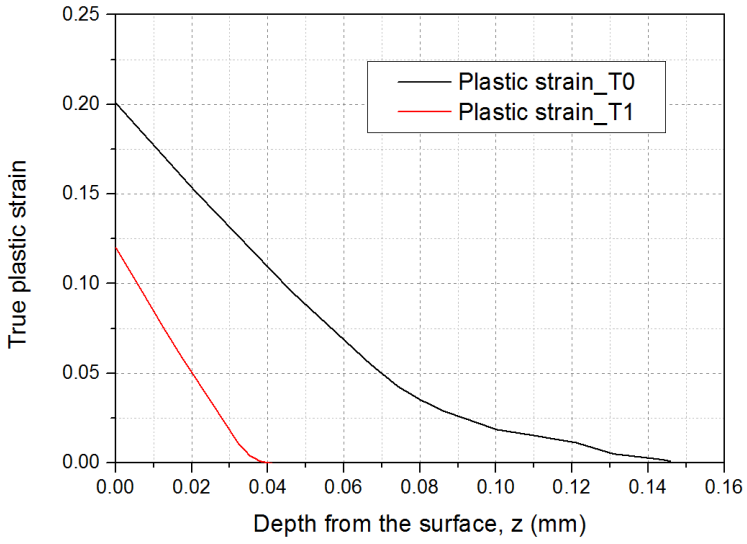

Figure 4-14: Predicted true plastic strain distributions caused by the T0 and T1 shot peening processes [17].

4.4 Modelling of residual stress relaxation

After incorporating the effects of the residual stress and strain hardening induced by shot peening into the FE model, a load step was defined to simulate the experimental fatigue load. Only one load cycle was simulated as cyclic mechanical properties were not considered in the applied material model. As shown in Figure 4-15, good correlation between the simulated and the experimental results was obtained in both directions (σ_{xx} and σ_{yy}) for the T0 plain bend bar and 4.5×1.25 notched samples. This validates the modelling techniques applied in the present study.

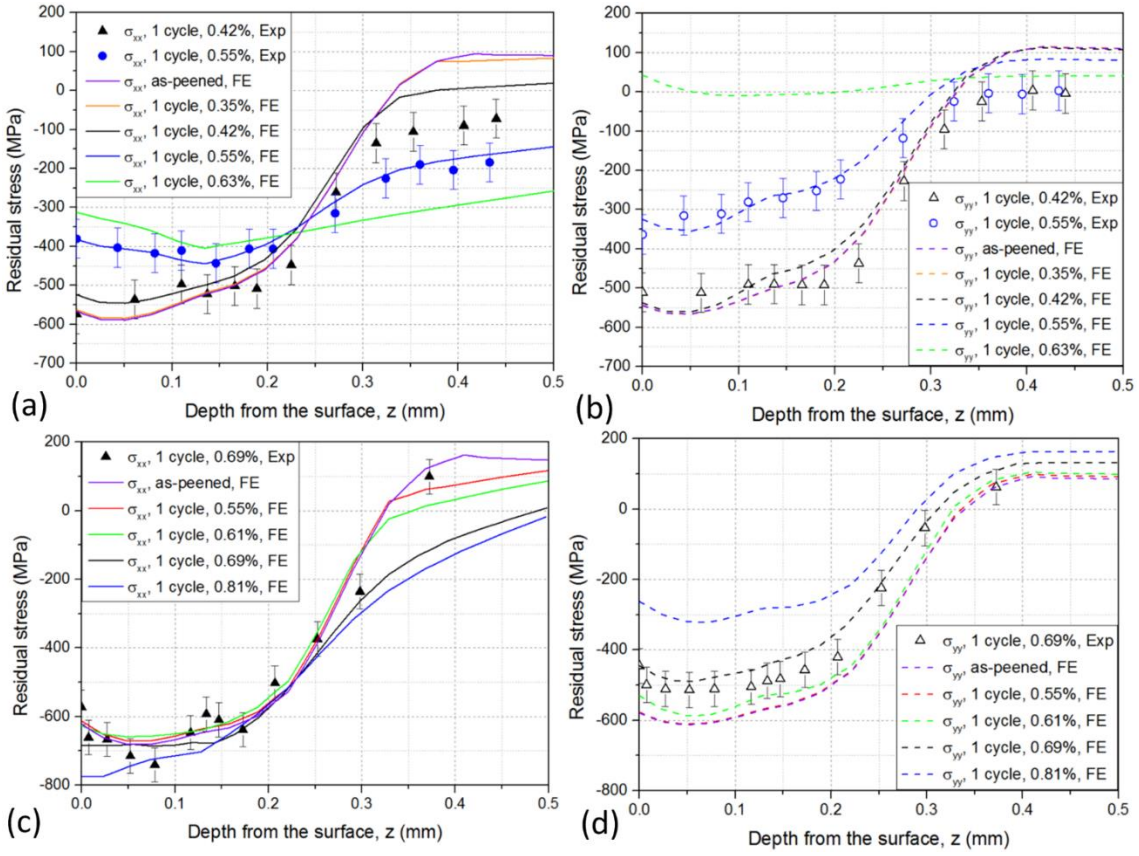

Figure 4-15: Simulated relaxation of (a) σ_{xx} and (b) σ_{yy} in the T0 plain bend bar sample, (c) σ_{xx} and (d) σ_{yy} in the T0 4.5×1.25 notched sample after 1 cycle at different load levels in terms of $\Delta\varepsilon_{xx}$.

According to previous work [46, 102, 185], shot-peened components preferentially show more notable residual stress relaxation in the direction parallel to the load (the longitudinal direction) than in the direction perpendicular to the load (the transverse direction) under uniaxial loading or reverse bending tests. In addition, it has also been found that if a higher load was applied, more significant relaxation was normally expected since greater local plastic deformation will lead to more reduction in the plastic

misfit (i.e. the eigenstrain). In order to investigate the residual stress relaxation behaviour in the current system, the quasi-static relaxation in both flat and 4.5×1.25 notched specimens has also been simulated at different load levels using the FE model.

The simulated results for the T0 plain bend bar sample are shown in Figure 4-15(a) and (b). As expected, the compressive residual stress relaxation in both directions becomes more significant with increasing load. Nevertheless, σ_{xx} is much less relaxed than σ_{yy} and the depth of the compressive residual stress profile is extended, which seems contradictory to the conclusions drawn by other researchers [102, 186]. In fact this is not surprising in the 3- or 4-point bend case: the inhomogeneous plastic deformation generated by the bending process itself develops a compressive residual stress layer after unloading as a result of the constraint exerted by the elastically deformed material beneath. This process compensates for any compressive residual stress relief occurring in the loading (longitudinal) direction. This can be demonstrated by Figure 4-16, which shows the simulated plastic strain distributions (ε_{pxx} and ε_{pyy} in the x and y directions respectively) in the T0 plain bend bar sample after one cycle under corresponding loading levels. The plastic strain components were determined as a superposition of the initial eigenstrain and the plastic deformation generated by external loads. It is noted that the true plastic strain profile which has been incorporated into the FE model to account for strain hardening effects was not considered here, since it was only defined as an initial condition of the material model rather than as true deformation. In Figure 4-16, it can be seen that the depth of the misfit layer in the x direction is extended from 0.4 mm in the as-peened condition to greater than 1 mm at the highest strain range level ($\Delta\varepsilon_{xx}$ = 0.63%), which explains the extension in depth of the σ_{xx} profile as shown in Figure 4-15(a). The stress relief of σ_{xx} can be attributed to the degraded incompatibility between layers at different depth, compared with that in the as-peened condition. In the y direction, the misfit layer gradually diminishes with increasing strain range levels, finally resulting in a complete σ_{yy} relaxation at $\Delta\varepsilon_{xx}$ = 0.63%. In addition, it can also be seen that there is no clear difference between the plastic strain profiles in the as-peened condition and those obtained under $\Delta\varepsilon_{xx}$ = 0.35%, which is consistent with the lack of stress relief at this strain range level as demonstrated in Figure 4-15(a) and (b).

The retention of compressive residual stresses in the loading direction has been found to be more notable in the notched sample as shown in Figure 4-15(c) and (d); the σ_{xx} profile even becomes more compressive at the highest load level ($\Delta\varepsilon_{xx}$ = 0.81%). This retention of compressive residual stress is thought to be as a result of the high constraint exerted by the notched geometry. Similar results are also reported in [58, 133]. In order to more explicitly explain this situation in terms of the mechanism, the simulated plastic

strain distributions at the notch root (ε_{pxx} and ε_{pyy} in the x and y directions respectively) in the T0 4.5×1.25 sample after one cycle under the same strain ranges used in Figure 4-15(c) and (d) are shown in Figure 4-17. It can be seen that unlike in the plain bend bar samples, the as-peened eigenstrain distributions in the notched samples are well preserved when $\Delta\varepsilon_{xx}$ < 0.69%, which is consistent with the lack of residual stress relaxation as demonstrated in Figure 4-15(c) and (d). With continuously increasing $\Delta\varepsilon_{xx}$, the as-peened eigenstrain effect in the x direction seems to be completely eliminated by external loads at $\Delta\varepsilon_{xx}$ = 0.81%. However, a deeper and greater misfit layer is generated by the bending process itself, which accounts for the corresponding more compressive residual stress shown in Figure 4-15(c). In the y direction, despite the fact that the misfit strain is reduced with increasing strain range levels, the effect of the as-peened condition is always maintained, which is sufficient to ensure a compressive residual stress layer. Hence, it is postulated that the constraint of the notch geometry is more beneficial than the un-notched geometry in maintaining the benefit of shot peening during fatigue loading.

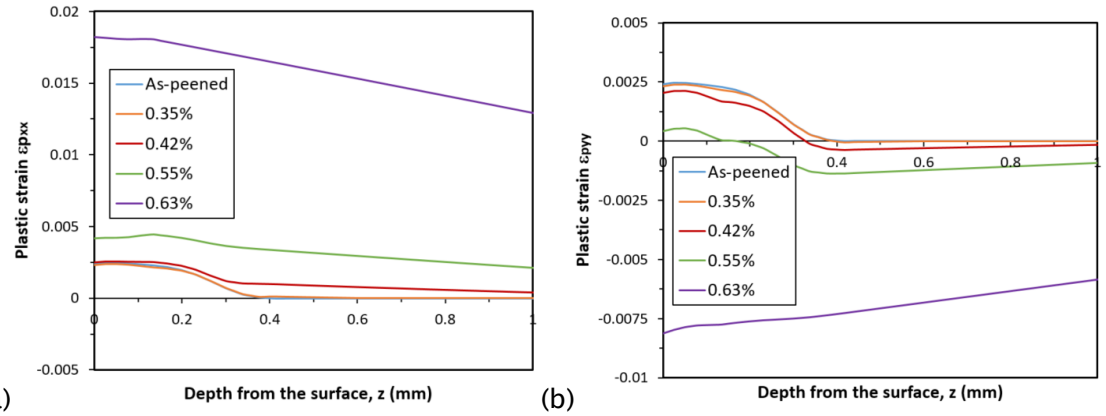

Figure 4-16: Simulated plastic strain evolution in the (a) longitudinal direction (ε_{pxx}) and (b) in the transverse direction (ε_{pyy}) in the T0 plain bend bar sample after 1 cycle at different load levels ($\Delta\varepsilon_{xx}$ = 0.35%, 0.42%, 0.55% and 0.63%).

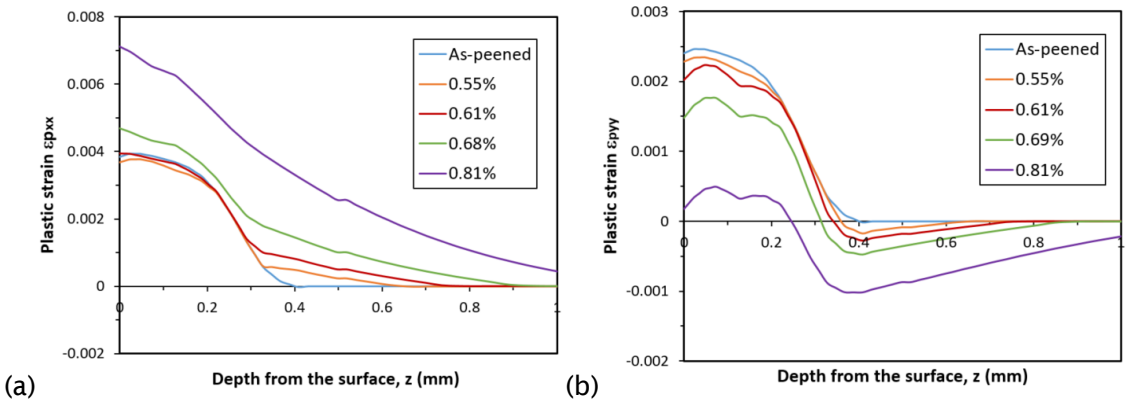

Figure 4-17: Simulated plastic strain evolution in the (a) longitudinal direction (ε_{pxx}) and (b) in the transverse direction (ε_{pyy}) in the T0 4.5×1.25 notched sample after 1 cycle at different load levels ($\Delta\varepsilon_{xx}$ = 0.55%, 0.61%, 0.69% and 0.81%).

4.5 Sensitivity analysis

Although the quasi-static residual stress relaxation can be reasonably predicted using the developed FE model, the prediction is highly dependent on the input data (i.e. the initial residual stress and strain hardening profiles) of the model. Errors in these experimentally determined input data are always inevitable, so a sensitivity analysis investigating how the accuracy of the input data affects the prediction was carried out. In this analysis, three varying eigenstrain and initial true plastic strain profiles were defined as shown in Table 4-2. The profiles with label *b* are the baseline profiles which have been used in the preceding analysis. The profiles with labels *a* and *c* represent the experimental error range presented in Figure 4-3. The parametric analysis matrix is shown in Table 4-3, which aims to assess the relative importance of scatter in the initial residual stresses and strain hardening values for the model. Analogous with the preceding modelling work, the plain bend bar and notched models with varying eigenstrain and initial true plastic strain profiles were loaded for 1 cycle. Then the simulated relaxed residual stresses based on these different initial starting points were compared. The results using the plain bend bar models are shown in Figure 4-18; only the σ_{xx} components are plotted for conciseness. The results for the notched models are omitted for brevity since very similar trends with the plain bend bar models were obtained.

From Figure 4-18(a) and (c), it can be seen that the variation of the initial residual stress definition results in different stress distributions after 1 loading cycle. The difference caused by differing initial residual stress conditions can be as much as 100 MPa when $\Delta\varepsilon_{xx} = 0.42\%$; however, this difference decreases to 50 MPa when the load level is

increased to give $\Delta\varepsilon_{xx} = 0.55\%$. Hence it can be concluded that the predicted residual stress relaxation is sensitive to the accuracy of the initial residual stress profile but this sensitivity tends to be less significant at high load levels when the effects caused by external loads are more dominant.

Table 4-2: Definition of the eigenstrain and the initial true plastic strain profile used for the sensitivity analysis.

Label	*a*	*b*	*c*
Eigenstrain profile	Baseline + 10%	Baseline profile	Baseline - 10%
True plastic strain profile	Baseline + 17%	Baseline profile	Baseline - 17%

Table 4-3: Matrix of the sensitivity analysis

		True plastic strain profile		
		a	*b*	*c*
Eigenstrain profile	*a*	N/A	*ab*	N/A
	b	*ba*	*bb*	*bc*
	c	N/A	*cb*	N/A

In contrast, the effect of the scatter in the initial strain hardening profile is much less notable, according to Figure 4-18(b) and (d). As discussed in Section 4.3.2, strain hardening affects local material properties mainly by modifying the yield surface (σ^0) and the backstresses ($\boldsymbol{\alpha}$) in terms of the equivalent plastic strain ($\bar{\varepsilon}^{pl}$) as described by Equation 3-3 and 3-4. In the current case, in the area near the surface (depth < 0.1 mm) where the strain hardening effects are significant ($0.02 < \bar{\varepsilon}^{pl} < 0.25$), a 17% variation of the baseline strain hardening profile only results in a difference < 1.5% and < 6% in local σ^0 and $\boldsymbol{\alpha}$ respectively, which is insufficient to cause a significant change in the model response especially when the external load level is relatively low.

In life assessment methods, consideration of residual stress relaxation is necessary. As a result of this, this sensitivity analysis will be extended to study the effects of the accuracy of the predicted residual stress relaxation on total life predictions in Section

5.6.4. According to the results presented in Figure 4-18, most experimental data (especially those near the peened surface) are just within the range defined by this sensitivity analysis, which makes the extended study more meaningful.

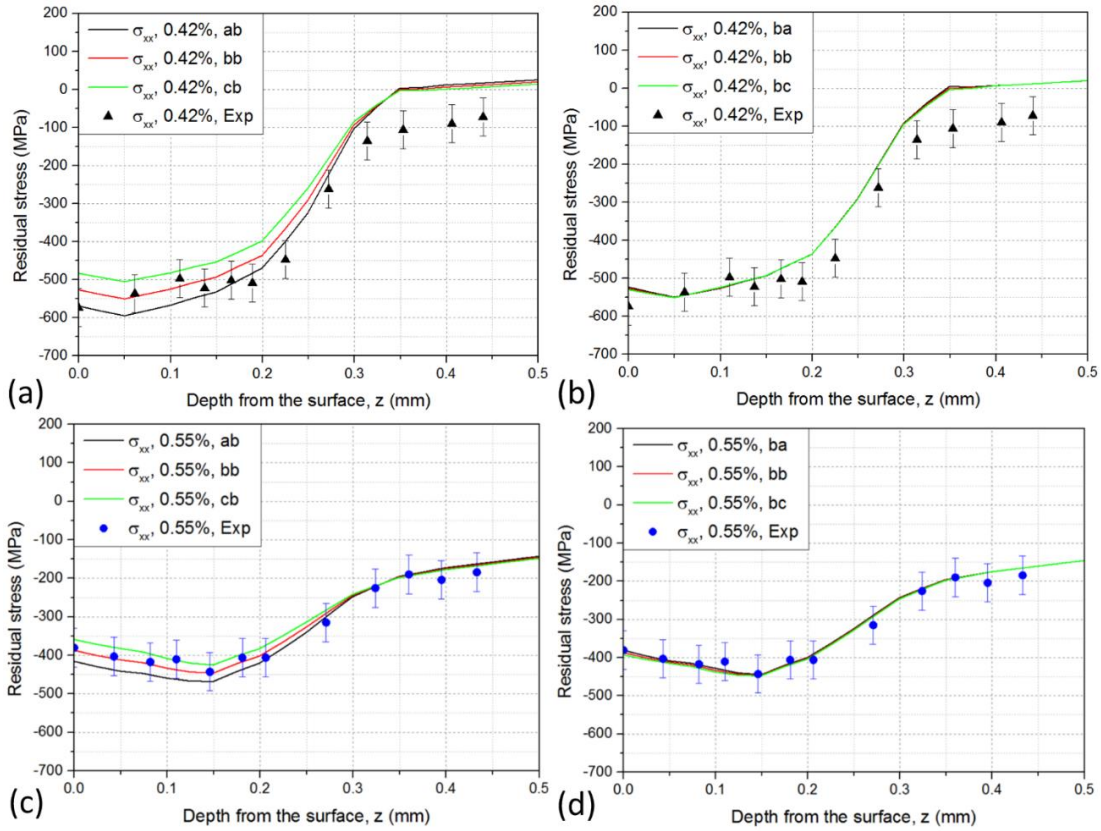

Figure 4-18: Sensitivity analysis results for the T0 plain sample; the effects of the initial (a) (c) residual stress and (b) (d) strain hardening profiles when $\Delta\varepsilon_{xx}$ = 0.42% and 0.55%.

4.6 Conclusion

In this chapter, an eigenstrain-based FE approach has been developed to predict the quasi-static residual stress relaxation in safety-critical shot-peened regions, taking the example of a stress-concentrating notch. The application of the conventional inverse eigenstrain method has been extended to the notched geometry. In this FE approach, the effects of strain hardening have also been accounted for by modifying the yield strength at different depths. In spite of the fact that more modelling work may be required to simulate the interaction between shot peening effects and external loads in a range of notched geometries, the FE approach developed in the current study has been demonstrated to be both accurate and efficient in evaluating the stress/strain status in safety-critical regions during fatigue loading. This will be particularly helpful in developing the fatigue life prediction of shot-peened components.

In addition, according to the modelling results, the misfit strain profile caused by shot peening has been found to be more stable and less affected by external loads in the notched sample than in the plain bar sample under bending. Consequently, the notched geometry is more effective in the retention of compressive residual stresses than the un-notched geometry during fatigue loading. This is postulated to result in a greater benefit of shot peening in enhancing the fatigue resistance of a component.

According to the sensitivity analysis presented here, the predicted residual stress relaxation using the developed model is more sensitive to the initial residual stress profile than to the initial strain hardening profile. So ensuring a good accuracy of the residual stress measurement in the as-peened condition is necessary. This sensitivity tends to be less significant at high loading levels when the effects of external loads dominate.

5 Fatigue life prediction using total life approaches

5.1 Introduction

This chapter aims to develop an approach which is capable of accurately predicting the LCF behaviour of shot-peened notch geometries, using both the Smith-Watson-Topper (SWT) and Fatemi-Socie (FS) critical plane criteria. As a comparison, the prediction was also carried out for the plain bend bar samples. The novelty of this work mainly lies in the incorporation of the effects of residual stresses and strain hardening induced by shot peening into the application of critical plane criteria in the LCF regime. To realise this, the complex interaction between the shot peening induced effects, external loads, their corresponding stress/strain distributions and possible concomitant residual stress relaxation during service has been investigated using the FE modelling approach introduced in Chapter 4. The application of this approach has also been extended to different notched geometries in the present study. The stress/strain terms required by the critical plane criteria have been evaluated using the modelling results, allowing for the effects of shot peening. In addition, a critical distance method has been applied to improve the accuracy of the life prediction and the effects of surface roughness were discussed. A sensitivity analysis was also carried out to investigate how the FE modelling results affected the accuracy of the life prediction. This chapter is largely based on the following paper:

You, C., Achintha, M., Soady, K., & Reed, P. (2017). *Low cycle fatigue life prediction in shot-peened components of different geometries – Part II: life prediction*. Fatigue and Fracture of Engineering Materials and Structures, 40(5), 749-760.

5.2 Experimental techniques and results

Since the maximum service temperature in LP turbines is 250℃ which is outside the creep regime for FV448, the temperature was thought to have no significant effect on fatigue life. Hence, all fatigue tests were carried out at room temperature with a sinusoidal waveform and a frequency of 20 Hz using a servo hydraulic Instron 8502. This work was carried out by Soady et al [166] and He et al. [77, 82]. The plain bend bar and notched specimens were loaded under 4- and 3-point bend respectively with a load ratio R_p = 0.1 and a loading span s = 15 mm as shown in Figure 3-13. 4-point bend loading is believed to generate more reliable fatigue life results for the plain bend bar

specimen, because it ensures the most uniform stress distribution in the surface region between the two inner rollers, exposing a large volume of material to the maximum stress. In the notched specimen, stress concentration usually plays a more important role in fatigue life and 3-point bend is sufficient to ensure the maximum stress occurs at the notch root. The true longitudinal strain range, $\Delta\varepsilon_{xx}$, experienced in the centre at the notch root (or in the centre of the top surface in the plain sample) was estimated using the FE model introduced in Chapter 4, allowing for both effects of compressive residual stresses and strain hardening induced by shot peening.

The strain-life ($\Delta\varepsilon_{xx} - N_f$) plots for the plain sample with different surface treatments are presented in Figure 5-1(a); grinding, T0 shot peening and T0 shot peening + grinding. The grinding treatment after shot peening (T0 shot peening + grinding) was used to remove the significant lips (as shown in Figure 5-2) in the edge region of the shot-peened sample which developed due to the large shear deformation occurring during the peening process. These edge lips were found to increase the propensity for fatigue initiation from the edges of the plain sample, resulting in corner crack initiation. The comparison between the ground and T0 shot-peened samples indicates that shot peening is beneficial in improving fatigue life but this benefit becomes less evident with increasing $\Delta\varepsilon_{xx}$. By grinding off the edge lips generated by shot peening, the benefit of shot peening becomes even more notable, especially in the HCF regime where crack initiation dominates the total life.

Figure 5-1(a) also presents the fatigue life of the 4.5 × 1.25 notched sample. Three surface treatments have been considered: grinding, T1 and T0 shot peening. It can be seen that the T0 process increases the fatigue life of the 4.5 × 1.25 notched sample at all $\Delta\varepsilon_{xx}$ levels, including the highest range $\Delta\varepsilon_{xx} = 0.81\%$. In contrast, the T1 process gives no clear benefit in life improvement when $\Delta\varepsilon_{xx} > 0.65\%$. Figure 5-1(b) further compares the total fatigue life of the T0 shot-peened specimens with varying notch geometries (as defined in Table 3-9) in terms of $\Delta\varepsilon_{xx}$, showing that wider notches appear to have a lower fatigue life. It is noted that the effect of the edge lips was found to be much less significant in the notched sample than in the plain sample. Crack initiation was observed at the notch root in all the notched specimens under investigation regardless of the specific notch geometry.

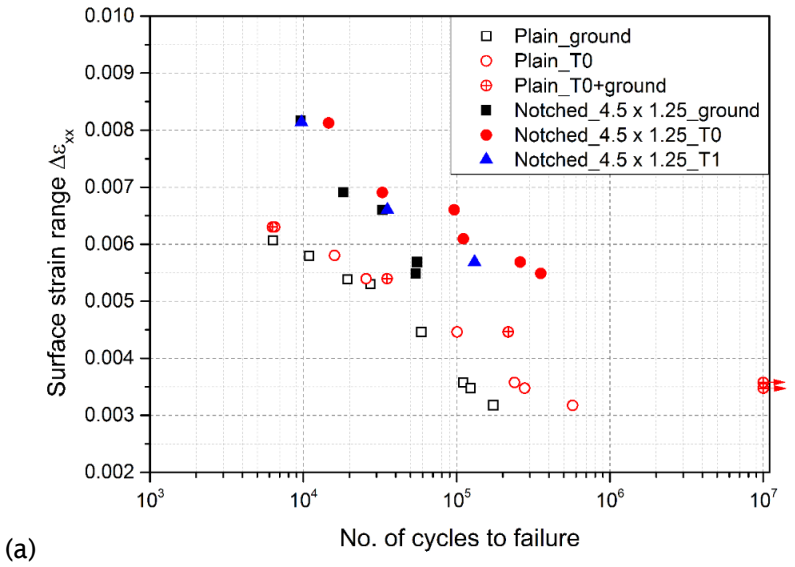

(a)

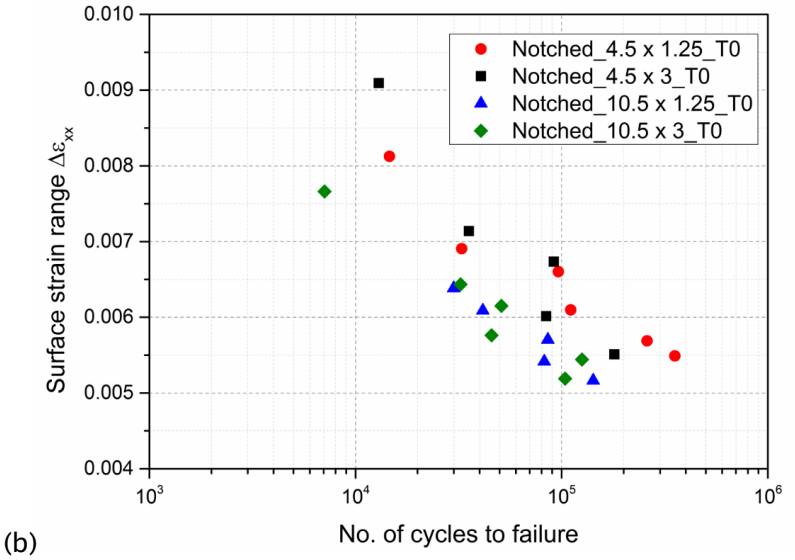

(b)

Figure 5-1: Strain-life comparison (a) between the plain bend bar and notched (4.5 × 1.25) samples with different surface conditions, and (b) between T0 shot-peened notched samples with different notch geometries (fatigue life data reported in [77, 166] and have here been re-plotted using the FE model incorporating shot peening effects on the locally experienced $\Delta\varepsilon_{xx}$.

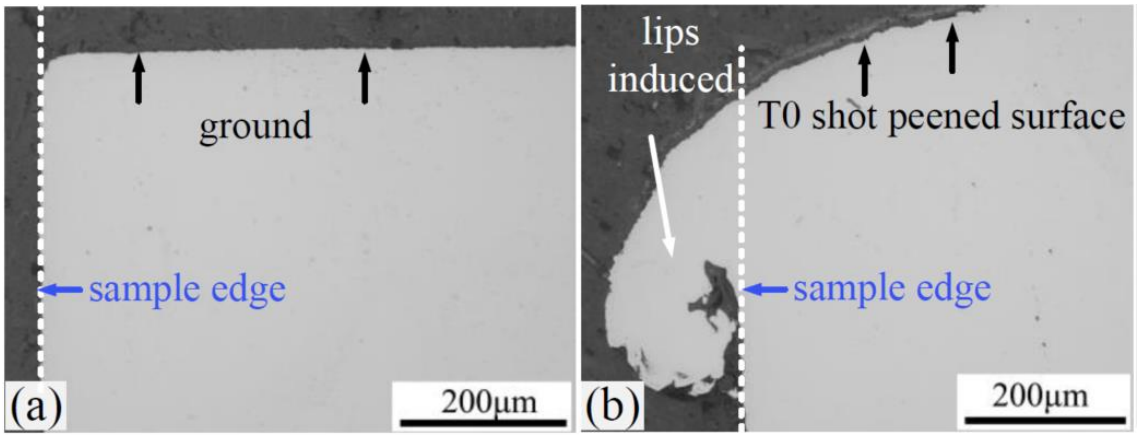

Figure 5-2: Shot peening lips, illustrating shear deformation in the edge region in the (a) ground and (b) T0 shot-peened condition [165].

5.3 Fatigue criteria

According to Figure 5-1, the actual local strain range ($\Delta\varepsilon_{xx}$) cannot uniquely characterise the fatigue life data for conditions with different surface treatments and geometries, even when the effects of compressive residual stresses and strain hardening are taken into account. This is thought to be a result of the mean stress level or the stress/strain ratios within the surface layer during fatigue loading being changed by shot peening, compared with the un-peened condition [57, 151]. Consequently, in order to predict the fatigue life of shot-peened components using total life approaches, a damage parameter applying to situations with varying loading amplitudes and mean stress levels should be selected instead of simply using the local strain range. According to the review detailed in Sections 2.3.1 and 2.3.3.2, critical plane approaches seem most robust since they reflect the physical nature of fatigue damage, especially the Smith-Watson-Topper (SWT) and the Fatemi-Socie (FS) approaches which are stress-strain-based. Hence, both the SWT and the FS damage parameters have been selected in the present study to account for shot peening effects in the application of total life approaches.

5.3.1 The Smith-Watson-Topper (SWT) criterion

Smith et al. [115] proposed a damage parameter governing the uniaxial fatigue of metals. It was then extended by Socie [121] to a critical plane multiaxial fatigue criterion, as defined by Equation 5-1, where $\sigma_{n,max}$ and $\Delta\varepsilon_n$ are the maximum stress and the strain range perpendicular to the critical plane during one cycle; the critical plane is defined as the one with the maximum damage accumulation. The SWT parameter can be related to fatigue life using Equation 5-2, where E is the Young's modulus and b, d, σ_f', and ε_f' are

material constants. By combining these constants, a general format is obtained as shown by Equation 5-3, where A_1, A_2, a_1 and a_2 are also material constants and can be determined by calibration tests. This criterion is most suitable for Mode I cracks which are developed by high tensile stresses.

$$\text{SWT} = \frac{1}{2}\sigma_{n,max}\Delta\varepsilon_n \tag{5-1}$$

$$\frac{1}{2}\sigma_{n,max}\Delta\varepsilon_n = \frac{\sigma_f'^2}{E}\left(2N_f\right)^{2b} + \sigma_f'\varepsilon_f'\left(2N_f\right)^{b+d} \tag{5-2}$$

$$\frac{1}{2}\sigma_{n,max}\Delta\varepsilon_n = A_1 {N_f}^{a_1} + A_2 {N_f}^{a_2} \tag{5-3}$$

5.3.2 The Fatemi-Socie (FS) criterion

For Mode II cracks growing on planes with high shear stress. Fatemi and Socie [122] suggested a damage parameter which was expressed as a function of the maximum shear strain range, $\Delta\gamma_{max}$, and the maximum normal stress acting on the maximum shear strain plane over one cycle, $\sigma_{n,max}$, as shown by Equation 5-4, where σ_y is the material monotonic yield strength and k is a material constant. The value of *k* can be determined by fitting uniaxial fatigue data to torsion fatigue data. In the present study, *k* = 1 has been used as a rough estimation due to the lack of relevant experimental data, as suggested in [123, 187]. The FS parameter can be related to fatigue life using a general format similar to Equation 5-3, as described by Equation 5-5.

$$FS = \frac{\Delta\gamma_{max}}{2}\left(1 + k\,\frac{\sigma_{n,max}}{\sigma_y}\right) \tag{5-4}$$

$$\frac{\Delta\gamma_{max}}{2}\left(1 + k\,\frac{\sigma_{n,max}}{\sigma_y}\right) = A_1 {N_f}^{a_1} + A_2 {N_f}^{a_2} \tag{5-5}$$

5.4 Life prediction procedures

Using the eigenstrain-based modelling approach that has been developed by the authors to incorporate the compressive residual stress and strain hardening effects caused by shot peening (Chapter 4), the residual stress distributions in the shot-peened plain and notched (4.5 × 1.25) samples were first reconstructed and relevant modelling results are shown in Figure 5-3(a). All the presented residual stress profiles have been validated with experimental data (see Figure 4-9, Figure 4-10, Figure 4-12 and Figure 4-13).

Then, the validated modelling approach was extended to different notched geometries (as presented in Table 3-9) treated with the T0 shot peening process: The modelled residual stress distributions are shown in Figure 5-3(b). In the modelling work, the

eigenstrain component tangential to the notch curvature, $\varepsilon_{\theta}^{eigen}$, was evaluated using an assumption described by Equation 5-6, where ε_{yy}^{eigen} is the eigenstrain component in the transverse direction and c is the ratio between the eigenstrains in the longitudinal direction and the transverse direction; details of this analysis are presented in Section 4.3.1.2. The value of *t* was numerically determined to be 1.58 for the 4.5 × 1.25 notched geometry in the T0 condition, being consistent with the K_t value of this notched sample. The corresponding value of other notched geometries, 4.5 × 3, 10.5 × 1.25 and 10.5 × 3, were numerically determined to be 1.48, 1.27 and 1.21 respectively. Although this empirical method may need further validation, as can be seen from the results presented in this study, the model predictions are at least consistent with the experimental results of the test specimens analysed in the current study. The third eigenstrain component, ε_{r}^{eigen}, which is perpendicular to the notch curvature, was calculated using Equation 5-7, considering volume conservation in plastic deformation.

$$\varepsilon_{\theta}^{eigen} = t\,\varepsilon_{yy}^{eigen} \tag{5-6}$$

$$\varepsilon_{r}^{eigen} = -(\varepsilon_{\theta}^{eigen} + \varepsilon_{yy}^{eigen}) \tag{5-7}$$

In addition to the residual stress effects, the strain hardening effects were also accounted for in the developed model by increasing the local material yield strength based on EBSD measurements, as introduced in in Section 4.3.2.

This modelling approach has been validated by showing a satisfactory prediction of the stress/strain evolution during fatigue loading, as demonstrated in Section 4.4. This is helpful to the application of fatigue criteria in assessing fatigue life by determining the required stress/strain terms allowing for shot peening effects.

To simulate the fatigue behaviour, the varying load levels which were applied to obtain the fatigue life data presented in Figure 5-1 were modelled, using the FE model with corresponding appropriate geometric features (as shown in Figure 5-4) and shot peening effects. In the present system, since all the cracks were observed to initiate from the surface [77], the surface stress and strain data during the first cycle were extracted from the modelling results based on corresponding geometric features and shot peening effects. A plane was defined in terms of φ, the angle measured counter-clockwise from the x axis of the specimen (i.e. the longitudinal direction) to the normal vector on an inclined plane. The normal stress, normal strain and shear strain on the plane were calculated using the extracted modelling results, according to Equations 5-8 - 5-10 respectively. To determine the critical plane, planes were checked at all angles between $-90^{\circ} < \varphi < 90^{\circ}$ with an interval of 1°. Then the SWT and FS parameters representing each

life data points shown in Figure 5-1 were calculated based on the determined critical plane.

$$\sigma_n = \frac{\sigma_{xx}+\sigma_{yy}}{2} + \frac{\sigma_{xx}-\sigma_{yy}}{2}\cos 2\varphi + \tau_{xy}\sin 2\varphi \quad (5\text{-}8)$$

$$\varepsilon_n = \frac{\varepsilon_{xx}+\varepsilon_{yy}}{2} + \frac{\varepsilon_{xx}-\varepsilon_{yy}}{2}\cos 2\varphi + \frac{\gamma_{xy}}{2}\sin 2\varphi \quad (5\text{-}9)$$

$$\gamma = -\sin 2\varphi\left(\varepsilon_{xx} - \varepsilon_{yy}\right) + \gamma_{xy}\cos 2\varphi \quad (5\text{-}10)$$

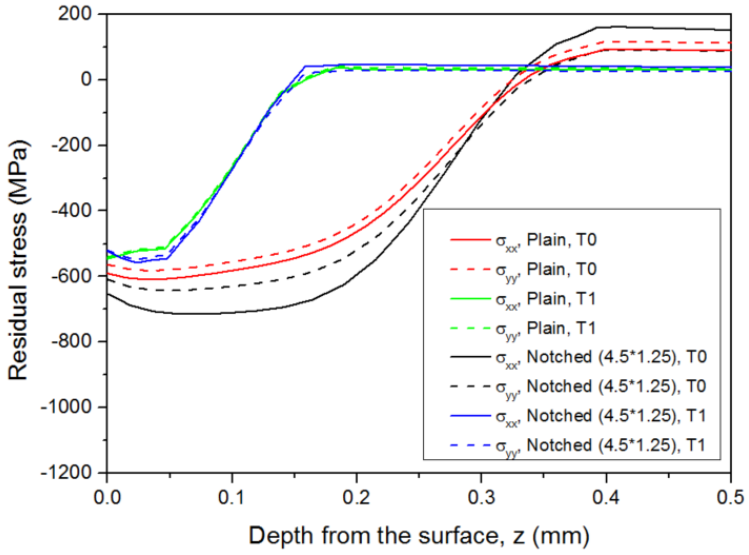

(a)

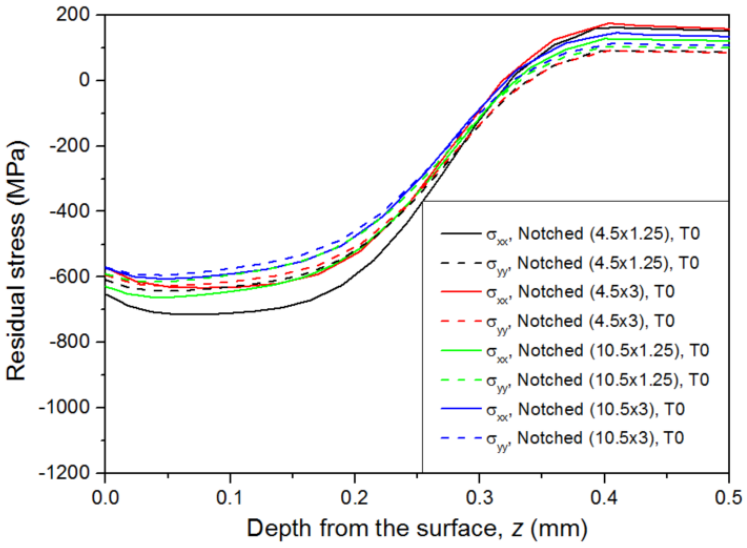

(b)

Figure 5-3: Modelled residual stress distributions (a) in the T0 & T1 shot-peened plain bend bar and notched (4.5 × 1.25) samples and (b) in the T0 shot-peened notched samples with different notch geometries.

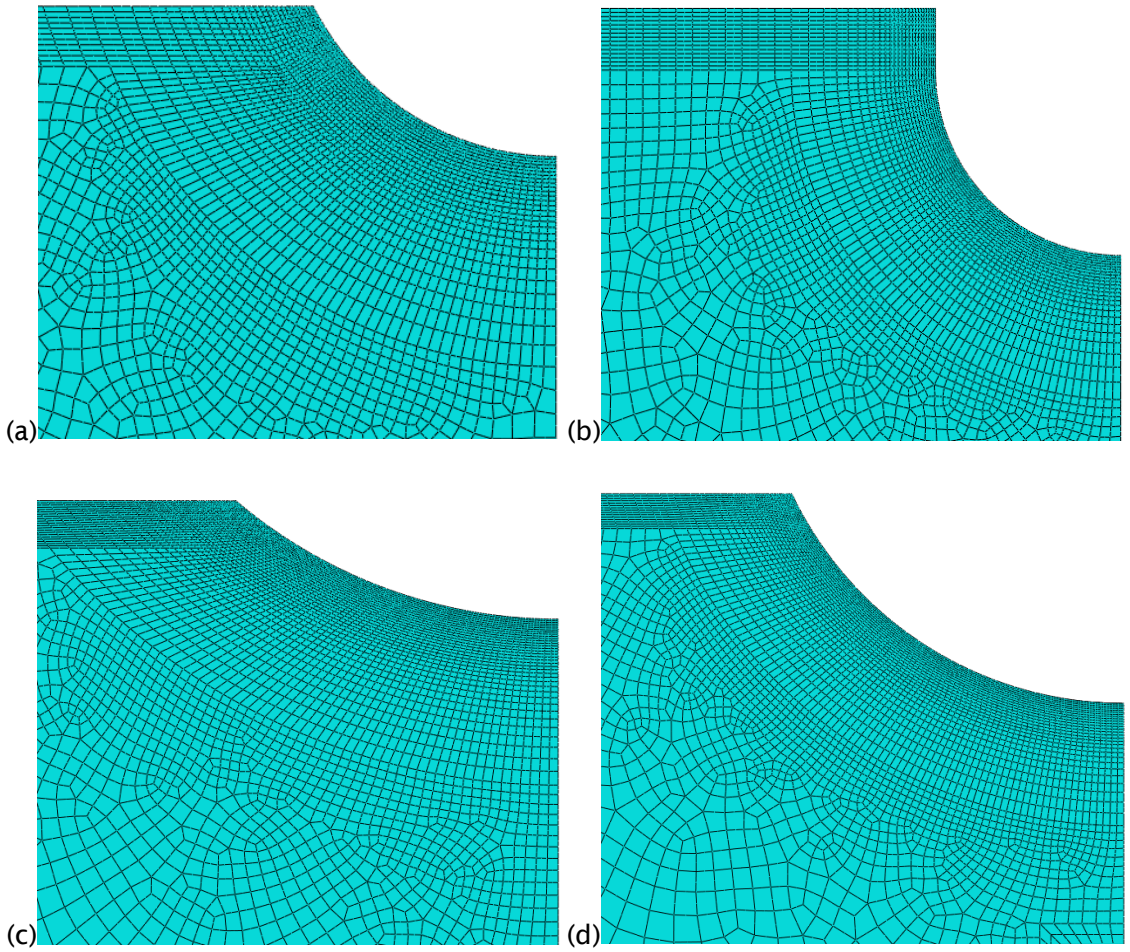

Figure 5-4: FE models for different notch geometries defined in Table 3-9: (a) 4.5 × 1.25 mm, (b) 4.5 × 3 mm, (c) 10.5 × 1.25 mm and (d) 10.5 × 3 mm.

The calibration curves were determined based on Equations 5-3 and 5-5, which are generally suggested to be fitted to the fatigue life data of simple smooth specimens under uniaxial loading (i.e. the calibration data) [115, 122]. But due to the lack of relevant data in the present study, the bending fatigue life of ground samples were regarded as the calibration data instead. The SWT and FS parameters for the ground sample at different load levels were evaluated at the sample surface using the FE model without shot peening effects. Surface modifications (i.e. roughness, residual stresses and strain hardening) introduced by grinding were neglected in the modelling work since it was found that their effects were limited in the LCF regime in the present system [82, 166].

The obtained calibration curves for the SWT and the FS criteria are shown in Figure 5-5 (a) and (b) respectively. It is noted that this fitting work was carried out for the plain bend bar and notched samples separately due to their different crack nucleation and growth mechanisms as explained in Section 5.2. Although the critical plane criteria are

typically used to predict the crack initiation and early propagation life, the total fatigue life data were directly used to simplify the life prediction process. This simplification was thought to have little influence on the accuracy of the predicted results, because the crack initiation and early propagation process took at least ~ 70% - 80% of the total life in the current case (relevant experimental evidence will be provided in Chapters 6 and 7).

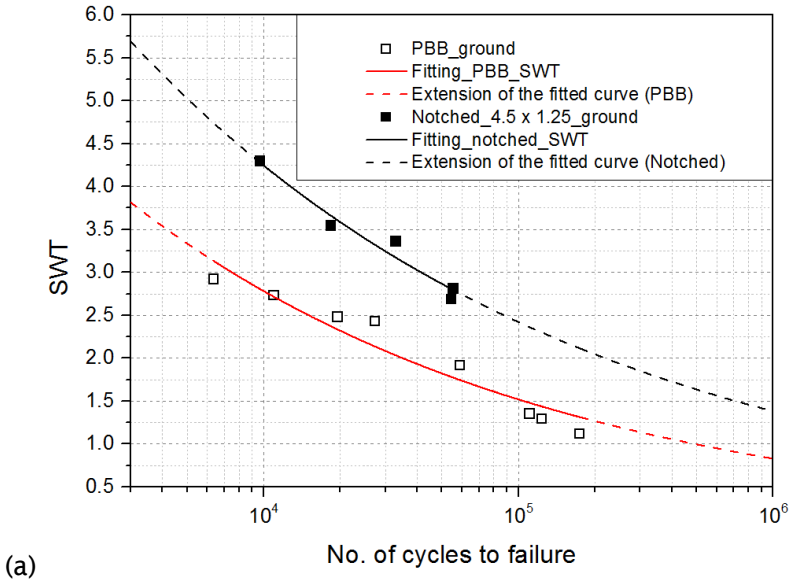

(a)

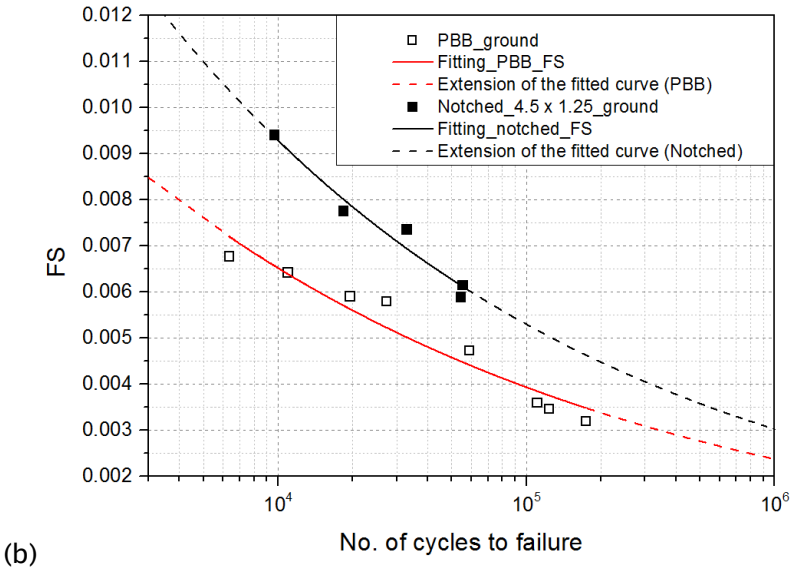

(b)

Figure 5-5: Fitted results based on the fatigue life of ground samples for the (a) SWT and (b) FS criteria using the surface stress/strain data.

In the next step, the reference curves (Figure 5-5) fitted for the two criteria were used to correct for shot peening effects; the fatigue life of shot-peened samples were expected to collapse onto the life-plot for ground samples if the fatigue life data were plotted in

terms of the appropriate damage parameter (SWT or FS). The value of the damage parameter at the surface of shot-peened samples was directly determined using the developed FE model incorporating shot peening effects. Finally, based on the reference curves, the fatigue life of the shot-peened samples was predicted.

It has been suggested by some references [129] that using the stabilised stress/strain state can lead to a more accurate life prediction. However, the FE approach applied in the present study is only capable of predicting the stress/strain evolution during the quasi-static loading stage (the first cycle) without considering the cyclic behaviour, as explained in Chapter 4. This simplification was assumed to have negligible influence on the accuracy of life prediction for the notched sample, because the experimental observation suggested that residual stress relaxation at the notch root only occurred during the first cycle owing to the high constraints exerted by the notch geometry with no further logarithmic relaxation though life (see Figure 4-5). As for the plain bend bar sample, although there was no direct experimental validation on how the residual stress relaxed beyond the first cycle, based on the notched results in the light of the material cyclic behaviour, it is reasonable to assume that the relaxation is most significant during the quasi-static loading stage [74, 86] such that the applied simplification was used as an appropriate approximation.

5.5 Life prediction results

The predicted critical planes using the SWT and FS criteria for the T0 shot-peened 4.5 × 1.25 notched specimen when $\Delta\varepsilon_{xx}$ = 0.69% are shown in Figure 5-6. The critical planes obtained using the two criteria differ significantly; $\varphi = 0^{\circ}$ and $\pm 45^{\circ}$ for the SWT and FS critical planes (i.e. the crack orientation) respectively. Similar results were obtained for other conditions with different geometries, peening intensities and load levels, so they are not presented here for brevity.

Despite the evident difference in the predicted critical plane, the predicted fatigue life data using the two criteria are similar, as shown in Figure 5-7 and Figure 5-8 respectively, and compared with corresponding experimental results. Regarding the plain bend bar sample, the predicted results are more consistent with the condition without edge lips (T0 shot peening + grinding); most predicted data fall within the factor of two error band. In contrast, in the condition with retained edge lips (T0), although the fatigue life data for less than 10^5 cycles were still accurately predicted, the life data between 10^5 and 10^6 cycles were significantly overestimated. As for the notched sample, both criteria have resulted in an acceptable prediction for specimens with different conditions (different

peening intensities and notch geometries) where most predicted data points are located within the factor of three error band.

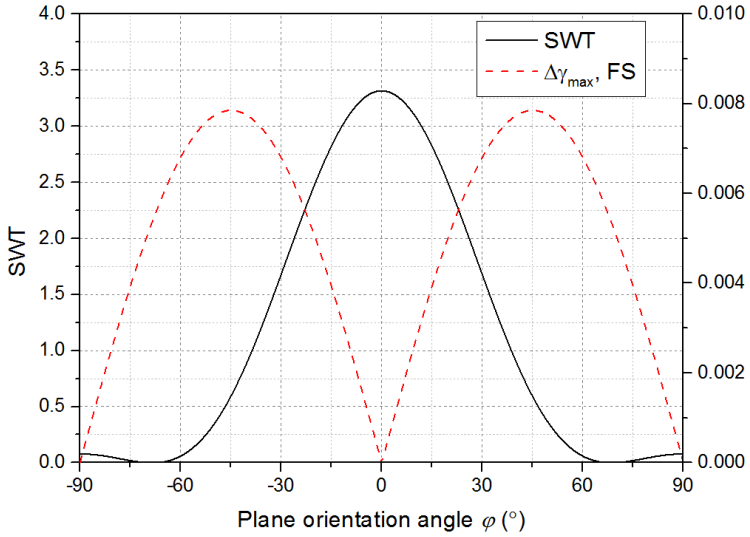

Figure 5-6: The predicted critical planes using the SWT and FS criteria.

5.6 Discussion

By utilising an FE modelling technique, the local effects of surface strain hardening and residual stresses caused by shot peening have been fully accounted for in the life prediction process. The stress and strain state at safety critical regions during fatigue loading were directly predicted using the FE model. This approach is believed to be more accurate than the simple stress superposition method applied by many researchers [85, 125, 126, 144, 188] because it ensures global stress equilibrium, strain compatibility and also matches the boundary conditions. Its advantages are more evident in the application to notched specimens where the stress concentration feature makes the local stress/strain state even more complex.

5.6.1 Improvement of the life prediction using a critical distance approach

The results shown in Figure 5-7 and Figure 5-8 were obtained simply using the surface stress/strain data. Nevertheless, for shot-peened samples, the compressive residual stress profile with a typical 'hook' shape may result in a high gradient of the stress distribution beneath the surface when external loads are applied. Furthermore, strain hardening may also influence the subsurface stress/strain distribution during fatigue loading due to the changed local yield stress. These effects may significantly affect the total fatigue life by influencing the crack growth behaviour [82]. Hence, the life

prediction results might be improved if the stress/strain state within a layer near the surface was taken into account, rather than simply using the surface stress/strain data.

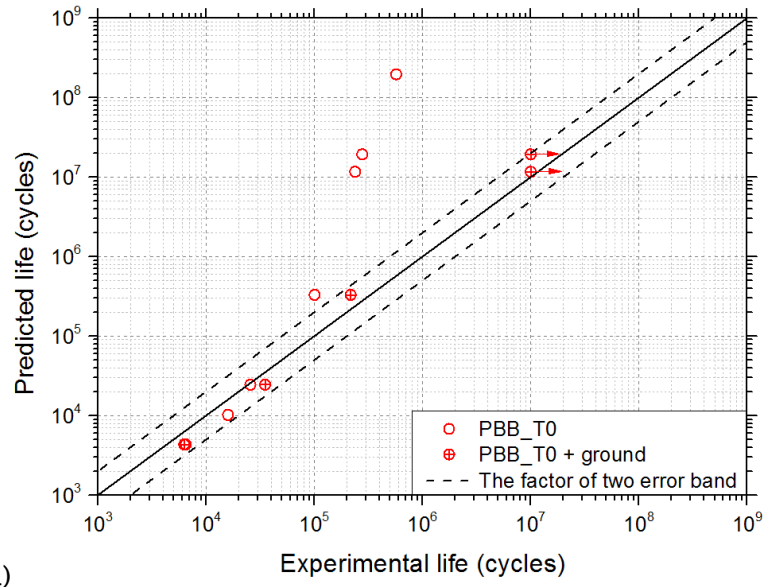

(a)

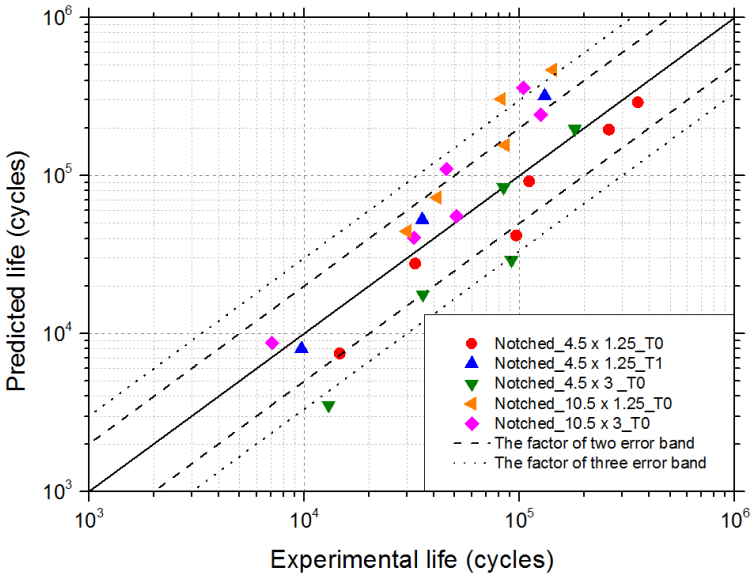

(b)

Figure 5-7: Life prediction using the surface SWT parameter for the (a) plain bend bar and (b) notched samples.

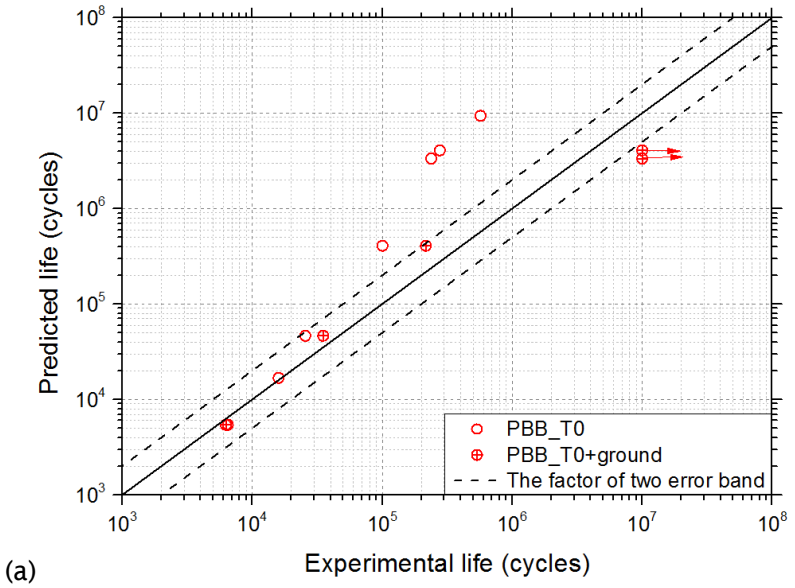

(a)

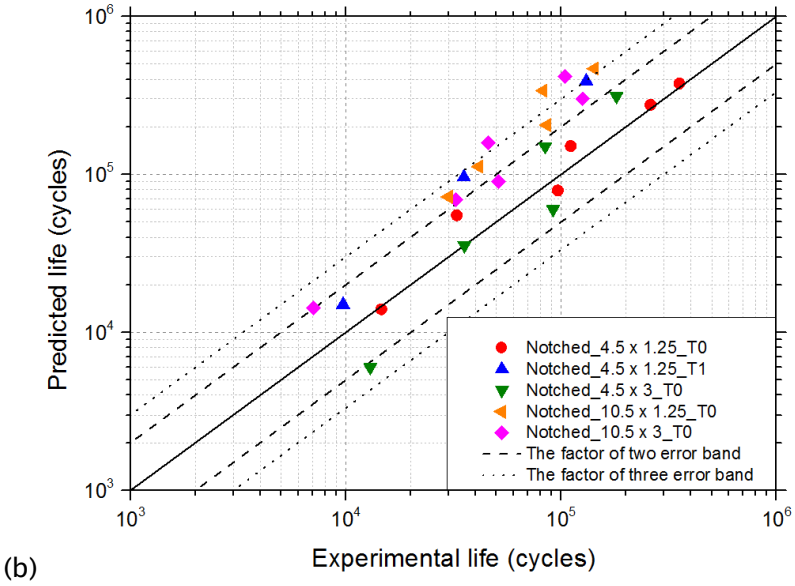

(b)

Figure 5-8: Life prediction using the surface FS parameter for the (a) plain bend bar and (b) notched samples.

Figure 5-9(a) shows the comparison between the mean stress level in the T0 shot-peened (solid lines) and un-peened (dashed lines) 4.5 × 1.25 notched samples when $\Delta\varepsilon_{xx} = 0.69\%$, which were determined using the FE model with and without shot peening effects respectively. The mean stress profile was calculated by averaging the maximum and minimum stress profiles within one cycle. In Figure 5-9(a), it is evident that the mean stress level in the un-peened sample is significantly reduced within a depth of 0.35 mm by the T0 process. Beyond this depth, no clear effects of shot peening can be observed. In contrast, T1 shot peening influences a much shallower depth (0.15 mm), as shown in Figure 5-9(b).

To better quantify the reduced mean stress, the degree of this reduction is defined using Equation 5-11, where σ_{m_SP} and σ_{m_UP} are the mean stress level in the peened and un-peened conditions respectively. This work has been carried out for different $\Delta\varepsilon_{xx}$ levels, as shown in Figure 5-10. It can be seen that the reduction of the mean stress is confined to within a depth of 0.35 and 0.15 mm in the T0 and T1 conditions respectively (similar to the depth of the compressive residual stress profile shown in Figure 5-3), which is independent of the $\Delta\varepsilon_{xx}$ level. However, the degree of the mean stress reduction becomes less evident with increasing $\Delta\varepsilon_{xx}$ levels. Similar trends have been obtained for the plain bend bar samples but are not presented here for brevity. This trend is consistent with that shown in Figure 5-1(a); the benefits of shot peening in improving fatigue life is usually less significant at higher load levels with higher $\Delta\varepsilon_{xx}$. Hence, in order to improve the accuracy of the life prediction, the reduced mean stress level within a layer near the shot-peened surface needs be taken into account.

$$\text{Reduced mean stress } (\%) = \frac{\sigma_{m\_SP} - \sigma_{m\_UP}}{\sigma_{m\_UP}} \times 100\% \qquad (5\text{-}11)$$

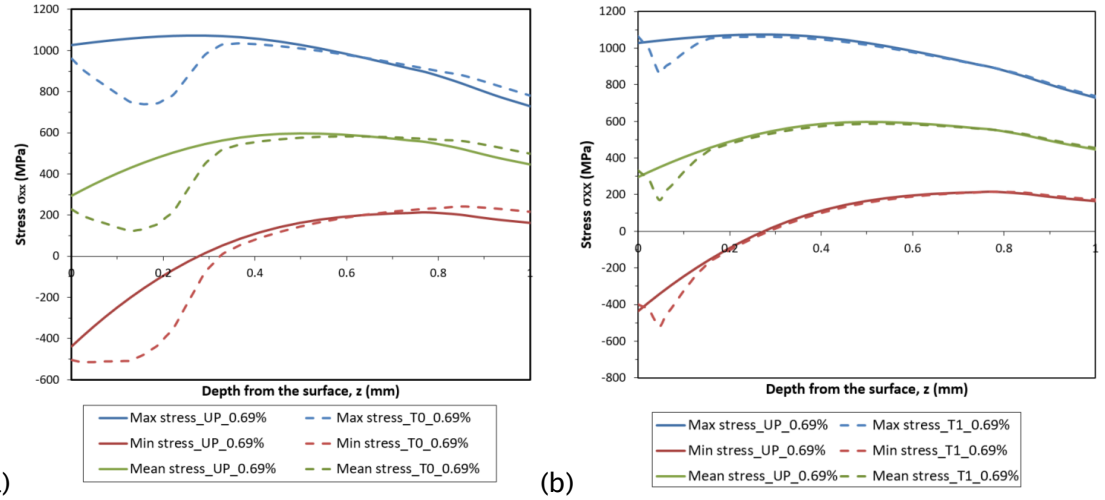

(a) (b)

Figure 5-9: Demonstration of the reduction in the mean stress level resulting from the (a) T0 and (b) T1 shot peening through a comparison between the un-peened (UP) and shot-peened conditions regarding the maximum, minimum and mean stress distributions during cyclic loading ($\Delta\varepsilon_{xx}$ = 0.69%) in the 4.5 × 1.25 notched sample.

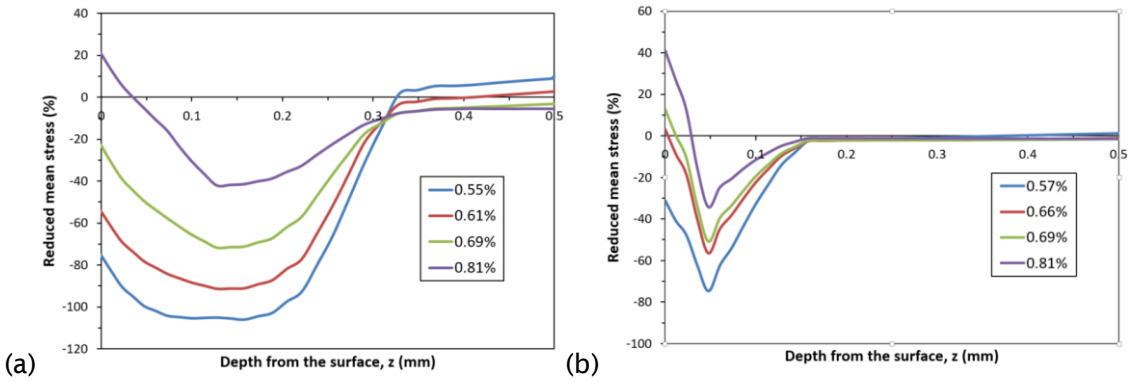

Figure 5-10: The degree of the reduction in the mean stress level by the (a) T0 and (b) T1 shot peening in the 4.5 × 1.25 notched sample at different $\Delta\varepsilon_{xx}$ levels.

To account for the mean stress effects associated with local stress/strain gradients within the shot peening affected layer, a critical distance approach [140] has been applied in the present study. In this approach, to calculate an engineering quantity representative of the real damage accumulated in the fatigue process zone, the stress/strain close to the stress concentration apex has to be averaged over a certain distance. Beyond this distance, the stress state has little influence on the crack initiation and early propagation behaviour. Although it is still an open issue about how to best estimate this distance, the concept of averaging is thought to be useful to deal with conditions with stress/strain gradients [124]. Referring to the definition of critical distances, the SWT and FS parameters were averaged over a depth of L = 0.35 mm and 0.15 mm for the T0 and T1 conditions respectively, as described by Equation 5-12. This depth, indicating the range of shot peening effects, was determined according to the compressive residual stress profiles shown in Figure 5-3.

$$\mathrm{SWT_{avg}} = \frac{\int_0^L SWT(z)\,dz}{L}, \quad \mathrm{FS_{avg}} = \frac{\int_0^L FS(z)\,dz}{L} \tag{5-12}$$

Figure 5-11 and Figure 5-12 show the life prediction results using the averaged damage parameters $\mathrm{SWT_{avg}}$ and $\mathrm{FS_{avg}}$ instead of the surface parameters SWT and FS. Compared with the results shown in Figure 5-7 and Figure 5-8, the application of the defined critical distance has effectively improved the accuracy of the life prediction, especially for the notched samples; most results are now located within the factor of two error band. On the other hand, the data points between 10^5 and 10^6 cycles for the plain bend bar sample with edge lips are still overestimated by 10 – 20 and 3 – 5 times using the averaged SWT and FS parameters respectively, although an improvement has been achieved compared with the results shown in Figure 5-7 and Figure 5-8.

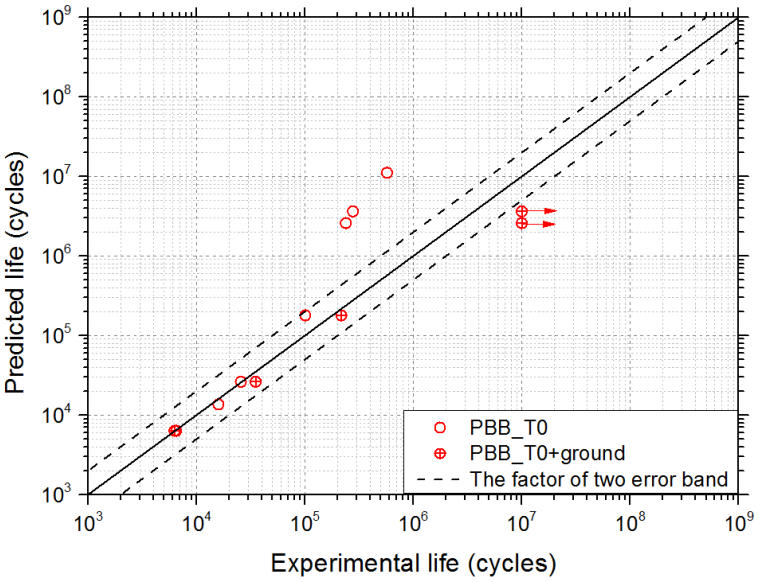

(a)

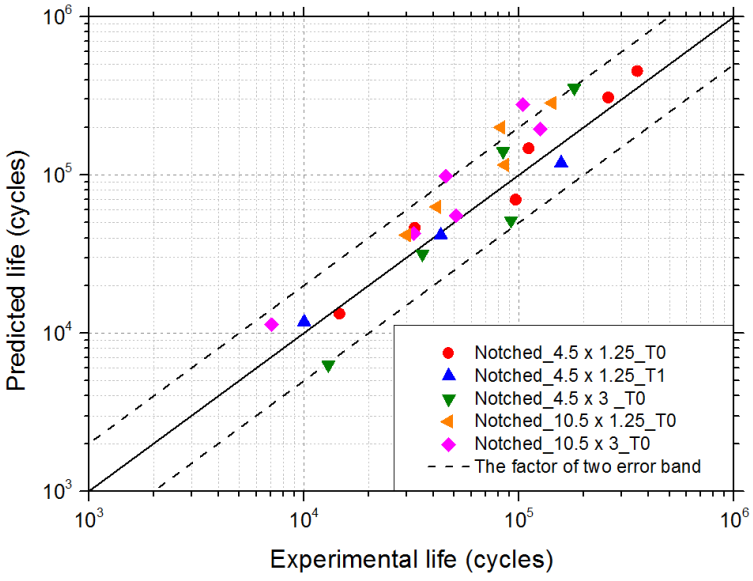

(b)

Figure 5-11: Life prediction using the averaged SWT parameter for the (a) plain bend bar and (b) notched samples.

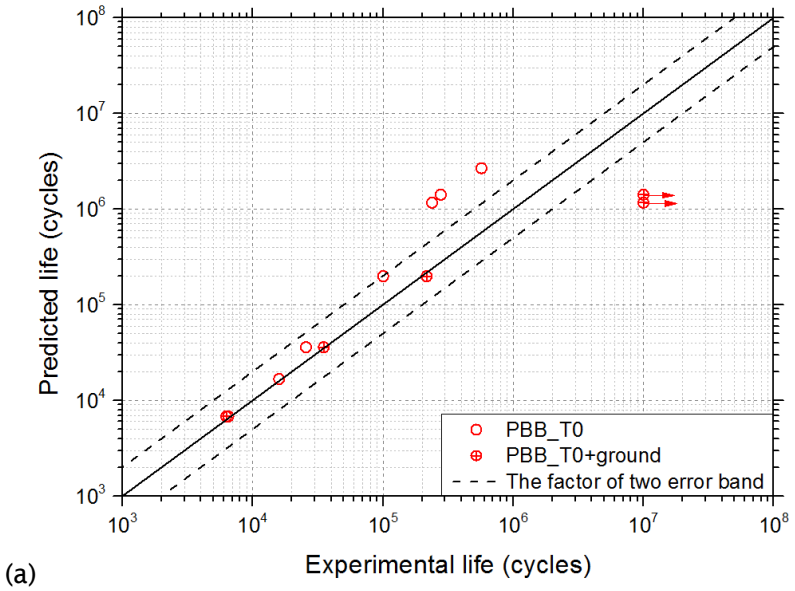

(a)

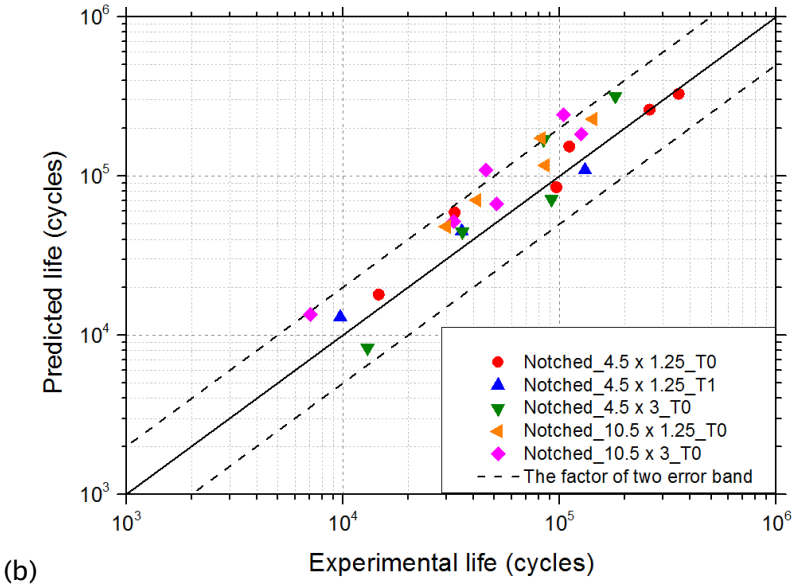

(b)

Figure 5-12: Life prediction using the averaged FS parameter for the (a) plain bend bar and (b) notched samples.

5.6.2 The effects of initial defects

In shot-peened plain bend bar samples, crack initiation was always observed at the corner where edge lips existed (as shown in Figure 5-2). These edge lips acted as stress concentration raisers which significantly accelerated the crack initiation life. This effect tended to be more significant for longer fatigue lives under low load levels, where crack initiation was more dominant determining in total life. However, the detrimental effect of edge lips was not considered in the life prediction process applied in the present study. Hence, the fatigue life data of the shot-peened plain bend bar samples have been

significantly overestimated when N_f is between 10^5 and 10^6 cycles, as shown in Figure 5-7(a), Figure 5-8(a), Figure 5-11(a) and Figure 5-12(a). By removing these edge lips by further grinding (i.e. the data points labelled as "Plain_T0 + ground"), this detrimental effect was significantly reduced, which made the experimental and predicted life data more consistent.

In contrast, centre crack initiation dominated in shot-peened notched samples. The edge lips were therefore found to have much less effect on the fatigue life of notched samples. The difference in crack initiation sites between the shot-peened plain bend bar and notched samples can be explained by consideration of the FE-predicted tensile stress distribution across the sample from the centre (y = 0 mm) to the edge (y = 4 mm) when they are loaded beyond the elastic limit, as shown in Figure 5-13. The σ_{xx} in the plain bend bar sample is more evenly distributed than in the notched sample, which means that defects at the edges of the plain bend bar sample are more likely to promote crack initiation compared with the notched sample. Hence, in any practical application, consideration must be given to removing any shear lips resulting from the peening process when there is no other geometric stress concentration in the treated area.

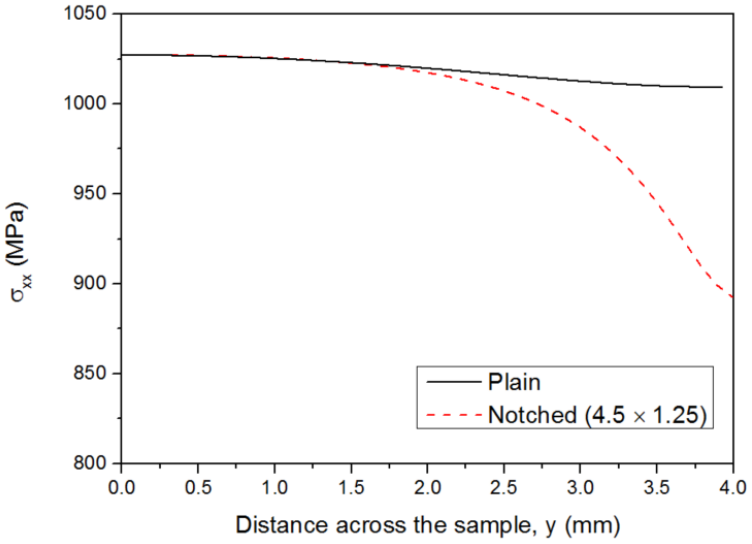

Figure 5-13: Comparison of tensile stress (σ_{xx}) distribution under maximum load in the 4.5 × 1.25 notched sample tested at σ_{nom} = 1034 MPa with that in the plain bend bar sample tested at the same maximum σ_{xx}.

In addition to the edge lips, shot peening may increase surface roughness or introduce some surface microcracks due to a high peening intensity. The increased surface roughness may accelerate crack nucleation when cracks initiate from the surface and the microcracks can potentially propagate during fatigue loading (as reviewed in Section

2.2.1). These detrimental effects were not considered in the life prediction process in the present study. This was because the benefit of shot peening resulting from compressive residual stresses and strain hardening dominated in most cases, where the surface compressive residual stress could counteract the stress concentration effect of the roughened surface and the microcracks were sometimes arrested [90, 91] or grew very slowly in the shot peening affected layer [78, 89, 90]. This has been validated to be the case for the shot-peened 4.5 × 1.25 notched sample under investigation [77, 82]. However, in conditions where an excessive peening intensity is applied [20] or compressive residual stresses relax rapidly (i.e. where high stresses are applied to a region of low constraint), a more advanced life assessment approach considering the detrimental effects of the imperfect surface should be applied instead, otherwise the fatigue life would be overestimated.

5.6.3 Comparison between the SWT and FS critical plane criteria

For the shot-peened notched samples under investigation, both the SWT and FS criteria have generated satisfactory life prediction results. However, the predicted crack orientations are quite different between the two criteria; $\varphi = 0^{\circ}$ and $\pm 45^{\circ}$ using the SWT and FS criteria respectively. This discrepancy is not unexpected and often exists in the application of critical plane models [189, 190], mainly due to the different mechanisms assumed between different critical plane criteria. In order to ensure good accuracy of the life prediction, it has been suggested that the applied critical plane criterion should be chosen according to the specific cracking mode. However, this is can be difficult to define due to the complexity of the cracking mechanism.

It is widely accepted that cracks usually nucleate along slip bands caused by irreversible shear deformation regardless of the external loading type [122]. Therefore, it is believed that the crack nucleation process is predominantly controlled by the maximum shear strain [191]. However, during the early crack propagation stage, the cracking mode usually depends on both the material type and external loads [122]. Some materials display shear cracking and some materials exhibit tensile cracking. Other materials display a mixed cracking behaviour; the actual cracking mode depends on the stress state [190, 192]. Generally, a tensile cracking mode tends to be more dominant in brittle materials with high hardness while a shear cracking mode usually plays a more important role in ductile materials. In shot-peened specimens, the residual stress field results in a multiaxial stress state in the surface layer. In addition, the hardness of the material within the strain-hardened layer is typically significantly increased such that the material becomes more brittle. Consequently, the cracking mode tends to be more complex in shot-peened components than in smooth ones. In such conditions, simply using a single

fatigue criterion apparently cannot describe all the possible situations, which may result in an unsatisfactory prediction of the crack orientation.

In addition to the materials and the stress state, the cracking behaviour also depends on the microstructure of the material. It has been observed that cracks prefer to initiate from internal defects such as inclusions and microvoids [82, 145], or surface defects introduced by shot peening as discussed in Section 5.6.2. However, most critical plane criteria assume that the material is defect-free. In most applications, the stress and strain terms required by the applied fatigue criteria were calculated without considering the effects of these micro defects, such that the complex stress state near these defects cannot be captured. Therefore, the cracking mode may be incorrectly predicted when it is more microstructure dependent, especially in the early crack propagation stage.

Despite many difficulties in accurately predicting the cracking mode in different systems, the critical plane criteria have been demonstrated to be relatively robust in predicting the fatigue life. This is supported by others' work [189, 190] and the results obtained in the present study. In the present case, the relation between $\mathrm{SWT}_{\mathrm{avg}}$ and $\mathrm{FS}_{\mathrm{avg}}$ is shown in Figure 5-14, which demonstrates an approximately proportional relation between the two damage parameters obtained for all the investigated notched samples. This indicates that the predicted damage accumulation trends during fatigue loading using the SWT and FS criteria are similar despite their different definitions of the damage parameter, which is consistent with the conclusion made by Jiang et al. [190]. Therefore, in conditions where microstructural defects do not significantly accelerate crack initiation and early propagation, acceptable life prediction results can be expected using either criteria as long as the macroscopic stress/strain evolutions at critical regions during fatigue loading are accurately predicted to make sure that the overall damage accumulation in the specimen is reasonably determined.

5.6.4 Sensitivity analysis

Although the SWT and FS critical plane criteria seem to work well in the current system, a sensitivity analysis is necessary to assess the influence of the FE modelling results on the accuracy of life predictions. This analysis is an extension of a previous sensitivity analysis presented in Section 4.5, which investigated how the accuracy of the input data of the FE model (i.e. the initial residual stress and strain hardening profiles) affected the prediction of residual stress relaxation. In the present study, the parametric analysis matrix was the same as the one used in Section 4.5 (see Table 4-3), which was composed of varying eigenstrain and initial true plastic strain profiles labelled as a, b and c (see

Table 4-2); the profiles with label b were the baseline profiles and the ones labelled as a and c reflected the experimental error range reported in [17].

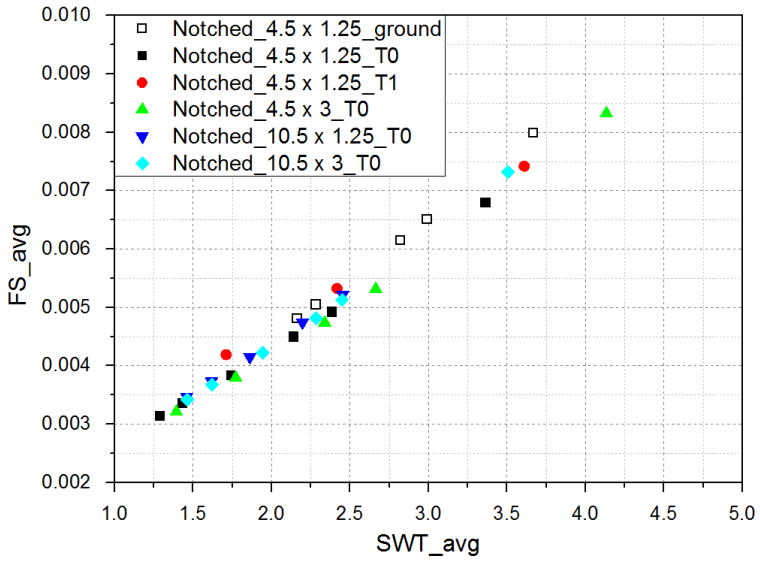

Figure 5-14: Relation between the averaged SWT and FS parameters.

The FE models with varying eigenstrain and initial true plastic strain profiles were used to predict the fatigue life of the T0 shot-peened 4.5 × 1.25 notched specimen at two differing load levels ($\Delta\varepsilon_{xx}$ = 0.69% and 0.81%), following the life prediction procedure outlined in Section 5.4. The results for the SWT criterion are shown in Figure 5-15; the results for the FS criteria are omitted since very similar results as the SWT criterion were obtained. From Figure 5-15(a), it can be seen that there is no clear effect of the variation in the initial strain hardening profiles, which is consistent with the sensitivity analysis of residual stress relaxation as detailed in Section 4.5. In Figure 5-15(b), although varying initial residual stress profiles result in some variation in the predicted fatigue life, all the predicted life points are still within the factor of two error band. Hence, an overall conclusion can be made that the accuracy of the developed life prediction approach is more sensitive to the initial residual stresses than to the initial plastic strain. However this analysis also shows that a typical experimental error range is unlikely to result in an unacceptable difference in the final life prediction results via this methodology.

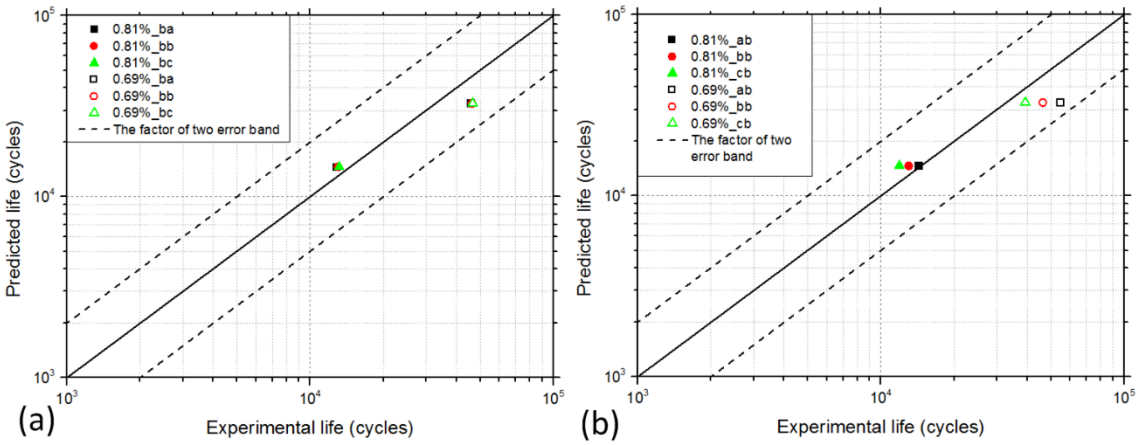

Figure 5-15: The results of the sensitivity analysis for the SWT criteria; the effects of varying (a) strain hardening and (b) initial residual stress profiles on the accuracy of life predictions.

5.7 Conclusion

In this chapter, the Smith-Watson-Topper (SWT) and Fatemi-Socie (FS) critical plane criteria have been applied to predict the total fatigue life of the shot-peened components with varying geometries. The main conclusions are summarised:

- By allowing for the effects of shot peening on local stress-strain evolution in terms of compressive residual stresses and strain hardening, the SWT and FS criteria have been demonstrated to accurately predict the LCF life of shot-peened specimens (especially those with stress concentration features). The stress/strain status during fatigue loading in shot-peened specimens can be effectively evaluated using an FE modelling approach.
- Shot peening effectively reduces the mean stress level within a surface layer during fatigue loading. The degree of this reduction becomes less significant at high load levels, giving reduced benefit from shot peening in terms of improving fatigue life. In this case, the principal benefit of shot peening can be linked to effective reductions in mean stress level. Application of the critical distance method to account for the stress/strain gradients near the surface can further improve the life prediction results using the SWT and FS criteria.
- Surface defects introduced by shot peening may significantly reduce the crack initiation time. In such situations, their detrimental effects need to be accounted for in the lifing procedure. Otherwise the fatigue life may be inappropriately overestimated.

- The crack orientation is more difficult to accurately predict than overall fatigue life. This is mainly ascribed to the inconsistency between the theoretical assumption of the critical plane and the complexity in the real cracking mechanism. Nevertheless, the predicted crack orientation seems not to play a decisive role in the accuracy of life prediction in this case.
- The predicted fatigue life using the developed FE-based approach is more sensitive to the initial residual stress profile than to the initial strain hardening profile. But as long as the initial input data are within a reasonable experimental error range, the accuracy of the predicted fatigue life will not be unacceptably affected.

6 Fatigue life prediction using damage tolerant approaches: 2D crack modelling

6.1 Introduction

This chapter investigates the short crack growth behaviour affected by shot peening using damage tolerant approaches. To facilitate this investigation, a 2D plane strain notched FE model containing a crack has been developed from the FE model incorporating shot peening effects which has been introduced in Chapter 4. The crack closure phenomenon induced by compressive residual stresses (CRS) has been simulated using the FE model. Compared with the previously reported modelling work (as reviewed in Section 2.3.3.3), the advantage of the developed model in this study is that strain hardening, as well as residual stress redistribution caused by both 'pre-cracking' mechanical loading and the subsequent appearance of the crack, have been taken into account.

In the modelling work, both LEFM and EPFM approaches considering potential crack closure effects have been used to predict the prolonged short crack propagation life by shot peening. A discussion was carried out based on the comparison between LEFM and EPFM, as well as the comparison between the damage tolerant approaches and the total life approaches introduced in Chapter 5. In addition, the relative contributions of the compressive residual stress and strain hardening caused by shot peening to improving fatigue life were analysed using this FE modelling tool.

This chapter is largely based on the following paper:

You, C., Achintha, M., He, B., & Reed, P. (2017). *A numerical study of the effects of shot peening on the short crack growth behaviour in notched geometries under bending fatigue tests*. International Journal of Fatigue, 103, 99-111.

6.2 Experimental techniques and results

All the fatigue tests were carried out using the 4.5 × 1.25 notched sample (as shown in Figure 3-13(b)) subjected to different surface treatments (i.e. ground, polished, T1 and T0 shot peening). Relevant fatigue life data shown in Figure 5-1 are summarised in Figure 6-1. Compared with the un-peened condition, it can be seen that the T0 process contributes to life improvement at all $\Delta\varepsilon_{xx}$ levels. By contrast, the T1 process gives much less benefit in life improvement when $\Delta\varepsilon_{xx} > 0.65\%$.

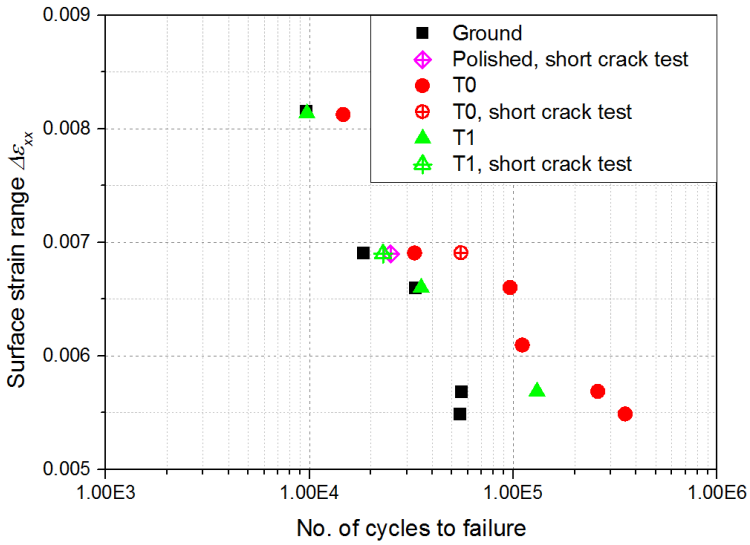

Figure 6-1: Strain-life comparison between the notched samples with different surface treatments (fatigue life data reported in He et al. [82] were replotted using the FE model incorporating shot-peening effects).

As indicated in Figure 6-1, short crack tests have been carried out at $\Delta\varepsilon_{xx} = 0.69\%$ for specimens treated by polishing, T0 and T1 shot peening respectively. Replicas have been used to track the surface crack ($2c$) evolution at the notch root. This work was carried out by He et al. and relevant details are elaborated in [82]. The obtained results are reproduced in Figure 6-2, demonstrating a more significantly delayed short crack growth behaviour caused by the T0 process than the T1 process. The crack size (a) evolution in the depth direction, which could not be directly measured in the short crack test, was also predicted based on a relation between the crack aspect ratio (a/c) and the surface crack length ($2c$). This relation, as elaborated in [82], was determined based on the experimental observations. The predicted a vs N results are illustrated in Figure 6-3.

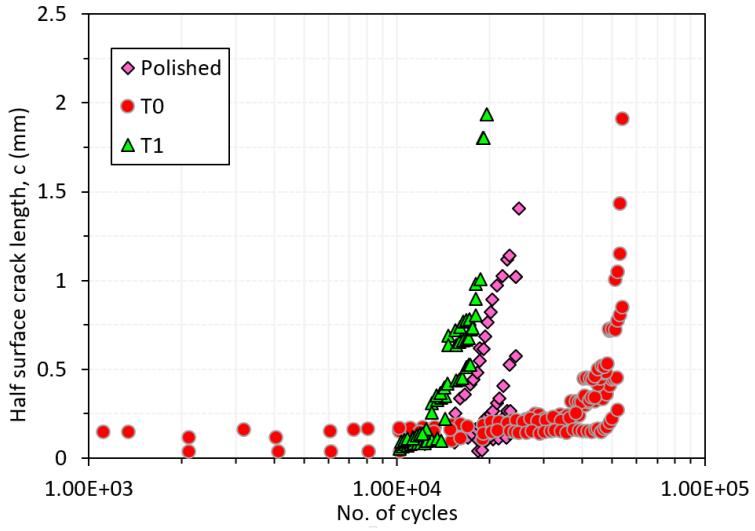

Figure 6-2: Surface crack evolution in the polished, T0 and T1 shot peening conditions under $\Delta\varepsilon_{xx} = 0.69\%$ [82].

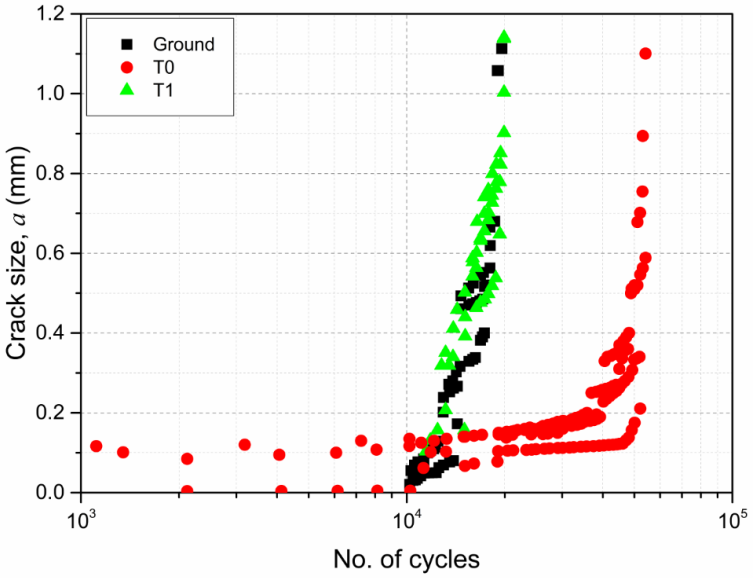

Figure 6-3: The predicted crack size evolution in the depth direction at the notch root of the specimens with different surface treatments under $\Delta\varepsilon_{xx} = 0.69\%$.

6.3 2D crack modelling

A 2D FE model has been developed incorporating both compressive residual stress and strain hardening effects caused by shot peening. This FE model, which can be used to accurately investigate the interaction between the shot-peening-induced effects (i.e. compressive residual stress and strain hardening) and service conditions, is a simplified version of the 3D FE model developed in Chapter 4. In order to understand the benefits of shot peening in retarding short crack growth, residual stress relaxation caused by

cyclic loading was first simulated and a stabilised stress and strain state was predicted, which was the same as in the application of the total life approaches (Chapter 5). Then, cracks with varying lengths were introduced into this stabilised stress and strain field and the crack driving force was characterised using both LEFM and EPFM approaches considering potential crack closure effects; the weight function and the J-integral methods were applied respectively.

6.3.1 Development of the 2D FE model

A 2D plane strain FE model (as shown in Figure 6-4) containing a compressive residual stress and strain hardening layer was developed using ABAQUS/Standard (v6.13), following the same modelling procedures in the 3D FE model as elaborated in Chapters 3 and 4. Only half of the notched specimen was modelled by restricting the longitudinal movement of the central face (U_x = 0) for symmetry (the crack was inactivated at this stage by the boundary condition along the crack face). It is noted that only the longitudinal residual stress σ_{xx} has been considered in the 2D modelling work and the effects of the transverse residual stress σ_{yy} on fatigue life were omitted, although a 20% relaxation of σ_{yy} was experimentally observed during the first cycle, as shown in Figure 4-5(b). This simplification was assumed reasonable because σ_{xx}, which was along the loading direction and was normal to the mode I crack opening direction, plays a more dominant role in fatigue life under the current circumstances.

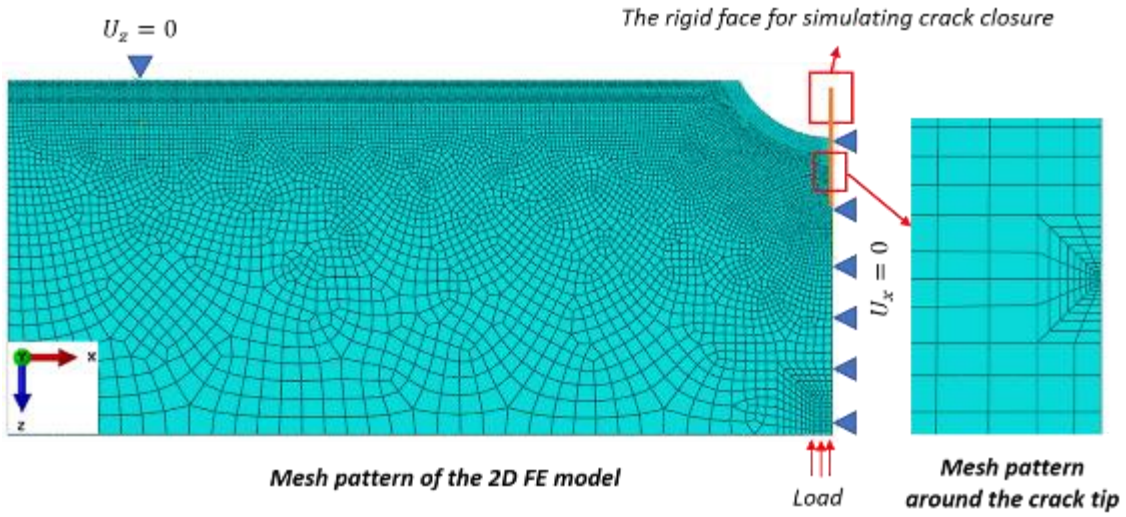

Figure 6-4: The 2D FE model of the notched specimen.

Before the cracks were activated, the 2D model was validated by both experimental measurements and 3D modelling results in reconstructing the as-peened residual stress field and in predicting residual stress relaxation after the first loading cycle under $\Delta\varepsilon_{xx}$ =

0.69%. In the 2D and 3D modelling work, residual stress data were extracted from the notch root area where experimental measurements were carried out. The comparison between experimental and modelling results are shown in Figure 6-5. Figure 6-5(a) illustrates the residual stress distribution caused by the first loading cycle in the ground specimen; it is noted that the initial surface condition caused by the grinding process was not considered in the modelling work because its effects tended to be easily overcome by external loads under the current circumstances [166], therefore, the ground condition was considered simply as the un-peened condition in this modelling work. In addition, Figure 6-5(b) and (c) illustrate the residual stress distribution in the T1 and T0 as-peened conditions respectively. Figure 6-5(d) shows the relaxation in residual stress after one cycle in the T0 specimen. According to Figure 6-5, the 2D modelling results are consistent with the 3D modelling and experimental results in both residual stress reconstruction (Figure 6-5(b) and (c)) and prediction (Figure 6-5(a) and (d)), especially when $z < 0.3$ mm. Hence, the 2D FE model applied in the current research was deemed reliable. The comparison between the two FE models has also been extended to other $\Delta\varepsilon_{xx}$ levels and similar consistency has been found, further demonstrating the reliability of the 2D FE model.

It is noted that this 2D FE model is only capable of predicting the stress and strain evolution during the quasi-static loading stage (the first cycle) without considering the cyclic behaviour, which is consistent with the 3D FE model introduced in Chapter 4. The predicted stress and strain field after the first cycle was assumed representative of the stabilised state during cyclic loading under the current circumstances, because Figure 4-5 demonstrated that residual stress relaxation mainly occurred during the quasi-static loading stage at the notch root in the low-cycle fatigue (LCF) regime in this material. Plastic deformation in the first loading cycle tended to significantly reduce the plastic misfit within the surface layer, which is the source of residual stresses. Similar results have also been reported by others [74, 86].

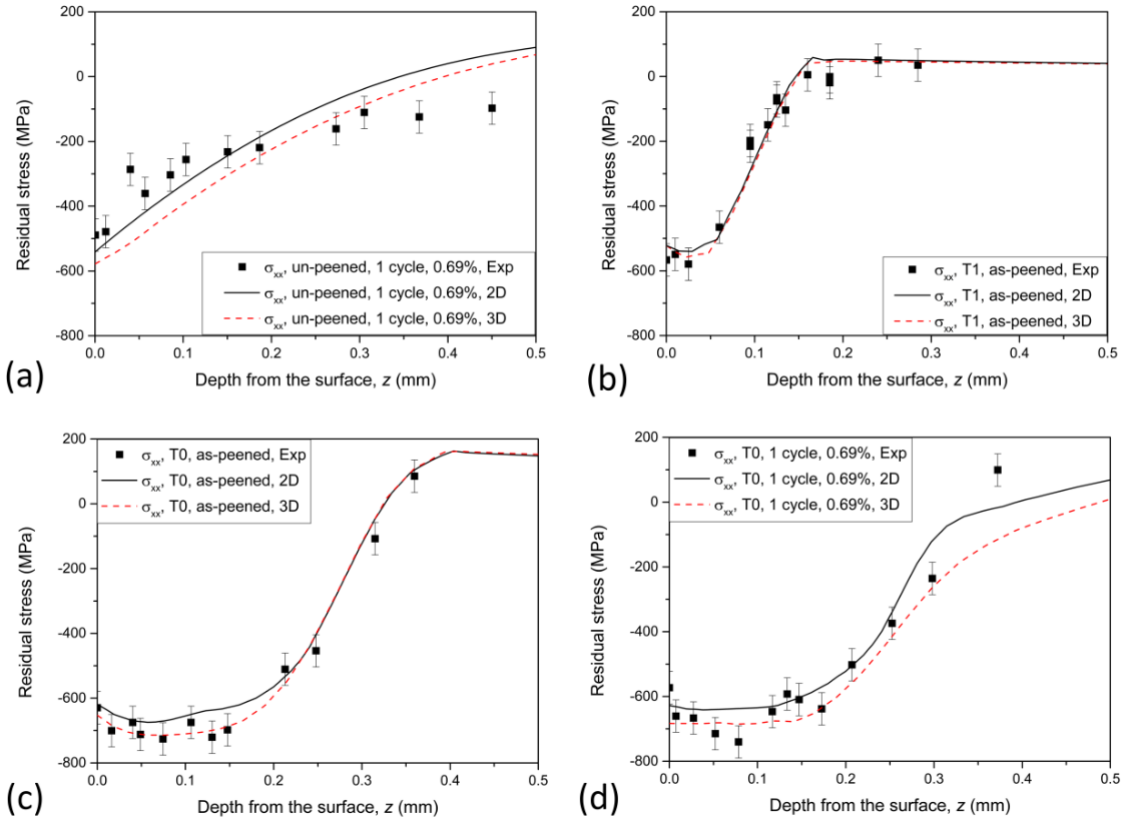

Figure 6-5: Comparison between the XRD measurements, 2D and 3D modelling of the residual stress profile (σ_{xx}) (a) in the un-peened condition after 1 loading cycle ($\Delta\varepsilon_{xx}$ = 0.69%), (b) in the T1 as-peened condition ,(c) in the T0 as-peened condition and (d) in the T0 condition after 1 loading cycle ($\Delta\varepsilon_{xx}$ = 0.69%).

6.3.2 The linear-elastic fracture mechanics (LEFM) approach

The LEFM approach applied in this study was based on calculating stress intensity factors using the weight function method, which was derived from the knowledge of the stress distribution present in the un-cracked geometry [193]. The stress intensity factor *K* for a given geometry under arbitrary loading is expressed by Equation 6-1, where $\sigma(z)$ is the stress distribution acting in the normal direction to the crack plane and $m(a,z)$ is a weight function associated with the crack length *a* and the coordinate *z* along the crack face. $m(a,z)$ depends only on the geometry and boundary conditions and is independent of the magnitude and type of external loads. The weight function $m(a,z)$ for the notched geometry shown in Figure 3-13(b) has been determined following the method introduced in [193].

$$K = \int_0^a \sigma(z) m(a,z) dz \tag{6-1}$$

Shot peening effects were considered by the weight function method based on the concept of superposition. The effective stress intensity factor, K_{eff}, can be determined by superposing the applied stress intensity factor due to external load, K_{app}, and the residual stress intensity factor, K_{res}, as described by Equation 6-2. K_{app} was calculated using the stress profile caused by external loads, $\sigma_{app}(x)$, which was predicted using an elastic FE model without considering shot peening effects. K_{res} was determined using the stabilised residual stress profile, $\sigma_{res}(x)$, which was predicted using an elasto-plastic FE model as introduced in Section 6.3.1.

$$K_{eff} = K_{app} + K_{res} \tag{6-2}$$

Cracks with varying lengths ($a \leq 1.2$ mm) were considered in this study and the chosen range of the crack size was estimated to cover the regime of steady crack growth beyond which unsteady crack propagation happened. In order to take the potential crack closure effects caused by compressive residual stresses into account, K_{eff_min} was taken to be zero at the minimum load when a negative value was obtained using Equation 6-2. The effective stress intensity factor range during cyclic loading, ΔK_{eff}, was then determined according the loading range, as expressed by Equation 6-3.

$$\Delta K_{eff} = K_{eff\_max} - K_{eff\_min} \tag{6-3}$$

6.3.3 The elasto-plastic fracture mechanics (EPFM) approach

The EPFM approach has been applied in order to make a comparison with the LEFM approach in understanding the effects of shot peening on the short crack growth behaviour. Static cracks with varying lengths ($a \leq 1.20$ mm) have been introduced into the 2D FE model. The mesh pattern around the crack tip is illustrated in Figure 6-4 and the mesh size at the crack tip is 1 μm. A mesh sensitivity analysis has been carried out to ensure that the crack modelling results are independent of the mesh size at this mesh density level. The crack driving force was characterised in terms of the J-integral which was calculated automatically by ABAQUS. Although the conventionally defined J-integral becomes path-dependent in the residual stress field, a local path-independence can still be achieved near the crack tip as long as the mesh is fine enough, and the corresponding value of the J-integral can still accurately represent the crack driving force [158, 194, 195]. This local path-independence of the J-integral has been achieved in the current modelling work and used to estimate the equivalent stress intensity factor, K_p, as expressed by Equation 4, where E is the Young's modulus and ν is the Poisson's ratio of FV448. It is noted that K_p does not have direct physical meaning in the EPFM approach

and has been used simply as an equivalent parameter to make a comparison with K which has been estimated using the LEFM approach.

$$K_p = \sqrt{\frac{JE}{1-\nu^2}} \tag{6-4}$$

In the modelling work, the procedure of introducing a crack into the shot-peening-affected area is illustrated in Figure 6-6. Since crack initiation usually occurs after the stabilisation of the stress and strain state during cyclic loading, the introduced crack was initially inactivated during the first cycle in the modelling work by applying boundary conditions for symmetry along the crack face. Then the 'un-cracked' model was used to predict the stabilised stress and strain state by simulating the residual stress relaxation behaviour, as introduced in Section 6.3.1. Finally, the boundary conditions along the crack face were removed and the crack was activated. By applying another loading cycle, the stress and strain redistribution around the crack tip during crack opening was simulated. The potential crack closure phenomenon caused by compressive residual stresses was modelled by defining a normal contact between the crack face and a rigid face fixed on the right hand side of the model (the central face of the real specimen) to avoid the overlapping effects, as shown in Figure 6-4. The contact was assumed to be frictionless, which was reasonable since only the mode I crack was considered in this study. The K_p value at which the crack was fully open (i.e. K_{p_op}) was determined when the contact force became zero. The effective equivalent stress intensity factor range, ΔK_{p_eff}, was then calculated using Equation 6-5, considering the crack closure effects.

$$\Delta K_{p\_eff} = K_{p\_max} - K_{p\_op} \tag{6-5}$$

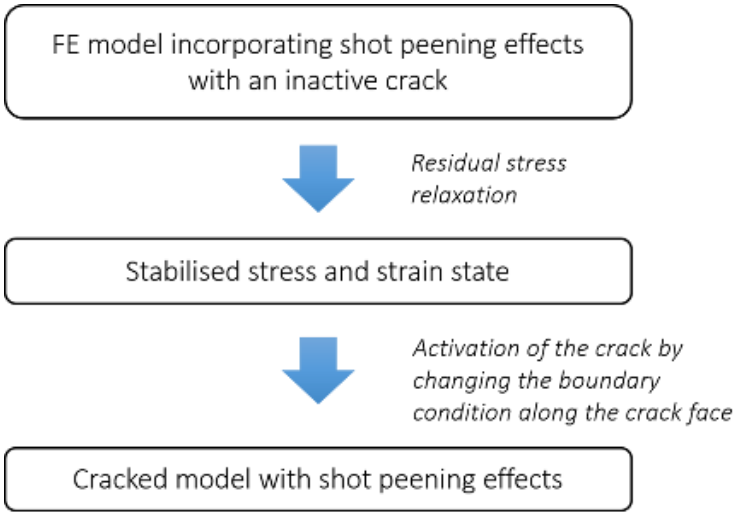

Figure 6-6: Procedure of introducing a crack into the shot-peening-affected area.

6.4 Modelling results and discussions

6.4.1 The effects of compressive residual stress and strain hardening on crack growth

The calculated crack driving force (ΔK_{eff} in LEFM and ΔK_{p_eff} in EPFM) for cracks in the un-peened, T0 and T1 conditions are shown in Figure 6-7; the effects of varying loading levels ($\Delta\varepsilon_{xx}$ = 0.57%, 0.69% and 0.81%) have been investigated. As illustrated in Figure 6-7, both the LEFM and EPFM approaches show similar results in terms of the trend of the data; compared with the un-peened condition, the crack driving force is reduced by shot peening by varying degrees depending on the peening intensity and the loading level.

Figure 6-7(a) and (b) demonstrate the results obtained at $\Delta\varepsilon_{xx}$ = 0.57% using the LEFM and EPFM approaches respectively. Compared with the un-peened condition, it can be seen that the T0 process significantly reduces the crack driving force. The T1 process also maintains noticeable beneficial effects at this loading level, although less benefit is observed than with the T0 process. When the loading level is increased to $\Delta\varepsilon_{xx}$ = 0.69%, the benefits of the T1 process in reducing the crack driving force are significantly reduced, although the T0 process still provides noticeable benefits, as shown in Figure 6-7(c) and (d). At the highest loading level (i.e. $\Delta\varepsilon_{xx}$ = 0.81%), the effects of the T1 process completely disappear and the T0 process only provides very limited benefits compared with at the lower loading levels. The discrepancy between the effects of the T0 and T1 processes can be explained by the predicted stabilised residual stress state shown in Figure 6-8, which illustrates that greater levels of compressive residual stresses are retained in the T0 condition than the T1 condition, especially at high loading levels where external loads tend to eliminate the effects resulting from the T1 process. The results of this numerical analysis are consistent with the observed trend in fatigue life difference between the ground and shot-peened specimens shown in Figure 6-1; the improvement of the fatigue life of the ground specimen by both T0 and T1 processes gradually decreases with increasing loading levels, especially the T1 process whose benefits in improving fatigue life are comparatively less significant than the T0 process and become very limited when $\Delta\varepsilon_{xx} > 0.65\%$.

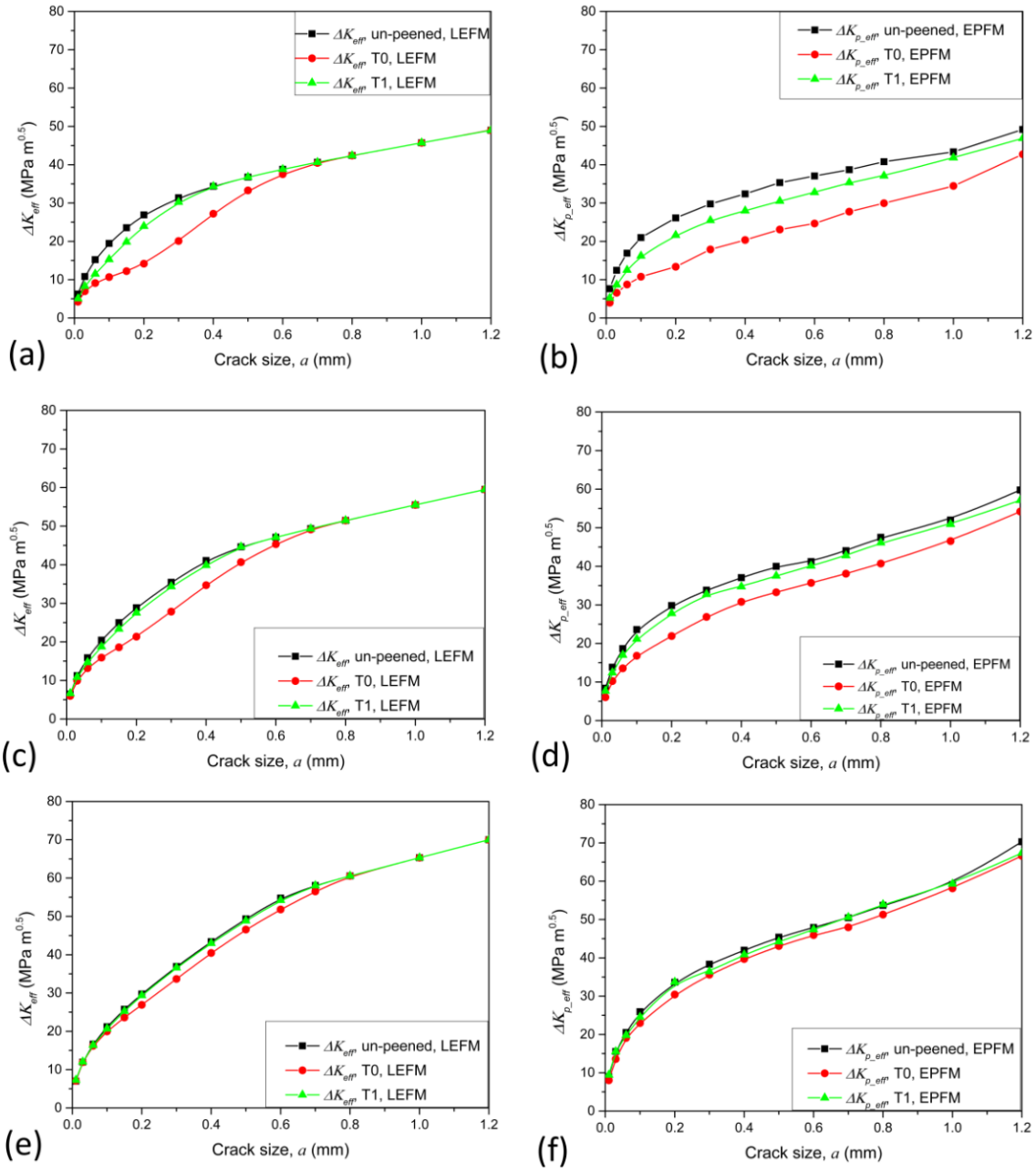

Figure 6-7: The comparison between the un-peened and shot peening conditions (T0 and T1) in the calculated ΔK_{eff} (or ΔK_{p_eff}) for different crack lengths under varying loading levels: (a)(b) $\Delta\varepsilon_{xx}$ = 0.57%, (c)(d) $\Delta\varepsilon_{xx}$ = 0.69% and (e)(f) $\Delta\varepsilon_{xx}$ = 0.81%, using both the (a)(c)(e) LEFM and (b)(d)(f) EPFM approaches.

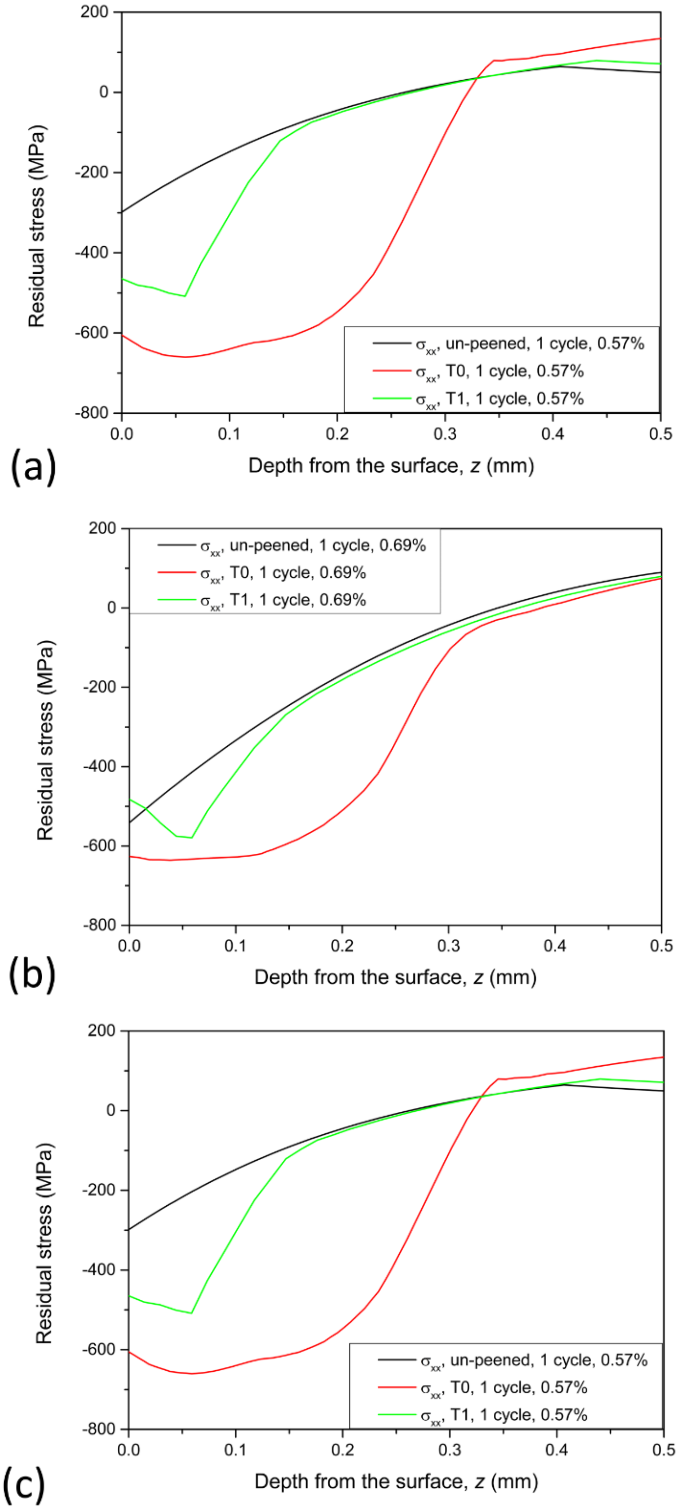

Figure 6-8: Comparison between the predicted stabilised residual stress distributions in the un-peened, T1 and T0 shot-peened specimens using the 2D FE model: (a) $\Delta\varepsilon_{xx}$ = 0.57%, (b) $\Delta\varepsilon_{xx}$ = 0.69% and (c) $\Delta\varepsilon_{xx}$ = 0.81%.

It is noteworthy that the effects of shot peening illustrated in Figure 6-7 result from the combined influence of strain hardening and compressive residual stresses caused by the shot peening process. It is easily intuitive to understand that the compressive residual stress tends to hinder both the crack initiation and propagation processes by counteracting the tensile stress exerted by external loads. Nevertheless, the mechanism of the effects of strain hardening are more complex to understand, as discussed in Section 2.2.3. In the current study, to improve the understanding of the influence of shot peening on crack growth, the effects of compressive residual stresses and strain hardening have been investigated individually in the FE modelling work. To achieve this, the approaches of modelling the strain hardening and compressive residual stress effects (as introduced in Section 6.3.1) have been applied separately in two FE models. The corresponding crack driving forces were calculated respectively using the EPFM approach. The modelling results for the T0 shot peening condition under $\Delta\varepsilon_{xx}$ = 0.69% are shown in Figure 6-9 as an example and consistently similar trends were also found for other shot peening or loading conditions in the current study. It can be seen that the compressive residual stress makes a significant contribution to the beneficial effects of shot peening in decelerating crack propagation, which reinforces the current commonly held understanding. Conversely, strain hardening increases the crack driving force compared with the un-peened condition. This is reasonable in a load-controlled bending test since the stress level in the strain-hardened layer is increased (as shown in Figure 6-10(a)) due to the increased yield strength of the material, which may result in higher energy release rate when the crack propagates through this layer. In addition, the effects of strain hardening on crack initiation were also investigated by predicting the plastic strain (ε_{p_xx}) distribution at the peak load using the 'un-cracked' FE model. As illustrated in Figure 6-10(b), the ε_{p_xx} distribution at the notch root is reduced by the strain hardening effects although the stress level has been increased (as shown in Figure 6-10(a)), implying a hindered crack initiation process.

6.4.2 Life prediction

When evaluating the fatigue life of shot-peened specimens, the influence of shot peening on crack growth has to be explicitly taken into account in order to ensure the accuracy of the life prediction results. In the current study, the numerical results elaborated in Section 6.4.1 have been applied in life prediction procedures used for the shot-peened samples.

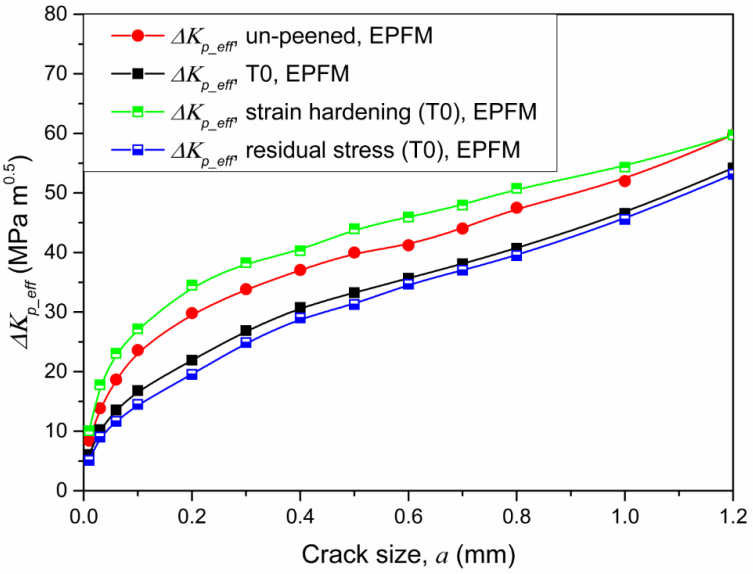

Figure 6-9: Relative importance of the strain hardening and residual stress effects caused by the T0 shot peening process on ΔK_{p_eff} at $\Delta\varepsilon_{xx}$ = 0.69%.

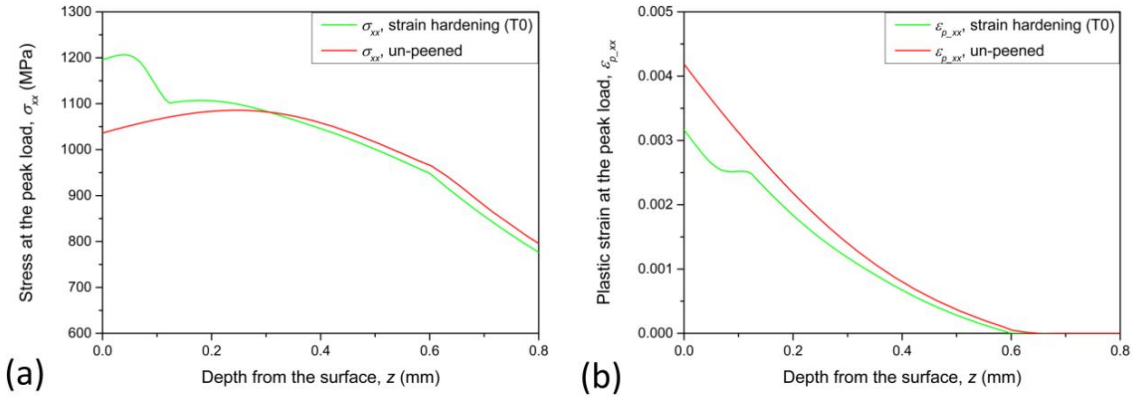

Figure 6-10: Comparison in the predicted longitudinal (a) stress (σ_{xx}) and (b) plastic strain (ε_{p_xx}) distribution at the notch root between the un-peened and strain hardening (T0) condition at the peak load of $\Delta\varepsilon_{xx}$ = 0.69%.

The crack growth rates (da/dN) in the ground, T0 and T1 shot-peened conditions have been characterised based on the calculated ΔK_{app}, ΔK_{eff} and ΔK_{p_eff}. The results are shown in Figure 6-11(a), (b) and (c) respectively along with the Paris law for the material under investigation (i.e. FV448); the Paris law was determined as $C = 1.66 \times 10^{-9}$ mm cycle^{-1} with the upper and lower limit of $6.74 \times 10^{-10} < C < 4.1543 \times 10^{-9}$ mm cycle^{-1} and m = 3.3 [10]. The data shown in Figure 6-11 are quite scattered which is a typical feature of short crack data. It is interesting to note that the data for the ground, T1 and T0 shot-peened samples form a more merged scatter band considering the shot peening effects using ΔK_{eff} or ΔK_{p_eff} (compared to the data

obtained when plotted in terms of ΔK_{app} calculated from global loading assumption), and on the whole, now better follow the trend determined by the Paris law in spite of the scatter of the data. This indicates the possibility of extending the application of the Paris law to the short crack regime in the shot-peened condition. It is noted that the d*a*/d*N* values were determined according to Figure 6-3, where the crack length (*a*) data were not directly measured, but were predicted based on the tracked surface crack growth data, due to the lack of reliable quantitative experimental data describing crack propagation into the bulk of the material. This may introduce some errors to the obtained d*a*/d*N*.

In the current study, the crack propagation life of the shot-peened samples have been predicted using the Paris law in combination with the modelling results regarding the crack driving force shown in Figure 6-7. The initial crack size, a_0, was assumed to be 0.005 mm. The critical crack length, a_c, was estimated to be within the range of 0.8 - 1.2 mm depending on the specific loading level, by equalising K_{eff} (or K_{p_eff}) to the K_{IC} ($55.3\ \mathrm{MPa\ m^{0.5}}$) of FV448. The predicted crack growth behaviour at $\Delta\varepsilon_{xx}$ = 0.69% in the ground, T0 and T1 conditions are shown in Figure 6-12 in comparison with experimental results. It can be seen that although there is a difference between experimental and predicted results, both LEFM and EPFM approaches successfully predict more significantly retarded short crack growth behaviour due to the T0 process than the T1 process. This work has been carried out for different $\Delta\varepsilon_{xx}$ levels. The resultant life prediction results are shown in Figure 6-13, illustrating that the experimentally-observed difference in fatigue life between samples with different surface treatments is successfully predicted.

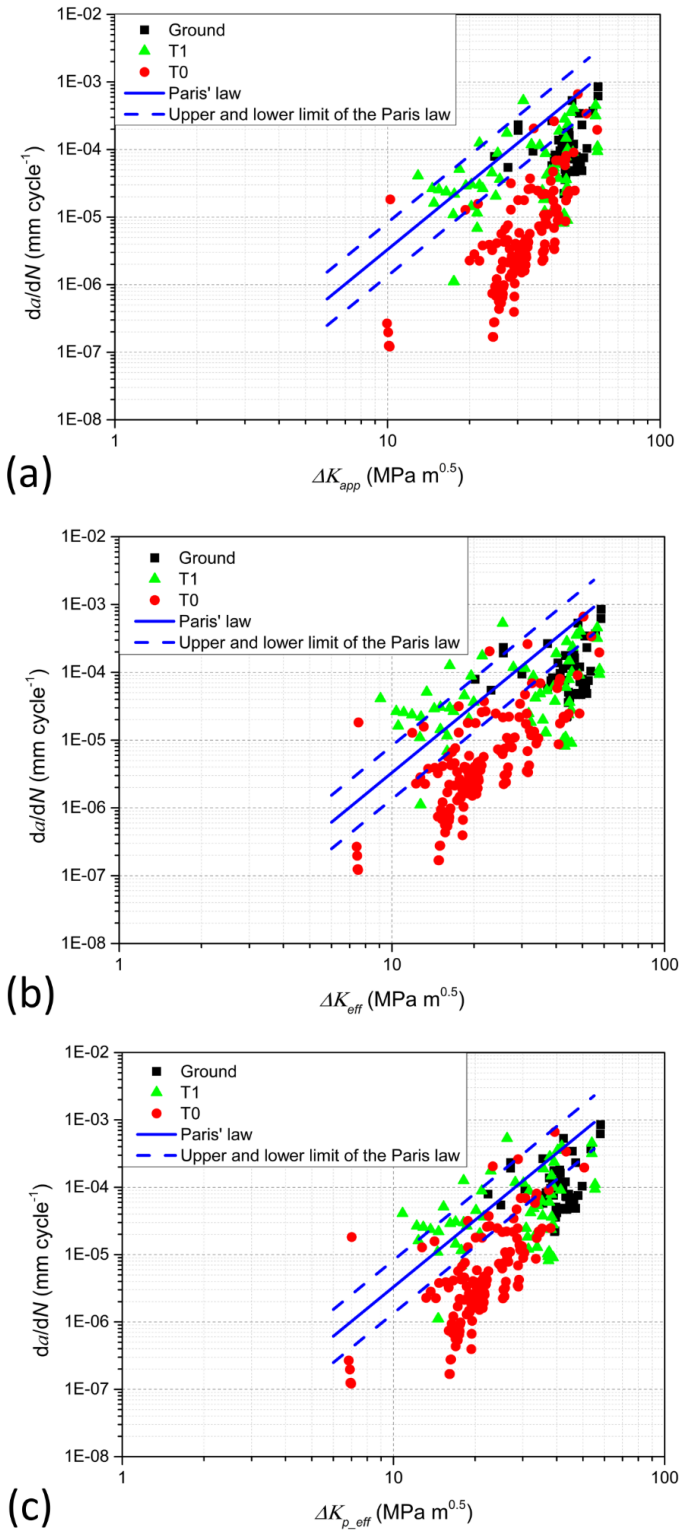

Figure 6-11: Plot of the crack growth rate (da/dN) using the (a) ΔK_{app}, (b) ΔK_{eff} and (c) ΔK_{p_eff}.

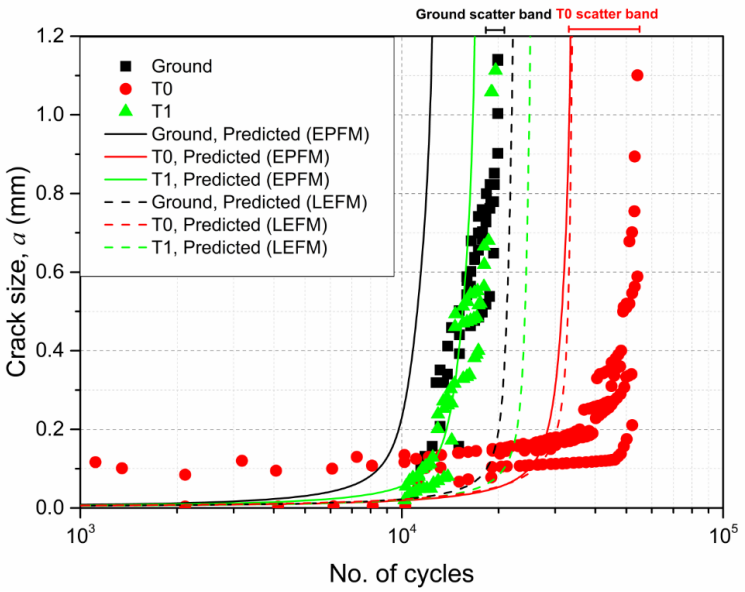

Figure 6-12: Comparison between the experimental and predicted crack growth behaviour in the ground, T0 and T1 conditions at $\Delta\varepsilon_{xx}$ = 0.69%.

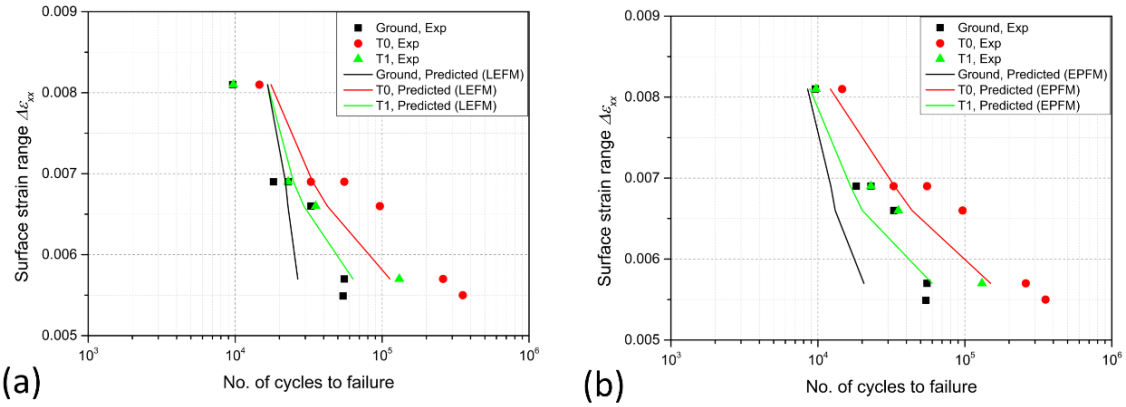

Figure 6-13: Comparison between the experimental and predicted fatigue lives using (a) LEFM and (b) EPFM approaches.

The errors of this life prediction are illustrated in Figure 6-14 along with an investigation regarding the effects of a_0 (a_0 = 0.005, 0.01 and 0.02 mm) on the predicted life. Again, both the LEFM and EPFM approaches have been applied and the results for the T0 and T1 conditions are shown in Figure 6-14(a)(b) and Figure 6-14(c)(d) respectively. According to Figure 6-14, as expected, smaller a_0 results in a longer fatigue life at each loading level, and compared with the experimental results, most of the predicted results in the LCF regime ($N_f < 10^5$) are within the factor of two error range regardless of the chosen a_0, demonstrating the life prediction can take account of these varying (realistic) initial defect sizes whilst still producing comparable lifetimes to those observed

experimentally. However, it is noteworthy that LEFM tends to result in non-conservative fatigue lives when $\Delta\varepsilon_{xx}$ > 0.69%, which is a clear drawback. It can also be seen that compared with the experimentally determined fatigue lives, the model tends to underestimate the lifetimes around 10^5 cycles or more (the medium- to high-cycle fatigue regime). This underestimation may be attributed to the crack initiation process which was not taken into account in the lifing procedure: At higher loading levels, cracks are expected to appear in the early stages of fatigue life at surface (or near surface) stress concentration sites, such as inclusions or surface imperfections introduced by shot peening, especially in the notched area [90, 96, 150, 154]. Hence the LCF life is dominated by crack propagation so that ignoring crack initiation can still result in acceptable life prediction results. However, with decreasing loading levels and prolonged fatigue lives, crack initiation gradually takes a greater proportion of the total fatigue life, therefore, ignoring the initiation stage will result in underestimation of the fatigue life. In addition, it is noted that the fatigue life data are expected to exhibit intrinsic scatter which was not considered in Figure 6-14 due to the limitations of the available experimental data (i.e. only one experimental fatigue life data point was considered for each loading level).

Additionally, as illustrated in Figure 6-15, both EPFM and LEFM approaches are compared with the total life approaches presented in Chapter 5. The predicted fatigue life data using both the SWT and FS criteria combined with the critical distance method are used in this comparison. The prediction results obtained using LEFM and EPFM are based on the assumption that a_0 = 0.005 mm. As illustrated in Figure 6-15, in spite of a good consistency between the life prediction results obtained using the damage tolerant and total life approaches, the former approach tends to predict a shorter fatigue life than the latter, apart from some LEFM predictions which are less reliable (which will be explained in the following section). It can be also seen that this difference between the two types of lifing approaches tends to become more evident at longer fatigue lives, which is unsurprising due to the ignorance of the crack initiation life in damage tolerant approaches as discussed in the preceding paragraph. This comparison reasonably demonstrates the relative agreement and divergence between the damage tolerant and total life approaches. It to some degree justifies the assumptions that have been applied to both approaches in this project, on the other hand, it also implies the limitation of the damage tolerant approach when the HCF life needs to be predicted.

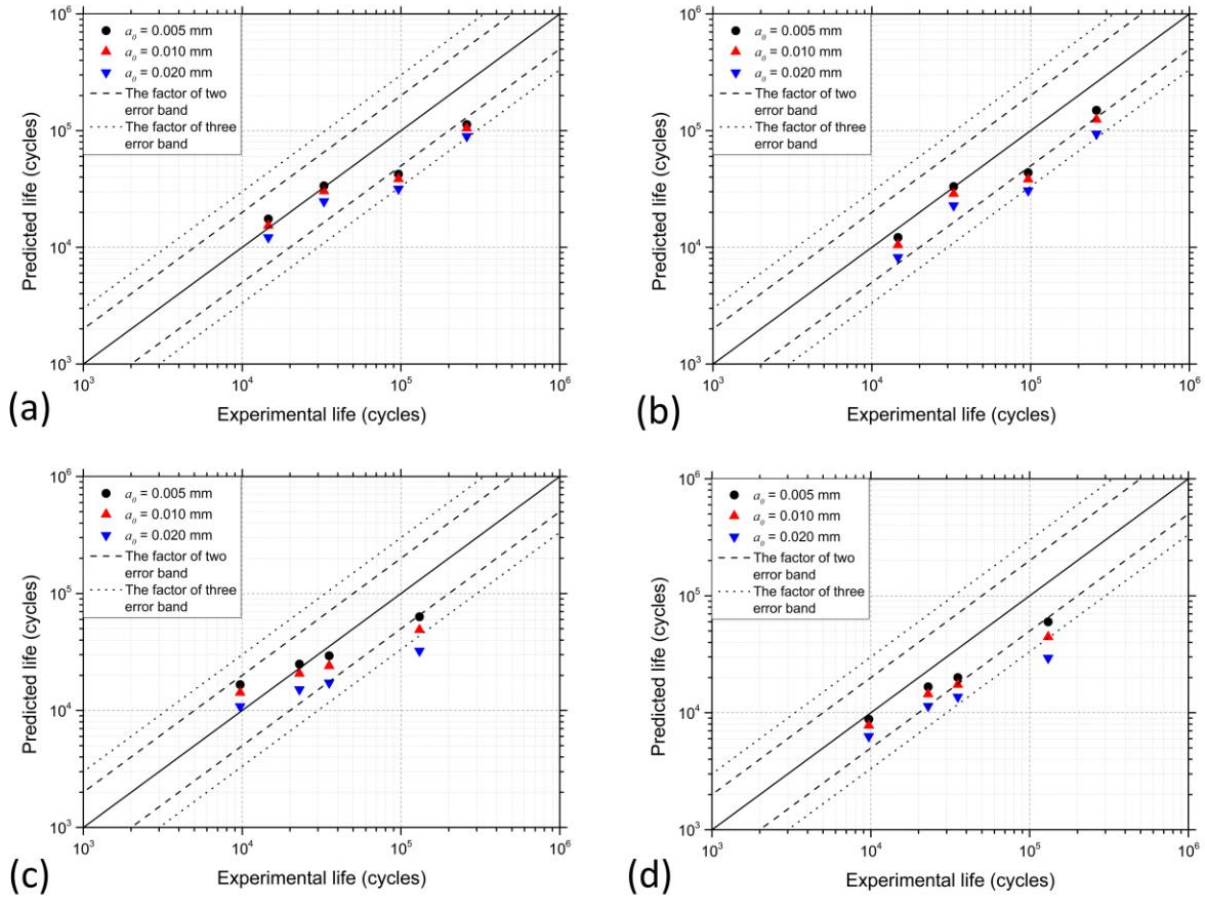

Figure 6-14: Comparison between the experimental and predicted fatigue lives of the T0 shot-peened samples using (a) LEFM and (b) EPFM, and of the T1 shot-peened samples using (c) LEFM and (d) EPFM.

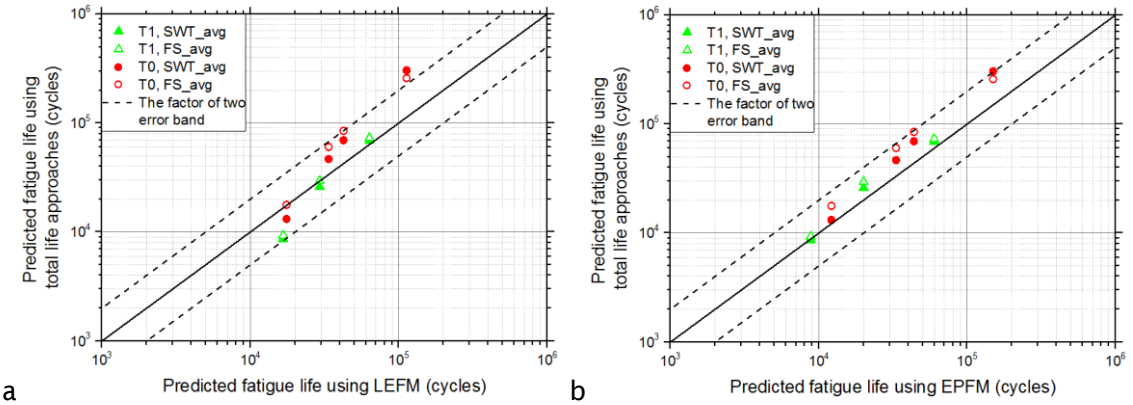

Figure 6-15: Comparison between the (a) LEFM, (b) EPFM approaches with total life approaches (SWT and FS): the suffix '_avg' in the caption indicates that the averaged SWT and FS parameters based on the critical distance method are used here.

6.4.3 Recommendations for application

As discussed in Section 6.4.2, similar but diverse results have been obtained using the LEFM and EPFM approaches, with the main difference observed at high loading levels. The two approaches are directly compared in this section in order to assess their relative merits. In Figure 6-16, K_{p_max} and K_{max} for cracks in the T0 condition at the peak load of $\Delta\varepsilon_{xx}$ = 0.81% and 0.57% are compared. It shows that at $\Delta\varepsilon_{xx}$ = 0.81%, K_{p_max} is 10 – 20% higher than K_{max} when a < 0.5 mm. This implies that the assumption of LEFM is likely to be invalid for short cracks at this loading level, where the plastic deformation around the crack tip cannot be ignored, although compressive residual stresses have been introduced by shot peening to counteract the external tensile stress. Since the major crack growth life is normally spent in short crack growth, the underestimation of the crack driving force by LEFM at such high loading levels accounts for the consequent non-conservative life prediction (as shown in Figure 6-13 and Figure 6-14). By contrast, when $\Delta\varepsilon_{xx}$ decreases to 0.57%, the difference between K_{p_max} and K_{max} becomes negligible (as shown in Figure 6-16), demonstrating the consistency between LEFM and EPFM at low loading levels. A similar situation has also been obtained in the un-peened and T1 shot peening conditions. Therefore, it can be concluded that EPFM is more reliable than LEFM in the LCF regime. But in the medium- to high-cycle fatigue regime, the consistency between LEFM and EPFM approaches can be ensured. Under such circumstances, the LEFM approach is deemed more advantageous than the EPFM approach in facilitating the lifing procedure, because the value of K can be conveniently determined using the weight function method without complex crack modelling.

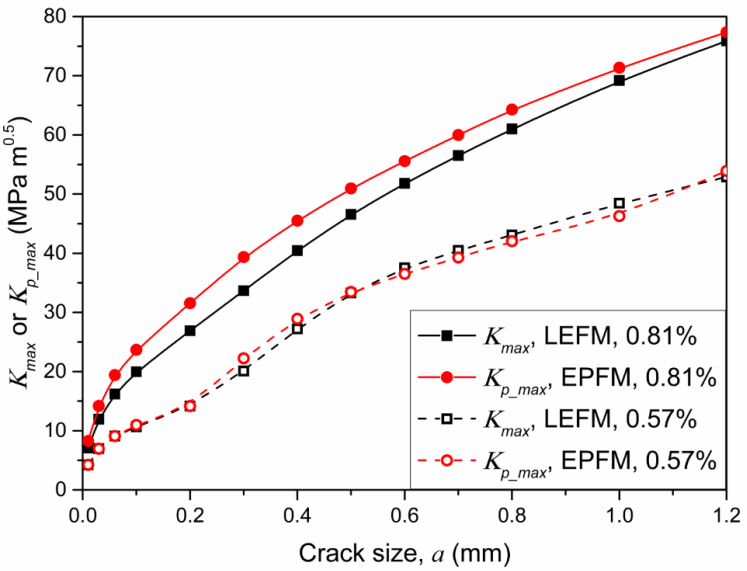

Figure 6-16: Comparison between the LEFM and EPFM approaches in the T0 shot peening condition at $\Delta\varepsilon_{xx}$ = 0.81% and 0.57% for varying crack sizes.

Although the developed 2D FE model has been demonstrated to be effective and efficient in assessing the effects of strain hardening and residual stress (with associated redistribution during cyclic loading), it still has some limitations which require cautious consideration in future work. One is that due to the applied 2D plane strain assumption (corresponding to a through-thickness crack), the crack shape evolution, which was found significantly affected by shot peening [82], was not considered in this study. This might lead to less accurate evaluation of *K* [196], thus affecting the life prediction results. Another limitation is that the microstructure of the material, which might significantly influence microstructurally short crack growth, was not taken into account in the developed model. This was limited by the employed material model, which only represented the macroscopic mechanical properties of the material. Solutions to these limitations may involve development of more robust (but also more complex) models, such as FE models containing 3D cracks describing the real crack shape, and crystal plasticity materials model including microstructural features.

6.5 Conclusion

This chapter introduces a methodology to explicitly consider the shot peening effects in a lifing procedure, using both LEFM and EPFM approaches. The following major conclusions of this chapter have been demonstrated.

- A 2D eigenstrain-based finite element model has been developed to reasonably predict the residual stress relaxation behaviour in safety-critical shot-peened regions, considering the effects of compressive residual stresses and strain hardening caused by shot peening.
- The effects of shot peening on crack driving force have been investigated using LEFM and EPFM approaches; the weight function method was applied to calculate the stress intensity factor (K) for the LEFM approach; the J-integral obtained using the 2D crack modelling was used to determine the equivalent stress intensity factor (K_p) for the EPFM approach. It was found that shot peening improved fatigue life mainly by retarding the short crack growth process within the shot-peening-affected layer. The compressive residual stress caused by shot peening made the main contribution to this benefit by reducing the effective crack driving force, as a result of crack closure. However, strain hardening caused by shot peening (when considered explicitly and separately) was found to increase the crack driving force in this study, so is expected to lead to an accelerated crack propagation process. Conversely, the plastic deformation in the shot-peening-affected layer (before cracks appeared) was reduced by the strain hardening effects, implying a hindered crack initiation process.

- Fatigue life prediction has been carried out for the shot-peened notched specimens. The short crack growth behaviour in the shot-peened samples has been successfully correlated to the baseline long crack growth data (i.e. the Paris law) by taking crack closure induced by the compressive residual stress into account. Acceptable life prediction has been achieved using the EPFM approach, especially in the LCF regime where crack propagation played a more important role than crack initiation.
- The LEFM approach tends to result in non-conservative life predictions if it is applied in the LCF regime, which requires cautious consideration in application. In the HCF regime, a good consistency between the LEFM and EPFM approaches was demonstrated.
- A good consistency between the damage tolerant approaches and the total life approaches in life prediction for the shot-peened notched samples has been demonstrated. The damage tolerant approaches tend to predict a shorter fatigue life due to its disregard of any crack initiation life.

7 Fatigue life prediction using damage tolerant approaches: 3D crack modelling

7.1 Introduction

In this chapter, 3D crack modelling work, which builds upon the advantages of the 2D model introduced in Chapter 6, is introduced. The developed 3D FE model containing a semi-elliptical crack has been used to first numerically investigate the residual stress redistribution caused by both mechanical loading and the presence of a crack. Then the developed model was used to predict the differences in crack shape evolution between varying surface conditions, and to quantify the retardation of short crack growth resulting from shot peening, allowing for the influences arising from crack shape evolution. Finally, the 3D model was compared with the 2D plane strain model to demonstrate the limitations of the 2D model in simulating the crack growth behaviour, and to emphasise the importance of taking the 3D crack shape into account when evaluating the short crack growth behaviour.

This chapter is largely based on the following paper:

You, C., He, B., Achintha, M., & Reed, P. (2017). *Numerical modelling of the fatigue crack shape evolution in a shot-peened steam turbine material*. International Journal of Fatigue. 104, 120-135.

7.2 Experimental techniques and results

In addition to the experimental results presented in Section 6.2, the evolution of crack shape at $\Delta\varepsilon_{xx}$ = 0.69% has also been systematically determined by He et al. [82], based on experimental observations in a number of notched samples. Details regarding the experimental methodologies are published in [82]. The crack aspect ratio, which was used as a representation of the crack shape, was defined as *a/c*, where *a* was the depth of the crack and *c* was half the surface crack length, as illustrated in Figure 7-1. Relevant experimental results reported in [82] are reproduced in Figure 7-2, showing that cracks initiated with a relatively high *a/c* (*a/c* = 1.2) in polished samples compared with the T0 condition, whereas much shallower cracks (*a/c* = 0.2) were observed at the very beginning. In the T1 condition, both crack initiation aspect ratios were observed. This difference found between different surface conditions can be shown by Figure 7-3, which shows the morphology of some initial cracks obtained using a scanning electron microscope (SEM) on the fracture surface [16, 82]. As can be seen in Figure 7-3(a), a

typical feature in the polished condition is that the inclusions distributed normal to the notch root surface seem to facilitate crack initiation in the depth direction, resulting in high initial *a/c*. While in the T0 condition shown in Figure 7-3(b), there is no clear evidence of the effects of inclusions, which are likely to be overwhelmed by the CRS induced by the T0 shot peening. Thus, cracks initiated from high stress concentration areas caused by surface roughness or crack-like surface defects lying at the bottom of the peened dimples, resulting in low initial *a/c*. In the T1 condition, as can be seen in Figure 7-3(c)(d), the effects of inclusions were not completely eliminated due to the low peening intensity, which accounted for the mixed crack initiation mechanism (both modes were observed). In Figure 7-2, data for all three surface conditions begin to merge at a = 0.1 mm, achieving a stabilised crack shape with a/c = 0.8 – 0.9, apart from some data in the T0 condition where crack coalescence frequently occurred as the cracks grew. According to previous research [197, 198], the crack shape evolution process, despite varying with the initial crack configuration, tends to develop asymptotically to a preferred equilibrium state where *a/c* converges to a stable range. This is consistent with the general trend of the experimental data shown in Figure 7-2 (apart from the data resulting from crack coalescence). However, the mechanism behind the experimental observations in terms of the shot peening effects is still less clear, although an intensive discussion is given in [82].

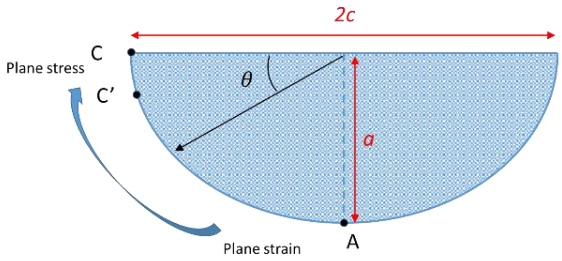

Figure 7-1: Schematic diagram showing the definition of the crack aspect ratio (*a/c*) based on surface crack length (2*c*) and the depth of the crack (*a*).

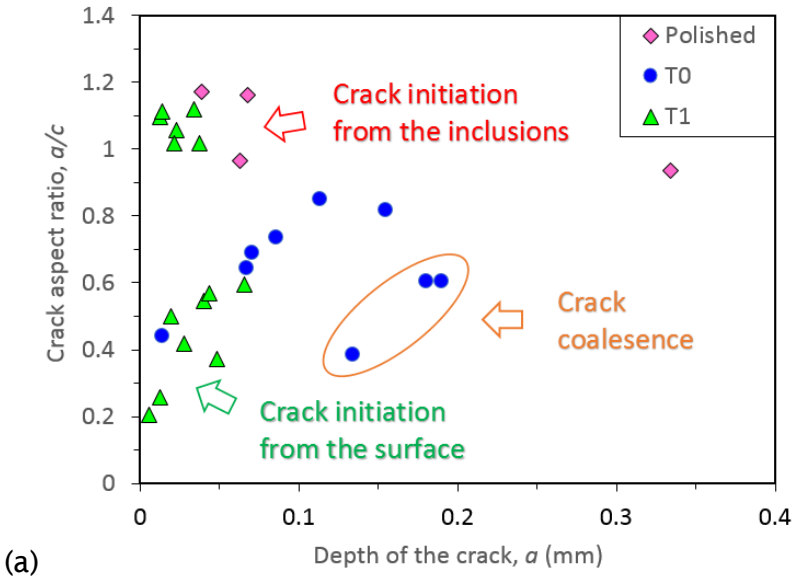

(a)

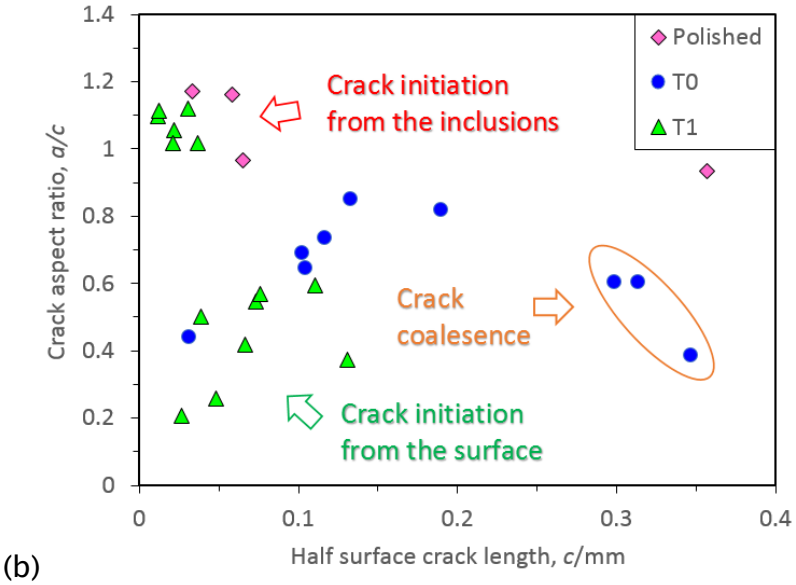

(b)

Figure 7-2: Crack aspect ratio *a/c* based on the fatigue crack morphology on fracture surface in polished, T0 and T1 conditions: (a) *a/c* vs *a* and (b) *a/c* vs *c* [82].

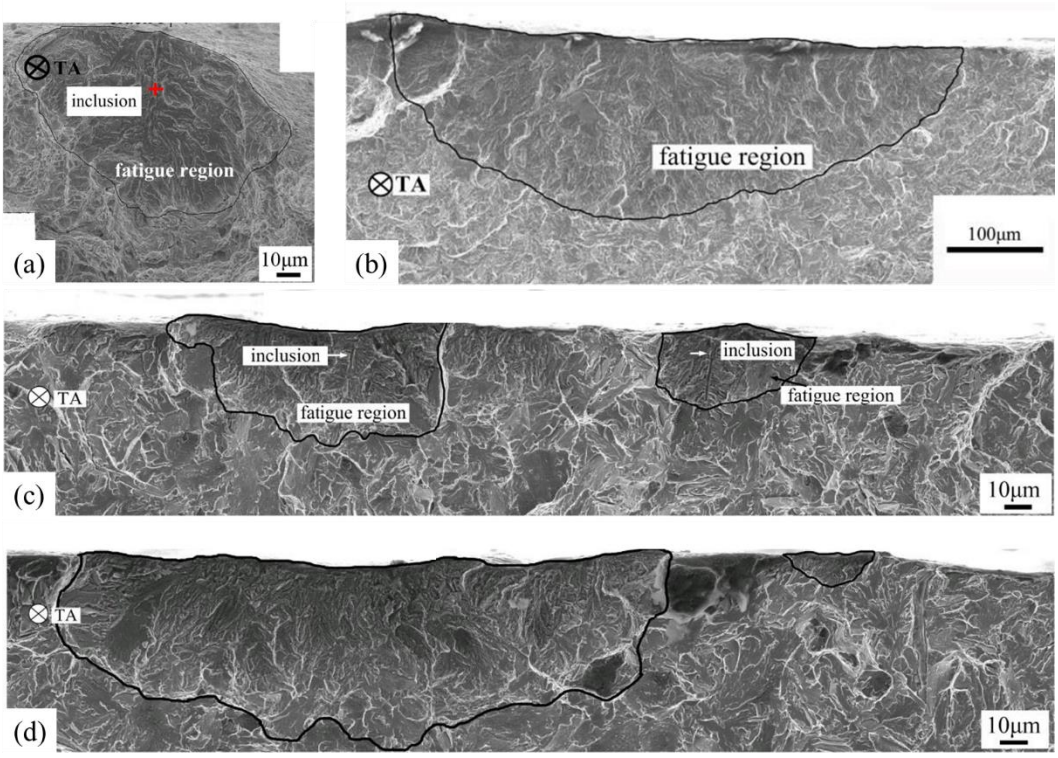

Figure 7-3: SEM micrographs of cracks with labelling in the (a) polished, (b) T0 and (c)(d) T1 shot peening conditions, demonstrating the crack initiation mechanism (a)(c) with and (b)(d) without the effects of inclusions [16, 82].

7.3 3D crack modelling

Figure 7-2 demonstrates a significant discrepancy between the short crack shape evolution in polished and shot-peened notched samples, which was closely related to the shot peening process and the microstructure of the material. This suggests the necessity of taking the crack shape effects into account when evaluating the influence exerted by shot peening on short crack growth, which was not considered in the 2D crack modelling work (Chapter 6). Hence, the current study utilised a 3D FE model containing a semi-elliptical crack to investigate how shot peening affects crack shape evolution, and how significant it is in life assessment. The loading level selected in this section was $\Delta\varepsilon_{xx} = 0.69\%$, which was consistent with the 2D crack modelling work and the condition where short crack tests were carried out. Both the crack size and crack shape evolution have been reasonably well predicted based on the modelling results.

The 3D FE model introduced in Chapters 3 and 4 has been upgraded to study the short crack growth behaviour affected by shot peening. Owing to symmetry, a quarter of the 4.5×1.25 notched sample (Figure 3-13(b)) has been modelled by applying adequate symmetry boundary conditions. In order to be less time consuming, the complete model

consisted of an intensely-meshed region near the notch root and a coarsely-meshed part for the rest of the geometry. A semi-elliptical crack has been introduced into the intensely-meshed region, as illustrated in Figure 7-4. A surface-to-surface tie constraint was applied to the interface between the coarsely- and intensely-meshed parts to ensure the consistency of the displacement. To simulate the crack closure under CRS, a similar approach that has been applied in 2D crack modelling (Section 6.3.1) has been chosen: a rigid face was attached along the symmetry plane to prevent the overlap of the crack flanks due to CRS, as shown in Figure 7-4(a). The contact between the crack face (i.e. the yellow-shaded area in Figure 7-4) and the rigid face was assumed to be frictionless since only the mode I crack was considered in this study.

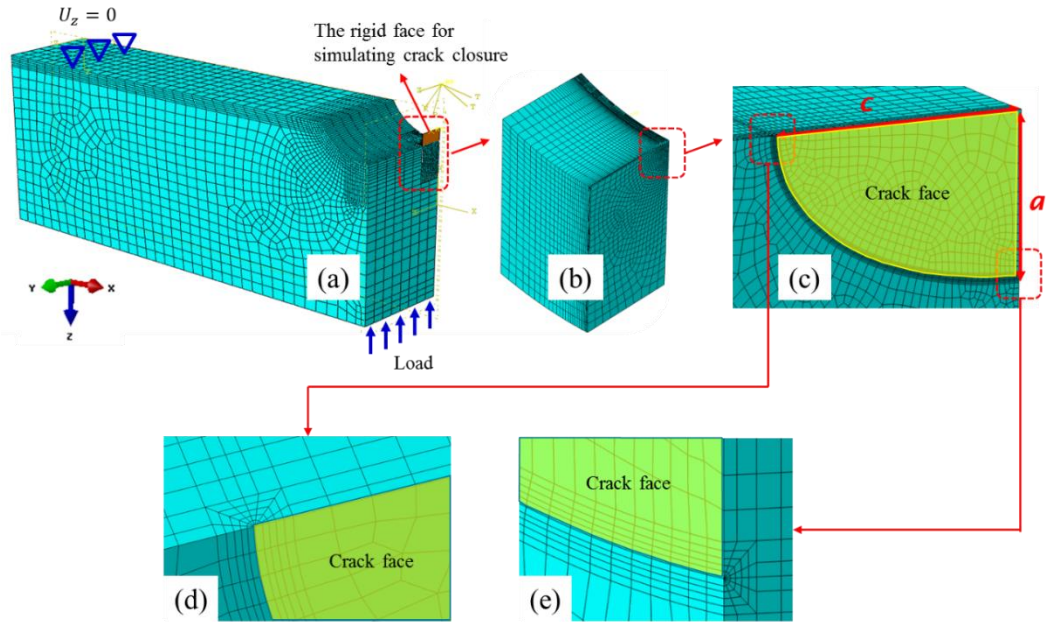

Figure 7-4: Geometry and mesh for the (a) complete model, (b) the intensely-meshed part and (c) the contained crack, with detailed mesh pattern near (d) the surface point and (e) the deepest point of the crack; the crack face is shaded in yellow.

The crack front was meshed using 15-node 3D wedge elements (C3D15) and a spider web mesh pattern was applied around the crack front, as shown in Figure 7-4(d)(e). The rest of the model was meshed using 20-node reduced integration brick elements (C3D20R). A mesh convergence analysis was carried out, according to which a transition of element size from 1 μm along the crack front to 0.1 mm along the edges was implemented in the intensely-meshed region. In the coarsely-meshed region, the global mesh size was chosen to be 0.5 mm, with relatively refined meshes (element size: 0.1 mm) near the top surface, which was deemed sufficient to obtain accurate results without huge computational costs.

The same FE model (without incorporating shot peening effects) has also been used in the present numerical study, representing the baseline polished condition (referred to as the 'un-peened' condition in the modelling work).

7.4 Modelling results and discussions

7.4.1 Residual stress redistribution

Residual stress redistribution can be caused by both mechanical loading and the presence of a crack. In order to separate the residual stress redistribution caused by the two diverse mechanisms, the method applied in the 2D crack model was employed here: The introduced crack was initially deactivated by applying symmetry boundary conditions on the crack face. The crack was then activated by removing the boundary conditions along the crack face after simulating the residual stress relaxation behaviour during the quasi-static loading stage (the first cycle). The simulated quasi-static residual stress relaxation ($\Delta\varepsilon_{xx}$ = 0.69%) in specimens subjected to different surface treatments are summarised in Figure 7-5, which has been discussed in Section 4.4.

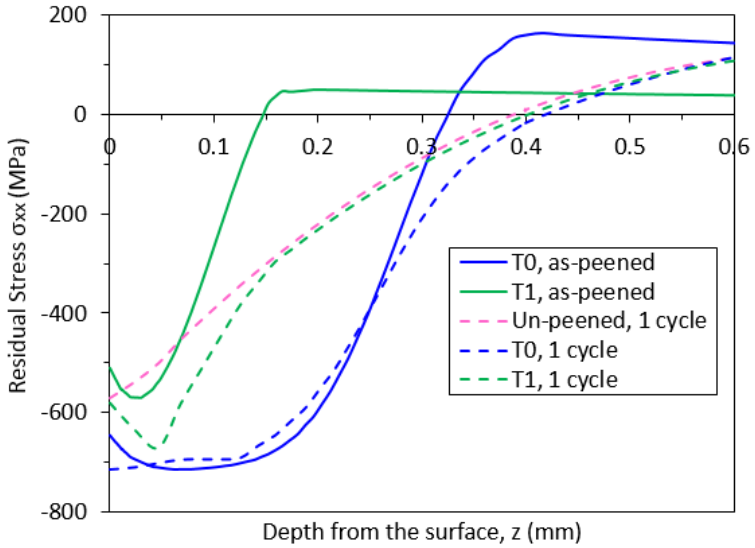

Figure 7-5: FE-predicted residual stress (σ_{xx}) redistribution caused by external loading (one cycle) under $\Delta\varepsilon_{xx}$ = 0.69%.

After activation of the crack, the interaction between the residual stresses and the presence of a crack was investigated by applying an additional loading cycle in the model. Four cracks with varying sizes (a = 0.01, 0.1, 0.2 and 0.4 mm) and with the same a/c (a/c = 0.8) were modelled to elucidate the effects of crack advance on the redistribution of residual stresses.

The modelling results for the un-peened, T0 and T1 shot peening conditions are shown in Figure 7-6(a)(b) and (c) respectively. The residual stress profiles shown in Figure 7-5 are also included in Figure 7-6, as baseline profiles. It can be seen from Figure 7-6 that the crack results in a greater compressive area near the crack front, compared with the baseline profiles. This phenomenon can be attributed to the plastic deformation distributed ahead of the crack front after unloading; in order to accommodate the misfit caused by the plastic deformation, greater constraints are exerted on the plastic zone ahead of the crack front by surrounding elastic material, resulting in more intense CRS. However, in areas further from the crack tip, the residual stress field is relatively stable, being much less affected by the presence of the crack, as long as the crack front is still confined within the main CRS field. This can be more intuitively illustrated by the contour plots on the x-z plane at the notch root for the T0 condition, as shown in Figure 7-7 (similar situations were observed in the un-peened and T1 conditions). This phenomenon is due to the plastic deformation caused by the crack being very localised and unable to significantly remove the overall misfits that are responsible for the original residual stress. This conclusion is consistent with the reported experimental observation using synchrotron X-ray diffraction in a laser shock peened specimen under LCF, which demonstrated the stability of the residual stress distribution before the crack penetrated into the area with tensile residual stresses [97]. Hence, although crack growth was not directly simulated as a continuous process in this study, the predicted residual stress fields related to varying crack lengths were deemed reliable. It is also noteworthy from Figure 7-6 that the size of the crack-affected zone increases when the crack becomes longer; from 0.02 mm at a = 0.01 mm to 0.15 mm at a = 0.4 mm. This can be explained by the broadening size of the plastic zone ahead of the crack front as the crack grows longer.

The effects of different a/c on residual stress redistribution were found to be limited compared with the effects of a. This can be reflected in Figure 7-8, which demonstrates that different a/c (at fixed a) only result in a small variance of the residual stress ahead of the crack front, without significantly affecting the overall residual stress distribution. Hence, the effects of a/c are not further discussed here.

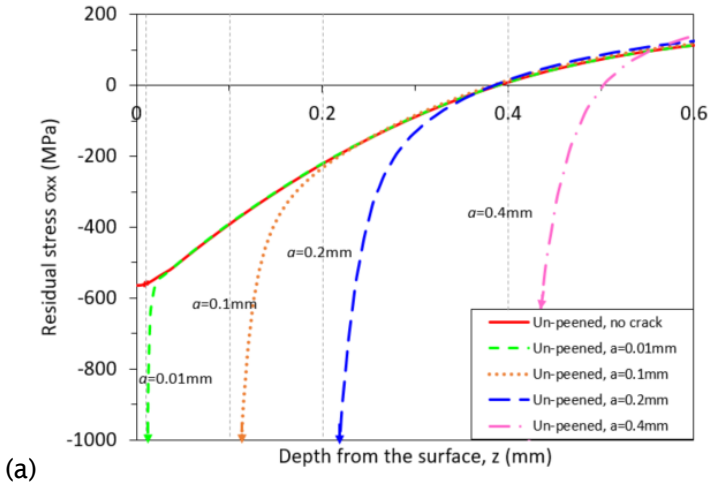

(a)

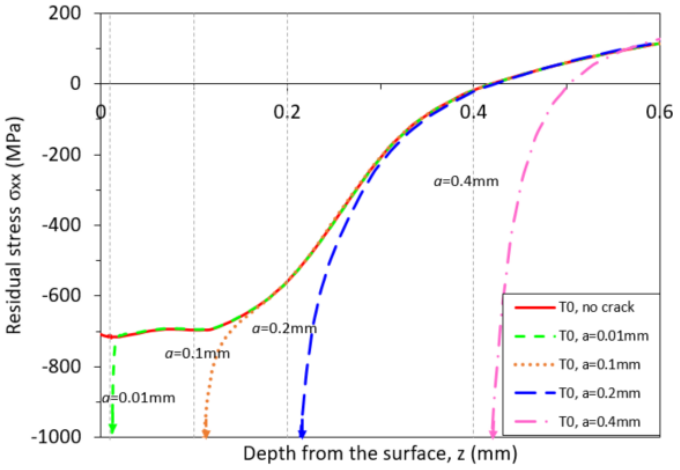

(b)

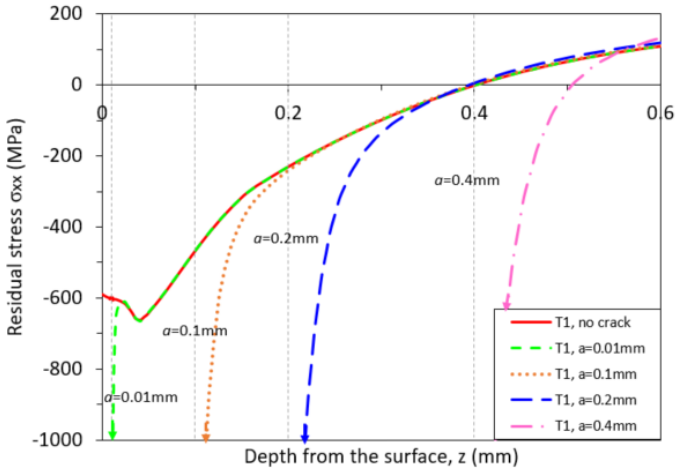

(c)

Figure 7-6: Residual stress (σ_{xx}) redistribution ahead of the crack caused by crack advance (a = 0.01, 0.1, 0.2 and 0.4 mm, a/c = 0.8) in the (a) un-peened, (b) T0 and (c) T1 shot peening conditions.

The results for a = 0.01, 0.1 and 0.4 mm displayed in Figure 7-6 are replotted in Figure 7-9, to examine the range of shot peening effects. When a = 0.01 mm, it can be seen clearly that the main favourable CRS in both the T0 and T1 conditions remains. When the crack grows to a = 0.1 mm, the benefits of the T1 process over the un-peened condition in terms of CRS are completely removed, while the T0 condition still maintains significant benefits until the crack penetrates through the whole CRS field at a = 0.4 mm. This analysis demonstrates that the effects of the T1 process are merely confined within a depth of 0.1 mm. By contrast, the T0 process more effectively delays short crack growth by extending the working depth of the CRS to nearly 0.4 mm.

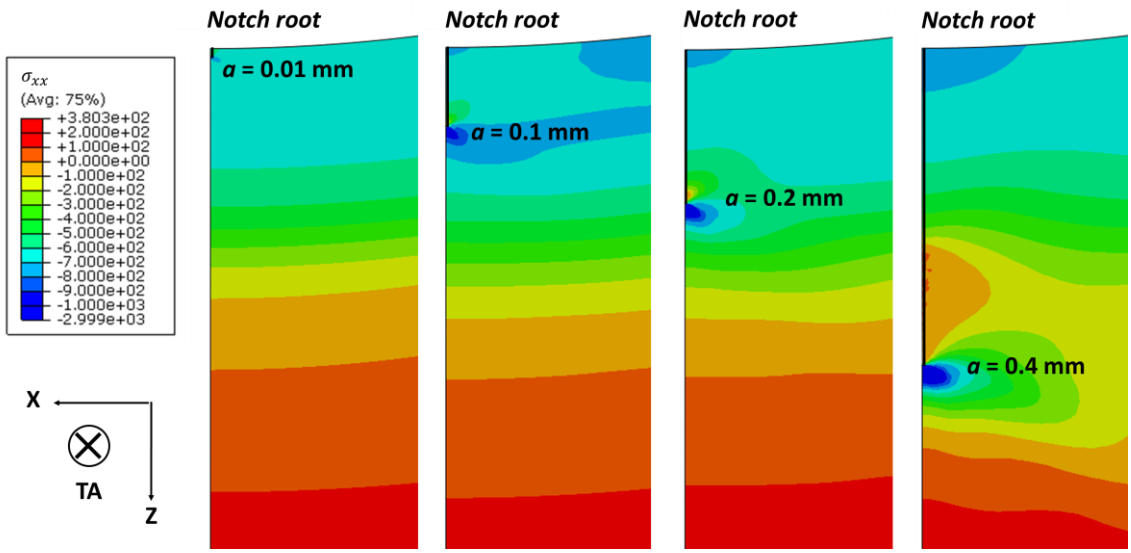

Figure 7-7: Contour plots of the residual stress (σ_{xx}) field in the T0 shot peening condition with crack advancing.

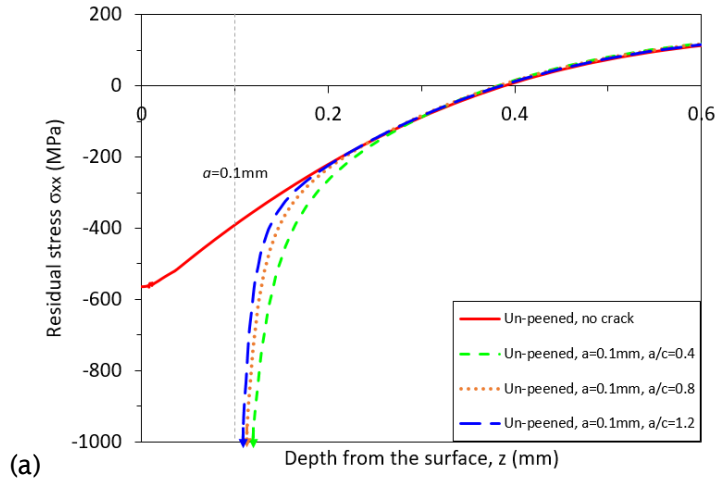

(a)

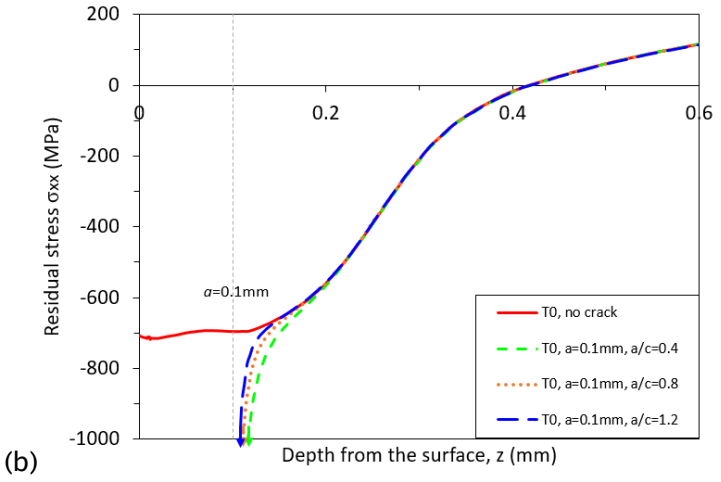

(b)

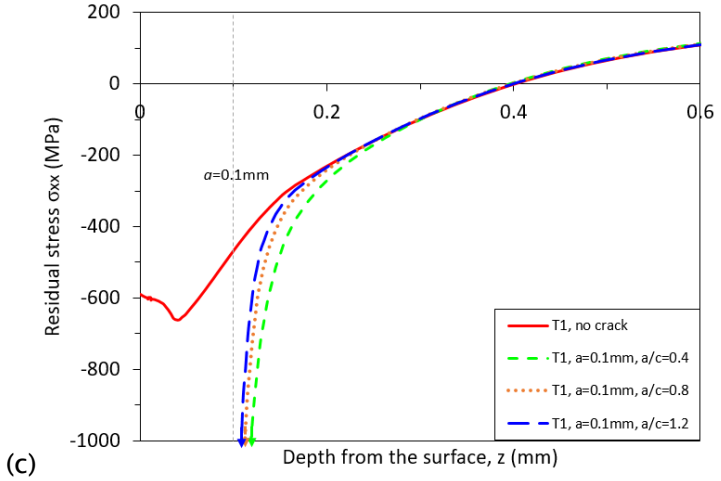

(c)

Figure 7-8: Residual stress (σ_{xx}) redistribution ahead of the crack caused by crack advance (a = 0.1 mm, a/c = 0.4, 0.8 and 1.2) in the (a) un-peened, (b) T0 and (c) T1 shot peening conditions.

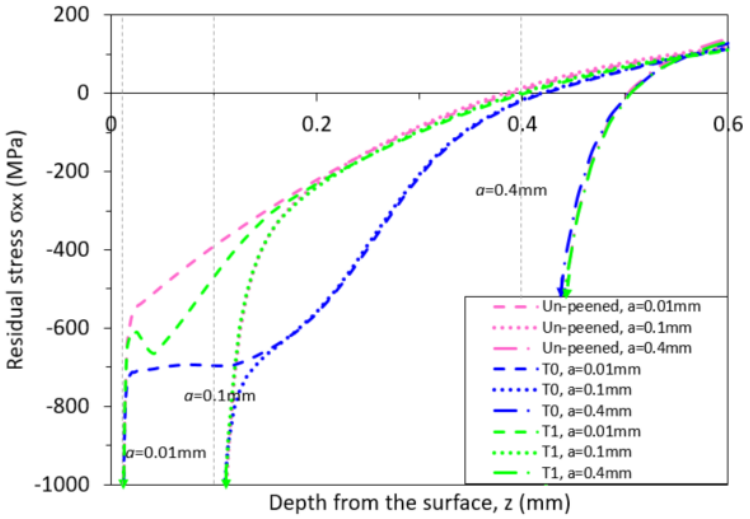

Figure 7-9: Comparison between the residual stress (σ_{xx}) redistribution ahead of the crack caused by crack advance in the un-peened, T0 and T1 shot peening conditions.

7.4.2 Prediction of the crack shape (a/c) evolution

Prediction of the changing position of the crack front during fatigue loading is a key issue in predicting the crack shape evolution. Since the crack shape was assumed to be semi-elliptical in this study, only the position of the surface point and the deepest point on the crack front are required to describe the crack shape. As indicated in Figure 7-1, a transition from the plane stress prevailing condition at the surface point (point C), to the plane strain prevailing condition at the deepest point (point A) generally exists along the crack front, which needs to be considered when evaluating the crack driving force [199-202]. According to the literature, numerical values of the crack driving force at point C should be treated cautiously due to two reasons: Firstly, intersection between the crack front and the free surface tends to result in a change of the power of the stress singularity at point C, where the assumption of the SIF in linear-elastic fracture mechanics (LEFM) is invalid [203-205]; secondly, the plasticity-induced crack closure (PICC) effect is more pronounced at the free surface than in the bulk material due to the plane stress state at the surface, which may reduce the surface crack growth rate and potentially leads to a front-turning-inward phenomenon, hampering accurate characterisation of the crack driving force [200-202, 206, 207]. To overcome this difficulty, a point near the free surface on the crack front (i.e. point C' in Figure 7-1) was selected instead of point C. In contrast to identifying point C' as the first point near the surface, which has been widely used in other modelling [203, 208, 209], in this work the position of point C' was determined with respect to the plastic deformation along the crack front. As illustrated in Figure 7-10, point C' is the transition between two distinct

types of plastic zone: the plastic zone with relatively uniform size in the interior region where plane strain effects dominate, and the larger plastic zone near the surface region, where plane stress effects dominate. Similar plastic zone distributions along the crack front have been obtained in [200, 201], and it was found that the larger plastic zone near the surface reasonably accounted for the PICC phenomenon. Therefore, selecting point C' is expected to simplify the crack modelling work by avoiding complex modelling of PICC of the surface crack. According to the modelling work, the exact position of point C' varied between $3^\circ < \theta < 20^\circ$ depending on the *a/c* of the crack, which was little affected by the residual stress levels under investigation. The error of replacing OC with O'C' (Figure 7-10) was within 5%, regardless of the crack size and shape.

According to the literature, methods applied to predict crack shape evolution can generally be classified into two categories: One is the adaptive remeshing technique [198, 199, 202, 210-212], which realises an automatic update of the mesh around the new crack front extended stepwise from an initially predefined crack. The extension at the points along the crack front during each cycle relies on the local SIF, which can be directly obtained from the FE software. A comprehensive review regarding this technique has recently been published [213]. Another category is the analytical process based on closed-form solutions for SIF, which are usually calibrated using the FE-determined SIFs along the crack front for varying crack shapes and sizes [197, 204, 214]. The similarity between the two categories is that the crack extension during each cycle is commonly predicted using the Paris Law based on local SIF. The main difference is that the cumulative effects during crack growth, such as residual stress redistribution caused by crack advance and the plastic wake left behind the crack front resulting in PICC, can be effectively considered using the remeshing technique, which simulates crack growth as a coherent process. By contrast, the analytical method treats crack growth as numerous separate steps without inheriting additional effects from the previous cycle. In the current case, the stability of the residual stress field with crack advancing has been demonstrated (Section 7.4.1), and the effects of surface PICC (which tends to be much less significant with CRS [153]) have been avoided by using point C' instead of point C. Therefore, the analytical approach based on closed-form solutions is deemed reliable in the current study, and thus has been applied to simplify the modelling process. To achieve this, cracks with a range of sizes and shapes have been defined in the modelling work in the un-peened, T0 and T1 shot peening conditions; a = 0.01, 0.05, 0.1, 0.15, 0.2, 0.3 and 0.4 mm, a/c = 0.2, 0.3, 0.4, 0.6, 0.8, 1.0 and 1.2, the ranges of which were determined to cover the experimental observations shown in Figure 7-2.

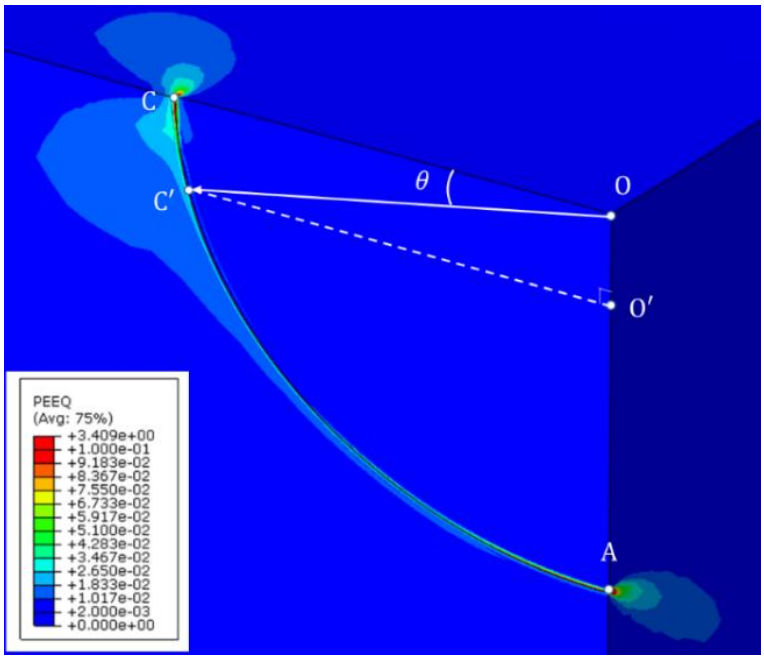

Figure 7-10: Demonstration of the equivalent plastic strain distribution (PEEQ) along the crack front (a = 0.1 mm, a/c = 0.8) in the un-peened condition.

The SIF values at point A and C' were calculated from the J-integral supplied by ABAQUS using the plane strain assumption, as described by Equation 7-1 where E is the Young's modulus and ν is the Poisson's ratio of the material. Although the conventionally defined J-integral becomes path-dependent in the residual stress field, a local path-independence can still be achieved near the crack tip as long as the mesh is fine enough, and the corresponding value of the J-integral can still accurately represent the crack driving force [158, 194, 195]. Based on this idea, the J-integral calculated based on the 6th contour was used in the present study to determine the corresponding SIF. The effective SIF range (ΔK_{eff}) during cyclic loading was used to characterise the crack growth behaviour, as defined by Equation 7-2, where K_{max} and K_{open} represent the SIF at the maximum load and the crack opening load (the moment when the crack is fully opened) respectively. To appropriately determine K_{open}, the crack closure phenomenon caused by CRS was studied in the FE model by monitoring the contact force between the crack face and the rigid face. Figure 7-11 shows that the values of the J-integral are zero at the minimum load due to partial closure of the crack, then slightly increase to a small positive value when the crack is fully opened, before rising up noticeably with increasing load. Hence, K_{open} was approximated as zero in the current modelling work.

$$K = \sqrt{\frac{EJ}{1-\nu^2}} \tag{7-1}$$

$$\Delta K_{eff} = K_{max} - K_{open} \tag{7-2}$$

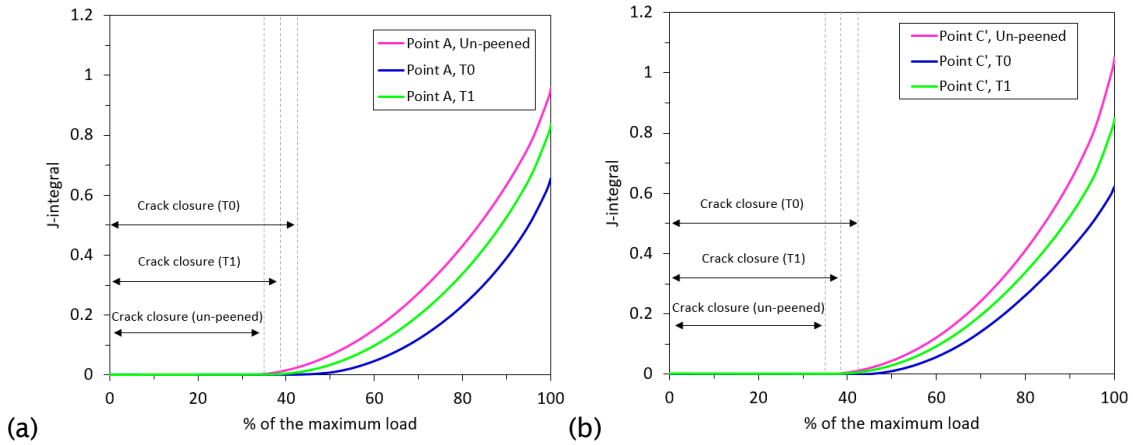

Figure 7-11: J-integral evolution at (a) point A and (b) point C' on the crack front (a = 0.1 mm, a/c = 0.8) with increasing load.

The process of calibrating the closed-form solution, which describes the J-integral value at the maximum load (J_{max}) for cracks with various combination of a and a/c, is expressed by Equations 7-3 – 7-5. This process was implemented for point A and point C' under un-peened, T0 and T1 conditions separately. As the first step, the variation of J_{max} with a was fitted using the polynomial relationship in Equation 7-3 at each fixed a/c, obtaining the corresponding fitting coefficients $B_i (i = 1, 2, 3, 4)$. Then, Equation 7-4 was calibrated to build up the relation between B_i and a/c. Finally, Equation 7-5 was obtained by combining Equations 7-3 and 7-4. The values of the calibrated parameters in Equation 7-5, and the subsequent validation work are shown in Appendix B.

$$J_{max}(a) = B_1 a + B_2 a^2 + B_3 a^3 + B_4 a^4 \tag{7-3}$$

$$B_i\left(\frac{a}{c}\right) = D_{i0} + D_{i1}\frac{a}{c} + D_{i2}\left(\frac{a}{c}\right)^2 + D_{i3}\left(\frac{a}{c}\right)^3 \qquad (i = 1,2,3,4) \tag{7-4}$$

$$J_{max}\left(a, \frac{a}{c}\right) = \sum_{i=1}^{4}\left[D_{i0} + D_{i1}\frac{a}{c} + D_{i2}\left(\frac{a}{c}\right)^2 + D_{i3}\left(\frac{a}{c}\right)^3\right]a^i \qquad (i = 1,2,3,4) \tag{7-5}$$

The growth of the crack in the depth direction and at the surface are described using Equation 7-6 and 7-7 respectively, where ΔK_{eff} ($\Delta K_{eff,A}$ for the crack in the depth direction, $\Delta K_{eff,C}$, for the surface crack) is used instead of ΔK in the Paris Law. The coefficients C and m were determined to be $C = 1.66 \times 10^{-9}$ mm cycle^{-1} and m = 3.3 [10]. The relative difference between crack growth in the two directions is described in Equation 7-8, which was obtained by combining Equations 7-6 and 7-7. Based on Equation 7-8, crack advance at the surface (dc) from a known crack shape was predicted by specifying an appropriate crack advance in the depth direction (da). Then a new crack front was obtained by connecting the updated points A and C' using the semi-elliptical assumption of the crack front. Thus, the crack shape evolution was predicted by

cyclically repeating this process with an initial (pre-defined) crack. Convergent results were obtained at *da* = 0.002 mm.

$$\frac{da}{dN} = C\Delta K_{eff,A}{}^{m} \tag{7-6}$$

$$\frac{dc}{dN} = C\Delta K_{eff,C'}{}^{m} \tag{7-7}$$

$$\frac{da}{dN} / \frac{dc}{dN} = \left(\frac{\Delta K_{eff,A}}{\Delta K_{eff,C'}}\right)^{m} \tag{7-8}$$

In order to appropriately define the initial crack used in the prediction, the difference in crack initiation sites between the three surface conditions, as shown in Figure 7-3, was interpreted by modelling a sharper crack (*a* = 0.05 mm, *a/c* = 1.2), which represented a small crack initiating from inclusions. ΔK_{eff} was obtained under the three surface conditions and the results are presented in Figure 7-12. It can be seen that the reduction of ΔK_{eff} by the T0 process is more pronounced than by the T1 process, implying that the T0 process is more effective in resisting crack initiation from the inclusions. This conclusion is consistent with experimental observations in Figure 7-3. In the modelling work, due to the varying crack initiation mechanism illustrated in Figure 7-3, sharper (*a/c* = 1.2) and shallower (*a/c* = 0.2) initial cracks were chosen for the un-peened and T0 conditions respectively. In the T1 condition, both types of initial cracks were modelled because of its combined crack initiation behaviour.

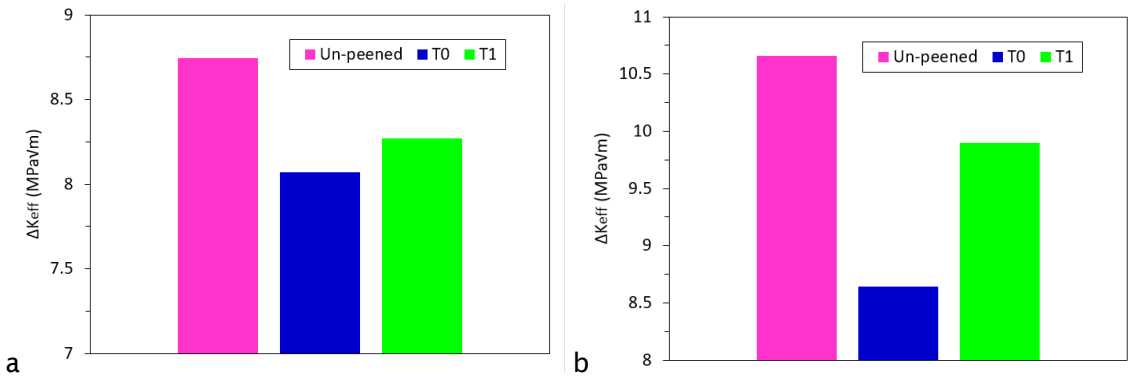

Figure 7-12: Comparison between ΔK_{eff} (*a* = 0.05mm, *a/c* = 1.2) under varying surface conditions at (a) point A and (b) point C'.

Comparison between the experimental data (reproduced from Figure 7-2) and the prediction results are shown in Figure 7-13. Generally speaking, the trend of the experimental data has been successfully predicted. Various initial crack configurations (indicated by the bracketed *a* and *a/c* values in the legend of each plot) were defined in the prediction to examine the scatter band of the experimental results. In the un-peened

condition shown in Figure 7-13(a)(b), with the initial a values set between $0.035 < a < 0.068$ mm, the experimental crack data in the early stages of growing were found to be well bounded by the prediction. The equilibrium state of the crack shape was predicted to be $a/c = 0.85$, which was slightly lower than the experimental observation ($a/c = 0.93$). In the T0 condition shown in Figure 7-13(c)(d), apart from the data representing crack coalescence, most experimental data stay within the scatter band determined by the prediction with the initial a values set between $0.012 < a < 0.019$ mm. One exception is the data point representing the shortest crack, which was expected to develop from an initial crack with smaller a or a/c, being outside the scope defined for this modelling work. It can also be observed that the a/c value begins to increase with growing crack sizes, after being relatively stable ($a/c = 0.83$) at $a = 0.15 - 0.2$ mm. This phenomenon, which was not observed in the un-peened condition, can be attributed to the CRS induced by the T0 shot peening. According to Figure 7-5, the CRS in the T0 condition starts to decrease sharply when $z > 0.2$ mm, implying the degradation of the beneficial effects from the T0 process on crack advance at point A when $a > 0.2$ mm. Meanwhile, the surface crack is still embedded in the CRS field, implying that the crack advance at point C' is still retarded by shot peening. Therefore, when $a > 0.2$ mm, cracks tend to grow quicker in the depth direction than at the surface, resulting in an increase in a/c. Results for the T1 condition are shown in Figure 7-13(e)(f). Again, both crack growth features were reasonably predicted by setting the initial a between $0.01 < a < 0.032$ mm (initial $a/c = 1.2$) and $0.01 < a < 0.025$ mm (initial $a/c = 0.2$) respectively. Similarly with the T0 condition, the experimental data outside the determined scatter band were probably caused by shallower or shorter initial cracks (i.e. $a < 0.01$ or $a/c < 0.2$). In spite of the various initial crack configurations, a converged a/c value is achieved between 0.91 - 0.97.

The initial cracks defined in Figure 7-13 were supposed to appear at the very early stages of crack growth, shortly after crack initiation. The crack initiation stage was negligible in this study because the surface (or near surface) stress concentration sites, which were caused by the notch geometry, the inclusions or surface crack-like imperfections introduced by shot peening, are always responsible for the rapid formation of a surface crack [90, 96, 150, 154]. The size and shape of these initial cracks are directly related to the configuration of the pre-existing defects. The determined scatter band in Figure 7-13 can be used to quantitatively evaluate the effects of the size and shape of initial cracks on the crack growth behaviour.

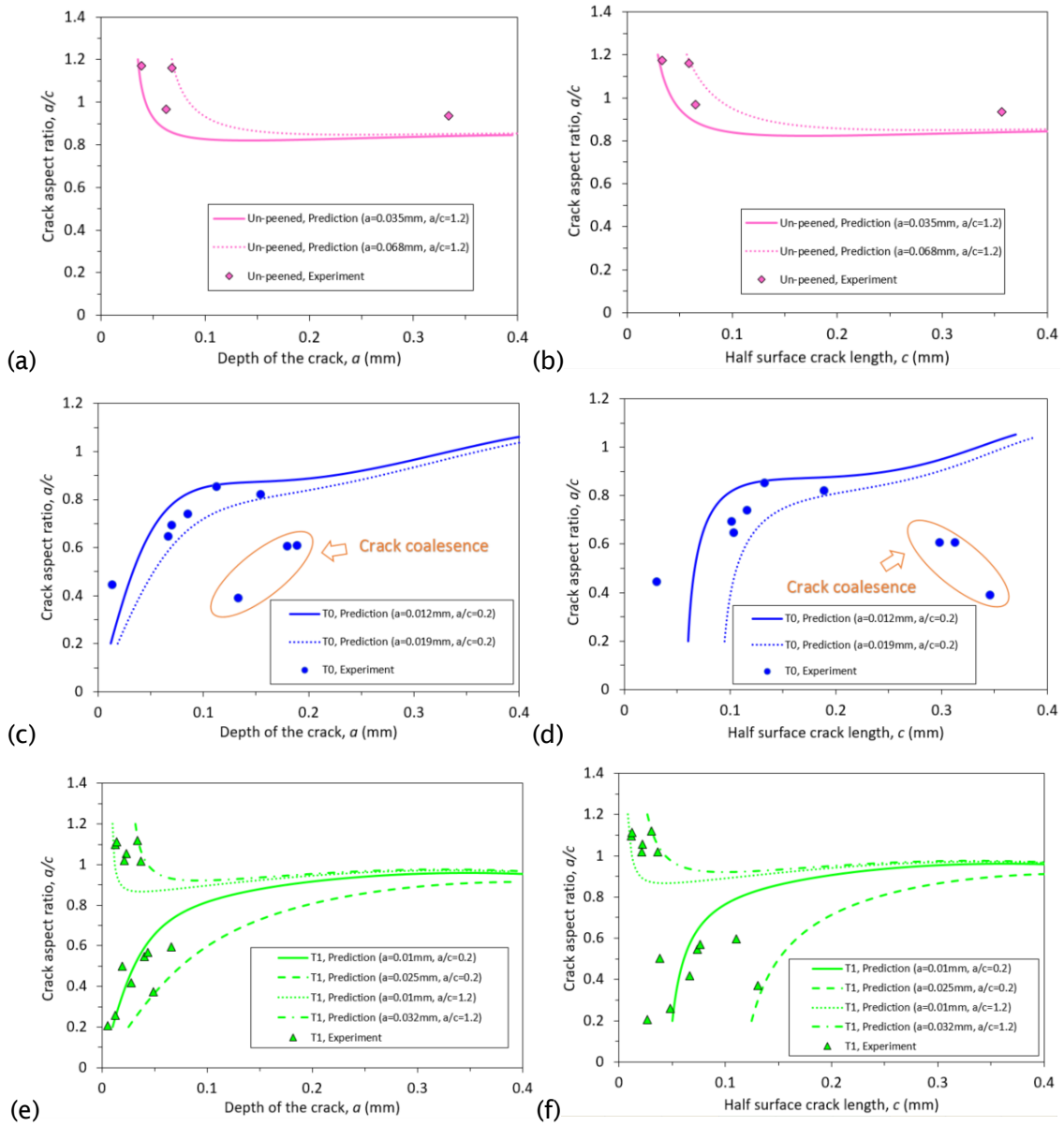

Figure 7-13: Comparison between the predicted crack shape evolution with experimental results in (a)(b) un-peened, (c)(d) T0 and (e)(f) T1 conditions: (a)(c)(d) *a/c* vs *a*, (b)(d)(f) *a/c* vs *c*. The bracketed *a* and *a/c* values in the legend of each plot refer to the initial crack shape used in the prediction.

7.4.3 Prediction of crack growth

The crack growth behaviour (*c* vs *N*, *a* vs *N*) has been predicted using the Paris Law (Equations 7-6 and 7-7), taking the effects of crack shape evolution into account. The *a* and *a/c* values of the initial crack, which were determined to define the experimental scatter band in Figure 7-13, have been used in this prediction as the configuration of the initial crack. As stated in Section 7.4.2, the crack initiation process was not considered

in this prediction. Due to the limitation of the model, the prediction was carried out up to a crack depth of a = 0.4 mm, the corresponding surface crack length ($2c$) was determined based on the predicted a/c.

The predicted surface crack growth (c vs N) results are compared with experimental data reproduced from Figure 6-2, as shown in Figure 7-14. Decent prediction results have been obtained for the un-peened (Figure 7-14(a)) and T0 (Figure 7-14(b)) conditions, although the experimental results for the T0 condition seem more scattered due to the presence of several parallel cracks. However, in the T1 condition displayed in Figure 7-14(c), the prediction results display a clear deviation from the experimental data; the prediction seems non-conservative regardless of the initial crack configurations. This mismatch might be attributed to the complicated crack initiation mechanism in the T1 condition (Figure 7-3(c)(d)), which adds more difficulty in accurately predicting the crack shape, especially when potential crack coalescence happens.

The predicted crack growth in the depth direction (a vs N) was also obtained, as shown in Figure 7-15. In addition, the prediction relying on the plane strain 2D FE model (introduced in Chapter 6) has been carried out as a comparison with the 3D modelling results, using the same initial a with the 3D model. According to Figure 7-15, a longer crack growth process is always predicted using the 3D model than the 2D model, in spite of different surface conditions. This discrepancy can be attributed to the neglect of the effects of crack shape on the crack driving force in the 2D model. As described in Figure 7-16, when the depth of the crack (a) maintains unchanged, the obtained ΔK_{eff} from the 3D FE model at point A increases with decreasing a/c, approaching the 2D FE modelling results. This is unsurprising since the 2D crack represents a through-thickness crack with an a/c effectively approaching zero, which is lower than the a/c of any 3D semi-elliptical crack. The same trend can be found in the un-peened, T0 and T1 conditions. Consequently, the overestimated crack driving force from the 2D FE model resulted in a more underestimated crack growth life compared with the 3D FE modelling results (Figure 7-15).

In addition, Figure 7-15(c) also shows a clear difference between the predicted crack growth life resulting from two diverse initial crack configurations (although with identical crack depth) in the T1 condition. The reasons accounting for this difference have been investigated. Figure 7-17(a) shows that the shallower initial crack (a/c = 0.2) leads to a higher ΔK_{eff} (hence shorter life) compared with the sharper initial crack (a/c = 1.2), until the crack grows to a = 0.15 mm. The crack shape evolution process under both circumstances is schematically illustrated in Figure 7-17(b), demonstrating an equilibrium state of the crack shape at a = 0.15 mm. This analysis, once more,

emphasised the necessity of considering the role of the crack shape during short crack growth investigations.

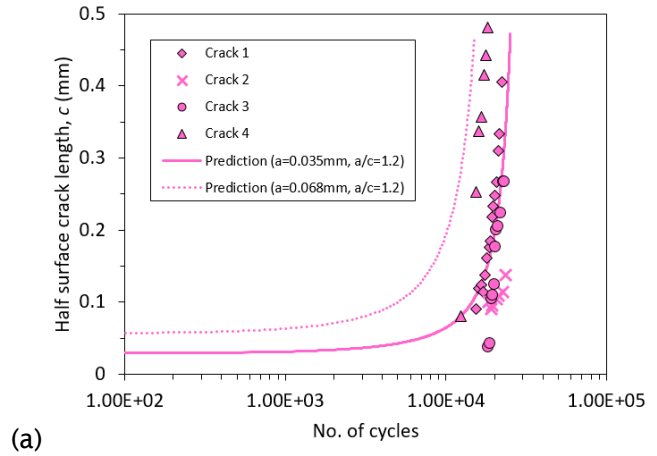

(a)

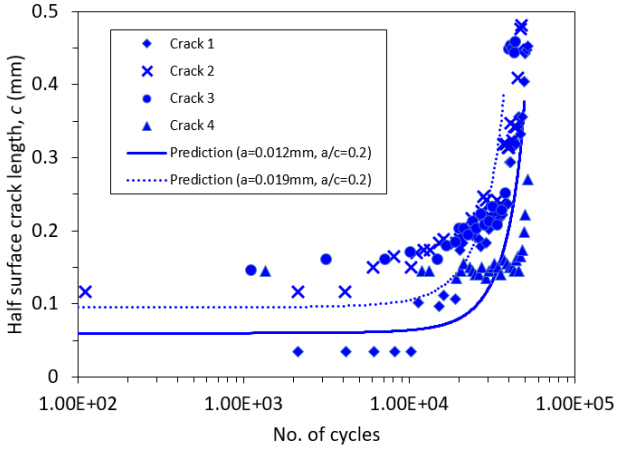

(b)

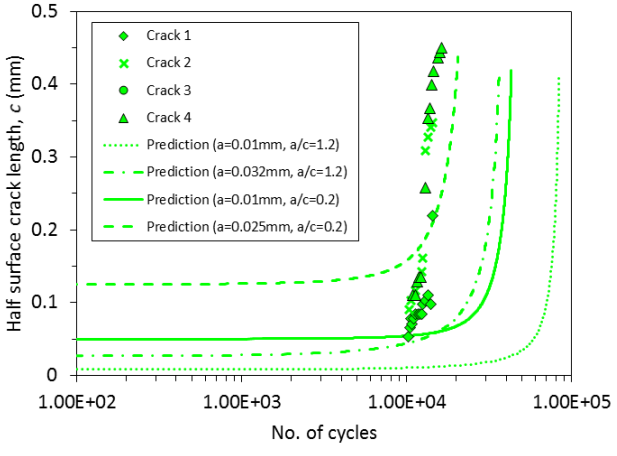

(c)

Figure 7-14: Comparison between the predicted surface crack growth and the corresponding experimental results in the (a) un-peened, (b) T0 and (c) T1 shot peening conditions. The bracketed *a* and *a/c* values in the legend of each plot refer to the initial crack shape used in the prediction.

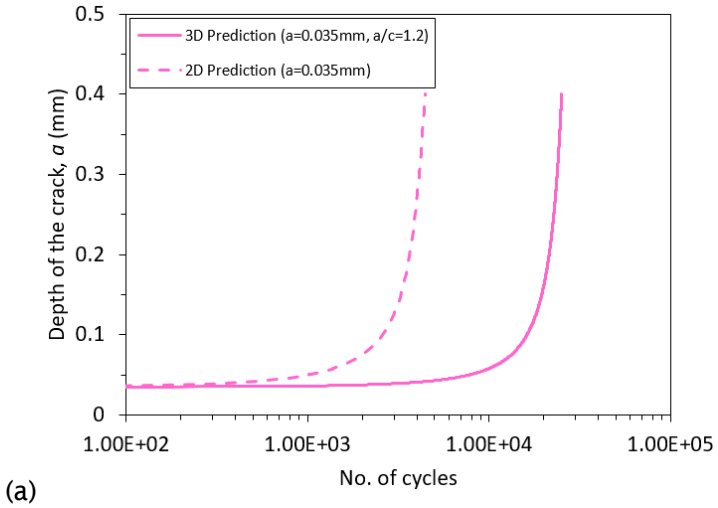

(a)

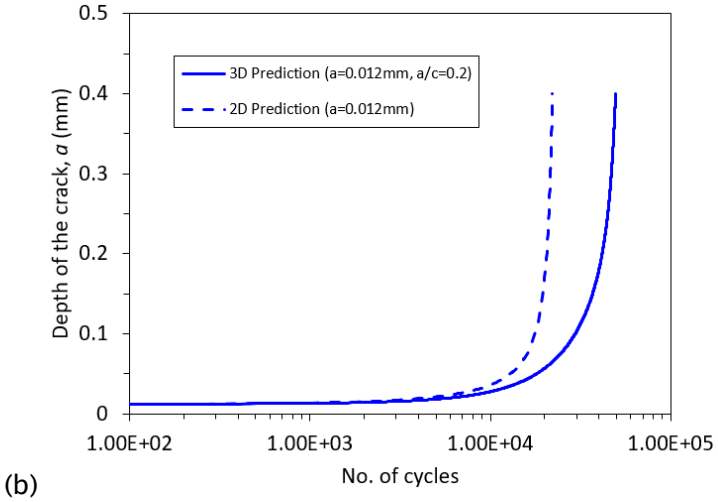

(b)

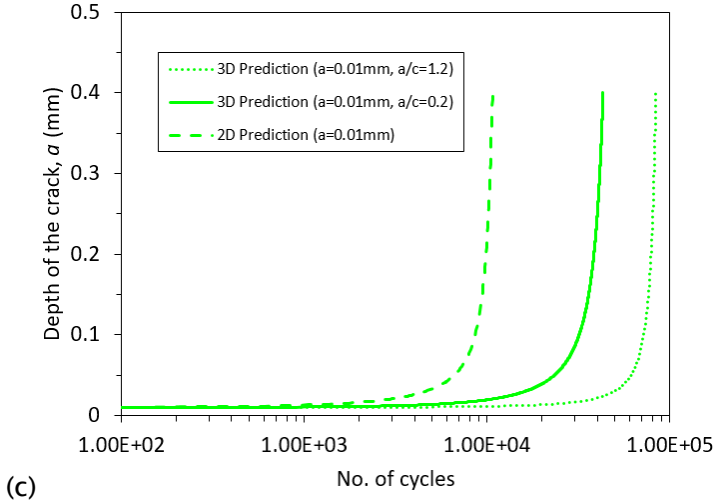

(c)

Figure 7-15: Comparison between the predicted crack growth behaviour in the depth direction (*a* vs *N*) using 3D and 2D FE models in the (a) un-peened, (b) T0 and (c) T1 conditions. The bracketed *a* and *a/c* values in the legend of each plot refer to the initial crack shape (3D) or size (2D) used in the prediction.

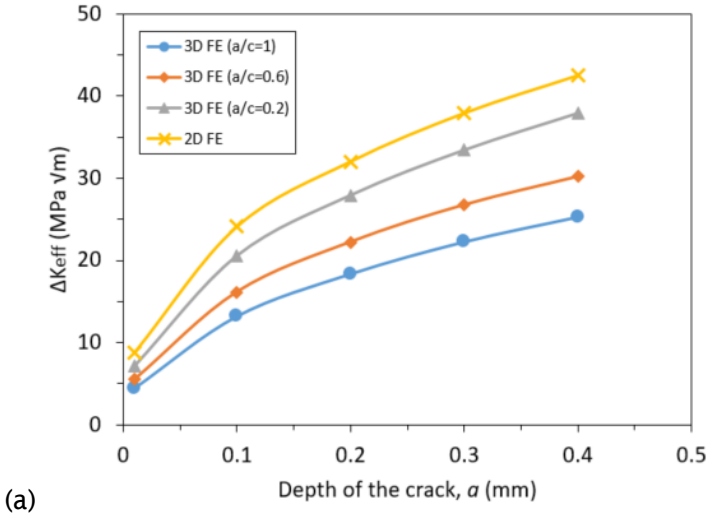

(a)

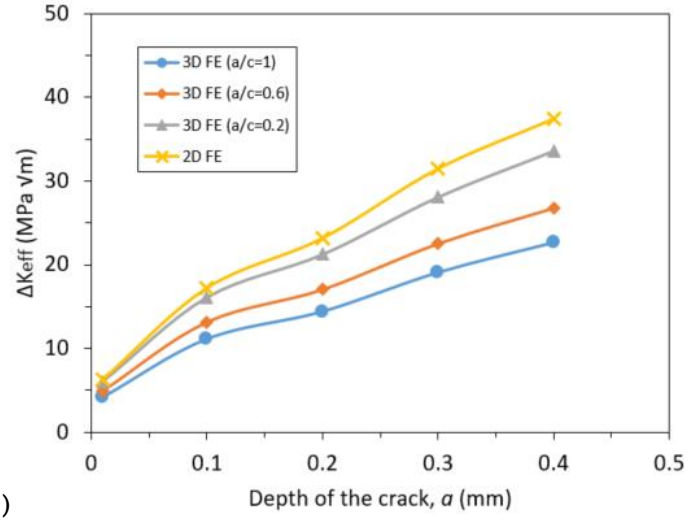

(b)

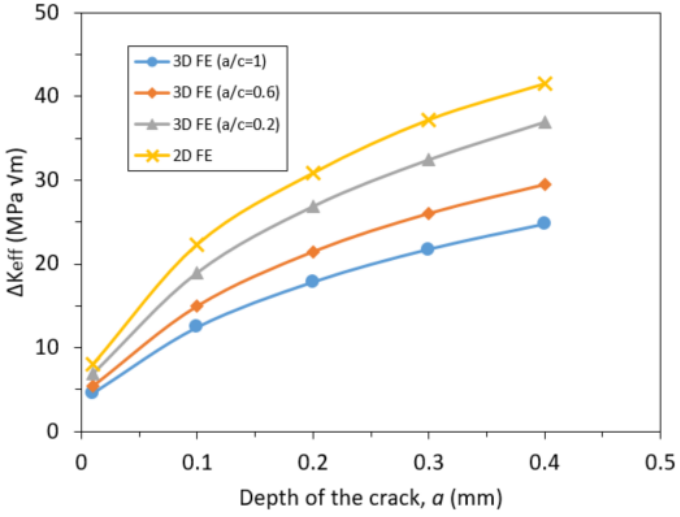

(c)

Figure 7-16: Comparison between the ΔK_{eff} at point A of the crack front with varying a/c values in the (a) un-peened, (b) T0 and (c) T1 conditions.

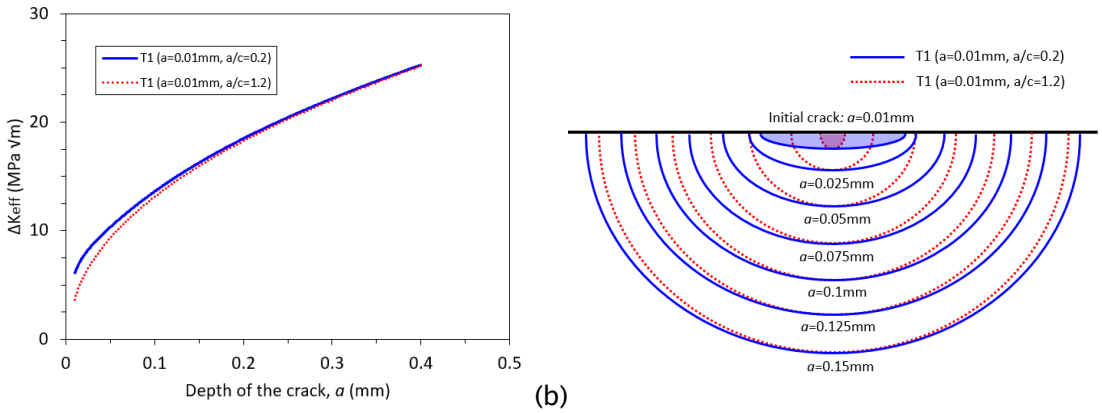

Figure 7-17: The difference resulting from two initial crack configurations in (a) ΔK_{eff} at point A and (b) crack shape evolution. The bracketed *a* and *a/c* values in the legend of each plot refer to the initial crack shape used in the prediction.

To further understand the effects of shot peening, crack growth from the identical initial crack configuration under different surface treatments (un-peened, T1 and T0) has been numerically investigated. The initial crack was set as a = 0.035 mm and a/c = 1.2, which represented the lower bound of the initial cracks nucleated from the inclusions in the un-peened condition, as shown in Figure 7-14(a). Figure 7-18(a) depicts the predicted crack growth behaviour in the depth direction (a vs N). Clearly, shot peening retards the short crack growth behaviour, and the T0 process is more effective than the T1 process. The associated ΔK_{eff} values at point A of a growing crack have also been obtained, as shown in Figure 7-18(b). It demonstrates a more evident reduction in the crack driving force resulting from the T0 process than the T1 process, which accounts for the difference between the two shot peening processes shown in Figure 7-18(a). Although this numerical analysis might be less consistent with reality since no inclusion-induced crack initiation was experimentally observed in the T0 condition, it intuitively demonstrates the shot peening effects in decelerating the crack growth rate in addition to affecting the crack initiation mechanism. Additionally, despite the fact that the initial crack configurations applied in different conditions are identical, the results presented in Figure 7-18 inherently involves different crack shape evolution processes, which accounts for the main difference with the 2D modelling results shown in Figure 6-7.

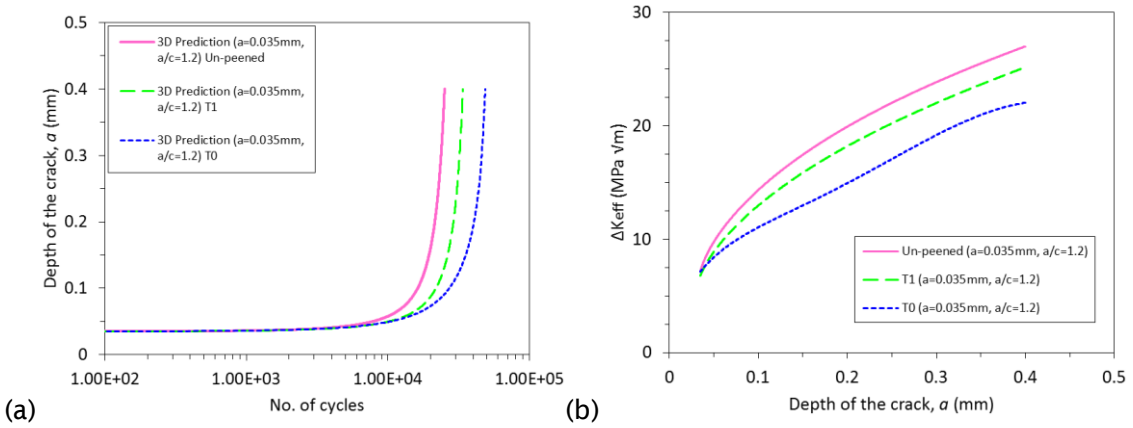

Figure 7-18: The difference resulting from surface treatments in (a) the predicted crack growth behaviour in the depth direction (a vs N) with the identical initial crack configuration (a = 0.035 mm, a/c = 1.2), and (b) the associated ΔK_{eff} at point A.

7.4.4 Discussion

Through comparing the T0 (high peening intensity) and T1 (low peening intensity) shot peening processes, it can be confirmed that crack initiation from the perpendicular stringer inclusions, which is the main initiation mechanism in the un-peened condition, is more likely to be resisted by a more intense CRS field because of the reduced crack driving force (Figure 7-12). It is also advantageous to produce a deeper CRS field to expand the influence of shot peening in terms of the depth through which the crack growth is delayed (Figure 7-9). From this point, a high peening intensity, which may result in a greater and deeper CRS field, is beneficial. However, high peening intensity is also likely to increase the surface roughness, or to introduce more surface defects, which may facilitate additional crack initiation and thus degrades the benefits of shot peening. Hence, with the same peening intensity, it is reasonable to expect a more prominent life improvement if the post-peening surface condition is ameliorated, and conversely, an unimproved (or even degraded) fatigue life if the post-peening surface is excessively roughened. Consequently, in order to more accurately quantify the influence of shot peening on fatigue life, a method capable of evaluating crack growth from different types of surface (or near surface) defects, would be helpful.

In the current modelling work, although the crack initiation process was not modelled nor predicted, the diversity in early crack configurations, which was directly related to the crack initiation mechanism caused by different surface (or near surface) defects, has been considered in the modelling work. It was found that the crack driving force depended on both the residual stress state and the crack shape, as shown in Figure 7-12 and Figure 7-16 respectively. Hence, neglecting the crack shape effects potentially may

affect true estimation of shot peening effects on delaying short crack growth. This implies that the modelling methodology introduced in this study is promising to more accurately assess shot peening effects, especially when the remeshing technique [213] is integrated in future work. It is also an important tool to use in optimising the shot peening process, where the trade-off between a greater CRS field and a more roughened post-peening surface (all resulting from a high peening intensity), is required.

7.5 Conclusion

In this chapter, a 3D FE model has been developed to investigate the short crack growth behaviour in a notched specimen subjected to shot peening. The compressive residual stress and strain hardening effects caused by shot peening have been incorporated into the model utilising the methods introduced in Chapter 4. The following major conclusions have been demonstrated.

- Residual stress redistribution caused by both mechanical loading and crack advance has been modelled. The compressive residual stress distribution tends to be stable while the crack advances until the crack penetrates through the compressive residual stress field, confining residual stress redistribution to a small area near the crack front.
- Different crack initiation mechanisms were experimentally observed in the un-peened and shot-peened conditions, which resulted in diversity of the initial crack configuration and thus different crack shape evolution processes. Using the developed 3D FE model, crack shape evolution in both the un-peened and shot-peened conditions has been successfully predicted, with appropriately defined initial crack configurations.
- Surface crack growth (c vs N) has been successfully predicted in the un-peened and T0 (high peening intensity) conditions, where crack initiation shows unique features respectively. In the T1 (low peening intensity) condition, c vs N was not reliably predicted due to the more complicated crack initiation mechanism.
- Compared with the 3D model, the prediction of short crack growth in the depth direction (a vs N) relying on the 2D model (with the plane strain assumption) underestimated the short crack growth life, as the 2D model does not consider the effects of crack shape.

8 Overall Conclusions of the Thesis

In order to develop a lifing approach considering shot peening effects, plain bend bar and notched 3D FE models have been developed in this study. The residual stress and strain hardening profiles resulting from shot peening have been incorporated into the FE model to define the as-peened condition. Residual stress relaxation during the first loading cycle (a quasi-static process) has been subsequently simulated and compared with experimental results. Utilising this FE model, the Smith-Watson-Topper (SWT) and the Fatemi-Socie (FS) critical plane criteria have been used to estimate the total fatigue life of shot-peened specimens. In addition, a crack has been introduced into the developed FE models (2D and 3D) to investigate the short crack growth behaviour affected by shot peening. The associated crack propagation life has been predicted using both the linear-elastic and elasto-plastic fracture mechanics (i.e. LEFM and EPFM). The effects of crack shape evolution have been included in the 3D crack modelling work.

In order to select an appropriate material model that can be conveniently applied in the FE model without unnecessarily complicating the modelling work, different material models have been developed and compared in this study. The cyclic material model has been firstly calibrated using the experimental results obtained under R_ε = -1. However, a poor transferability of this model was demonstrated; the ratcheting behaviour was unacceptably overestimated when it was applied to other conditions with different load ratios (e.g. R_ε = 0). Additionally, a monotonic material model has also been developed to accurately describe the monotonic mechanical properties of the material. Despite its lack in accounting for the cyclic mechanical properties, it has been regarded as an appropriate starting point, considering the fact that residual stresses usually relax most significantly during the first cycle especially for notched samples.

The inverse eigenstrain method has been demonstrated to be an effective and efficient approach to reconstruct the residual stress distribution in the FE model. This approach is essentially a process determining the eigenstrain distribution based on the experimentally measured residual stress distribution. In the present study, the residual stress field in both the T0 and T1 shot-peened plain samples have been successfully reconstructed using this approach with an acceptable accuracy. Its application has also been extended to the notched geometry by successfully reconstructing the residual stress field in the shot-peened 4.5 × 1.25 notched sample; the effect of notched geometries on eigenstrain components have been taken into account. In addition, the strain hardening layer resulting from shot peening has also been modelled in the FE model. This was achieved by modifying local monotonic yield strength, representing the

varying material properties at different depths. The monotonic stress-strain relation at each depth was determined based on the previous EBSD results indicating the true plastic strain profile resulting from shot peening.

After incorporating both residual stresses and strain hardening caused by shot peening into the FE model, residual stress relaxation after one loading cycle in both the shot-peened plain bend bar and 4.5 × 1.25 notched samples has been satisfactorily simulated. This validated modelling approach has been used to investigate the effect of load levels on residual stress relaxation in both the plain bend bar and the 4.5 × 1.25 notched samples. It was found that a higher load level did not necessarily lead to a more significant residual stress relief under bend load. The degree of residual stress relaxation depends on the change in the distribution of eigenstrain, which is linked to the plastic deformation generated by external loads. The comparison between the simulated results for the plain bend bar and the notched samples demonstrates the advantage of notched geometries in retaining compressive residual stresses during fatigue loading, which is consistent with the experimental observation showing a greater benefit of shot peening in improving fatigue life in the notched specimen than in the plain bend bar specimen.

The developed FE models have been used to facilitate the application of the SWT and FS critical plane criteria to predict the fatigue life of both the shot-peened plain bend bar and notched samples, by evaluating the stress and strain states within the specimen during cyclic loading. The stress- and strain-related parameters required by the critical plane criteria were calculated using the modelling results, combined with a critical distance method considering an averaged stress/strain state over a reasonably defined distance into the depth. Most of the life prediction results are acceptably within a factor of two error range. Nevertheless, in situations where surface defects (lips at the sample edges resulting from shot peening) considerably accelerated crack initiation and propagation, the fatigue life was significantly overestimated by the applied methods. The implication is that since the conventional total life approaches typically assume a defect-free condition, additional modifications are required if their application is extended to situations with severe surface imperfections or internal discontinuities.

Considering the inapplicability of total life approaches in investigating short crack growth behaviour, the application of damage tolerant approaches to the shot-peened notched samples has been investigated, which is potentially more appealing to industrial users. Both 2D (with plane strain assumption) and 3D FE models containing a crack have been developed from the model that has been used to simulate residual stress relaxation.

In the 2D crack modelling work, both linear-elastic and elasto-plastic fracture mechanics (i.e. LEFM and EPFM) have been applied. The retardation of short crack growth resulting

from shot peening has been reasonably interpreted, and the contributions made by compressive residual stresses and strain hardening have been investigated separately with the help of the FE model. It was found that the compressive residual stress field generated by shot peening made the main contribution by reducing the effective crack driving force and inducing crack closure; while in contrast, strain hardening caused by shot peening increased the crack driving force in this study, so was expected to lead to an accelerated crack propagation process. Nevertheless, it was also found that the plastic deformation in the shot peening affected layer (before cracks appeared) was reduced by the strain hardening effects, implying a hindered crack initiation process. Additionally, the fatigue life of the shot-peened notched samples has been predicted using both the LEFM and EPFM approaches. In spite of the dependency of the prediction on the selected initial crack size, reasonable results were obtained using both approaches. However, it is noteworthy that the LEFM approach tends to result in non-conservative life predictions if it is applied in the LCF regime, which requires cautious consideration in application.

Due to the plane strain assumption applied in the 2D modelling work, only the crack size (a) in the depth direction was considered and the crack shape effects were ignored. In order to more explicitly investigate the short crack growth behaviour in the shot-peened notched samples, a 3D FE model containing a semi-elliptical crack has been developed, which is more consistent with reality. Before studying the short crack growth behaviour, residual stress redistribution caused by the presence of a crack has been investigated. It was found that the compressive residual stress distribution tended to be stable during crack advance, confining residual stress redistribution to a small area near the crack front, until the crack penetrated through the compressive residual stress field. This conclusion has been demonstrated to be largely independent of the surface crack length ($2c$) and only depends on the depth of the crack (a). According to experimental observations, cracks usually initiated from inclusions with high a/c in the un-peened condition, which tended to be resisted by shot peening, resulting in crack initiation from surface microcracks (caused by high peening intensities) with low a/c in the shot-peened condition. This discrepancy in crack initiation mechanisms led to a diversity of the initial crack configuration and thus different crack shape evolution processes. Using the developed 3D FE model, crack shape evolution in both the un-peened and shot-peened conditions has been successfully predicted, with appropriately defined initial crack configurations. The EPFM approach has been applied to characterise the crack driving force at the deepest and a near-surface point along the crack front based on the concept of crack closure. Based on the predicted crack shape evolution, surface crack growth (c vs N) has been successfully predicted in the un-peened and shot-peened conditions, apart from the T1 condition where the crack initiation mechanism is more complicated.

The prediction of short crack growth in the depth direction (a vs N) has also been conducted using this 3D model. The obtained results were compared with the 2D (with the plane strain assumption) modelling results, concluding that the 2D model underestimated the short crack growth life as the 2D model did not consider the effects of crack shape. This study emphasises the significance of considering the crack shape effects when evaluating the short crack growth behaviour.

In general, the application of the developed residual stress related modelling framework is believed to be able to be extended to other metals, as long as the material model is appropriately calibrated and the shot peening induced effects (compressive residual stress and strain hardening) are accurately characterised (by either experimental, numerical or analytical approaches) to define the input of the model. In conditions where the crack initiation life plays a more important role (such as in HCF), the current model can be potentially used along with crack initiation criteria to enhance the accuracy of the life prediction. The potential improvements that can be applied to the developed model are discussed in Chapter 9.

9 Future work

9.1 Introduction

It is noted that some of the assumptions that have been applied in this study might be less reasonable in other systems with different materials, geometries, loading conditions, shot peening parameters, etc. Therefore, the developed FE modelling tool in this study can still be improved to ensure its good applicability in different systems with various materials and service conditions.

9.2 Application of a cyclic material model

The monotonic material model was chosen in this study due to two reasons: (1) residual stress relaxation mainly occurred during the first cycle in the investigated notched specimen under the selected loading range, predominantly depending on the monotonic mechanical properties of the material; (2) it was found non-trivial to calibrate a material model independent of strain ranges with good transferability for FV448. However, in conditions where residual stress relaxation exhibits a more evolutionary behaviour depending on fatigue cycles, the monotonic material model tends to result in an underestimation of the degree of compressive residual stress relief (hence an overestimated stabilised compressive residual stress field). This would potentially exaggerate the benefits of shot peening and consequently result in a non-conservative life assessment. Under such circumstances, the application of a cyclic material model is required. To conquer the obstacles associated with reason (2) stated above, a more complex but more powerful Chaboche model [170] could be applied, which would require some additional coding work using the ABAQUS subroutine UMAT.

9.3 Application of the remeshing technique

In Chapters 6 and 7, the crack propagation process was not directly simulated, but was predicted based on modelling several static cracks with different sizes (2D) or sizes and shapes (3D). According to the literatures, there are several techniques that have been applied in FE modelling to achieve the simulation of automatic crack propagation [213, 215, 216]. The most popular one for 3D crack modelling is the adaptive remeshing technique. A comprehensive review regarding this technique is reported in [213]. The application of this technique can be divided into four main steps: (1) development of a 3D FE model containing a pre-defined initial crack; (2) calculation of the effective SIFs along the crack front; (3) determination of the crack advance at each point along the crack front based on the fatigue crack growth law; (4) definition of a new 3D FE model

containing the newly determined crack front. These steps are repeated up to final fracture or a pre-defined crack length indicating termination of the simulation, which is normally controlled by a Python code.

Compared with the modelling method applied in the present study, the remeshing technique allows defining the crack with an arbitrary shape, since it predicts crack propagation based on distributed points along the crack front. This is believed to be more consistent with reality, compared with the assumption describing crack shape as semi-elliptical simply based on two points (the deepest and the surface points at the crack front), which has been applied in the present study. Additionally, the remeshing technique can also be employed to assess the effects accumulated during crack propagation, i.e. generation of the plastic wake, which accounts for the plasticity-induced crack closure (PICC) phenomenon. Although PICC is deemed to be much less important than the crack closure caused by compressive residual stresses in the shot-peened condition [153], taking it into account would ensure a better consistency with reality and promote a wider application of the developed modelling framework.

9.4 Prediction of crack initiation

Although the crack initiation behaviour has not been predicted in the current study, it is critical in assessing the benefits of shot peening, as discussed in Section 2.2. In the shot-peened condition, crack initiation may occur at various sites depending on the surface condition after shot peening, the distribution of inclusions as well as the load levels. An accurate prediction of the crack initiation area would be significantly advantageous to the subsequent application of the total life and the damage tolerant approaches to carry out fatigue life prediction, since both approaches require the associated local stress/strain state to determine the corresponding dependent variables (such as $\Delta\sigma$, $\Delta\varepsilon$ and ΔK). In the current study, life predictions presented in Chapters 5, 6 and 7 are based on known crack initiation sites from experiments. Therefore, crack initiation prediction would be significant when the developed method is applied to other circumstances without sufficient crack initiation information.

To predict the crack initiation area, the microstructural effects have to be taken into account. One of the main reasons is that the residual stress value of an element at a given depth will differ depending on the orientation of the grain in which the element is located and its interactions between its neighbour grains, due to the different orientation and distribution of the grains. This will result in a deviation of the local actual residual stress level from a given ideal/target mean stress value. A more accurate local residual stress distribution allowing for the microstructural effects can be predicted by employing

a crystal plasticity model in areas where cracks are most likely to nucleate [134]. This will facilitate the investigation on the effect of certain microstructural features (such as the largest grain, inclusions, pores, etc.) on crack initiation, which also requires the incorporation of the experimentally scanned microstructural features into the FE model. For instance, in the current research, the different crack initiation behaviours from either the inclusions or surface microcracks under a specific residual stress state can be predicted. This would also be significant in allowing optimisation of the the shot peening parameters, ensuring sufficient peening intensity to resist crack initiation from the inclusions while avoiding any excessively high shot peening intensity.

Appendix A Mesh sensitivity analysis

In order to ensure a good running efficiency and accuracy of the FE model, a refined mesh was applied to the most relevant region (i.e. the notched area) where crack growth has been observed in experiments, while a coarse mesh was applied to less important regions with a global element size of 0.5 mm, as explained in Section 3.6.1.

A mesh sensitivity analysis has been carried out using the 4.5×1.25 notched model without shot peening effects to determine a proper mesh density level applied to the area with refined mesh, ensuring the modelling results are independent of the applied mesh sizes. Conditions with varying mesh sizes have been considered in this analysis and are shown in Table A-1; since mesh dimensions were defined to vary with positions in the FE model, only the minimum mesh dimensions in each condition are shown to indicate the corresponding mesh density level.

Table A-1: Different minimum element dimensions (length × width × thickness) applied in the mesh sensitivity analysis.

No.	1	2	3	4	5	6
Minimum element dimensions / mm	0.3×0.3×0.5	0.3×0.3×0.25	0.3×0.17×0.17	0.2×0.2×0.1	0.1×0.2×0.05	0.05×0.1×0.025

The longitudinal stress (σ_{xx}) at a load level of 2400 N at the notch root was simulated using the mesh conditions listed in Table A-1. The modelling results are shown in Figure A-1. It can be seen that the simulated σ_{xx} tends to converge at ~503 MPa with decreasing mesh dimensions. Compared with No.5, the result for No.6 only shows a 0.02% difference, which means that the modelling results have already been independent of mesh sizes at the mesh density level indicated by No.5. However, in order to accurately describe the 'hook' shape of the compressive residual stress profile when shot peening effects are taken into account, the mesh density level indicated by No.6 has been finally selected. Similar mesh conditions have also been applied to other notch geometries in the present study.

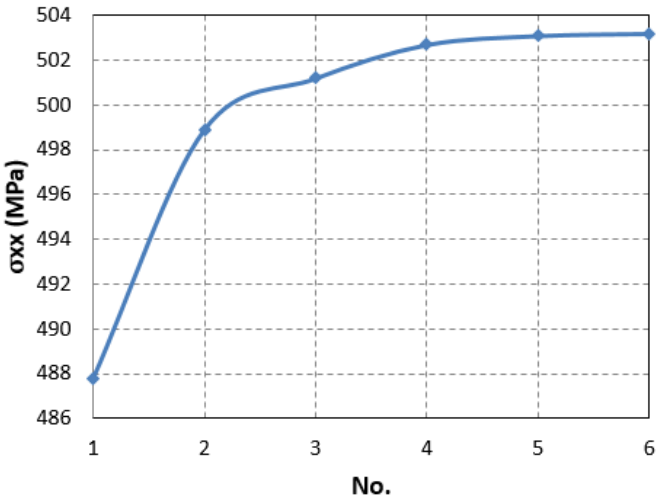

Figure A-1: Predicted σ_{xx} at the notch root of the 4.5×1.25 notched sample at a load level of 2400 N using different mesh dimensions listed in Table A-1.

Appendix B Calibration results and validation for J_{max}

The values of the calibrated parameters in Equation 7-5 are shown in Table B-1. It was found that an order of three of Equation 7-3 (i.e. B_4 =0) was sufficient to ensure a good fitting accuracy for the un-peened and T1 conditions, while an order of four was required for the T0 condition. Hence the values of D_{4j} (j = 0, 1, 2 and 3) in Equation 7-5 are only available for the T0 condition, as shown in Table B-1.

The quality of the fitting work was checked by comparing the FE-determined results, which were used as the 'training' data, with corresponding predictions obtained using the calibrated Equation 7-5. Figure B-1 and Figure B-2 show the comparison under the un-peened, T0 and T1 shot peening conditions at point A and C' respectively, demonstrating a good fit. The applicability of the calibration of Equation 7-5 has been validated using additional 'test' FE modelling results that were not used in the fitting work. The validation results at point A and C' are shown in Figure B-3 and Figure B-4 respectively, demonstrating the reliability of the calibrated Equation 7-5 within the defined range ($0.01 \leq a \leq 0.4$ mm, $0.2 \leq a/c \leq 1.2$).

Table B-1: Calibrated values of the parameters in Equation 7-5 for point A and point C' under un-peened, T0 and T1 conditions.

D_{ij}	Un-peened		T0		T1	
	Point A	Point C'	Point A	Point C'	Point A	Point C'
D_{10}	28.2	9.928	23.905	5.1225	22.342	9.8967
D_{11}	- 42.274	12.965	- 26.093	8.1245	- 33.1	- 1.5095
D_{12}	32.455	- 18.341	15.758	- 7.8109	25.811	1.1492
D_{13}	-10.172	6.547	-4.074	1.9712	-8.0663	-0.7514
D_{20}	- 37.799	- 22.81	- 147.05	- 6.5369	- 9.3678	- 32.275
D_{21}	105.46	26.099	147.59	- 5.7683	54.801	96.483
D_{22}	- 114.06	- 26.264	- 83.5	- 21.463	- 71.973	- 128.65
D_{23}	43.591	12.447	20.547	18.399	28.853	52.252
D_{30}	50.034	40.117	611.9	14.915	9.3024	55.935
D_{31}	178.78	96.549	- 652.01	-35.873	101.63	- 166.6
D_{32}	218.61	120.06	399.57	97.236	149.76	231.56
D_{33}	-88.529	-52.392	-104.67	-56.668	-63.376	-97.344
D_{40}	N/A	N/A	- 724.09	N/A	N/A	N/A
D_{41}	N/A	N/A	757.75	N/A	N/A	N/A
D_{42}	N/A	N/A	- 446.66	N/A	N/A	N/A
D_{43}	N/A	N/A	108.72	N/A	N/A	N/A

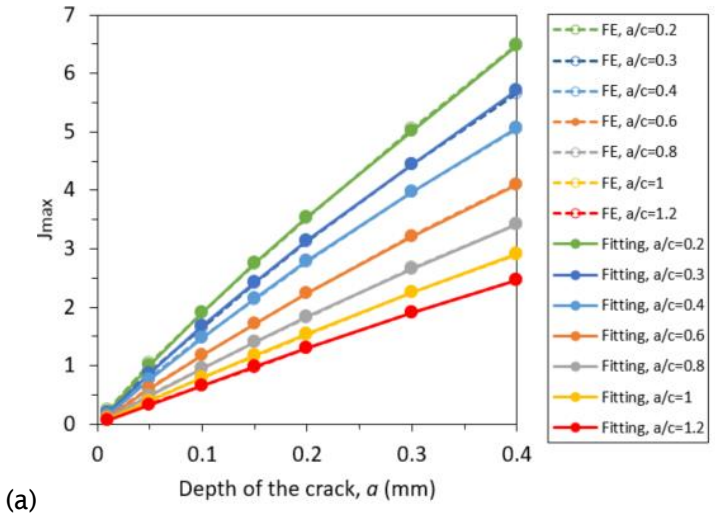

(a)

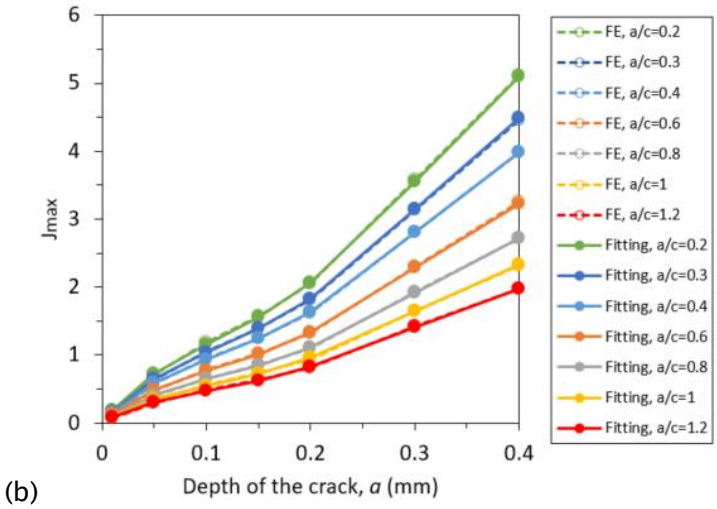

(b)

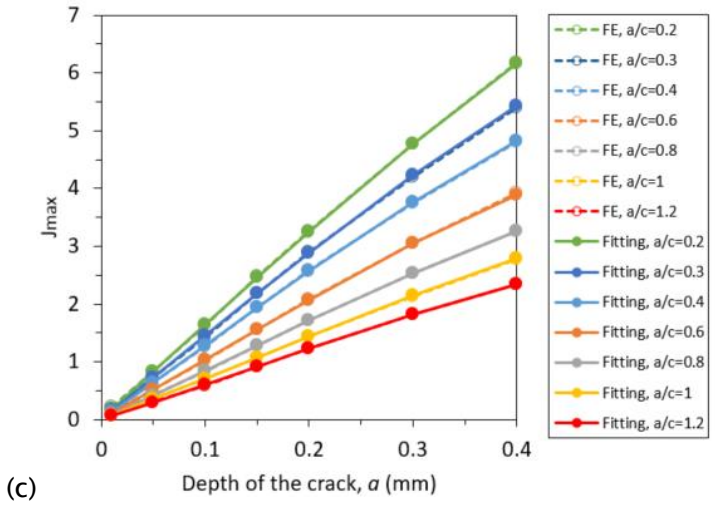

(c)

Figure B-1: Comparison of the FE-determined J_{max} at point A with corresponding fitted predictions under (a) un-peened, (b) T0 and (c) T1 conditions.

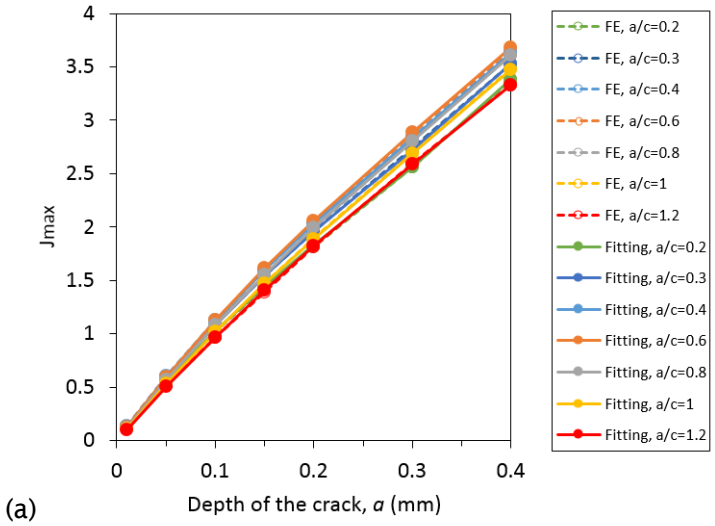

(a)

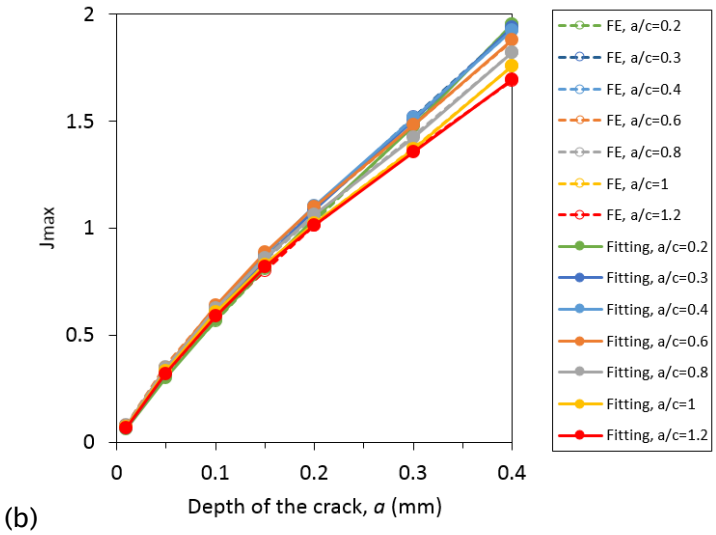

(b)

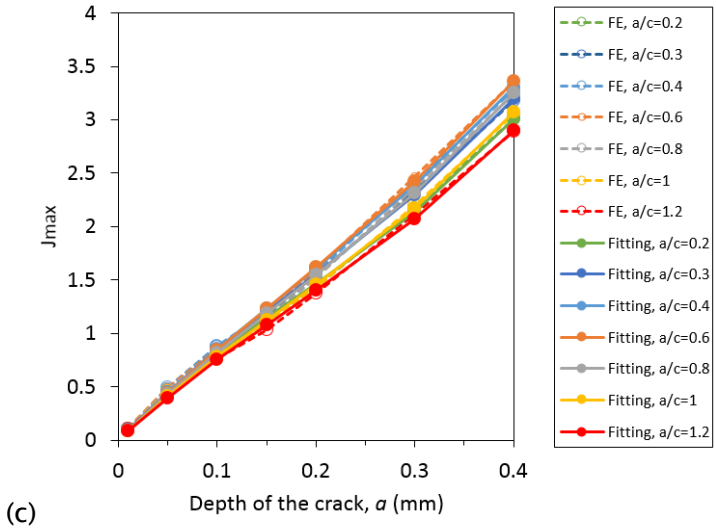

(c)

Figure B-2: Comparison of the FE-determined J_{max} at point C' with corresponding fitted predictions under (a) un-peened, (b) T0 and (c) T1 conditions.

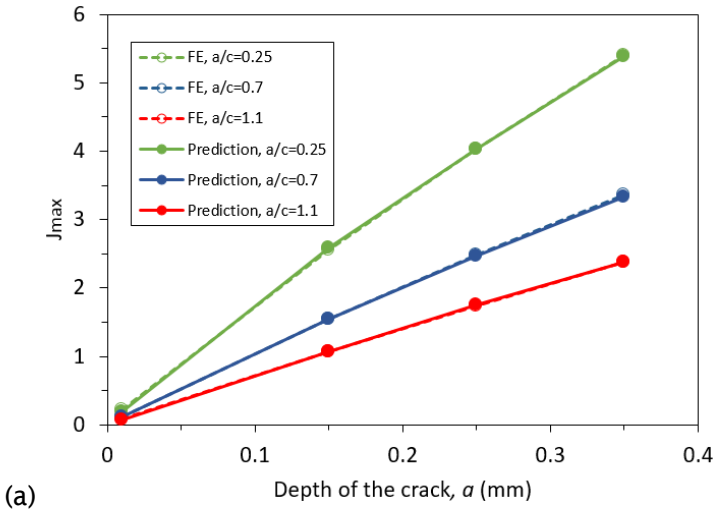

(a)

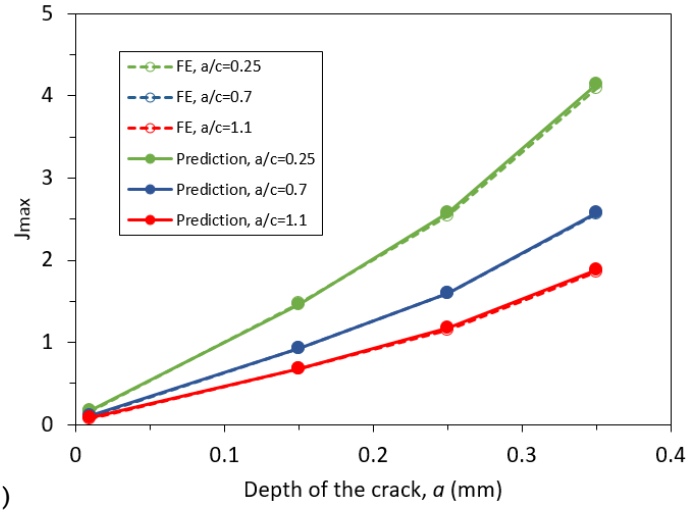

(b)

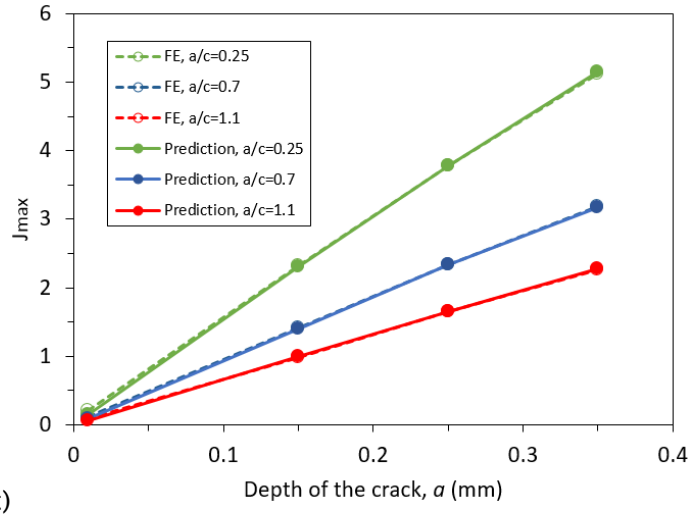

(c)

Figure B-3: Validation of the fitting approach by comparing the FE-determined J_{max} at point A with corresponding predicted results using the calibrated Equation 7-5, under (a) un-peened, (b) T0 and (c) T1 conditions. Note this FE data was not used to determine the fitting equation.

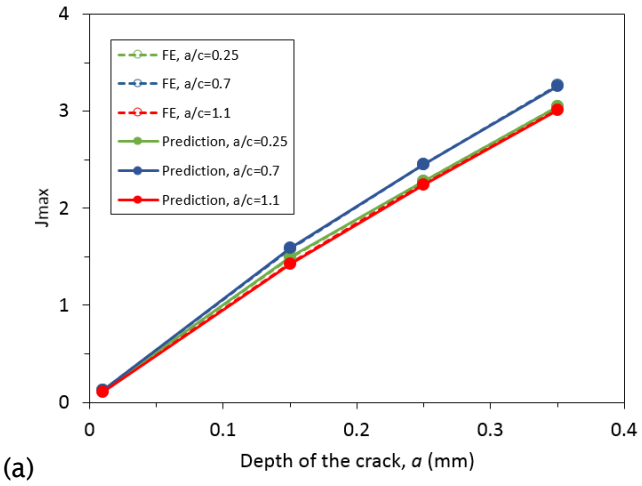

(a)

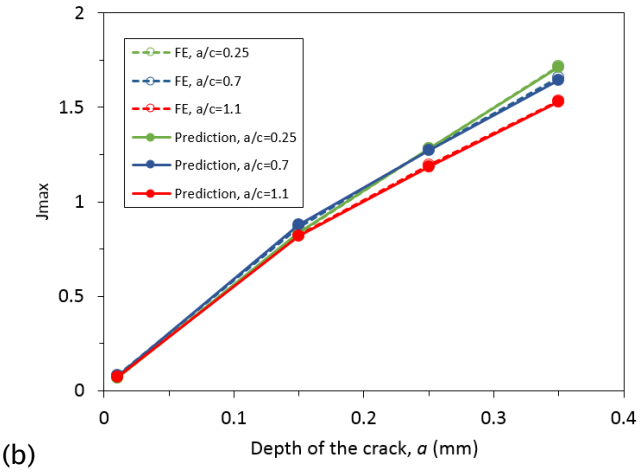

(b)

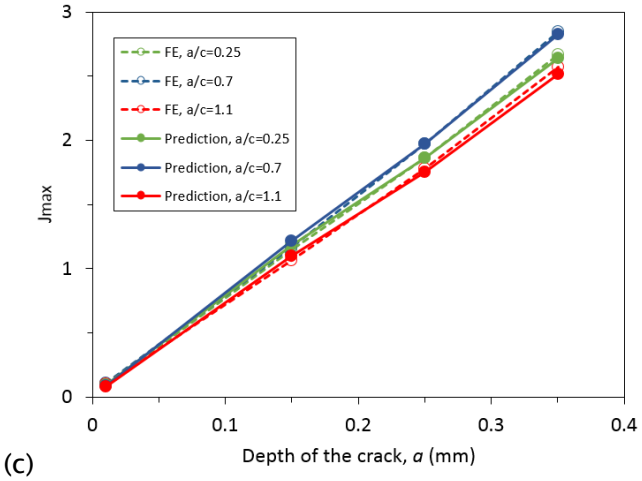

(c)

Figure B-4: Validation of the fitting approach by comparing the FE-determined J_{max} at point C' with corresponding predicted results using the calibrated Equation 7-5, under (a) un-peened, (b) T0 and (c) T1 conditions. Note this FE data was not used to determine the fitting equation.

References

1. Zhou, S. and Turnbull, A., *Steam turbine operating condition, chemistry of condensates, and environment assisted cracking - a critical review.* NPL Report MATC (A) 95, 2002.
2. Soady, K.A., *Life Assessment Methods for Industrial Steam Turbine Blade to Disc Interfaces*. 2011, University of Southampton.
3. Miller, M., Reed, P., and Joyce, M., *Effect of temperature and secondary orientation on notch fatigue resistance of CMSX4.* International Journal of Fatigue, 2005.
4. Mukhopadhyay, N.K., Chowdhury, S.G., Das, G., Chattoraj, I., Das, S.K., and Bhattacharya, D.K., *An investigation of the failure of low pressure steam turbine blades.* Engineering Failure Analysis, 1998. **5**(3): p. 181-193.
5. Booysen, C., Heyns, P.S., Hindley, M.P., and Scheepers, R., *Fatigue life assessment of a low pressure steam turbine blade during transient resonant conditions using a probabilistic approach.* International Journal of Fatigue, 2015. **73**: p. 17-26.
6. Atrens, A., Meyer, H., Faber, G., and Schneider, K., *Steam turbine blades.* Corrosion in power generating equipment, 1983: p. 299-330.
7. Mešt'áneka, P., *Low cycle fatigue analysis of a last stage steam turbine blade.* Applied and Computational Mechanics, 2008. **2**: p. 71-82.
8. Maruyama, K., Sawada, K., and Koike, J., *Strengthening mechanisms of creep resistant tempered martensitic steel.* ISIJ international, 2001. **41**(6): p. 641-653.
9. Robson, J.D., *Modelling of Carbide and Laves phase precipitation in 9-12 wt% Chromium Steels*. 1996, University of Cambridage.
10. Soady, K.A., *Reducing conservatism in life assessment approaches: Industrial steam turbine blade to disc interfaces and the shot peening process*, in *University of Southampton*. 2013.
11. Hamlett, R., *NDT in the Power Generation Industry Appreciation Course Lecture Notes*. 2009: Lavender International.
12. Suresh, S., *Fatigue of Materials*. 1998: Cambridge University Press.
13. Lukáš, P. and Kunz, L., *Cyclic plasticity and substructure of metals.* Materials Science and Engineering: A, 2002. **322**(1): p. 217-227.

14. Hales, R., Holdsworth, S.R., O'Donnell, M.P., Perrin, I.J., and Skelton, R.P., *A code of practice for the determination of cyclic stress-strain data.* Materials at High Temperatures, 2002. **19**(4): p. 164-185.

15. Cottrell, A. and Hull, D. *Extrusion and intrusion by cyclic slip in copper*. in *Proceedings of the Royal Society of London A: Mathematical, Physical and Engineering Sciences*. 1957. The Royal Society.

16. He, B., *Fatigue crack growth behaviour in a shot peened low pressure steam turbine blade material*. 2015, University of Southampton.

17. Soady, K.A., Mellor, B.G., West, G.D., Harrison, G., Morris, A., and Reed, P.A.S., *Evaluating surface deformation and near surface strain hardening resulting from shot peening a tempered martensitic steel and application to low cycle fatigue.* International Journal of Fatigue, 2013. **54**: p. 106-117.

18. Groover, M.P., *Fundamentals of Modern Manufacturing: Materials, Processes, and Systems*. 4 ed. 2010: Wiley.

19. Child, D.J., West, G.D., and Thomson, R.C., *Assessment of surface hardening effects from shot peening on a Ni-based alloy using electron backscatter diffraction techniques.* Acta Materialia, 2011. **59**(12): p. 4825-4834.

20. Dorr, T., Hilpert, M., Beckmerhagen, P., Kiefer, A., and Wagner, L. *Influence of shot peening on fatigue performance of high-strength aluminum and magnesium alloys*. in *the 7th International Conference on Shot Peening ICSP-7*. 1999. Warsaw.

21. Drechsler, A., Dorr, T., and Wagner, L., *Mechanical surface treatments on Ti–10V–2Fe–3Al for improved fatigue resistance.* Materials Science and Engineering: A, 1998. **243**(1): p. 217-220.

22. Zhang, P. and Lindemann, J., *Influence of shot peening on high cycle fatigue properties of the high-strength wrought magnesium alloy AZ80.* Scripta Materialia, 2005. **52**(6): p. 485-490.

23. Wagner, L. and Luetjering, G. *Influence of shot peening on the fatigue behavior of titanium alloys*. in *The First International Conference on Shot Peening*. 1996. Paris, France.

24. Wohlfahrt, H. *The influence of peening conditions on the resulting distribution of residual stress*. in *The Second International Conference on Shot Peening*. 1984.

25. O.Vohringer, *Changes in the State of the Material by Shot Peening (Retroactive Coverage).* Deutsche Gesellschaft fur Metallkunde e. V,, 1987: p. 185-204.

26. Noyan, I.C. and Cohen, J.B., *An X-ray diffraction study of the residual stress-strain distributions in shot-peened two-phase brass.* Materials Science and Engineering, 1985. **75**(1): p. 179-193.

27. Prevéy, P.S., *The measurement of subsurface residual stress and cold work distributions in nickel base alloys.* Residual Stress in Design, Process & Materials Selections, ed. WB Young, Metals Park, OH: Am. Soc. For Metals, 1987: p. 11-19.

28. Zinn, W. and Scholtes, B. *Influence of shot velocity and shot size on Almen intensity and residual stress depth distributions*. in *The 9th international conference on shot peening ICSP9*. 2005. Paris.

29. Zupanc, U. and Grum, J., *Surface Integrity of Shot Peened Aluminium Alloy 7075-T651.* Strojniški vestnik - Journal of Mechanical Engineering, 2011. **57**(05): p. 379-384.

30. Tosha, K. *Characteristics of shot peened surfaces and surface layers*. in *Asia-Pacific Forum on Precision Surface Finishing and Deburring*. 2001.

31. Withers, P.J. and Bhadeshia, H.K.D.H., *Residual stress. Part 1–measurement techniques.* Materials science and Technology, 2001. **17**(4): p. 355-365.

32. Tanaka, K. and Akiniwa, Y., *Diffraction Measurements of Residual Macrostress and Microstress Using X-Rays, Synchrotron and Neutrons.* JSME International Journal Series A, 2004. **47**(3): p. 252-263.

33. Soady, K.A., *Life assessment methodologies incoroporating shot peening process effects: mechanistic consideration of residual stresses and strain hardening Part 1 - effect of shot peening on fatigue resistance.* Materials Science and Technology, 2013. **29**(6): p. 637-651.

34. Scardi, P., Bortolamedi, T., Frendo, F., and Fontanari, V., *Comparison of the hole-drilling and X-ray diffraction methods for measuring the residual stresses in shot-peened aluminium alloys.* The Journal of Strain Analysis for Engineering Design, 2005. **40**(2): p. 199-209.

35. Micro-Measurements, V., *Measurement of residual stresses by the hole drilling strain gage method*. 2005, Tech Note TN-503-6.

36. Nobre, J.P., Kornmeier, M., and Dias, A.M., *Use of the hole-drilling method for measuring residual stresses in highly stressed shot-peened surfaces.* Experimental mechanics, 2000. **40**(3): p. 289-297.

37. Mahmoudi, A.H., Hossain, S., Truman, C.E., Smith, D.J., and Pavier, M.J., *A New Procedure to Measure Near Yield Residual Stresses Using the Deep Hole Drilling Technique.* Experimental Mechanics, 2008. **49**(4): p. 595-604.

38. Smith, D.J., *Deep hole drilling.* Practical residual stress measurement methods, 2013: p. 65-87.

39. Prime, M.B., *Cross-Sectional Mapping of Residual Stresses by Measuring the Surface Contour After a Cut.* Journal of Engineering Materials and Technology, 2001. **123**(2): p. 162.

40. DeWald, A.T. and Hill, M.R., *Multi-Axial Contour Method for Mapping Residual Stresses in Continuously Processed Bodies.* Experimental Mechanics, 2006. **46**(4): p. 473-490.

41. Pagliaro, P., Prime, M.B., Swenson, H., and Zuccarello, B., *Measuring Multiple Residual-Stress Components using the Contour Method and Multiple Cuts.* Experimental Mechanics, 2010. **50**(2): p. 187-194.

42. Smith, D.J., Farrahi, G.H., Zhu, W.X., and McMahon, C.A., *Experimental measurement and finite element simulation of the interaction between residual stresses and mechanical loading.* International Journal of Fatigue, 2001. **23**(4): p. 293-302.

43. Yin, F. and Fatemi, A., *Monotonic and Cyclic Deformations of Case-Hardened Steels Including Residual Stress Effects.* Strain, 2011. **47**(s1): p. e74-e83.

44. Laamouri, A., Sidhom, H., and Braham, C., *Evaluation of residual stress relaxation and its effect on fatigue strength of AISI 316L stainless steel ground surfaces: Experimental and numerical approaches.* International Journal of Fatigue, 2013. **48**: p. 109-121.

45. Coules, H.E., Smith, D.J., Abburi Venkata, K., and Truman, C.E., *A method for reconstruction of residual stress fields from measurements made in an incompatible region.* International Journal of Solids and Structures, 2014. **51**(10): p. 1980-1990.

46. Benedetti, M., Fontanari, V., and Monelli, B.D., *Numerical Simulation of Residual Stress Relaxation in Shot Peened High-Strength Aluminum Alloys Under Reverse Bending Fatigue.* Journal of Engineering Materials and Technology, 2010. **132**(1): p. 011012.

47. Jun, T.S., Venter, A.M., and Korsunsky, A.M., *Inverse Eigenstrain Analysis of the Effect of Non-uniform Sample Shape on the Residual Stress Due to Shot Peening.* Experimental Mechanics, 2010. **51**(2): p. 165-174.

48. Korsunsky, A.M., *Residual elastic strain due to laser shock peening: modelling by eigenstrain distribution.* The Journal of Strain Analysis for Engineering Design, 2006. **41**(3): p. 195-204.

49. Achintha, M., Nowell, D., Shapiro, K., and Withers, P.J., *Eigenstrain modelling of residual stress generated by arrays of laser shock peening shots and determination of the complete stress field using limited strain measurements.* Surface and Coatings Technology, 2013. **216**: p. 68-77.

50. Korsunsky, A.M., Regino, G.M., and Nowell, D., *Variational eigenstrain analysis of residual stresses in a welded plate.* International Journal of Solids and Structures, 2007. **44**(13): p. 4574-4591.

51. Walsh, M., Nowell, D., Liu, J., Latham, D., Regino, G.M., and Korsunsky, A.M., *Eigenstrain Analysis of Synchrotron X-Ray Diffraction Measurement of Residual Strains in Machined Nickel Alloy Plates.* The Journal of Strain Analysis for Engineering Design, 2006. **41**(5): p. 381-395.

52. Walsh, M.J., Li, H.Y., Latham, D.P., Regino, G.M., and Korsunsky, A.M., *Residual stresses in rolled and machined nickel alloy plates: synchrotron X-ray diffraction measurement and three-dimensional eigenstrain analysis.* The Journal of Strain Analysis for Engineering Design, 2007. **42**(1): p. 1-12.

53. Achintha, M. and Balan, B., *Characterisation of the mechanical behaviour of annealed glass–GFRP hybrid beams.* Construction and Building Materials, 2017. **147**: p. 174-184.

54. Achintha, M. and Balan, B.A., *An experimentally validated contour method/eigenstrains hybrid model to incorporate residual stresses in glass structural designs.* The Journal of Strain Analysis for Engineering Design, 2015. **50**(8): p. 614-627.

55. Balan, B.A. and Achintha, M., *Assessment of Stresses in Float and Tempered Glass Using Eigenstrains.* Experimental Mechanics, 2015. **55**(7): p. 1301-1315.

56. Korsunsky, A.M., *On the modelling of residual stresses due to surface peening using eigenstrain distributions.* The Journal of Strain Analysis for Engineering Design, 2005. **40**(8): p. 817-824.

57. Cláudio, R.A., Silva, J.M., Branco, C.M., and Byrne, J., *Fatigue life prediction of shot peened components.* Ciência & Tecnologia dos Materiais, 2008. **20**(1-2): p. 99-105.

58. Newby, M., James, M.N., and Hattingh, D.G., *Finite element modelling of residual stresses in shot-peened steam turbine blades.* Fatigue & Fracture of Engineering Materials & Structures, 2014. **37**(7): p. 707-716.

59. Jun, T.-S. and Korsunsky, A.M., *Evaluation of residual stresses and strains using the Eigenstrain Reconstruction Method.* International Journal of Solids and Structures, 2010. **47**(13): p. 1678-1686.

60. Hill, M.R. and DeWald, A.T., *Eigenstrain-based model for prediction of laser peening residual stresses in arbitrary three-dimensional bodies. Part 2: model verification.* The Journal of Strain Analysis for Engineering Design, 2009. **44**(1): p. 13-27.

61. Coratella, S., Burak, T.M., and Fitzpatrick, M.E., *Application of the Eigenstrain Theory to Predict Residual Stress around Curved Edges after Laser Shock Peening.* Materials Science Forum, 2014. **768**: p. 185-192.

62. King, A., Steuwer, A., Woodward, C., and Withers, P.J., *Effects of fatigue and fretting on residual stresses introduced by laser shock peening.* Materials Science and Engineering: A, 2006. **435**: p. 12-18.

63. Frija, M., Hassine, T., Fathallah, R., Bouraoui, C., and Dogui, A., *Finite element modelling of shot peening process: Prediction of the compressive residual stresses, the plastic deformations and the surface integrity.* Materials Science and Engineering: A, 2006. **426**(1-2): p. 173-180.

64. Bagherifard, S., Ghelichi, R., and Guagliano, M., *A numerical model of severe shot peening (SSP) to predict the generation of a nanostructured surface layer of material.* Surface and Coatings Technology, 2010. **204**(24): p. 4081-4090.

65. Meguid, S.A., Shagal, G., Stranart, J.C., and Daly, J., *Three-dimensional dynamic finite element analysis of shot-peening induced residual stresses.* Finite Elements in Analysis and Design, 1999. **31**(3): p. 179-191.

66. Sanjurjo, P., Rodríguez, C., Peñuelas, I., García, T.E., and Belzunce, F.J., *Influence of the target material constitutive model on the numerical simulation of a shot peening process.* Surface and Coatings Technology, 2014. **258**: p. 822-831.

67. Jun, T.S., Hofmann, F., Hofmann, M., and Korsunsky, A.M., *Residual stress characterization in 12%-Cr steel friction stir welds by neutron diffraction.* The Journal of Strain Analysis for Engineering Design, 2012. **47**(4): p. 203-213.

68. Kamaya, M., Wilkinson, A.J., and Titchmarsh, J.M., *Measurement of plastic strain of polycrystalline material by electron backscatter diffraction.* Nuclear Engineering and Design, 2005. **235**(6): p. 713-725.

69. Cahoon, J.R., Broughton, W.H., and Kutzak, A.R., *The Determination of Yield Strength from Hardness Measurements.* METALLURGICAL TRANSACTIONS, 1971. **2**.

70. Kamaya, M., Wilkinson, A.J., and Titchmarsh, J.M., *Quantification of plastic strain of stainless steel and nickel alloy by electron backscatter diffraction.* Acta Materialia, 2006. **54**(2): p. 539-548.

71. Gariépy, A., Bridier, F., Hoseini, M., Bocher, P., Perron, C., and Lévesque, M., *Experimental and numerical investigation of material heterogeneity in shot peened aluminium alloy AA2024-T351.* Surface and Coatings Technology, 2013. **219**: p. 15-30.

72. Dalaei, K., Persson, C., and Karlsson, B., *Stability of Residual Stresses Created by Shot Peening in Monotonic Loading and at the Presence of Load Reversals—Experiments and Modeling.* Journal of Engineering Materials and Technology, 2012. **134**(2): p. 021010.

73. Zhuang, W.Z. and Halford, G.R., *Investigation of residual stress relaxation under cyclic load.* International Journal of Fatigue, 2001. **23**.

74. Song, X., Liu, W.C., Belnoue, J.P., Dong, J., Wu, G.H., Ding, W.J., Kimber, S.A.J., Buslaps, T., Lunt, A.J.G., and Korsunsky, A.M., *An eigenstrain-based finite element model and the evolution of shot peening residual stresses during fatigue of GW103 magnesium alloy.* International Journal of Fatigue, 2012. **42**: p. 284-295.

75. Benedetti, M., Fontanari, V., Scardi, P., Ricardo, C.L.A., and Bandini, M., *Reverse bending fatigue of shot peened 7075-T651 aluminium alloy: The role of residual stress relaxation.* International Journal of Fatigue, 2009. **31**(8-9): p. 1225-1236.

76. Novovic, D., Dewes, R.C., Aspinwall, D.K., Voice, W., and Bowen, P., *The effect of machined topography and integrity on fatigue life.* International Journal of Machine Tools and Manufacture, 2004. **44**(2-3): p. 125-134.

77. He, B.Y., Soady, K.A., Mellor, B.G., Morris, A., and Reed, P.A.S., *Effects of shot peening on short crack growth rate and resulting low cycle fatigue behaviour in low pressure turbine blade material.* Materials Science and Technology, 2013. **29**(7): p. 788-796.

78. Wagner, L., *Mechanical surface treatments on titanium, aluminum and magnesium alloys.* Materials Science and Engineering: A, 1999. **263**(2): p. 210-216.

79. Torres, M.A.S. and Voorwald, H.J.C., *An evaluation of shot peening, residual stress and stress relaxation on the fatigue life of AISI 4340 steel.* International Journal of Fatigue, 2002. **24**(8): p. 877–886.

80. Gao, Y.K., *Improvement of fatigue property in 7050–T7451 aluminum alloy by laser peening and shot peening.* Materials Science and Engineering: A, 2011. **528**(10-11): p. 3823-3828.

81. Webster, G.A. and Ezeilo, A.N., *Residual stress distributions and their influence on fatigue lifetimes.* International Journal of Fatigue, 2001. **23**: p. 375-383.

82. He, B.Y., Soady, K.A., Mellor, B.G., Harrison, G., and Reed, P.A.S., *Fatigue crack growth behaviour in the LCF regime in a shot peened steam turbine blade material.* International Journal of Fatigue, 2016. **82**: p. 280-291.

83. Gérin, B., Pessard, E., Morel, F., and Verdu, C., *Competition between surface defects and residual stresses on fatigue behaviour of shot peened forged components.* Procedia Structural Integrity, 2016. **2**: p. 3226-3232.

84. Kim, J.-C., Cheong, S.-K., and Noguchi, H., *A non-microstructural crack formation model for understanding fatigue life degradation in shot peened carbon steel under LCF loading.* International Journal of Fatigue, 2014. **63**: p. 110-117.

85. Terres, M.A., Laalai, N., and Sidhom, H., *Effect of nitriding and shot-peening on the fatigue behavior of 42CrMo4 steel: Experimental analysis and predictive approach.* Materials & Design, 2012. **35**: p. 741-748.

86. Dalaei, K., Karlsson, B., and Svensson, L.E., *Stability of shot peening induced residual stresses and their influence on fatigue lifetime.* Materials Science and Engineering: A, 2011. **528**(3): p. 1008-1015.

87. Kim, J.-C., Cheong, S.-K., and Noguchi, H., *Evolution of residual stress redistribution associated with localized surface microcracking in shot-peened medium-carbon steel during fatigue test.* International Journal of Fatigue, 2013. **55**: p. 147-157.

88. Koster, W.P. *Effect of Residual Stress on Fatigue of Structural Alloys*. in *Practical Applications of Residual Stress Technology*. 1991. Indianapolis, Indiana.

89. Rios, E.R.d.l., Walley, A., Milan, M.T., and Hammersley, G., *Fatigue crack initiation and propagation on shot-peened surfaces in A316 stainless steel.* International Journal of Fatigue, 1995. **17**(7): p. 493-499.

90. Zhang, P., Lindemann, J., and Leyens, C., *Influence of shot peening on notched fatigue strength of the high-strength wrought magnesium alloy AZ80.* Journal of Alloys and Compounds, 2010. **497**(1-2): p. 380-385.

91. Guagliano, M. and Vergani, L., *An approach for prediction of fatigue strength of shot peened components.* Engineering Fracture Mechanics, 2004. **71**(4-6): p. 501-512.

92. Starker, P., Wohlfahrt, H., and Macherauch, E., *Subsurface Crack Initiation During Fatigue as a Result of Residual Stresses.* Fatigue of Engineering Materials & Structures, 1979. **1**(3): p. 319-327.

93. Doremus, L., Cormier, J., Villechaise, P., Henaff, G., Nadot, Y., and Pierret, S., *Influence of residual stresses on the fatigue crack growth from surface anomalies in a nickel-based superalloy.* Materials Science and Engineering: A, 2015. **644**: p. 234-246.

94. Lin, B., Lupton, C., Spanrad, S., Schofield, J., and Tong, J., *Fatigue crack growth in laser-shock-peened Ti–6Al–4V aerofoil specimens due to foreign object damage.* International Journal of Fatigue, 2014. **59**: p. 23-33.

95. Černý, I., Sís, J., and Mikulová, D., *Short fatigue crack growth in an aircraft Al-alloy of a 7075 type after shot peening.* Surface and Coatings Technology, 2014. **243**: p. 20-27.

96. Gao, Y.K. and Wu, X.R., *Experimental investigation and fatigue life prediction for 7475-T7351 aluminum alloy with and without shot peening-induced residual stresses.* Acta Materialia, 2011. **59**(9): p. 3737-3747.

97. Zabeen, S., Preuss, M., and Withers, P.J., *Evolution of a laser shock peened residual stress field locally with foreign object damage and subsequent fatigue crack growth.* Acta Materialia, 2015. **83**: p. 216-226.

98. Bergström, J. and Ericsson, T., *RELAXATION OF SHOT PEENING INDUCED COMPRESSIVE STRESS DURING FATIGUE OF NOTCHED STEELSAMPLES.* Surface Engineering, 1986. **2**(2): p. 115-120.

99. Nalla, R.K., Altenberger, I., Noster, U., Liu, G.Y., Scholtes, B., and Ritchie, R.O., *On the influence of mechanical surface treatments—deep rolling and laser shock peening—on the fatigue behavior of Ti–6Al–4V at ambient and elevated temperatures.* Materials Science and Engineering: A, 2003. **355**(1-2): p. 216-230.

100. Benedetti, M., *Bending fatigue behaviour of differently shot peened Al 6082 T5 alloy.* International Journal of Fatigue, 2004. **26**(8): p. 889-897.

101. Dalaei, K., Karlsson, B., and Svensson, L.E., *Stability of residual stresses created by shot peening of pearlitic steel and their influence on fatigue behaviour.* Procedia Engineering, 2010. **2**(1): p. 613-622.

102. Kim, S.-B., Evans, A., Shackleton, J., Bruno, G., Preuss, M., and Withers, P.J., *Stress Relaxation of Shot Peened Udimet 720Li under Solely Elevated-Temperature Exposure and under Isothermal Fatigue.* Metallurgical and Materials Transactions A, 2005. **36**(11): p. 3041-3053.

103. Evans, A., Kim, S., Shackleton, J., Bruno, G., Preuss, M., and Withers, P., *Relaxation of residual stress in shot peened Udimet 720Li under high temperature isothermal fatigue.* International Journal of Fatigue, 2005. **27**(10-12): p. 1530-1534.

104. Holzapfel, H., Schulze, V., Vohringer, O., and Macherauch, E., *Residual stress relaxation in an AISI 4140 steel due to quasistatic and cyclic loading at higher temperatures.* Materials Science and Engineering A, 1998. **248**(1): p. 9-18.

105. James, M.N., Newby, M., Hattingh, D.G., and Steuwer, A., *Shot-peening of steam turbine blades: Residual stresses and their modification by fatigue cycling.* Procedia Engineering, 2010. **2**(1): p. 441-451.

106. Eleiche, A.M., Megahed, M.M., and Abd-Allah, N.M., *The shot-peening effect on the HCF behavior of high-strength martensitic steels.* Journal of Materials Processing Technology, 2001. **113**(1): p. 502-508.

107. Altenberger, I., Scholtes, B., Martin, U., and Oettel, H., *Cyclic deformation and near surface microstructures of shot peened or deep rolled austenitic stainless steel AISI 304.* Materials Science and Engineering A, 1999. **264**(1): p. 1-16.

108. Pangborn, R.N., Weissmann, S., and Kramer, I.R., *Prediction of Fatigue Life by X-Ray Diffraction Methods.* Fatigue of Engineering Materials and Structures, 1979. **1**(3): p. 363-369.

109. Coffin, L., *Fatigue in Machines and Structures--Power Generation.* Fatigue and microstructure, 1978: p. 1-27.

110. Coffin Jr, L., *A study of the effect of cyclic thermal stresses on a ductile metal.* American Society of Mechanical Engineers, 1954. **76**: p. 931-950.

111. Manson, S.S., *Behavior of materials under conditions of thermal stress*. 1953: NACA TN 2933.

112. Gerber, H., *Bestimmung der zulässigen spannungen in eisen-constructionen*. 1874: Wolf.

113. Goodman, J., *Mechanics Applied to Engineering*. 1899, Longmans, Green, London.

114. Soderberg, C.R., *Factor of safety and working stress.* Transactions of the American Society of Mechanical Engineers, 1939. **52**: p. 13-28.

115. Smith, K.N., Topper, T.H., and Watson, P., *A stress-strain function for the fatigue of metals.* Journal of Materials, 1970. **5**: p. 767-778.

116. Flavenot, J.F. and Skalii, N., *A comparison of multiaxial fatigue criteria incorporating residual stress effects.* Mechanical Engineering Publications, 1989: p. 437–457.

117. Sines, G., Waisman, J.L., and Dolan, T.J., *Metal fatigue*. 1959: McGraw-Hill.

118. Crossland, B. *Effect of large hydrostatic pressures on the torsional fatigue strength of an alloy steel*. in *Proc. Int. Conf. on Fatigue of Metals*. 1956. Institution of Mechanical Engineers London.

119. Van, K.D., *Sur la résistance à la fatigue des métaux*. 1971.

120. Findley, W.N., *A theory for the effect of mean stress on fatigue of metals under combined torsion and axial load or bending*. 1958: Engineering Materials Research Laboratory, Division of Engineering, Brown University.

121. Socie, D.F., *Multiaxial Fatigue Damage Models.* Journal of Engineering Materials and Technology, 1987. **109**(4): p. 293-298.

122. Fatemi, A. and Socie, D.F., *A critical plane approach to multiaxial fatigue damage including out-of-phase loading.* Fatigue & Fracture of Engineering Materials & Structures, 1988. **11**(3): p. 149-165.

123. Fatemi, A. and Shamsaei, N., *Multiaxial fatigue: An overview and some approximation models for life estimation.* International Journal of Fatigue, 2011. **33**(8): p. 948-958.

124. Liu, J. and Pang, M., *Fatigue life prediction of shot-peened steel.* International Journal of Fatigue, 2012. **43**: p. 134-141.

125. Benedetti, M., Fontanari, V., Santus, C., and Bandini, M., *Notch fatigue behaviour of shot peened high-strength aluminium alloys: Experiments and predictions using a critical distance method.* International Journal of Fatigue, 2010. **32**(10): p. 1600-1611.

126. Benedetti, M., Fontanari, V., and Bandini, M., *A simplified and fast method to predict plain and notch fatigue of shot peened high-strength aluminium alloys under reverse bending.* Surface and Coatings Technology, 2011.

127. Rice, J.R., *A path independent integral and the approximate analysis of strain concentration by notches and cracks.* Journal of applied mechanics, 1968. **35**(2): p. 379-386.

128. Wells, A., *Application of fracture mechanics at and beyond general yielding.* British Welding Journal, 1963. **10**(11): p. 563-70.

129. Benedetti, M., Fontanari, V., Bandini, M., and Taylor, D., *Multiaxial fatigue resistance of shot peened high-strength aluminum alloys.* International Journal of Fatigue, 2014. **61**: p. 271-282.

130. Zhuang, W.Z. and Halford, G.R., *Investigation of residual stress relaxation under cyclic load.* International Journal of Fatigue, 2001. **23**: p. 31-37.

131. Zaroog, O.S., Ali, A., Sahari, B.B., and Zahari, R., *Modeling of residual stress relaxation of fatigue in 2024-T351 aluminium alloy.* International Journal of Fatigue, 2011. **33**(2): p. 279-285.

132. Benedetti, M., Fontanari, V., and Bandini, M., *A simplified and fast method to predict plain and notch fatigue of shot peened high-strength aluminium alloys under reverse bending.* Surface and Coatings Technology, 2014. **243**: p. 2-9.

133. Buchanan, D.J. and John, R., *Residual stress redistribution in shot peened samples subject to mechanical loading.* Materials Science and Engineering: A, 2014. **615**: p. 70-78.

134. Musinski, W.D. and McDowell, D.L., *On the eigenstrain application of shot-peened residual stresses within a crystal plasticity framework: Application to Ni-base superalloy specimens.* International Journal of Mechanical Sciences, 2015. **100**: p. 195-208.

135. Zhou, Z., Gill, A.S., Qian, D., Mannava, S.R., Langer, K., Wen, Y., and Vasudevan, V.K., *A finite element study of thermal relaxation of residual stress in laser shock peened IN718 superalloy.* International Journal of Impact Engineering, 2011. **38**(7): p. 590-596.

136. Zhou, Z., Bhamare, S., Ramakrishnan, G., Mannava, S.R., Langer, K., Wen, Y., Qian, D., and Vasudevan, V.K., *Thermal relaxation of residual stress in laser shock peened Ti–6Al–4V alloy.* Surface and Coatings Technology, 2012. **206**(22): p. 4619-4627.

137. Ren, X.D., Zhan, Q.B., Yuan, S.Q., Zhou, J.Z., Wang, Y., Ren, N.F., Sun, G.F., Zheng, L.M., Dai, F.Z., Yang, H.M., and Dai, W.J., *A finite element analysis of thermal relaxation of residual stress in laser shock processing Ni-based alloy GH4169.* Materials & Design, 2014. **54**: p. 708-711.

138. Chaboche, J.L., *Time-independent constitutive theories for cyclic plasticity.* International Journal of Plasticity, 1986. **2**(2): p. 149-188.

139. Susmel, L., *The theory of critical distances: a review of its applications in fatigue.* Engineering Fracture Mechanics, 2008. **75**(7): p. 1706-1724.

140. Taylor, D., *The theory of critical distances.* Engineering Fracture Mechanics, 2008. **75**(7): p. 1696-1705.

141. Benedetti, M., Fontanari, V., Bandini, M., and Savio, E., *High- and very high-cycle plain fatigue resistance of shot peened high-strength aluminum alloys: The role of surface morphology.* International Journal of Fatigue, 2015. **70**: p. 451-462.

142. Benedetti, M., Fontanari, V., Winiarski, B., Withers, P.J., Allahkarami, M., and Hanan, J.C., *Fatigue Behavior of Shot Peened Notched Specimens: Effect of the Residual Stress Field Ahead of the Notch Root.* Procedia Engineering, 2015. **109**: p. 80-88.

143. Benedetti, M., Fontanari, V., Allahkarami, M., Hanan, J.C., and Bandini, M., *On the combination of the critical distance theory with a multiaxial fatigue criterion for predicting the fatigue strength of notched and plain shot-peened parts.* International Journal of Fatigue, 2016. **93**: p. 133-147.

144. Cuellar, S.D., Hill, M.R., DeWald, A.T., and Rankin, J.E., *Residual stress and fatigue life in laser shock peened open hole samples.* International Journal of Fatigue, 2012. **44**: p. 8-13.

145. Prasannavenkatesan, R., Zhang, J., McDowell, D.L., Olson, G.B., and Jou, H.-J., *3D modeling of subsurface fatigue crack nucleation potency of primary inclusions in heat treated and shot peened martensitic gear steels.* International Journal of Fatigue, 2009. **31**(7): p. 1176-1189.

146. Fridrici, V., Fouvry, S., Kapsa, P., and Perruchaut, P., *Prediction of cracking in Ti–6Al–4V alloy under fretting-wear: use of the SWT criterion.* Wear, 2005. **259**(1-6): p. 300-308.

147. Ding, J., Kang, G., Zhu, Y., and Zhu, M., *Finite element analysis on bending fretting fatigue of 316L stainless steel considering ratchetting and cyclic hardening.* International Journal of Mechanical Sciences, 2014. **86**: p. 26-33.

148. Lykins, C.D., Mall, S., and Jain, V., *An evaluation of parameters for predicting fretting fatigue crack initiation.* International Journal of Fatigue, 2000. **22**(8): p. 703-716.

149. Zhu, Y., Kang, G., Ding, J., and Zhu, M., *Study on bending fretting fatigue of LZ50 axle steel considering ratchetting by finite element method.* Fatigue & Fracture of Engineering Materials & Structures, 2013. **36**(2): p. 127-138.

150. Rios, E.R.D.L., Trull, M., and Levers, A., *Modelling fatigue crack growth in shot-peened components of Al 2024-T351.* Fatigue & Fracture of Engineering Materials and Structures, 2000. **23**(8): p. 709-716.

151. Xiang, Y. and liu, Y., *Mechanism modelling of shot peening effect on fatigue life prediction.* Fatigue & Fracture of Engineering Materials & Structures, 2010. **33**(2): p. 116-125.

152. Liu, Y. and Mahadevan, S., *Fatigue limit prediction of notched components using short crack growth theory and an asymptotic interpolation method.* Engineering Fracture Mechanics, 2009. **76**(15): p. 2317-2331.

153. Smyth, N., *Effect on Fatigue Performance of Residual Stress induced via Laser Shock Peening in Mechanically Damaged 2024-T351 Aluminium Sheet*, in *School of Applied Science*. 2014, Cranfield University: Cranfield.

154. Cláudio, R.A., Burgess, A., Branco, C.M., and Byrne, J., *Failure analysis of scratch damaged shot peened simulated components at high temperature.* Engineering Failure Analysis, 2009. **16**(4): p. 1208-1220.

155. Cláudio, R.A., Silva, J.M., Branco, C.M., and Byrne, J., *A fracture mechanics based approach to predict fatigue life of scratch damaged shot peened components.* Procedia Engineering, 2011. **10**: p. 2672-2677.

156. Bueckner, H.F., *Novel principle for the computation of stress intensity factors.* Zeitschrift fuer Angewandte Mathematik & Mechanik, 1970. **50**(9).

157. Newman, J.C., *FASTRAN-2: a fatigue crack growth structural analysis program.* NASA technical memorandum 104159, 1992.

158. Pavier, M.J., Poussard, C.G.C., and Smith, D.J., *Effect of residual stress around cold worked holes on fracture under superimposed mechanical load.* Engineering Fracture Mechanics, 1999. **63**(6): p. 751-773.

159. Al-Mukhtar, A.M., *Consideration of the residual stress distributions in fatigue crack growth calculations for assessing welded steel joints.* Fatigue & Fracture of Engineering Materials & Structures, 2013. **36**(12): p. 1352-1361.

160. Stuart, D.H., Hill, M.R., and Newman, J.C., *Correlation of one-dimensional fatigue crack growth at cold-expanded holes using linear fracture mechanics and superposition.* Engineering Fracture Mechanics, 2011. **78**(7): p. 1389-1406.

161. Larue, J. and Daniewicz, S., *Predicting the effect of residual stress on fatigue crack growth.* International Journal of Fatigue, 2007. **29**(3): p. 508-515.

162. Beghini, M. and Bertini, L., *Fatigue crack propagation through residual stress fields with closure phenomena.* Engineering Fracture Mechanics, 1990. **36**(3): p. 379-387.

163. Ma, Y.E., Staron, P., Fischer, T., and Irving, P.E., *Size effects on residual stress and fatigue crack growth in friction stir welded 2195-T8 aluminium – Part II: Modelling.* International Journal of Fatigue, 2011. **33**(11): p. 1426-1434.

164. Courtin, S., Gardin, C., Bézine, G., and Ben Hadj Hamouda, H., *Advantages of the J-integral approach for calculating stress intensity factors when using the commercial finite element software ABAQUS.* Engineering Fracture Mechanics, 2005. **72**(14): p. 2174-2185.

165. He, B.Y., Katsamenis, O.L., Mellor, B.G., and Reed, P.A.S., *3-D analysis of fatigue crack behaviour in a shot peened steam turbine blade material.* Materials Science and Engineering: A, 2015. **642**: p. 91-103.

166. Soady, K.A., Mellor, B.G., Shackleton, J., Morris, A., and Reed, P.A.S., *The effect of shot peening on notched low cycle fatigue.* Materials Science and Engineering: A, 2011. **528**(29-30): p. 8579-8588.

167. He, B., *Fatigue crack growth behaviour in a shot peened low pressure steam turbine blade material*. 2015, University of Southampton.

168. Perkins, K.M. and Bache, M.R., *The influence of inclusions on the fatigue performance of a low pressure turbine blade steel.* International Journal of Fatigue, 2005. **27**(6): p. 610-616.

169. Yaguchi, M., *Ratchetting of viscoplastic material with cyclic softening, part 1: experiments on modified 9Cr?1Mo steel.* International Journal of Plasticity, 2005. **21**(1): p. 43-65.

170. Chaboche, J.L., *A review of some plasticity and viscoplasticity constitutive theories.* International Journal of Plasticity, 2008. **24**(10): p. 1642-1693.

171. Yung Fan, B.B., *Implementation of the Eigenstrain Deep-Hole Method of Residual Stress Measurement.*

172. Tong, J., *Modelling of cyclic plasticity and viscoplasticity of a nickel-based alloy using Chaboche constitutive equations.* International Journal of Fatigue, 2004. **26**(8): p. 829-837.

173. Badnava, H., Pezeshki, S.M., Fallah Nejad, K., and Farhoudi, H.R., *Determination of combined hardening material parameters under strain controlled cyclic loading by using the genetic algorithm method.* Journal of Mechanical Science and Technology, 2012. **26**(10): p. 3067-3072.

174. Lemaitre, J. and Chaboche, J.L., *Mechanics of solid materials*. 1994: Cambridge University Press.

175. Zhao, L.G., Tong, J., Vermeulen, B., and Byrne, J., *On the uniaxial mechanical behaviour of an advanced nickel base superalloy at high temperature.* Mechanics of materials, 2001. **33**(10): p. 593-600.

176. Chaboche, J.L., *On some modifications of kinematic hardening to improve the description of ratchetting effects.* International journal of plasticity, 1991. **7**(7): p. 661-678.

177. John H. Crews, J., *Elastoplastic stress-strain behaviour at notch roots in sheet specimens under constant-amplitude loading.* NASA, 1969.

178. Fatemi, A. and Zeng, Z., *Elasto-plastic stress and strain behaviour at notch roots under monotonic and cyclic loadings.* The Journal of Strain Analysis for Engineering Design, 2001. **36**(3): p. 287-300.

179. SHINGAI, K., *Study on Elastic-Plastic Strain Behavior of Notched Specimen.* Reports of the Faculty of Engineering, Nagasaki University, 1998. **28**.

180. M.E. Fitzpatrick, A.T. Fry, P. Holdway, F.A. Kandil, Shackleton, J., and Suominen, L., *Determination of residual stresses by X-ray diffraction*, in *Measurement Good Practice Guide No. 52*. 2005.

181. Zhang, D., Xu, K., and He, J., *Aspects of the residual stress field at a notch and its effect on fatigue.* Materials Science and Engineering: A, 1991. **136**: p. 79-83.

182. Nobre, J.P., Batista, A.C., Coelho, L., and Dias, A.M., *Two experimental methods to determining stress–strain behavior of work-hardened surface layers of metallic components.* Journal of Materials Processing Technology, 2010. **210**(15): p. 2285-2291.

183. Vasu, A. and Grandhi, R.V., *Effects of curved geometry on residual stress in laser peening.* Surface and Coatings Technology, 2013. **218**: p. 71-79.

184. Vasu, A., Hu, Y., and Grandhi, R.V., *Differences in plasticity due to curvature in laser peened components.* Surface and Coatings Technology, 2013. **235**: p. 648-656.

185. Bergström, J. and Ericsson, T., *Relaxation of shot peening induced compressive stress during fatigue of notched steel samples.* Surface Engineering, 1986. **2**(2): p. 115-120.

186. Holzapfel, H., Schulze, V., Vohringer, O., and Macherauch, E., *Residual stress relaxation in an AISI 4140 steel due to quasistatic and cyclic loading at higher temperatures.* Materials Science and Engineering: A, 1998. **248**(1): p. 9-18.

187. Shamsaei, N. and Fatemi, A., *Effect of hardness on multiaxial fatigue behaviour and some simple approximations for steels.* Fatigue & Fracture of Engineering Materials & Structures, 2009. **32**(8): p. 631-646.

188. Palin-Luc, T., Coupard, D., Dumas, C., and Bristiel, P., *Simulation of multiaxial fatigue strength of steel component treated by surface induction hardening and comparison with experimental results.* International Journal of Fatigue, 2011. **33**(8): p. 1040-1047.

189. Araujo, J.A. and Nowell, D., *The effect of rapidly varying contact stress fields on fretting fatigue.* International Journal of Fatigue, 2002. **24**(7): p. 763-775.

190. Jiang, Y., Hertel, O., and Vormwald, M., *An experimental evaluation of three critical plane multiaxial fatigue criteria.* International Journal of Fatigue, 2007. **29**(8): p. 1490-1502.

191. Findley, K.O. and Saxena, A., *Low Cycle Fatigue in Rene 88DT at 650 ˚C: Crack Nucleation Mechanisms and Modeling.* Metallurgical and Materials Transactions A, 2006. **37**(5): p. 1469-1475.

192. Zhao, T. and Jiang, Y., *Fatigue of 7075-T651 aluminum alloy.* International Journal of Fatigue, 2008. **30**(5): p. 834-849.

193. WU, X.R. and Carlsson, A.J., *Weight functions and stress intensity factor solutions*. 1991, Oxford: Pergamon Press.

194. Lei, Y., O'Dowd, N.P., and Webster, G.A., *Fracture mechanics analysis of a crack in a residual stress field.* International Journal of Fracture, 2000. **106**(3): p. 195-216.

195. Lei, Y., *J calculation for a crack in a welding residual stress field following a FE welding simulation.* Trans SMiRT, 2015. **23**.

196. Scott, P.M. and Thorpe, T.W., *A critical review of crack tip stress intensity factors for semi-elliptic cracks.* Fracture of Engineering Materials & Structures, 1981. **4**(4): p. 291-309.

197. Carpinteri, A., *Shape change of surface cracks in round bars under cyclic axial loading.* International Journal of Fatigue, 1993. **15**(1): p. 21-26.

198. Lin, X.B. and Smith, R.A., *Finite element modelling of fatigue crack growth of surface cracked plates Part II Crack shape change.* Engineering Fracture Mechanics, 1999. **63**(5): p. 523-540.

199. Branco, R., Antunes, F.V., Ricardo, L.C.H., and Costa, J.D., *Extent of surface regions near corner points of notched cracked bodies subjected to mode-I loading.* Finite Elements in Analysis and Design, 2012. **50**: p. 147-160.

200. Hou, C.-Y., *Three-dimensional finite element analysis of fatigue crack closure behavior in surface flaws.* International Journal of Fatigue, 2004. **26**(11): p. 1225-1239.

201. Daniewicz, S.R. and Aveline, C.R., *Strip-yield and finite element analysis of part-through surface flaws.* Engineering Fracture Mechanics, 2000. **67**: p. 21-39.

202. Gardin, C., Fiordalisi, S., Sarrazin-Baudoux, C., Gueguen, M., and Petit, J., *Numerical prediction of crack front shape during fatigue propagation considering plasticity-induced crack closure.* International Journal of Fatigue, 2016. **88**: p. 68-77.

203. Predan, J., Močilnik, V., and Gubeljak, N., *Stress intensity factors for circumferential semi-elliptical surface cracks in a hollow cylinder subjected to pure torsion.* Engineering Fracture Mechanics, 2013. **105**: p. 152-168.

204. Shin, C.S. and Cai, C.Q., *Experimental and finite element analyses on stress intensity factors of an elliptical surface crack in a circular shaft under tension and bending.* International Journal of Fracture, 2004. **129**(3): p. 239-264.

205. Toribio, J., Matos, J.C., González, B., and Escuadra, J., *Numerical modelling of crack shape evolution for surface flaws in round bars under tensile loading.* Engineering Failure Analysis, 2009. **16**(2): p. 618-630.

206. Hou, C.-Y., *Simulation of surface crack shape evolution using the finite element technique and considering the crack closure effects.* International Journal of Fatigue, 2011. **33**(5): p. 719-726.

207. Ferrié, E., Buffière, J.-Y., Ludwig, W., Gravouil, A., and Edwards, L., *Fatigue crack propagation: In situ visualization using X-ray microtomography and 3D simulation using the extended finite element method.* Acta Materialia, 2006. **54**(4): p. 1111-1122.

208. Carpinteri, A., Brighenti, R., and Vantadori, S., *Surface cracks in notched round bars under cyclic tension and bending.* International Journal of Fatigue, 2006. **28**(3): p. 251-260.

209. Carpinteri, A., Brighenti, R., and Vantadori, S., *Influence of the cold-drawing process on fatigue crack growth of a V-notched round bar.* International Journal of Fatigue, 2010. **32**(7): p. 1136-1145.

210. Lin, X.B. and Smith, R.A., *Finite element modelling of fatigue crack growth of surface cracked plates Part I The numerical technique.* Engineering Fracture Mechanics, 1999. **63**(5): p. 503-522.

211. Lin, X.B. and Smith, R.A., *Finite element modelling of fatigue crack growth of surface cracked plates Part III Stress intensity factor and fatigue crack growth life.* Engineering Fracture Mechanics, 1999. **63**(5): p. 541-556.

212. Burke-Veliz, A., Syngellakis, S., and Reed, P.A.S., *Assessment of three-dimensional crack growth in ductile layered material systems.* Engineering Fracture Mechanics, 2012. **88**: p. 15-27.

213. Branco, R., Antunes, F.V., and Costa, J.D., *A review on 3D-FE adaptive remeshing techniques for crack growth modelling.* Engineering Fracture Mechanics, 2015. **141**: p. 170-195.

214. Newman, J.C. and Raju, I.S., *An empirical stress-intensity factor equation for the surface crack.* Engineering fracture mechanics, 1981. **15**(1-2): p. 185-192.

215. Ammar, O., Haddar, N., and Remy, L., *Numerical computation of crack growth of Low Cycle Fatigue in the 304L austenitic stainless steel.* Engineering Fracture Mechanics, 2014. **120**: p. 67-81.

216. Singh, I.V., Mishra, B.K., Bhattacharya, S., and Patil, R.U., *The numerical simulation of fatigue crack growth using extended finite element method.* International Journal of Fatigue, 2012. **36**(1): p. 109-119.